

# Rolling Contact Fatigue of Hypoeutectoid Steel

ZUR ERLANGUNG DES AKADEMISCHEN GRADES  
**Doktor der Ingenieurwissenschaften**  
DER FAKULTÄT FÜR MASCHINENBAU  
KARLSRUHER INSTITUT FÜR TECHNOLOGIE (KIT)

genehmigte  
**Dissertation**  
von

Dipl.-Ing. Sager Dave Sircar

aus Ahlen (Westfalen)

TAG DER MÜNDLICHEN PRÜFUNG: 04. MAI 2015  
HAUPTREFERENT: PROF. DR.RER.NAT. ALEXANDER WANNER  
KOREFERENT: PROF. DR.-ING. GERHARD POLL



This document is licensed under the Creative Commons Attribution – Share Alike 3.0 DE License (CC BY-SA 3.0 DE): <http://creativecommons.org/licenses/by-sa/3.0/de/>

*Für meinen geliebten Vater, dem es nicht mehr vergönnt  
war die Vollendung dieser Arbeit zu erleben.*



# Contents

<b>Acknowledgement / Danksagung</b>	<b>iii</b>
<b>Abstract / Zusammenfassung</b>	<b>iv</b>
<b>List of Abbreviations</b>	<b>vi</b>
<b>1. Introduction</b>	<b>1</b>
<b>2. State of the Art</b>	<b>2</b>
2.1. Bearings: An Overview . . . . .	2
2.2. Bearing Life Calculation . . . . .	2
2.3. Microstructural Changes within Bearings . . . . .	7
2.3.1. Dark Etching Regions . . . . .	7
2.3.2. Three Stage Rolling Contact Fatigue Model . . . . .	7
2.3.3. Flat White Bands / Low Angle Bands . . . . .	10
2.3.4. Decrease of X-Ray Peak Full Width at Half Maximum Height . . . . .	13
2.4. Indentation of Particles into Raceways . . . . .	15
2.5. Lubrication . . . . .	21
2.6. Determination of Non-Metallic Inclusions . . . . .	23
<b>3. Dynamic Testing under Time-invariant Loading</b>	<b>30</b>
3.1. Motivation . . . . .	30
3.2. Testing Method . . . . .	30
3.3. Specimen Geometry . . . . .	31
3.4. Investigated Materials . . . . .	34
3.5. Testing procedure . . . . .	38
3.6. Results . . . . .	38
3.6.1. Weibull Curves . . . . .	38
3.6.2. Observed Damage Mechanisms . . . . .	39
3.7. Discussion . . . . .	46
3.7.1. General Discussion . . . . .	46
3.7.2. Origin of Indentation Causing Metallic Particles . . . . .	47
3.7.3. Influence of Residual Stresses on Crack Growth . . . . .	49
3.8. Summary . . . . .	55
<b>4. Service Life Determination for Time-invariant Loading</b>	<b>56</b>
4.1. Motivation . . . . .	56
4.2. Micrographic Analysis of Bearing Life . . . . .	56

## Contents

---

4.3.	Determination of Subsurface L10-Life with Means of Microstructural Decay	57
4.3.1.	Calibration of FWHM Curves for Service Life Rating	57
4.3.2.	Calculation of Dynamic Capacity	67
4.4.	Modelling of Surface Crack Growth	70
4.4.1.	Overview	70
4.4.2.	Short Crack Growth Model	71
4.4.3.	Linear Elastic Fracture Mechanics Calculations	73
4.5.	Summary	80
<b>5.</b>	<b>Design and Development of a Test Rig for Dynamic Testing under highly Time-variant Load Changes</b>	<b>82</b>
5.1.	Motivation	82
5.2.	Overview of Existing Test Methods	82
5.2.1.	Dynamic Testing	82
5.2.2.	Twin Disc Testing	83
5.2.3.	Ball-on-Disc / Pin-on-Disc Test	83
5.2.4.	FE8 Test	83
5.2.5.	Thrust Type Testing	84
5.2.6.	BTR	84
5.3.	Design Guidelines	85
5.4.	Definition of Goals	87
5.4.1.	Observation of the Real Application	87
5.4.2.	Additional Requirements	89
5.5.	Principle Designs	91
5.6.	Overview and Evaluation of Major Components	95
5.6.1.	Actuator	95
5.6.2.	Bearing Bracket	97
5.7.	Overview of Sensory Data	97
5.8.	Realisation of the Test Rig	100
5.9.	Preliminary Tests	102
5.10.	Functional Validation	102
5.11.	Summary	107
<b>6.</b>	<b>Conclusion</b>	<b>108</b>
<b>A.</b>	<b>Cross Section of Bar Materials</b>	<b>111</b>
<b>B.</b>	<b>Oil Analysis</b>	<b>112</b>
<b>C.</b>	<b>Bearing Cleanliness Analysis</b>	<b>114</b>
<b>D.</b>	<b>Equation Hertzian Solutions</b>	<b>120</b>
<b>E.</b>	<b>Bearing Kinematic Formulas</b>	<b>128</b>

# Acknowledgement / Danksagung

Die vorliegende Arbeit entstand während meiner Doktorandenzeit bei der Daimler AG zwischen Februar 2011 und Juli 2014. Ich danke allen, die zum Gelingen dieser Arbeit beigetragen und mich unterstützt haben.

Mein besonderer Dank gilt den Professoren Herrn Prof. Dr. rer. nat. Jürgen Gegner und Prof. Dr.-Ing. Gerhard Poll, die mich sowohl mit ihren Anlagen und ihrem Wissen unterstützt und einen wesentlichen Einfluss für das Gelingen dieser Arbeit haben.

In gleichem Maße geht mein Dank an Herrn Dr.-Ing. Karl-Heinz Lang und Herrn Dr.-Ing. Rainer Joos für die Betreuung der Arbeit, den Diskussionen, Anregungen und der moralischen Unterstützung bei den vielen Rückschlägen, die ich im Aufbau des Prüfstandes erlitten habe.

Auch danke ich Herrn Prof. Dr. rer. nat. Alexander Wanner für die Betreuung meiner Arbeit, für die er sich trotz eines vollen Terminplans immer Zeit genommen hat.

Ebenfalls bedanken möchte ich mich bei Herrn Ralf Rössler, Arndt Hermeneit, Goran Krstic, Marc Brecht und Roman Böttcher für die Unterstützung an den Prüfständen. In dieser Liste dürfen meine Praktikanten und Abschlussarbeiter Daniel Reckinger, Felix Josten und Kai Daubert ebenso wenig fehlen wie Frau Manuela Josteit und Herr Andreas Grossmann für ihre Unterstützung bei den Öl- und Bauteilsauberkeiten. Auch Danke ich Herrn Dr.-Ing. Reiner Heigl, Tim Weyhmüller, Dr.-Ing. Alvaro Fernandez und Dr.-Ing. Cesár Pastor für ihr Mitwirken in der Konzeption des Prüfstandes.

Mein ehemaliger Team Kollege und Leiter der Metallographie Herrn Dirk Löffler, seiner Vorgängerin Frau Dr.-Ing. Kurz und dem zugehörigen Team bin ich für die Unterstützung durch REM und gelegentlicher Hilfestellung bei der Probenpräparation zu Dank verpflichtet.

At last, but not at least möchte ich sehr herzlich Herr Gerhard Mack erwähnen, den ich immer bei Fragen zur Interpretation röntgenographischer Eigenspannungsmessungen aufsuchen konnte.

Die Unterstützung und der Zuspruch, die ich von meinen Eltern erfahren habe, haben mir viel bedeutet. Ohne meinen Vater, der unbewusst mein größter Ansporn für die Arbeit gewesen ist und dessen dahinscheiden eine große Lücke hinterlässt, wäre die Motivation für eine derartige Arbeit nie zustande gekommen.

## Abstract / Zusammenfassung

Increasing demands for fuel efficient vehicles and legal restrictions to journal bearings, such as lead free bearings, are increasing the attractiveness of alternative bearing technologies like rolling bearings. A major factor for this development is the circumstance that further decrease of friction without impairing the reliability of journal bearings rapidly increases costs. Investigations show that a replacement of journal bearings with roller bearings can reduce fuel consumption of combustion engines in the range of 2-5 %. Due to limitations in the processing of conventional, 100Cr6 bearing steel (SAE 52100), however, induction hardened hypoeutectoid bearing steel become of interest. No publicly accessible data for service life rating is available for these steel grades. In this work the service life limiting effects for these grades are investigated and, due to exclusively tribological failures, the microstructural changes – also known as material response – are analysed in order to determine the subsurface failure probability.

Presently, applications with strong and repeated impact loads, such as automotive combustion engines, are seeing a widespread use of journal bearings. Especially in the case of combustion engines, long periods of almost zero load are interrupted by periods of strong loads. In the case of combustion engines some bearings experience rapid changes of the direction of force during periods of maximum load. Long-time effects, e.g. friction increase due to wear and material responses, are not thoroughly investigated. The current work proposes a novel method to test the long-time behaviour of rolling bearings at very high impact loads. The method is realised by a test bench designed to create reproducible impact loads on rotating bearings. Special care has been taken to ensure the impact loads are being imposed at the same location. During a test run vibration, torque and lubricant temperature are being monitored and controlled.

Steigende Kundenanforderungen an umweltfreundliche, verbrauchsarme Fahrzeuge und rechtliche Bestimmungen wie z.B. bleifreie Lager erhöhen die Attraktivität, anstelle von Gleitlagern, Wälzlager einzusetzen. Ein wichtiger Faktor für diese Entwicklung ist der Umstand, dass eine weitere Verringerung unerwünschter Reibung bei gleichbleibender Zuverlässigkeit zu rapide steigenden Kosten bei Gleitlagerungen führen. Untersuchungen haben ergeben, dass der Einsatz von Wälz- anstelle von Gleitlagern zu einer Verbrauchsreduzierung von 2-5 % führen kann. Aufgrund von Einschränkungen in der Verarbeitung herkömmlichen Wälzlagerstahls aus 100Cr6 sind untereutektoide Wälzlagerstähle an dieser Stelle besonders interessant. Es sind jedoch keine öffentlich zugänglichen Daten über die Lebensdauer für diese Stähle erhältlich. In der vorliegenden Arbeit werden die lebensdauereinschränkenden Effekte bei Verwendung dieser Stahlsorte untersucht und, bedingt durch rein tribologische Ausfälle, die Gefügeveränderung – auch bekannt als Material Response – analysiert um die Ausfallwahrscheinlichkeit durch Wälzermüdung

---

zu bestimmen.

Aktuell werden in Anwendungen mit starken, sich wiederholenden Stoßbelastungen, z.B. PKW Verbrennungsmotoren, zum größten Teil Gleitlager verwendet. Insbesondere im Fall von Verbrennungsmotoren wechseln sich lange Zeiten mit annähernd Nulllast und kurzen Zeiten mit hohen Lasten ab. Dabei erfahren einige Lager in Vollastphasen schnelle Wechsel der Lastrichtung. Langzeiteffekte wie Reibungsanstieg aufgrund Verschleiß und Gefügeveränderungen sind bisher nicht untersucht worden. Diese Arbeit stellt ein neues Verfahren zur Untersuchung des Langzeitverhaltens stoßartig belasteter Wälzlager vor. Das Verfahren ist in Form eines Prüfstandes realisiert worden, welches in der Lage ist reproduzierbare Stoßbelastungen auf rotierende Lager auszuüben. Ein besonderer Augenmerk liegt auf die Einleitung der Stoßbelastung an der selben Position am Lager. Während eines Versuchslaufs können Körperschall, Drehmoment und Schmiermitteltemperatur aufgezeichnet und geregelt werden.

## List of Abbreviations

DER	Dark Etching Region
EHL	elasto-hydrodynamic lubrication
FWHM	Full-Width at Half-Maximum of XRD
HAB	High Angle Bands (White Etching Area)
LAB	Low Angle Bands (White Etching Area)
NMI	Non-metallic inclusions
XRD	X-Ray diffractometry
$\beta_{10}$	retention value (oil filter) @10 $\mu\text{m}$
$\beta_{max}$	shape parameter (Weibull distribution)
$\delta$	scale parameter (Gumbel distribution)
$\Delta K$	stress intensity factor
$\Delta K_{th}$	threshold stress intensity factor
$\Delta K_t$	intrinsic $\Delta K_{th}$
$\eta$	FEHLT
$\eta_C$	lubrication cleanliness factor
$\kappa$	ratio of kinematic viscosity
$\lambda$	location parameter (Gumbel distribution)
$\mu$	friction coefficient
$\nu$	viscosity
$\nu_1$	kinematic viscosity
$\sigma_{vM}$	von Mises stress
$\sigma_{w0}$	intrinsic fatigue limit
$\sigma_u / \tau_u$	fatigue limit
$\sigma_x$	stress in x-direction, i.e. in surface direction
$\sigma_z$	stress in z-direction, i.e. depth
$\sqrt{AREA}$	area of largest NMI cross section
$T_{max}$	scale parameter (Weibull distribution)
$\tau_{xz}$	ortho. shear stress
$\tau_0$	max. orthogonal shear stress
$\tau_1$	max. principal shear stress
$A$	random parameter
$a$	elastic contact half width
$a_{skf} / a_{iso}$	factor for SKF model
$a_1$	service life factor for less than 10% failure probability

---

$A_1 / A_2$	area of cross section
$a_2$	lubrication factor
$a_3$	material factor
$A_{ref}$	reference area of cross section
$b$	min. value FWHM
$B$	max. value FWHM
$C$ (fatigue limit)	proportionality constant
$C$ (Service Life)	basic dynamic load rating (formerly known as dyn. capacity)
$e, c, h$	empiric material constants
HV, $Hv$	Vickers hardness
$K_I$	stress intensity factor mode 1
$K_{IC}$	fracture toughness intensity factor
$K_{II}$	stress intensity factor mode 2
$l$	crack length
$L_{10}$	bearing service life for 10 % failure probability
$l_0$	intrinsic fatigue crack length
$N$	no. of revolutions
$P$	equivalent dynamic load rating
$p$	exponent of the life equation
$P(x)$	cumulative distribution probability
$p_{max}$	max. hertzian contact stress (pressure)
$R$	load ratio
$R_a$	arithmetic roughness
$R_m$	tensile strength
$R_z$	max. roughness
$S$	survival probability (Lundberg & Palmgren model)
$S_R$	survival probability for one bearing (SKF Model)
$t$	ratio of cross section area
$Y$	geometric factor of crack
$z''-k$	stress weighted average depth
$z_{0Mises}$	depth of max. von Mises stress
$z_0$	depth of $\tau_0$



# 1. Introduction

A growing demand for environmental friendly products results in a strive to reduce frictional losses. Especially consumer product manufacturers, such as automotive OEMs, face rapidly increasing demands for fuel efficiency and low pollution. Aside of strong consumer awareness, they face harsh regulatory demands with regard of CO<sub>2</sub> and NO<sub>x</sub> emission.

At present electrified drives with batteries and hydrogen fuel cells are entering the market. Currently these technologies are in most cases only capable to support combustion engines and thus permit further engine downsizing. Until these technologies will attain a maturity level to substitute combustion engines in passenger vehicles a few decades will pass. In the domain of heavy duty commercial vehicles combustion engines will prevail for an even longer period of time.

In the mean time combustion engines will have to be further improved regarding their environmental balance and efficiency. One way to increase fuel efficiency is to substitute journal bearings of crank and cam shafts with integrated rolling bearings to reduce friction. Researches indicate that replacement of journal bearings can help to reduce fuel consumption by 2-5 % [TKO07, Pla11, Sha09].

The integration of bearing raceways into components like connection rods, crank shafts, etc. made of 100Cr6 would represent challenges to common manufacturing processes with regard to forging and heat treatment, notwithstanding the expenses for 100Cr6 itself.

Due to these considerations hypoeutectoid bearing steels are explored in this work regarding their suitability. Also, a novel test rig design for investigation of very high impact loads on rolling bearings is presented. This test rig is designed for endurance testing with reproducible impact loads at the same inner ring angle in the regime of  $2.5 \cdot 10^8$  cycles in order to simulate severe crankshaft loading conditions.

## 2. State of the Art

### 2.1. Bearings: An Overview

Bearings are applied to support and separate two objects with common contact surfaces and relative movement to each other while minimising friction between these objects in motion. In most technical applications bearings separate rotating objects, like shafts and axles, from their corresponding housing. The most common bearing technologies are the plain or friction bearings and the rolling bearings.

Friction bearings mainly consist of two surfaces, one finished into the housing or realised by an insert into the housing and one surface finished on the shaft. In automotive applications friction bearings are realised as full journal bearings. These bearings consist of two outer surfaces called shells and a so called journal, i.e. a surface on the shaft without any inserts or coatings. To reduce wear on solid parts practically to nil the hydrodynamic effect of fluids – commonly oil – is exploited. Friction in journal bearings occur within the oil.

Rolling bearings commonly consist of inner and outer rings which contain raceways for rolling bodies. These rolling bodies transmit the load from inner ring to outer ring and vice versa depending on the mode of loading. Rolling bearings are divided into ball bearings and roller bearings depending on the design of the rolling bodies. Moreover it can be distinguished between thrust and radial bearings depending on their respective direction of loading in axial or radial direction. Generally cages are used to counter gravity and other adverse effects on the motion of rolling bodies and maintain constant speed and distance between two rolling bodies. In common catalogue rolling bearings cages do not guide the bodies. This function is taken over by flanges on one or both rings.

Lubrication, either grease or oil, is used to mechanically separate rolling bodies and raceways in order to reduce wear. This separation results in thin lubricant films of 1-10  $\mu\text{m}$  [San08] or even less between raceway and roller. The resulting stress distribution cannot be described by mere Hertzian or hydrodynamic models. Complex interactions of pressure and elastic deformations of roller and raceways with lubricant have to be taken into account as much as compressibility and phase changes of lubricants within the gap [Dow95, IBG01, LS95, Joh85].

### 2.2. Bearing Life Calculation

The success of rolling bearings is based on the existence of reliable bearing life calculation models [Hah11, IH85]. The most common service life calculation models are based on the



fig. 2.1.: Crack initiation at NMIs as published in [LP47]

work of Lundberg and Palmgren in 1947 [LP47]. The calculation model is based on the observation that impurities like non-metallic inclusions (NMIs) can lead to fatigue failure of bearings made of 100Cr6 (fig. 2.1). The Lundberg-Palmgren fatigue theory presumes that a once initiated crack will continue to grow until failure occurs, if the crack is propagating in the right layers. These fatigue cracks are initiated at inhomogeneities at a distance below the surface due to the occurrence of large orthogonal shear stresses induced by the rolling motion's hertzian stress field. The theory also presumes that the crack initiating inhomogeneities are stochastically distributed throughout the material and that the weakest site within the stressed volume will lead to failure.

The basic relation of the Lundberg-Palmgren theory is given by:

$$\ln \frac{1}{S} \sim \frac{N^e \tau_0^c V}{z_0^h} \quad (2.1)$$

In this term (eq. 2.1)  $S$  denotes the survival probability, while  $N$  denotes the number of revolutions,  $V$  denotes the stressed Volume and  $\tau_0$  is the maximum orthogonal shear stress as illustrated in fig 2.2.  $z_0$  is the corresponding depth in which  $\tau_0$  occurs. The factors  $e$ ,  $c$  and  $h$  are defined as empiric material constants.

Eq. 2.1 can be transformed into a more practical shape by taking geometric considerations of rolling bearings into account:

$$L_{10} = \left( \frac{C}{P} \right)^p \times 10^6 \text{ rev} \quad (2.2)$$

In eq. 2.2  $L_{10}$  denotes the number of revolutions of bearings at which 10% of all bearings of a larger population have already failed.  $C$  is the *Basic Dynamic Load Rating* of a bearing, while  $P$  is the *Equivalent Dynamic Load*.  $C$  is the – for  $10^6$  revolutions – endurable load of a bearing in the unit [kN] for surviving  $10^6$  revolutions with a probability of 90% and  $P$  is the equivalent radial and axial load of a bearing.  $p$  is the *Exponent of the Life Equation*. For point contacts  $p$  is 3 and 4 for ideal line contacts. For

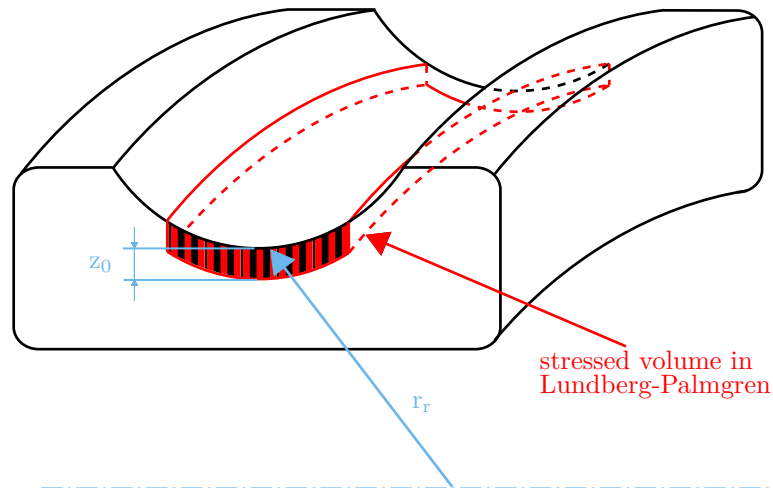


fig. 2.2.: The stressed volume according to Lundberg and Palmgren [LP47]

physically real line contacts, however,  $10/3$  is more appropriate. [LP47, Lun10, Hah11, IH85]

In Lundberg and Palmgren's period of time the achievable steel cleanliness and manufacturing precision permitted the assumption of continuous crack growth until failure. In the 1970s the Lundberg-Palmgren model as given in eq. 2.2 has become international standard ISO 281 [ISO281-77] and is till date the basic fatigue life model [DIN281].

Subsequent improvements of manufacturing processes, especially in the domain of cleanliness in 100Cr6, led to revise the fatigue life criterion in the 1970s and '80s. Observations of long service lives resulted in introduction of the fatigue load limit stating that maximum contact stresses beneath a certain level do not lead to bearing failure in the regime of regular engineering applications. In the current edition of ISO 281 this fatigue load limit is given as  $1500 \text{ N/mm}^2$ . [DIN281]

In the 1980s Lorösch et al. [Lor84] reported that most bearings of that period have been failing due to inadequate lubrication cleanliness. Increase of the lubrication cleanliness resulted for investigated bearing types in 35 times higher bearing lives then predicted by the Lundberg-Palmgren model. The same source also reports that the higher lubrication cleanliness shows that Lundberg-Palmgren model's bearing life calculation, which is fitted to a two-parametric Weibull curve, is not strictly valid below 10% bearing failure for tolerably clean lubrication. The failures occur considerably later for reduced failures service lives (fig. 2.3). In the light of these findings the, Lundberg-Palmgren model was amended by addition of the factors  $a_1$ ,  $a_2$  and  $a_3$ . It was introduced into ISO 281 as the *extended bearing life rating* in 1990 [ISO281-90].

Thereby  $a_1$  is a charted correction value for service lives less than 10% failure.  $a_2$  and  $a_3$  are factors for lubrication and material quality respectively. Due to the interdependency between factors  $a_2$  and  $a_3$  and the necessity of provision of  $a_3$ , these factors have been merged to  $a_{23}$  and with the integration of the SKF model (see below) modified to  $a_{SKF} / a_{ISO}$ . [Lun10, ISO281-77, IH85, IBG01, Lor84]

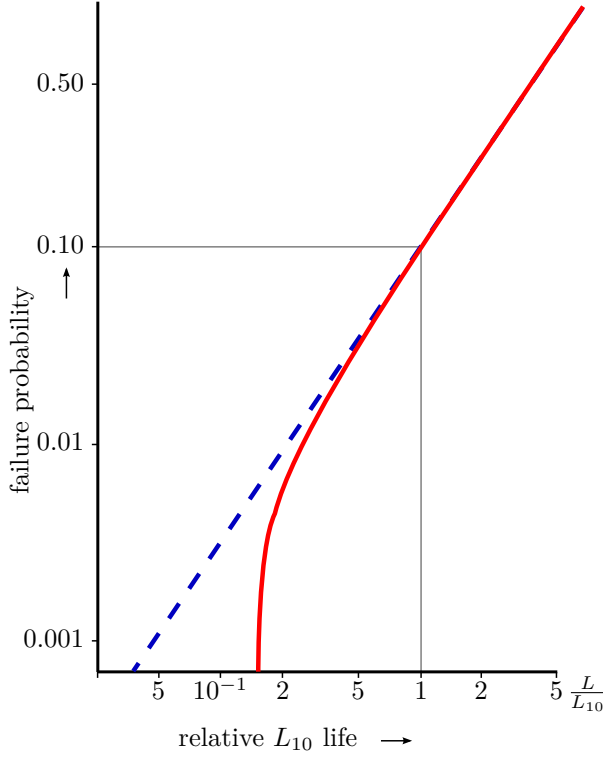


fig. 2.3.: Relative  $L_{10}$  life time [Lor84]

With the prevalence of the knowledge that crack growth is arrested for defects and cracks of a certain size or elongation in the high cycle fatigue regime (ca.  $10^7$ ) modifications of the Lundberg-Palmgren model were made. In 1985 Ioannides and Harris [IH85] extended the Lundberg-Palmgren model with a fatigue limit  $\sigma_u / \tau_u$  as lower crack growth level and generalised it for application on any fatigue life testing. Formally the basic equation is defined as

$$\ln \frac{1}{S_r} = AN^e \int_{v_r} H(\sigma - \sigma_u) \frac{(\sigma - \sigma_u)^c}{z'^h} dV \quad (2.3)$$

For rolling bearings a better fitting can be achieved by use of shear stresses.

$$\ln \frac{1}{S_r} = AN^e \int_{v_r} H(\tau - \tau_u) \frac{(\tau - \tau_u)^c}{z'^h} dV \quad (2.4)$$

This formula describes the survival probability of one bearing as  $S_r$ .  $A$  is a random parameter,  $H(\tau - \tau_u)$  is the step function and  $z'^{-h}$  the stress weighted average depth. This probability is then multiplied with the observed service life probability. The major difference between eq. (2.1) and eq. (2.4) is the fact that now a lower shear stress threshold is defined. [IH85]

Equation (2.4) has been initially applied to assess the fatigue risk in numerically solved 3D stress fields. In their original publication Ioannides and Harris explicitly considered effects of creep and lubrication on subsurface shear stress development for a ball bearing. [IH85]

For strictly Hertzian solutions eq. (2.4) can be simplified due to self-similarity of Hertzian stress fields. Thus eq. (2.4) can be expressed as

$$\ln \frac{1}{S_r} = AN^e \left\langle \frac{\tau_0 - \tau_u}{z_0^h} \right\rangle az_0 l = AN^e \left\langle 1 - \frac{\tau_0}{\tau_u} \right\rangle \frac{\tau_0^c}{z_0^h} az_0 l \quad (2.5)$$

In this formulation Macauley brackets are used, i.e. the term is set to zero if the value within is negative. Equation (2.5) differs from the original Lundberg and Palmgren form (eq. (2.1)) only by the Macauley bracket on the right side. Therefore eq. (2.5) can be solved in analogy to Lundberg and Palmgren's formulation resulting in an expression almost identical to eq. (2.2).

$$L_{10ma} = A \left\langle 1 - \eta \left( \frac{C_u}{P} \right)^w \right\rangle^{-\frac{\epsilon}{e}} \left( \frac{C}{P} \right)^p \quad (2.6)$$

In this formulation the factor  $\eta$  is introduced to account for the deviation of real stresses within a bearing from the strictly Hertzian solution assumed in eq. (2.5). Sources for deviation are lubrication and environmental conditions leading to e.g. creep forces, micro-scale stress concentrations at imperfections like dents and asperities due to contamination, etc.

To simplify the use of eq. (2.6) the stress life factor  $a_{SKF}$  has been introduced for each specific bearing type. With  $a_{SKF}$  given as a function of lubrication condition, bearing diameter, cleanliness and viscosity ratio. Thus it is

$$a_{SKF} = A \left\langle 1 - \eta \left( \frac{C_u}{P} \right)^w \right\rangle^{-\frac{\epsilon}{e}} \quad (2.7)$$

. The factor  $a_{SKF}$  was first introduced by SKF in 1989 and subsequently amended in in the 90's. This *modified, extended service life rating* replaced the *extended service life rating* in the current version of the ISO 281 renaming  $a_{SKF}$  to  $a_{ISO}$  (and  $a_{DIN}$  in the German version). As this model was developed and introduced by SKF, it is also known as the SKF model. Being the more feasible name this model will be called thus throughout this work. [IBG01, DIN281]

Sadeghi et al. [SAJ09] give an overview of various alternative life rating models for subsurface related rolling contact fatigue. The models are differentiated into probabilistic engineering models and deterministic research models. The latter ones mainly focus on specific aspects of the failure process in great detail and great number of material details, while the engineering models are largely empirical. The more present engineering models try to incorporate elements of fracture mechanics and microstructural changes of the bearing material such as dislocation theories and (micro-)plastification. [SAJ09, WSK12, CY12, BSA14, PAS14]

## 2.3. Microstructural Changes within Bearings

### 2.3.1. Dark Etching Regions

Severe loads, as often applied to bearings, lead to microstructural changes beneath the raceway. Cross sections of bearings with high maximum Hertzian contact stresses and long service lives exhibit beneath the raceways dark patches when etched with nital (fig. 2.4). Since the 1960s' researchers report the formation of these so called *Dark Etching Regions* (DER) [SBV76].

In early stages DERs are patches beneath the raceways. With increasing service time they turn into one continuous layer of DER and then increase the layer thickness, thereby the lower side of the DER band grows faster than the upper side moving the centreline of the DER deeper. Extrapolations of the lower and upper boundaries of DERs of the same contact stresses and different service times pinpoint to the depth of the maximum orthogonal shear stress  $z_0$  (fig. 2.5). The orthogonal shear stress is assumed to cause the formation of DERs. This is further affirmed by the observation of faster growth of the lower boundary of DERs, which fits elastic considerations of the redistribution of stresses due to loss of carrying capacity of the material in the vicinity of  $z_0$ . [Vos97]

Investigation into the nature of DERs show that they consist of finely dispersed martensite and ferrite grains. Transformation of martensite to ferrite in a formerly homogeneous matrix can only be invoked by loss of carbon atoms, which cannot be dispersed outside the bearing due to the large distance of DERs from the surface. A thermodynamically activated carbon migration is not possible under static conditions. However, stress induced phase transformation is not improbable under high cyclic contact stresses. Swahn et al. [SBV76] calculated that carbon migration to segregated dislocations during  $10^8$ - $10^9$  revolutions of a bearing would only require a directed jump of the carbon atom every  $3 \cdot 10^7$  revolutions. Observations by Voskamp [Vos97] show that the ferrite domains are heavily deformed, which is in accordance with Swahn's theory. [SBV76, Vos97]

### 2.3.2. Three Stage Rolling Contact Fatigue Model

Extensive investigations by Voskamp [Vos97] show that Hertzian contact stresses above 1.9 GPa not only lead to visible deterioration of the martensite matrix, but also to transformation of retained austenite to - most probably - martensite and the formation of residual stresses. Employing x-ray diffractometry (XRD) Voskamp was able to chart the decomposition of retained austenite for 6309 ball bearings with 15% austenite as a function of number of revolutions and Hertzian stress (fig. 2.6) and to correlate it with microstructural changes. An initial decomposition of retained austenite can be observed within a hundred to thousand revolutions succeeded by a stress dependent period of no change and finally a period of continuous decomposition. Voskamp defined these three periods as *Stage I* to *Stage III*:

In *Stage I* or *shakedown stage* an initial decomposition of austenite, work hardening and the formation of residual stresses are observed. The shakedown stage is completed when the entire load exposed volume is altered by plastic micro-straining such that

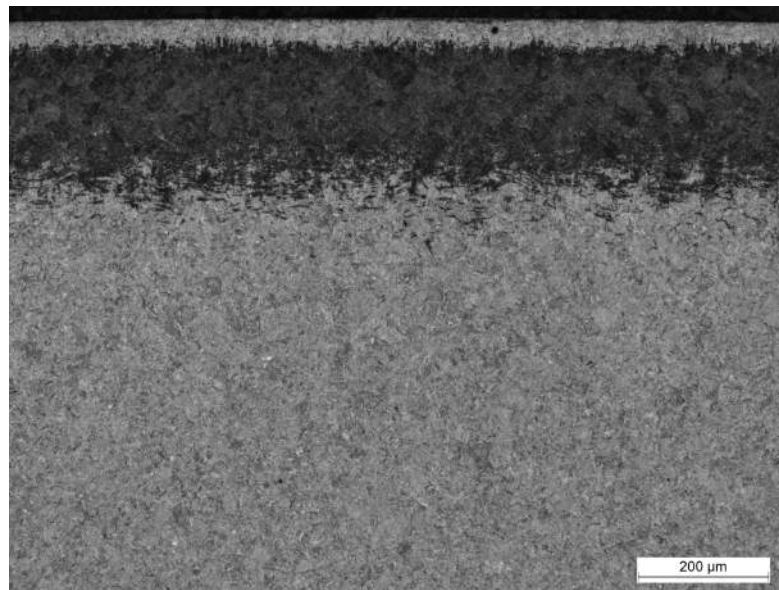


fig. 2.4.: Dark etching regions (DER) become visible in micrographs of cross sections of bearings with high max. contact stresses and long service life. The depicted DER is in an advanced state, visible by the continuing DER patch (DER band)

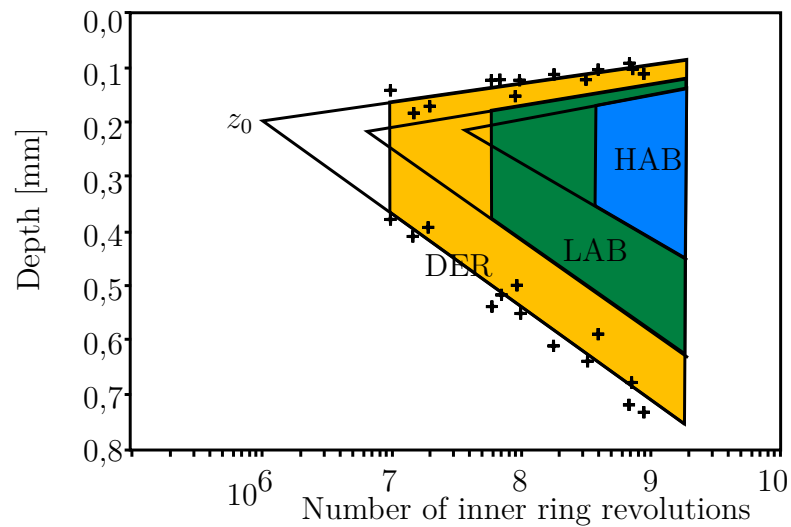


fig. 2.5.: Extrapolation of upper and lower boundaries of DERs, LABs and HABs to lesser revolutions corresponds to the layer of max. ortho. shear stress  $z_0$ . Experiments have been conducted with ball bearings of type 6309 and 3.7 GPa max. contact stress. The outer ring temperature is set to 53 °C. Image acc. [Vos97]

### 2.3. MICROSTRUCTURAL CHANGES WITHIN BEARINGS

---

further load cycles are carried elastically. During this stage local deviations of the material's elastic response within the exposed volume lead to plastic micro-deformations and thus to work hardening and the formation of residual stresses as a result of geometric constraints inhibiting large-scale deformation. Due to the micro-deformations the shape of the bearing is slightly altered meaning that in subsequent load cycles (which in the case of constant load is the next rolling element's passage) yet unaltered regions will be affected to the same consequence. The shakedown is finished after about 1000 revolutions, implying that all subsurface regions have been exposed to the highest occurring stress. Further plastification is less easy as the entire load-exposed volume is now work hardened. The lowest point of transition has been named shakedown limit. Stresses above this limit lead to continuous, macroscopic plastic deformations.

During *stage II* or *steady-state stage* no significant alterations of the microstructure can be detected. It is the incubation period for stage III. In this period the conditioned volume loses gradually its ability to carry the load elastically and transits into stage III. The duration of stage II is also temperature dependent. (fig. 2.7)

*Stage III* or *instability stage* is the final stage of a bearing. Depending on the loading conditions stage III occurs between 1000 and post  $10^9$  revolutions. In this stage Voskamp observed

1. material softening
2. microplastic deformations
3. martensite decay
4. cementite decay
5. residual stress build-up
6. austenite decay
7. ring growth
8. texture development
9. increasing probability for spalling fatigue

. As explained in chapter 2.3.1 points 1-4 of the above enumeration are observed during DER formation as a result of the orthogonal shear stress. Austenite decay is thought to be supported by martensite decay, as the hydrostatic pressure within the DER patch is reduced due to volume shrinkage during martensite to ferrite transformation and carbon migration out of the martensite grain due to the shear stress itself. As can be taken from figs. 2.5 and 2.6 austenite decay and extrapolated DER start time are in the same order of revolutions and occur simultaneously. Fig. 2.8 shows the depth of austenite decay and the depth of residual stress built-up as a function of revolutions. It can be seen that the depth of austenite decay is in the depth of  $z_0$  as is DER formation. The residual stress development is shifted to the depth of the max. von-Mises stress  $z_{0Mises}$  which

correlates to  $z_0$ . The high residual pressures and reduced austenite content in the surface and near surface layers are caused by machining processes. Voskamp observed point 9 by testing bearings finished from 100Cr6 with typical bearing cleanliness versus reduced cleanliness and larger NMIs (unfortunately exact values are not given only that the 'bad' grade contains 25 ppm oxygen) and observed that subsurface initiated failures in 'clean' steel are highly unlikely. Moreover, he observed that in the 'bad' steel grade spallings due to subsurface fatigue without microstructural changes are limited in circumferential length while spallings in altered steel have larger lengths. To imitate the effects of material weakening in a reproducible manner bearings were annealed after shakedown and then compared with bearings without annealing. He concluded that cracks at NMIs in bearings made of standard bearing grade steel are initiated when microstructural softening occurs. The time for crack propagation he assumes to be roughly 2% of the service life. It remains unclear whether Voskamp was aware of short crack growth and therefore assumed that no crack propagation was taking place, however, it is not unlikely that (short) crack propagation is accelerated by microstructural changes within the bearing. [Vos97]

### 2.3.3. Flat White Bands / Low Angle Bands

Bearings with high contact stresses and very long service lives develop white etching structures of parallel bands within the DER layer (fig. 2.9). In the first stage these bands occur in a low angle of 25-35° to the surface. With further increasing service times another structure of thick, parallel white bands develops with an angle of approximately 80° to the surface. Naming of these structures is not consistent in literature. The earlier of the two structures is known as Low Angle Bands (LAB) or Flat White Bands (FWB), while the later appearing structures are named High Angle Bands (HAB) or Steep White Bands (SWB). LABs appear in etched sections as white stripes with dark coronae on one or both sides. TEM investigations of the LABs show that they consist of long stripes of heavily plasticised ferrite grains which are surrounded by carbon rich regions or heavily deformed grains. Globular secondary cementite as present in 100Cr6 is partly integrated into the LABs while other parts are fragmented along the LABs. In carburised bearing steel grade 20NiCrMo2-2, which is free of such globular carbides LABs develop over much longer distances suggesting that globular cementite are obstacles to LAB growth. Annealing experiments at 400 °C and for at least 1 h show that annealing of LAB afflicted bearings increase the coronae of precipitated carbon. HABs appear generally with higher inclination than LABs, although inclinations of 20° are known at very high bearing speeds. Rotation speed has a stronger influence on their inclination than it has on LABs. Unlike the strips like structure of LABs HABs consist of tiny, equi-axed ferrite grains with a small fraction of tiniest cementite particles within the bands. The hardness of HABs is reported to be significantly lower than in the original matrix (ca. 650 HV to 820 HV). Latter observation can be explained by the fact that carbon drops below detection level in these bands. [SBV76, Vos97, Geg11, GN12]

### 2.3. MICROSTRUCTURAL CHANGES WITHIN BEARINGS

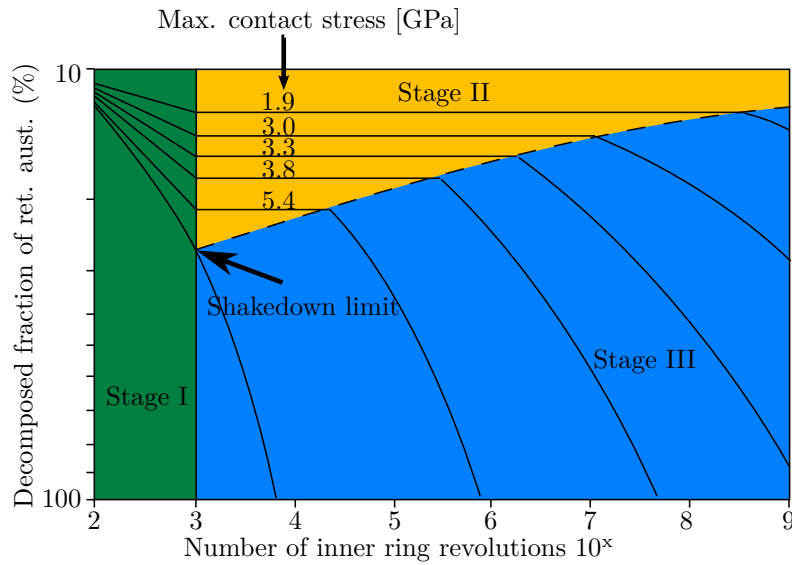


fig. 2.6.: Map of the decomposed retained austenite fraction as a function of inner ring revolutions and different maximum contact stresses. Contact stresses are measured in 6309 type ball bearings at 0.2 mm depth, close to the depth of load induced maximum shear stress. Bearings are tested under lubrication conditions yielding complete separation of the surfaces in contact. Operating temperature was kept at 53 °C at the outer ring. [Vos97]

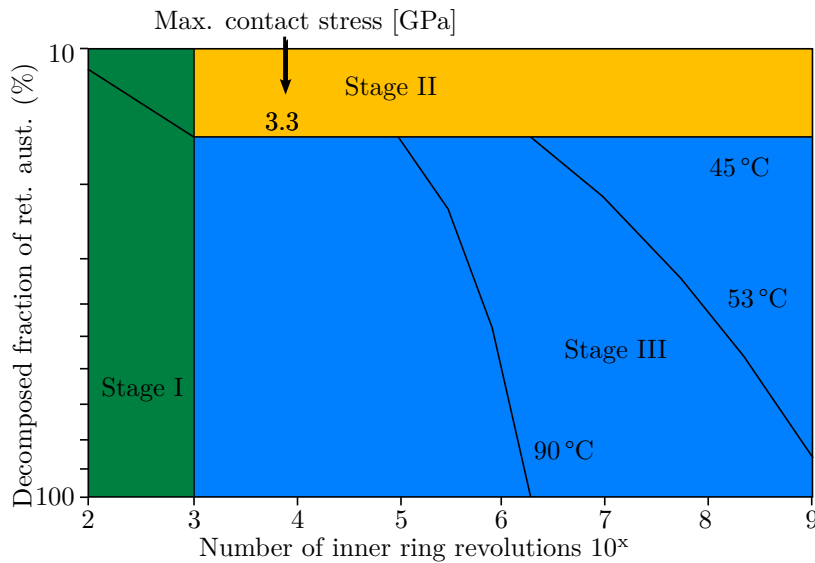


fig. 2.7.: Influence of operating temperature on decomposition of retained austenite. Testing and measuring conditions are identical to fig.2.6. The temperatures was measured at the outer ring. [Vos97]

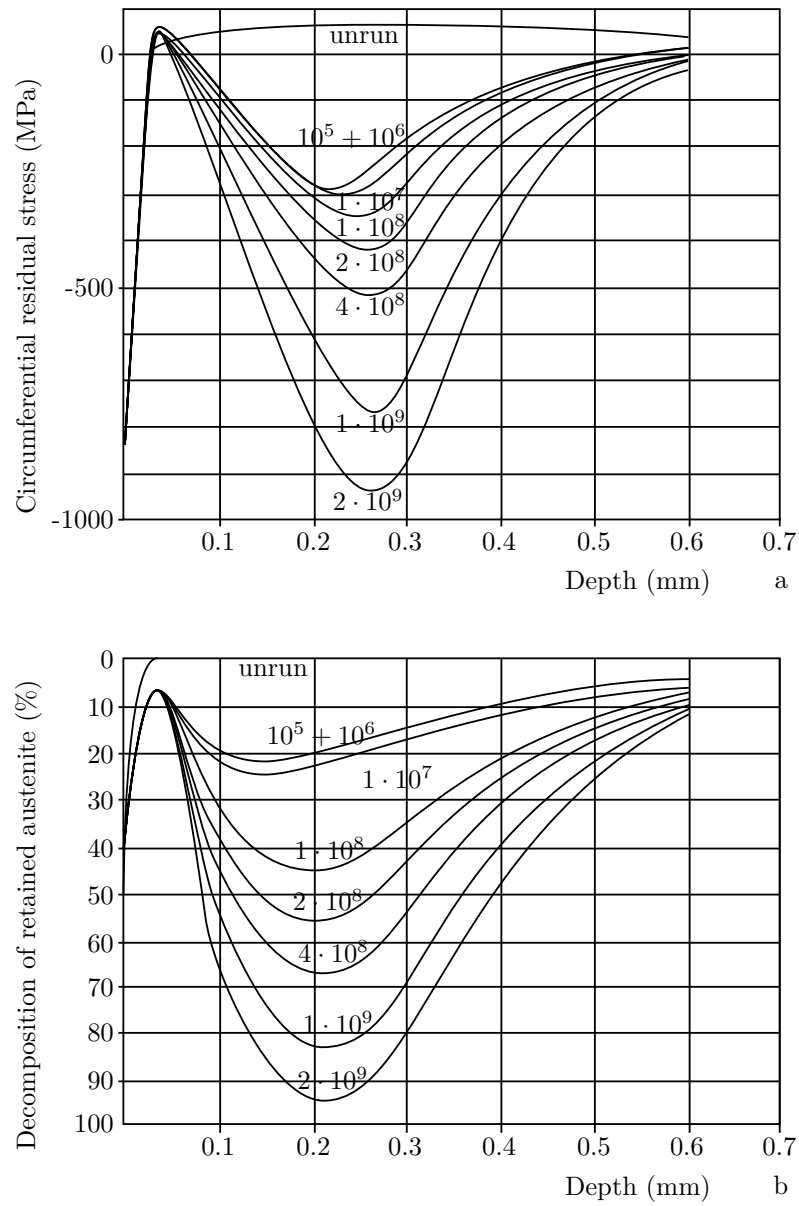


fig. 2.8.: Residual stress (a) and decomposed retained austenite (b) curves for maximal contact stress of 3.3 GPa as a function of depth beneath raceway for various number of inner ring revolutions.  $z_0$  and  $z_{0Mises}$  have been calculated to 0.19 mm and 0.27 mm respective. Operating temperature: 53 °C at outer ring. [Vos97]

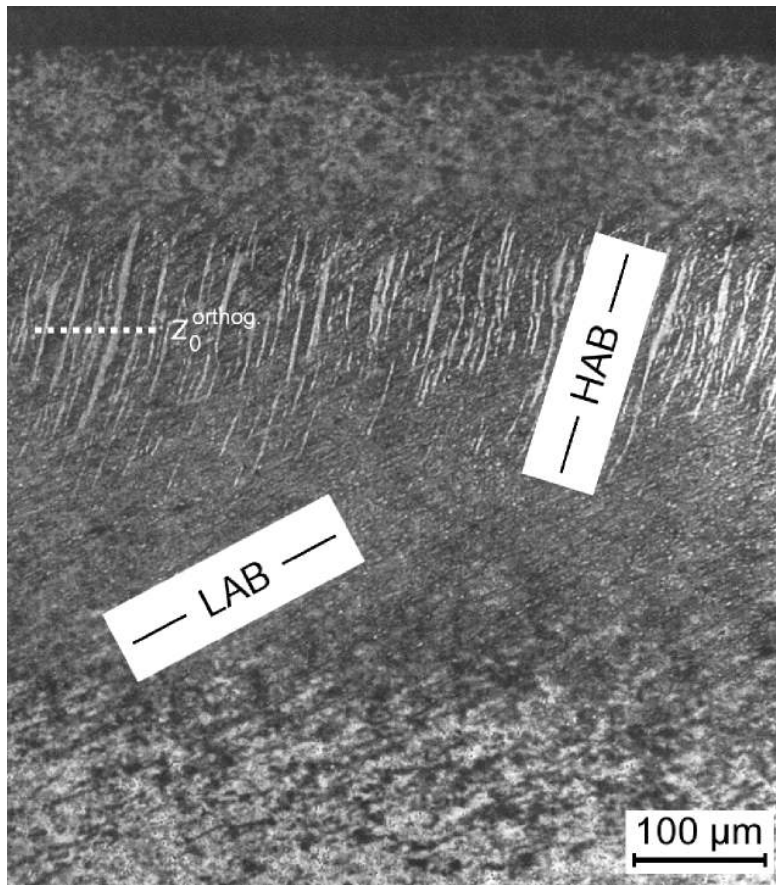


fig. 2.9.: Optical micrograph of an etched circumferential cross section of the IR of 6309 type ball bearing rig tested at a max. hertzian contact stress of 3.7 GPa.  $z_0^{orthog}$  refers to the depth of max. orthogonal shear stress. Source: [Vos97]

### 2.3.4. Decrease of X-Ray Peak Full Width at Half Maximum Height

In the late 1990's and 2000's Voskamp, Nierlich and Gegner published several papers on the change of the x-ray Full Width at Half Maximum (FWHM) and its applicability to determine the fatigue state of bearings. Nierlich's focus has been on tribological effects such as lubricant contamination and boundary lubrication conditions while Voskamp concentrates on subsurface fatigue.

Extreme surface conditions lead to ratcheting, which marks the upper fatigue strength limit response of the material, while the lower fatigue strength boundary response is marked by the three stage RCF in the near-surface volume although with some peculiarities (fig 2.10). Stage I lasts longer for surface fatigue than in its subsurface counterpart at the expense of a shorter stage II. In stage III compressive residual stresses may be reduced instead of increased depending on the damage mechanism. In both cases the microstructural changes during stage III are characterised by decay of retained austenite

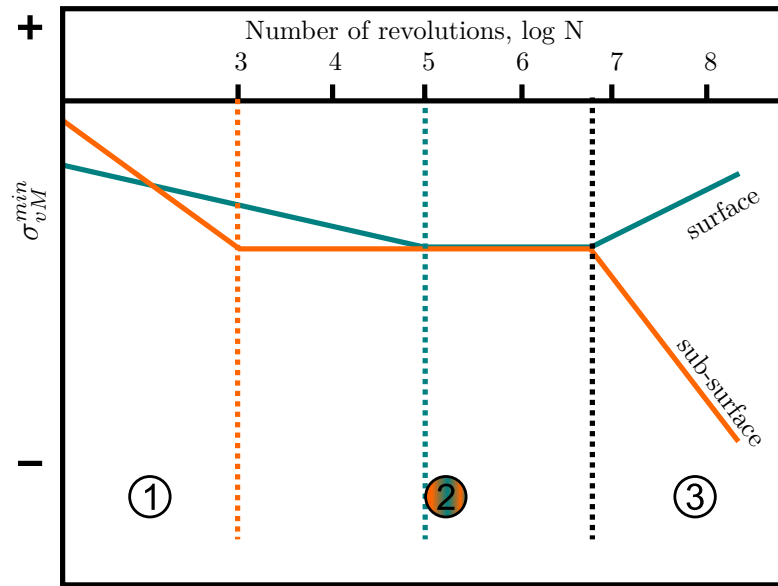


fig. 2.10.: Qualitative depiction of the differences within the three stage model for surface and subsurface fatigue damage. Stage I lasts longer, while stage II is shorter for surface fatigue effects than subsurface fatigue. Also the compressive stress is reduced in surface failure during stage III. In all other matters both stage models have equal properties. [Vos00].

and decay of martensite. [Vos00, VNH98, Vos02]

The decay of martensite can also be observed via the decrease of the XRD FWHM. (A description of the mode of operation for XRD is omitted at this point for the sake of simplicity and referenced to the relevant literature. Also see the citations given in this work.) The decrease of the FWHM is caused by reduced distortions of the  $\alpha$ -lattice space which naturally is lesser in ferrite than in martensite. Since the angle of FWHM is device and (and also to some extent) sample specific a comparability is only given for normalised values. For practical reasons the FWHM of the unaltered and unstressed volume of the samples are used to normalise.

Following a proposal of Nierlich, who found that normalised FWHM data correspond with failure probability in the case of surface failure, Voskamp revised the FWHM data generated during Voskamp's investigations [Vos97] and found a correlation between normalised subsurface FWHM and failure probability (figs 2.11 & 2.12). A once existing value for  $L_{10}$  enables to determine the remaining service life of a bearing and even allows the usage of a small number to determine the performance of a bearing type or any other application with similar conditions, e.g. gear teeth. This method is also capable to determine the exerted loads as the smallest normalised FWHM will occur in the depth of orthogonal shear stress and can be complemented by the depth of maximum von Mises stress in order to determine the contact stress. This method is unable to detect RCF initiated by NMIs, however, presuming Voskamps assump-

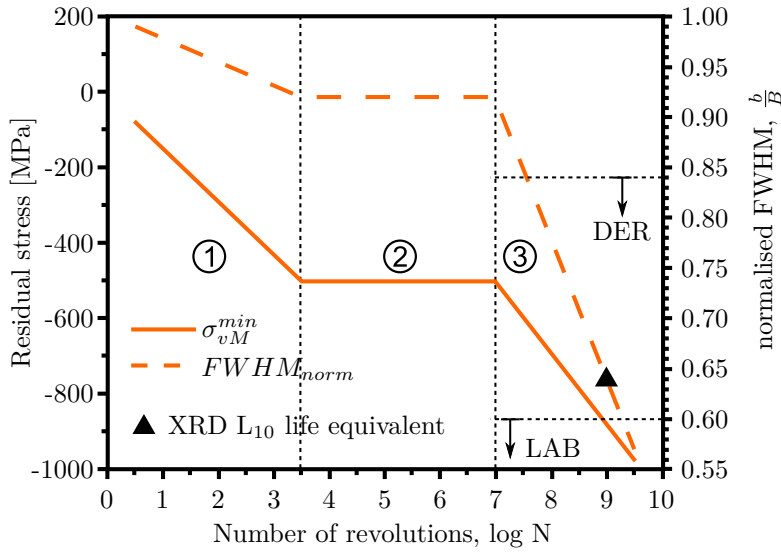


fig. 2.11.: Schematic representation of the three stage model for subsurface damage. Beginnings of DER and LAB formation are marked. So is the rig tested  $L_{10}$  point ( $b/B=0.64$ ). LABs start shortly after this point. Note that values of normalised FWHM in stage I and II may vary respective the actual maximum hertzian stress. The number of revolutions is also stress dependent and only serve as a graphical representation in this schematic. Values are valid for 100Cr6 and similar materials. Image acc. [Geg11].

tion of increasing microstructural softening and crack propagation (c.f. last section of chapter 2.3.2) an empirical link between RCF probability and normalised FWHM is given. The calibration curves given in figs.2.11 & 2.12 are recorded for 100Cr6 in line contact and can account for 100Cr6 and related steel grades with line contact loading. Changes in the chemical composition, e.g. carbonitrated 100Cr6, may impact the lattice distortion making it necessary to record new calibration curves (c.f. fig. 2.13). A convenient aspect of subsurface  $L_{10}$  fatigue life determination from material response is the onset of LABs shortly after exceeding subsurface  $L_{10}$ , thus allowing to estimate the normalised FWHM value at subsurface  $L_{10}$  without full fledged rig tests. [NG12, Vos97, NGB06, VNH98, Vos98, Vos02, GNB07, Vos00, GN12, Geg11]

## 2.4. Indentation of Particles into Raceways

As explained in chapter 2.2 lubrication cleanliness has a major impact on bearing service lives. In most technical applications a perfectly clean lubricant is next to impossible. Residuals from production, like chips, remains from grinding processes, etc. cannot be avoided or would cause intolerable efforts to further increase cleanliness, e.g. in gearboxes and combustion engines. Failures as a result of indentation are rather easily identified by their distinctive 'V' shape of the flaking which occur at the trailing edge of the indentation

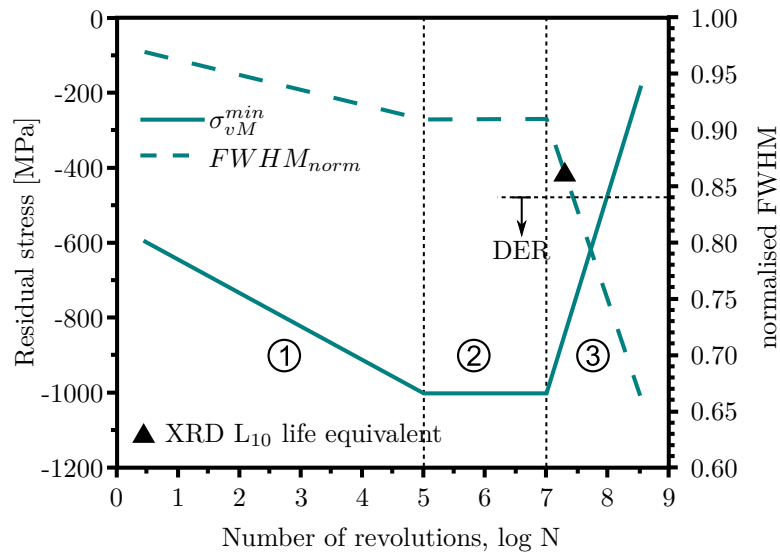


fig. 2.12.: Schematic representation of the three stage model for surface damage in line contact. Compared to fig. 2.11 the rig tested  $L_{10}$  point is much earlier in terms of  $b/B$  ( $b/B=0.84$  line contact,  $b/B=0.86$  for point contact). Note that values of normalised FWHM in stage I and II may vary with respect to the actual maximum contact stress. The number of revolutions is also stress dependent and only serve as a graphical representation in this schematic. [Geg11]

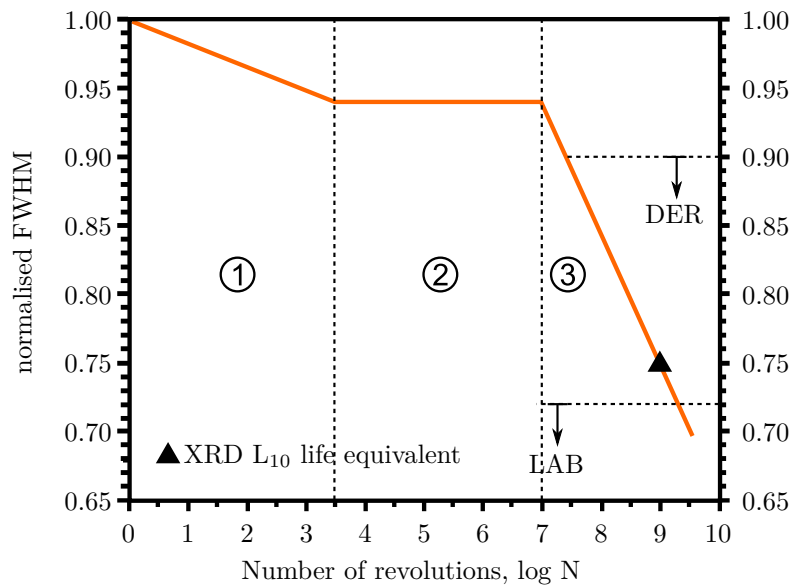


fig. 2.13.: Subsurface calibration curve for carbonitridated 100Cr6. Due to the lattice space distortion of nitrogen  $b/B$  values are much higher for DER formation than in regular 100Cr6 c.f. fig. 2.11. Image acc. [GN12]

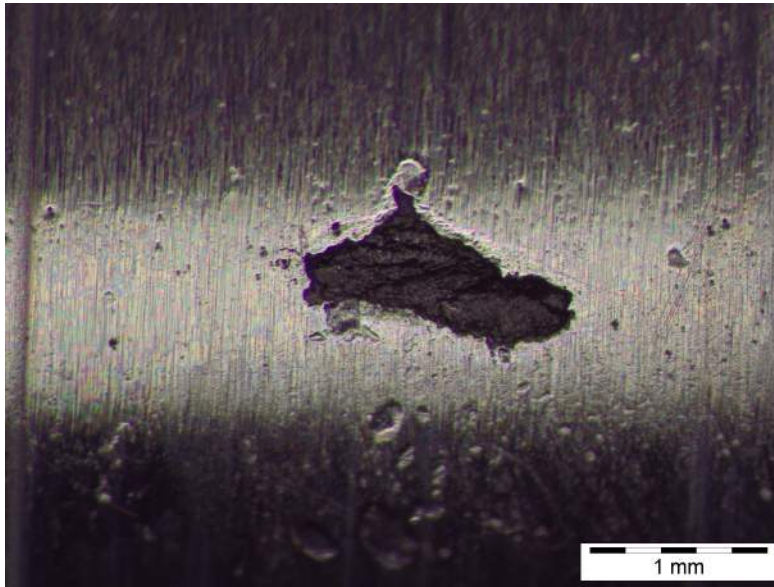


fig. 2.14.: Indentation of a soft particle - probably steel - on C56 E2 specimen.

as depicted in fig. 2.14. Also see [Sch00, Lor84] for reference.

Ueda et al. [UM09, UM08] damaged the raceways of deep groove ball bearings of type 6202 with foreign matters while letting the bearings roll for one hour with a load of 6.2 kN ( $C/P=1.3$ ). The matter consisted of particles in the range of 74 - 147  $\mu\text{m}$  with a hardness of 520 HV. These raceways are then paired with new, clean balls damaged for an hour either with particles with the hardness 870 HV, 520 HV and a test group with undamaged balls. While thus all the raceways possess a similar roughness of  $R_a = 0.039$ ,  $R_z = 0.61$  the balls differ greatly in their roughness. Balls damaged with very hard particles possess a roughness of  $R_a = 0.024$ ,  $R_z = 0.53$ , while the others possess roughnesses of  $R_a = 0.022$ ,  $R_z = 0.28$  and  $R_a = 0.007$ ,  $R_z = 0.11$  depending on their treatment. The actual testing has been conducted with the same parameters as the damaging, however, clean lubrication is used now. The lubrication used in all tests is an ISO-VG 68 oil. The resulting lifetimes till failure can be seen in fig. 2.15. Ueda et al. could thus establish that the surface quality of rolling elements greatly influences the life of bearings. Curve 'A' denotes bearings with balls damaged with particles of 870 HV hardness and 'B' denotes balls damaged with particles of 520 HV hardness. Consequently curve 'C' consists of undamaged balls. Ueda et al. assert that all failures not specially denoted are raceway damages due to visible indentations. As the balls and raceways had been previously cleaned it is claimed that these failures are the result of surface roughness.

Parallel to these experiments Ueda et al. also undertook investigations of the mechanisms leading to failures due to indentation. For this experiment twin-disc tests (c.f. 5.2.2) have been carried out observing that not pure rolling movements of rolling bodies but rather tangential forces responsible for slipping / rolling movements commonly found at

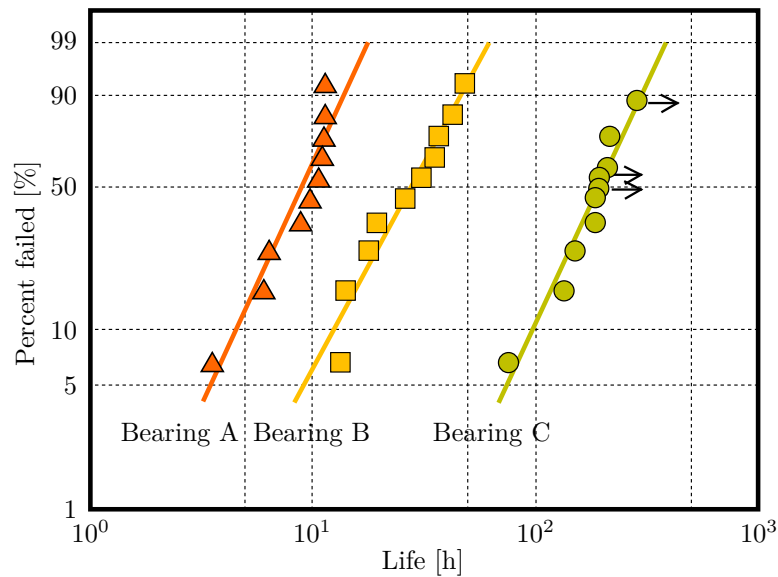


fig. 2.15.: Influence of surface roughness of rolling element on dent initiated flaking. [UM09].

bearings lead to cracking. A reversal of the direction of the acting tangential force without changing the overrolling direction leads to a change of the crack from the trailing edge of a dent to the leading edge of the same. Moreover it is noted that cracks at the leading edge appear to be less severe. These findings are then verified with a testing called ball-on-rod test which is a set-up consisting of a turning rod with balls held in a fixed orbit by a two-piece raceway not interfering with the contact orbit of the balls with the rod, fig. 2.17. As the tangential stresses in ball contacts experience a reversal as a function of axial direction along their rolling band Ueda et al. introduced Rockwell C indentations in the centre and rim of the rod's rolling band. These tangential stresses happen due to slipping caused by elastic compression of the balls. Fig.2.16. Again the crack sites depend on the direction of tangential stresses and not the overrolling direction. Following these findings it is concluded that cracks initiate and grow where tensile stresses exceed compressive stresses. This model also explains why cracks on leading edges appear less severe: Due to the rolling bodies movement the cracks are first closed at the crack tip and last at the crack mouth causing little crack growth by pressurisation of trapped lubrication (The tip of the cracks show in the opposite direction than trailing cracks as the direction on tensile stress is reversed). Moreover Ueda reports of additional experiments with two oils of different friction coefficients but similar kinematic viscosity (necessary for maintaining comparable Elasto-hydrodynamic conditions) and pre-damaged bearings, in which the oil with higher friction coeff. propagates earlier flaking. [UM09, UM08]

In reference [NDC98] the influence of roughness on initiation and propagation of micro-pittings is investigated. Experiments are carried out with a twin-disc machine for 100Cr6 and M50 steels. Like in Ueda et al. work it is reported that the direction

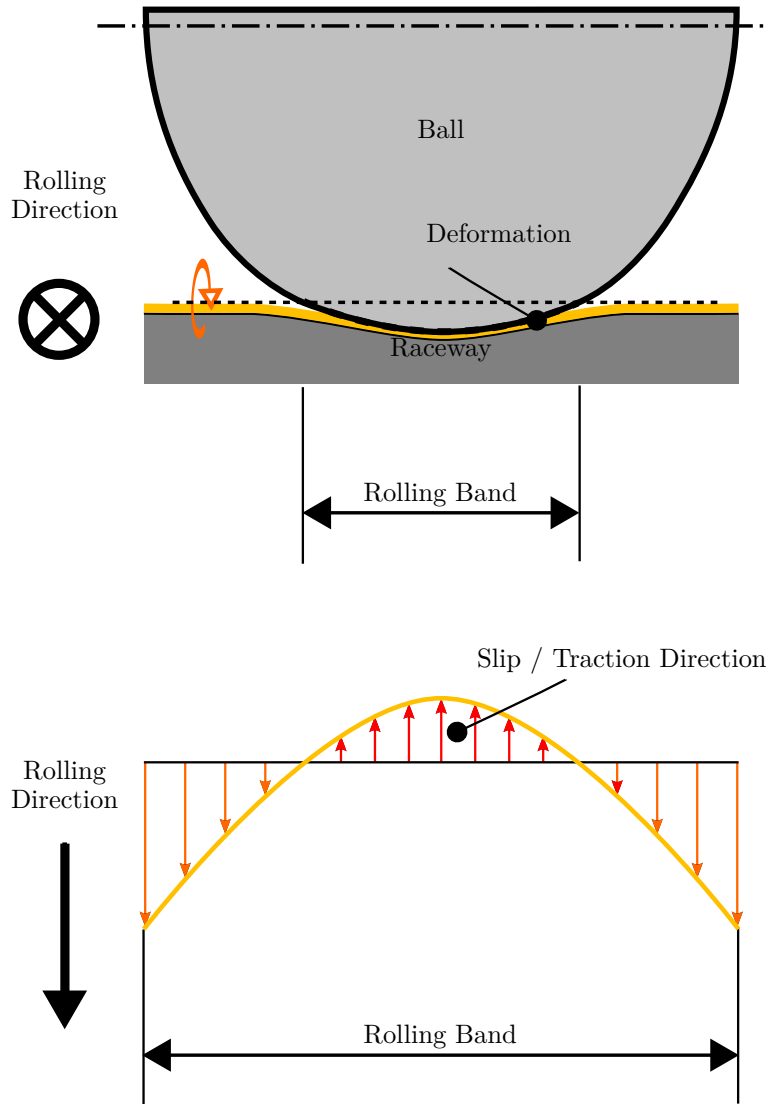


fig. 2.16.: Tangential forces of a ball on a raceway. A ball element has in sum a slip in the direction of ball movement, part of the elastic deformed zone in the contact zone, however, has a negative slip as the rotation axis of the ball is atop of the virtually undeformed zone.

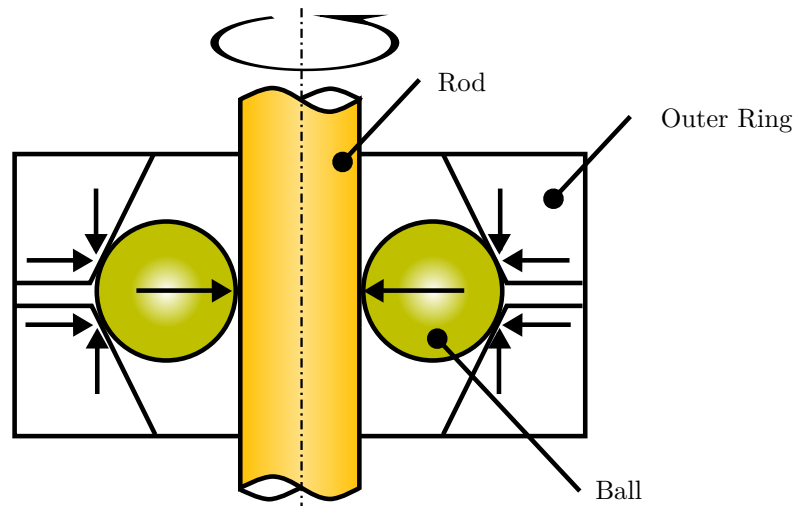


fig. 2.17.: Schematic of the ball-on-rod test conducted by Ueda et al. in [UM08]

of micro-pittings are depending on the orientation of friction forces, i.e. on the tangential forces. The orientation of crack growth / tangential force agree with the findings of Ueda. It is also reported that no differences were observed for the two steel grades. Additionally, simulations of the EHL conditions (chapter 2.5) at the pitting are conducted showing that micro-pittings act as precursors for future micro-pittings. This explains why usually micro-pittings are observed in clusters or circumferential bands on the raceways. Experiments conducted with and without sliding show that with almost no sliding micro-pittings occur in axial and tangential direction while sliding leads to tangential distribution of micro-pittings. [NDC98]

da Mota et al. [MMF08] observed the behaviour of dents on the surface of raceways as a function of rolling numbers and simulated the stress intensity factors in a crack at the trailing edge. For this purpose twin-disc tests were carried out. Dents were introduced into the raceways with Rockwell C indenters and 2500 N load. Tests were conducted with grease and oil as lubricant. The experiments in oil show that the shoulders are reduced rapidly in less than  $10^6$  over rollings. A simulation of the Rockwell dents showed that the shoulder height is reduced after only two over rolling cycles to approximately half of its early size. The generated residual stresses are mainly introduced during indentation (about 1300 Mpa) and only change slightly with each over rolling (1500 Mpa after two cycles). During calculation of stress intensity factors (SIF) considerations have been taken for fluid pressures at the crack gap, Hertzian contact stresses, residual stresses of the raceway and crack angles  $30^\circ$ ,  $45^\circ$  and  $60^\circ$  (parallel to the raceway.) The Green function was taken as basis for the SIF calculation of  $K_I$  and  $K_{II}$ . The crack length to Hertzian surface pressure width is given with 0.24. As per calculation the dominating factor is  $K_I$ , while  $K_{II}$  has a considerably smaller value and mostly negative sign. The sign, however, becomes shortly positive just as the Hertzian contact stresses are fully zero. Fluid pressure nearly doubles the SIF of a purely Hertzian consideration, however,

residual stresses play a minor role. The consideration of different angle shows that the SIF become the stronger the lesser the angle is. [MMF08]

The latter observation is in accordance with findings of other researchers. In a overview Santus et al. [SBB12] report for surface initiated rolling contact fatigue in gear teeth shallow crack angles of 20-30° parallel to the surface with orientation in direction of sliding due surface roughness and poor lubrication in gear teeth, which lead to micro-pittings and in a later stage to pittings. Similarly Hannes and Alfredsson [HA11, HA12, HA13] report for asperity initiated gear teeth failures angles of 30-35° and in direction of creeping. Ekberg and Kabo [EK05] report in a review of rolling contact fatigue in wheel-rail systems that surface fatigue can occur on sites with local micro plastification (ratcheting), asperities, surface defects and due poor lubrication or high surface roughness. They also report shallow cracking angles. [SBB12, EK05, HA11, HA12, HA13]

## 2.5. Lubrication

In rolling bearings grease or oil are used to avoid cold welding and fretting of raceways. Thereby oils generate less friction than grease, however, latter ones are practical in environments where oil feeding cannot be established, as is often the case. Greased and sealed ready made bearings are widely available. The lubrication oils thereby separate the surfaces of rollers and raceways and thus affect the transmission of forces. Therefore lubricant properties and tribology are essential for proper bearing functionality. [SKF08, Sch12]

The factor  $a_{ISO}$  of the extended service life rating (chapter 2.2) mainly covers the effects by the parameters  $\kappa$ ,  $P$ ,  $C_u$  and lubrication cleanliness, with  $\kappa$  being the ratio of kinematic viscosity  $\nu$  to required kinematic viscosity  $\nu_1$ :

$$\kappa = \frac{\nu}{\nu_1} \quad (2.8)$$

$\kappa$  values equal or better than ‘4’ are known to completely and safely separate the surfaces, while values lower than ‘1’ are by definition not capable of separating surfaces unless special measures like extreme pressure additives are in use. In practice values below ‘2’ are to be considered as critical in regard of metallic contact. As higher  $\kappa$  values increase friction and power loss, a  $\kappa$  in the regime between 2 and 4 is generally advisable. The effect of surface roughness variation is not included in the standard  $\kappa$  values. [ISO281-90, DIN281]

The thickness of the lubrication film in the contact zone of roller and raceway is small. Generally film thickness is within a single micron. The elastic properties of the separated materials can thus not be neglected resulting in the use of *elastohydrodynamic lubrication* (EHL) models. [SKF08, San08]

Fig. 2.18 is a qualitative representation of film shape and pressure distribution within the contact area. An almost parallel film occupies the central region within the Hertzian contact zone, while the minimum film thickness, which is approximately 75-80 % of the central film thickness, is to be found at a constriction near the outlet. It is also noteworthy that a pressure spike occurs, the height of which height may exceed the

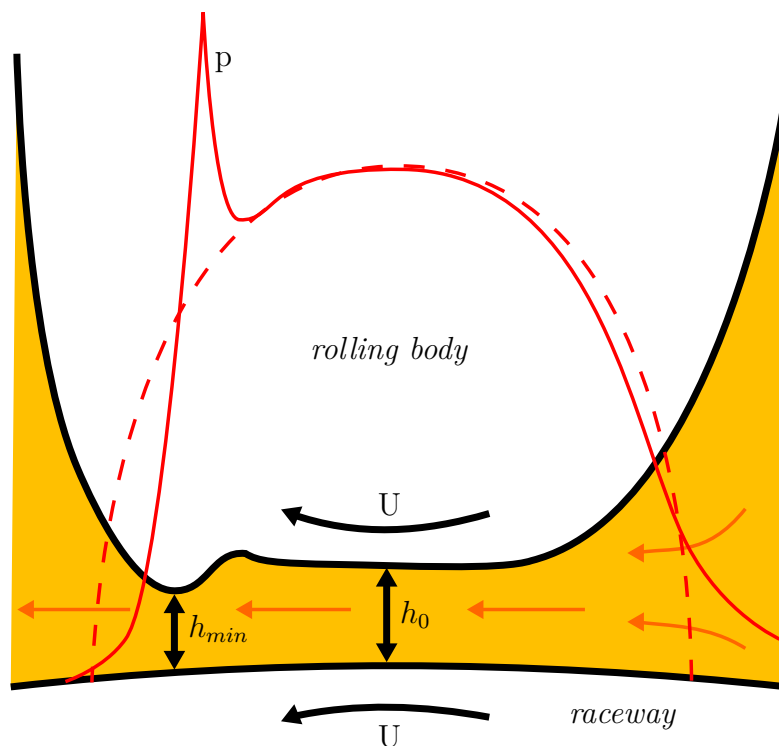


fig. 2.18.: Qualitative EHL Filmshape. The arrows indicate the direction of lubricant flow. The red line represents the EHL pressure, which differs slightly from the hertzian contact stress (dashed line). Shortages are given in tab 2.1.

maximum Hertzian contact stress. This pressure peak is mostly the result of pressure dependent changes of viscosity of the lubricant. Due to the interdependency of pressure, geometry, resulting film shape and the nature of the Reynolds equations Hertzian contact stresses can only be calculated iteratively with the aid of numerical solutions. Dowson and Higginson [DH61] found that the predicted minimum thickness can be represented by the empiric dimensionless formula

$$H = 1.6 \frac{G^{0.6} U^{0.7}}{W^{0.13}} \quad (2.9)$$

for line contact. Dowson later revised eq. 2.9 to

$$H = 2.65 \frac{G^{0.54} U^{0.7}}{W^{0.13}} \quad (2.10)$$

in order to make it compatible with dimensionless analysis. In these equations  $H$ ,  $G$ ,  $U$ ,  $W$  represent the dimensionless film thickness, material parameters, speed and load per unit length respectively. Details are given in tab 2.1.

For point contact Hamrock and Dowson found

$$H = 2.69 \frac{G^{0.49} U^{0.68}}{W^{0.067}} (1 - 0.61e^{-0.73k}) \quad (2.11)$$

## 2.6. DETERMINATION OF NON-METALLIC INCLUSIONS

---

$H = h_0/R_x$	min. average film thickness
$U = \eta_0 u/(E'R)$	dimensionless speed
$G = \alpha E'$	dimensionless materials parameter
$W = q/(E'R)$	dimensionless load per unit length (line contacts)
$E'$	effective Young's modulus (Hertz equation)
$R_x$	principle radius of curvature
$R$	effective radius
$h_{min} = 0.75h_0$	film thickness in the constriction
$u$	relative speed
$\alpha$	viscosity pressure coefficient (Barus equation)
$\eta$	viscosity

tab. 2.1.: List of formulas to eq. 2.9 & 2.10.

to be fitting.  $k$  is the coefficient of half-axis ( $k = a/b$ ). [LS95, Joh85], [DH61] & [Dow68] acc. [Dow95], [HSJ04] acc. [Mey10]

The effects of inadequate lubrication can be numerous. In the common case of  $2 \leq \kappa \leq 4$  a complete separation is not given. The damage to the surfaces is, however, limited to truncated summits of finishing marks. A further decrease of  $\kappa$  increases the intensity of mixed friction until polishing wear occurs on the raceways resulting in considerable smoothing of finishing marks. In addition to polishing wear dense micropittings may also be observed. These few micrometer deep, shallow pittings are initiated at surface inhomogeneities like honing marks or micro-indentations. Indentations do not necessarily have to be the result of micro-scale particles, but can occur due to chemically aggressive mediums like degenerating lubricant (etching on the raceways) and fuel contamination. Also dissolution of surface NMIs like MnS by aggressive mediums may initiate bands of micropittings and small cracks on highly loaded surfaces may also cause micropittings. Due to the surface deformation caused by an initial micropit in combination with moderate sliding motion at the edge of the pitting high EHL pressure peaks in the vicinity of the leading edge result in new micropits at the leading edge of existing pittings. [Geg11, NV00]

## 2.6. Determination of Non-Metallic Inclusions

Non-metallic inclusions (NMI) are inorganic, mineral impurities in the matrix of steels. They are formed either willingly, e.g. to improve chipping / increase wear resistance, or unwillingly during the steel making process and thus may be wanted or unwanted. The found residual NMIs depend on the composition, processing of the respective steel and location of the observed specimen within the billets. NMIs commonly found in steels have compositions containing oxygen, silicon or sulphur, but also other compositions are possible.

NMIs can be classified by shape, size, amount, volume, composition and mechanical properties. In the milling process some types of NMIs, such as sulphides or silicates are

stretched with the hot steel matrix in milling direction and squeezed in cross section, while other types of NMIs are brittle and at most break into smaller pieces during hot milling, e.g. aluminium oxide. Various standards [ASTME45, ASTM2283, DIN50602, DIN10247, ISO4967] have been devised for determining the cleanliness of metals. Noteworthy cleanliness methods are *ASTME45 A*, *DIN 50602 K*, *EN 10 247 K* and *ISO 4967*. These methods discern NMIs according to their respective morphology into four different types regardless of the chemical composition. Greyish, long stretched inclusions are called *sulphides*. Dark, sometimes bluish shimmering inclusions, which are also long stretched are known as *silicates*. Hard particles, with seemingly round shape at lower magnification (i.e. 100x) are called *oxides*. Sometimes they are differentiated as *aluminates* and *globular oxides* depending whether the NMIs have broken into smaller particles or remained as one singular large particle, respectively. These type names do not necessarily reflect the composition of the NMI, but are legacy names.

Although afore mentioned legacy names do not necessarily return information of chemical composition, they often correlate with chemical composition of frequently found NMIs. A common representative of sulphide type inclusions is manganese sulfide. It is a soft, deformable inclusion found in clustered, oblong shapes in longitudinal cross sections of milled steel bars. Generally MnS retains a bonded interface to its surrounding steel matrix. A certain amount of sulfur is always found in steels and is already contained in pig iron, while manganese is added to bind sulfur and improve the steels properties. Silicates and aluminates often consist of silicium oxide ( $\text{SiO}_2$ ) and aluminium oxide ( $\text{Al}_2\text{O}_3$ ). Both elements can be introduced to de-oxidise a steel heat. Oxygen is introduced earlier for decarburisation of pig iron. While  $\text{SiO}_2$  has similar properties as MnS,  $\text{Al}_2\text{O}_3$  forms hard, brittle inclusions of roughly round shapes which may or may not break during milling. It has a weak interface bonding and is often found detached of the matrix. Other chemical elements, such as calcium, nitrogen, etc. are introduced for alloying purposes or stem from the crucible's lining.

NMIs are not equally distributed throughout billets. NMIs heavier than the liquid steel are found in continuous casts at the end, as they sink to the bottom of crucibles, while lighter inclusions are found throughout the steel. Magnetic stirring and the recrystallisation front from the outside layers of the billet to the centre of the cast also generate a cleanliness gradient from highly clean steel in the outside layers to less cleaner steel in the core.

Rolling contact fatigue observations as early as Lundberg and Palmgren [LP47] report of NMIs as locations for subsurface crack initiations (2.1). NMI are still considered as the service life limiting factor in most of the more recent service life models. In classic fatigue testing many researchers have reported that in the absence of surface defects NMI initiate cracks within the specimen, as they represent stress raisers within the volume. Investigations in the very high cycle fatigue regime ( $\geq 10^8$  cycles) of high strength steels show that NMI initiated crack propagation continues till failure, albeit cracks propagate at very low rates in vacuum. The difference in Young's modulus and hardness between NMIs and matrix increases the crack initiation probability. The highest risk for crack initiation, however, are inclusions with weak or no interface bonding. During cyclic stressing of the matrix they debond and the resulting difference between steel matrix

## 2.6. DETERMINATION OF NON-METALLIC INCLUSIONS

---

and vacuum is much higher than with any bonded inclusion. NMIs weaken a steel and in the absence of notches or any other defects on the surface of a component under cyclic stress they lead to fatigue fracture [Sak09, STS10]. The larger the NMI the higher is the probability that a crack will be formed and propagated throughout the steel, leading to fatigue failure. With decreasing grain sizes the steels resistance to fracture decreases, as the grain boundaries do not represent any more adequate barriers to restrain a crack from growing. In steel grades with small grains, as is the case with high strength steel of high hardness, NMIs might become larger than micro-structural barrier distances and effectively be unaffected from these barriers. As a consequence, the fatigue limit in high strength steels with high hardness is reduced due to increased sensitivity to inclusions. The weakening of the steel by an inclusion in the stressed volume can be described by the empiric Murakami formula developed by Endo and Murakami [ME94] which correlates inclusion size and hardness with the fatigue limit  $\sigma_w$  of steels:

$$\sigma_w = \frac{C (120 + Hv)}{(\sqrt{AREA})^{1/6}} \left[ \frac{1 - R}{2} \right]^\alpha \quad (2.12)$$

with

$$\alpha = 0.226 + Hv \cdot 10^4$$

$Hv$  is the matrix hardness measured in Vicker's hardness.  $R$  is the load ratio between lower and upper load.  $\sqrt{AREA}$  is the square root of the largest NMI's cross section normal to the stress field (fig. 2.19) in  $\mu\text{m}$ .  $C$  is a proportionality constant determined it to be 1.43 and 1.56 for surface and subsurface notches respectively. In recent years Bathias et al. [Bat10] found that  $C$  is 1.83 for 100Cr6 in the very high cycle fatigue regime ( $\approx 10^{10}$  cycles). The difference in the values for  $C$  between [ME94] and [Bat10] stem from the fact that [ME94] assumed (based on the knowledge of that time) no further fatigue strength reduction at the end of the high cycle fatigue regime, however, subsurface failure occurs even at later points of time. With decreasing inclusion size the fatigue limit will increase. However, it is limited to the matrix fatigue limit, which can be estimated by

$$\sigma_w = 1.6 \cdot Hv \quad (2.13)$$

. Another group of damage mechanism introduced by NMIs in high strength steels can be termed *White Etching Area / White Etching Cracks* (WEA / WEC). The term is derived from the fact that these structures consist of a non-etching phase when Nital is applied as etchant during metallographic analysis. As the name suggest cracks are promoted along this phase in bearings. WEA consists of extremely small ferrite grains of cellular shape and the almost complete absence of carbon within the phase. In early stages WEA form wing-like shapes around the NMI, known as butterflies. With increasing growth they turn into white bands. In the case that failure has not promoted yet, they are linked to networks of bands. In push-pull fatigue test also round structures around NMIs are found. These structures are known in literature as fisheye.

[LP47, SAJ09, THF10a, THF10b, MKK89, MU89, ME94, Bat10, Bat12, LLR12, GLL12, Luy11, Sak09, STS10]

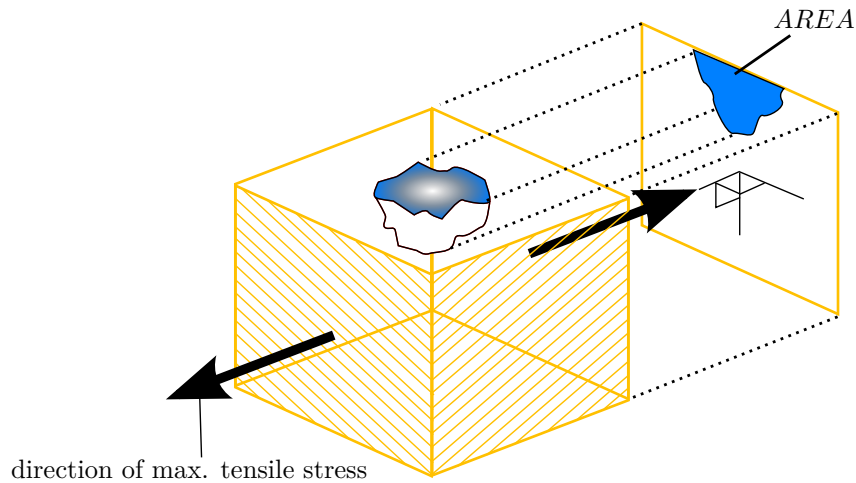


fig. 2.19.: The *AREA* parameter is an inclusions surface normal to the stress direction.

The ASTM E45 Method A is of special interest for bearing steels, as the steel cleanliness is graded by severity levels which in turn depend on the largest NMI observed. It differentiates NMI as sulphides, silicates, aluminates and oxides. The first three types are further divided into thin and thick according to their width. It is flexible enough to include additional categories to include nitrates or other NMI types and state explicitly certain compositions of NMI. It is currently the only valid standard for which the minimum bearing steel cleanliness is specified by the international standard ISO 683-17 [DIN683]. Latter standard also gives threshold values for use with DIN 50602 Method K, however, the DIN 50602 has been replaced by the fundamentally different EN 10 247 in 2007. In the absence of reasonable threshold values the DIN is still in use for bearing steel cleanliness evaluation. The DIN Method K evaluates the severity based on the total area taken by NMIs in longitudinally sectioned polishes, which then are normalised to a surface area of  $1000 \text{ mm}^2$ . It allows to clip off NMI cross sections below definable areas in its severity calculation. The value given by this method does not discern different types of NMIs. In a sub-state it allows to discern between sulphides and oxides. As silicates mostly consist of  $\text{SiO}_2$  and Si they are counted in this method to the oxides. The newer EN 10 247 differentiates like the ASTM E45 A NMIs into four types and returns the values of the total percentage of area taken by these NMIs in  $\mu\text{m}$  per  $\text{mm}^2$  and the number of NMIs per  $\text{mm}^2$ . In the draft for the upcoming edition of ISO 683-17 the ASTM E45 A values will be replaced by the ISO 4967, which is similar to the ASTM E45.

All four standards focus on providing descriptive methods to determine cleanliness of milled steels. They are, however, incapable of predicting the largest NMI within the stressed volume of an actual component nor is it possible to incorporate Murakami & Endos' fatigue limit estimation of components (eq. 2.12 & 2.13). With increasing cleanliness of a steel, however, the chances to observe an inclusion of the top most size diminishes greatly.

## 2.6. DETERMINATION OF NON-METALLIC INCLUSIONS

---

These standards, although very powerful in assessing the cleanliness of a steel grade, are insufficient to return the *AREA* parameter of a real component without overestimating its fatigue limit, as they rely on the sampling of at least six longitudinal sections with a limited total surface area. With increasing cleanliness of the steel, however, the chances to observe an inclusion of the top most size diminishes. To visualise the import of the above statement think of an one-by-one-by-one cm<sup>3</sup> Swiss cheese. We do not know the size of the largest hole in this piece of cheese, however, we can safely assume that its volume will be smaller than one cubic-centimetre. But when we dissect an entire body of the same cheese, we might find holes much larger in size than the piece of cheese relished before. If we would have assumed from our small piece of cheese to know the size of the largest possible hole within the body we would have been gravely mistaken. While the holes in our Swiss cheese allow us to measure the cross surface area perpendicular to the surface, we do not have this option for solid inclusions. Thus in order to estimate the size of the largest inclusion within our component from the few samples analysed it is absolutely necessary to know the distribution pattern of inclusions and to scale the distribution pattern to a much larger size. Since the observation is not necessarily done in the layer in which the largest cross section of an inclusion is presented we also have to take enough samples to safely assume the observation of such NMIs. Murakami and Beretta et al. tackled this matter in several papers [ME94, BAM06, BM98, ZMB02, BM01, MKK89, MU89] and report that inclusions follow the Gumbel distribution, which is better known as largest extreme value distribution or type I extreme value distribution. Zhou et al. [ZMB02] showed that a three dimensional sampling of cross sections does not greatly differ in distribution parameters observed by inspection of a sufficiently large total two dimensional area. The distributions cumulative distribution probability is given by

$$P(x) = \exp\left(-\exp\left[-\frac{x-\lambda}{\delta}\right]\right) \quad (2.14)$$

where  $\lambda$  and  $\delta$  are the location and the scale parameter, respectively.  $x$  represents the  $\sqrt{AREA}$  parameter of a given NMI. To simplify calculations and graphical representations the reduced variate

$$y = \frac{x-\lambda}{\delta} \quad (2.15)$$

is used. The cumulative probability plotting position of an actually observed inclusion of the size  $x_i$  is given by

$$P_i = \frac{i}{n+1} \quad (2.16)$$

thereby  $i$  runs over  $n$  defects of the sample sorted in ascending order of inclusion size.

In order to normalise the distribution of different measurement areas  $A_1$  and  $A_2$  or in order to normalise to a reference area  $A_{ref}$  the ratio  $t$  can be introduced being  $t = A_2/A_1$  or  $t = A_{ref}/A_1$ , respectively. A probability distribution of the area  $A_1$  can be transformed to area  $A_2$  or  $A_{ref}$  by

$$P_{A_{ref}}(x) = [P_{A_1}(x)]^t \quad (2.17)$$

. To avoid two or more different kinds of NMI compositions being oversampled during a type based detection, e.g. two different kinds of oxides, the block maxima method is applied. This fact utilises the observation that the  $m$  largest inclusions per area most probably belong to the same chemical composition, as  $\lambda$  and  $\delta$  differ by composition of inclusions leading to different  $x$  values for equal  $P$ . Moreover an oversampling of different composition types will lead to an knee in the distribution curve enabling the investigator to remove all observations belonging to the steeper, left bend of the curve. A qualitative example is given in fig. 2.20. After successfully fitting of the curves  $P = 1$  returns the largest NMI expected. It can be shown that the standard error  $SE$  obtained is larger or equal to a theoretically defined standard deviation  $SD$  given by

$$SD(x) \leq SE(x) = \frac{\delta}{\sqrt{n}} \cdot \sqrt{0.60793 y^2 + 0.51404 y + 1.10866}$$

It follows that the 95 % confidence interval is

$$x \pm 1.96 \cdot SD(x)$$

. An overview of the entire procedure is given in fig. 2.21. An almost identical procedure is also given in standard ASTM 2283, however, non-concurrently the use of feret diametre is demanded. [ASTME45, ASTM2283, DIN50602, DIN10247, ISO4967, ME94, BAM06, BM98, ZMB02, BM01, MKK89, MU89]

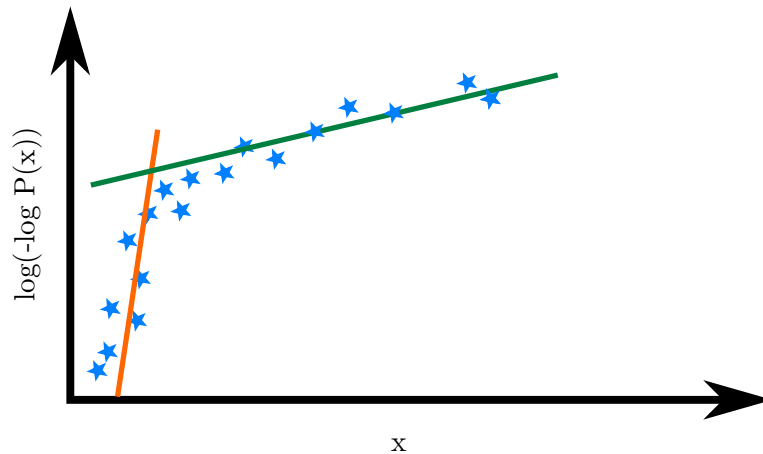


fig. 2.20.: An knee in the cumulative probability plot indicates two different compositions of NMIs of the same type. The largest  $x$  of the orange composition, however, will never quite reach the values of the green composition. The risk of such effects can be avoided by employing a block maxima.

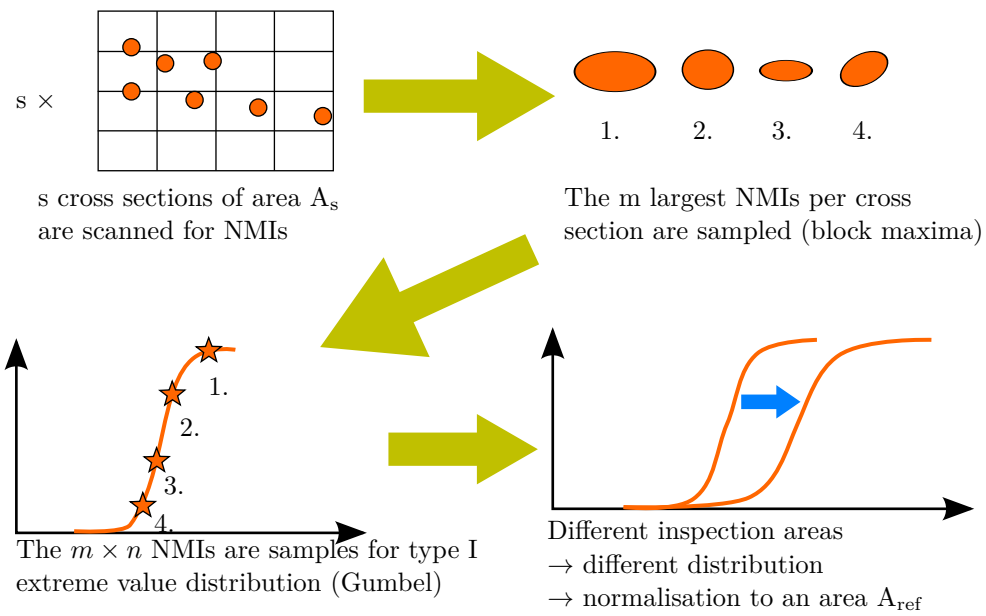


fig. 2.21.: Overview of the extreme value distribution analysis for NMIs.

## 3. Dynamic Testing under Time-invariant Loading

### 3.1. Motivation

Common dynamic bearing tests conducted in order to determine the dynamic capacity  $C$  or  $L_{10}$  are of a static nature regarding the employed forces. The dynamic nature of these bearing tests stems from the fact that rings of a bearing experience alternating loads. Since this method is in practice for a long time and generally accepted as *the* method to determine the dynamic properties of bearings, it shall be used to determine the general properties of the hypoeutectoid steel used in this work.

### 3.2. Testing Method

Testing is conducted on an existing test rig described in [PMS10]. The strength of this test rig is an easy to achieve statistics of service life. Moreover reference service times for cylindrical roller bearings (CRB) made of 100Cr6 are already in existence.

The test rig consists of a base unit and six individually operating test housings. Each housing contains a shaft with four raceways and bearings. To achieve as equal a load as possible on each bearing the system – consisting of the shaft and bearings – is braced in such a manner that forces are not conducted into the base unit (fig.3.1). The load on the bearings is set by a stack of disc springs. The load of this spring stack is divided on both central bearings. Thermometer lances in contact with the OR measure the OR temperature of the bearings. Moreover, the housings are rigged with vibration sensors for detecting solid borne sounds. These sounds are being monitored and analysed by a condition monitoring system which at the occurrence of failure triggers a stop signal to the corresponding motor controller in the base unit. This condition monitoring system has been developed during a preceding Ph.D. thesis [Hac11]. The raceways are lubricated by oil injection. The lubricant jet hits the surface of the shaft slightly beside the raceway in order to avoid repelling by passing rolling bodies. The base unit contains the electric motors for driving the shafts. It also contains for each housing independent oil circuits for lubrication and cooling of the bearings. In each lubrication circuit there is an oil filter with a retention value of  $\beta = 200$  at  $10\ \mu\text{m}$  particle size. Thermometers show that the temperature of the system reaches  $72^\circ\text{C}$  at the outer rings in equilibrium state.

Elastic shaft bending is inevitable in this arrangement. Even if in theory the shaft bending would be symmetrical between two central bearings, it is never the case for a real component. Slight differences in tolerances and position lead to different misalignments

and axial forces. Further it is known from needle bearings that internal axial forces arise especially when elastic deflections of the shaft lead to misalignments [Sch12].

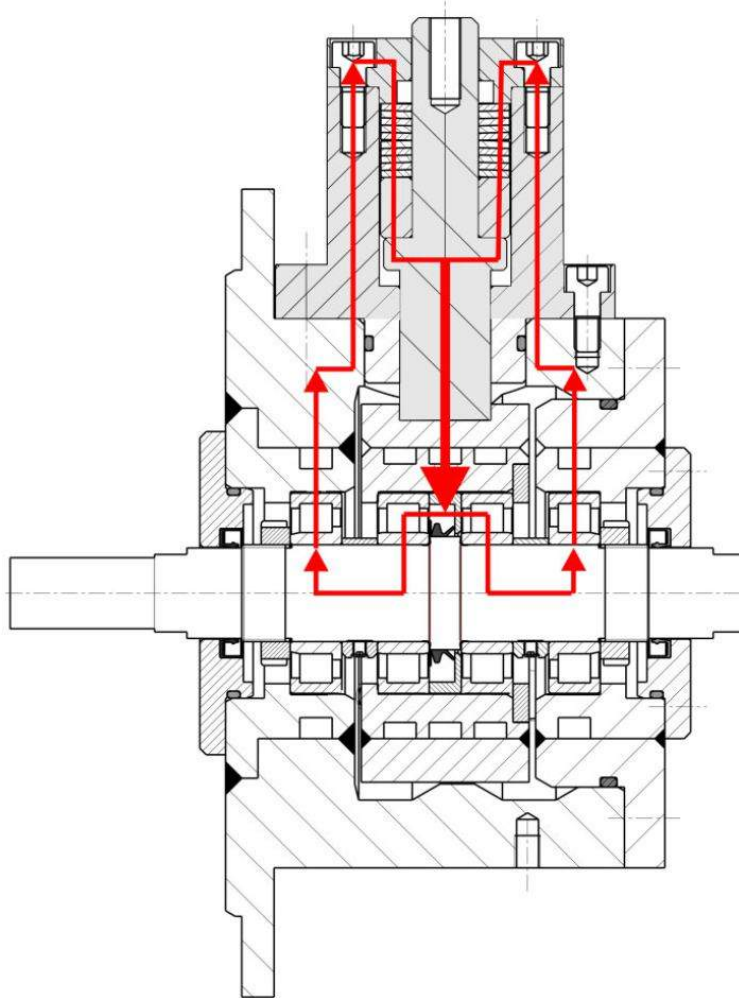


fig. 3.1.: Load distribution at the test head for constant load investigations. [Hac11]

### 3.3. Specimen Geometry

CRBs of type of NU 206 are used. They are standard catalogue bearings made of 100Cr6. The outer ring (OR) of this type of bearings have flanges to guide the rollers and thus the cages and rollers within the cages cannot be easily disassembled from the OR. The inner rings (IR), however, are designed to allow displacement in axial direction for the application as non-locating bearing. Thus they do not possess any flanges and can be easily removed and replaced by shafts made of the testing material with the same diameter as the raceways of the IRs. This method was chosen to reduce the effort necessary to

### CHAPTER 3. DYNAMIC TESTING UNDER TIME-INVARIANT LOADING

test new materials. The manufacturing of entire bearings of a different material would have been extremely time consuming and would not have been easily accomplished in a satisfying quality. The bearing clearance is C3. The shaft geometry is depicted in fig. 3.2. Note that the IR raceways of actual bearings have convex or convex-logarithmic shapes to avoid edge pressure. This is not the case for the shafts. The resulting nominal maximum hertzian contact stresses in the IR and the shaft have been calculated with LAGER2 and can be taken from fig. 3.3. These results show that edge stresses occur, however, within the limits of normal operating conditions for bearings and thus will not generate unintended effects. A detailed overview of all parameters are given in tab. 3.1.

As each shaft has four raceways and the failure of one raceway determines the end of testing for that particular shaft, a Weibull sudden death algorithm is employed to calculate a first shot  $L_{10}$  service life. The sudden death algorithm is also known as right censored Weibull statistics.

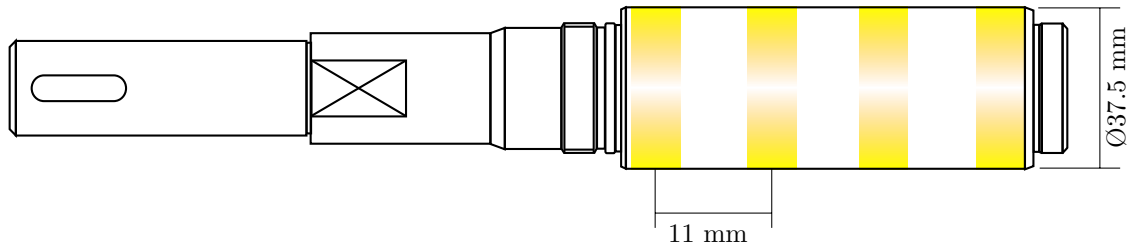


fig. 3.2.: Geometry of used shafts. The raceways (yellow) are equally spaced from each other.

revolutions	4050 rpm
lubrication condition $\kappa$	2.13
used oil	ISO VG 68
oil filter	10 $\mu\text{m}$
oil filter retention $\beta_{10}$	200
lubrication cleanliness factor $\eta_c$	0.3
system-temperature (average)	72°C
nominal load / bearing	11,25 kN
dynamic Capacity C (Nu 206)	44 kN
nominal C / P	3.91
bending of shaft (calculated)	38 $\mu\text{m}$
inclination of outer bearings (calculated)	0,1912 mrad
inclination of inner bearings (calculated)	0,3920 mrad
$h_0$ (Hamrock & Dowson)	4.6 $\mu\text{m}$
$h_0$ (Dowson & Higginson)	11 $\mu\text{m}$

tab. 3.1.: Constant parameters of testing

### 3.3. SPECIMEN GEOMETRY

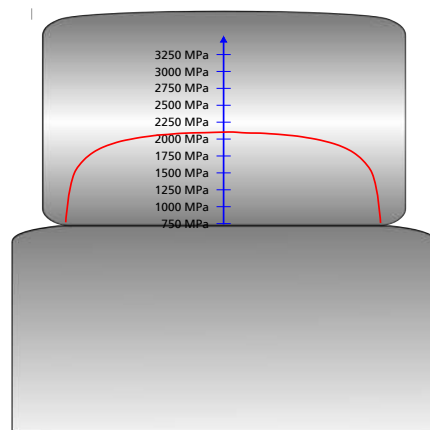
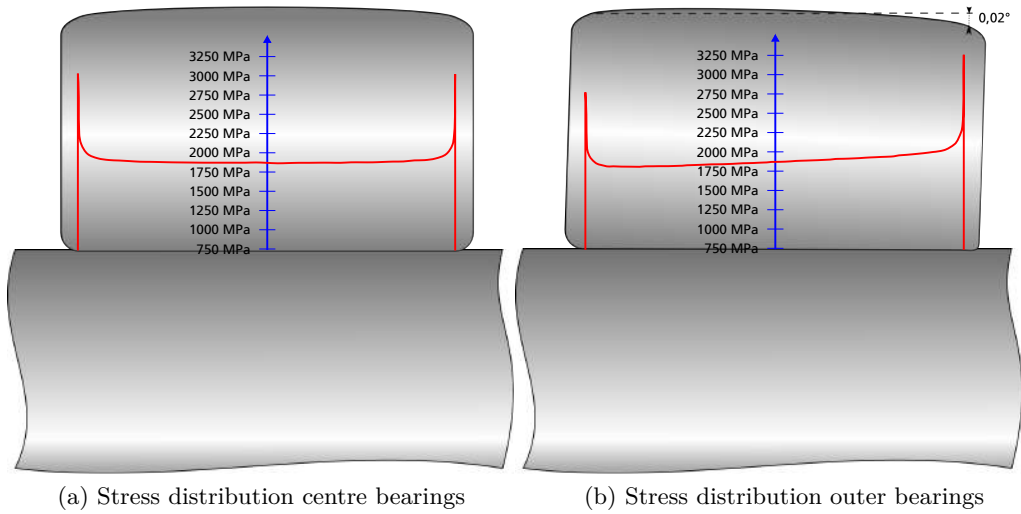


fig. 3.3.: The calculated stress distributions show that stresses are by all means of similar order. The edge pressures on the raceways of the shaft are still within application limits. The edge stresses might be overestimated by Lager2.

### 3.4. Investigated Materials

Two different compositions of hypoeutectoid steels have been tested at different steel cleanliness and at different states of residual stresses. The first steel grade is a regular carbon steel with approximately 0.5% of carbon known as C56E2. The other grade is an experimental grade dubbed C55V. It is very similar to C56E2, but has additional alloys to enhance its hardness and tensile strength. The chemical compositions as used are listed in tab. 3.2.

Alloy [%]	C	Si	Al	Mn	S	Ni	Mo	V	Cr	N
C56E2	0.56	0.23	0.034	0.81	0.006	0.09	0.02	-	0,16	0,01
C55V	0.55	0.72	0.04	0.65	0.013	0.09	0.04	0.09	0,07	0,09

tab. 3.2.: Chemical composition of used steel grades

The cleanliness of bars made of these steels decreases from the surface of the bar to its core. Only a small portion of the outer layers of the bars achieve very high cleanliness. After a few millimetres from the edge cleanliness drops and then gradually decreases to the core of the bar. As the targeted components in the real application are to be forged it seems plausible that these layers may be displaced or destroyed. For testing purposes crankshafts made of both steel grades have been forged with serial production facilities and the die for a V8-engine crankshaft. Analysis of cleanliness show that the resulting outer layers are not the layers of highest cleanliness. To simulate this circumstance mostly shafts turned from Ø55 mm bar material are used. In contrast to these low cleanliness shafts high cleanliness shafts are turned from Ø40 mm bars. The shafts made from C55V were turned from Ø75 mm material. In the case of the latter bar extra clean layers are not found, for it is an experimental heat and not produced in large enough scale to take advantage of scale. Micrographs of both grades can be found in appendix A.

Both steel grades contain low concentrations of oxides. The low cleanliness steels have cleanliness at the minimum specifications given in ISO 683-17 [DIN683] measured with method A of ASTM E45 [ASTME45]. The high cleanliness steels have considerably lesser inclusion sizes.

The cleanliness of the critical (i.e. stressed) shaft volume have been determined by methods ASTM E45 Method A [ASTME45], DIN 50602 Method K (K2) [DIN50602] and EN 10 247 Method K [DIN10247] simultaneously with an optical measuring system. Moreover the visible surface of detected particles have been determined in order to find the largest NMI by means of largest extreme value distribution. Instead of analysing the surface area as a parameter of area the square root of area ( $\sqrt{AREA}$ ) is taken in order to comply with the so called Murakami formulas (chapter 2.6). In the latter method only sulphides and oxides are distinguished as silicates can be hardly found in the steel grades used in this work. As aluminates are clusters of small globulars, they are considered within the globulars. Figs 3.4 - 3.7 depict the results of the different cleanliness standards.

### 3.4. INVESTIGATED MATERIALS

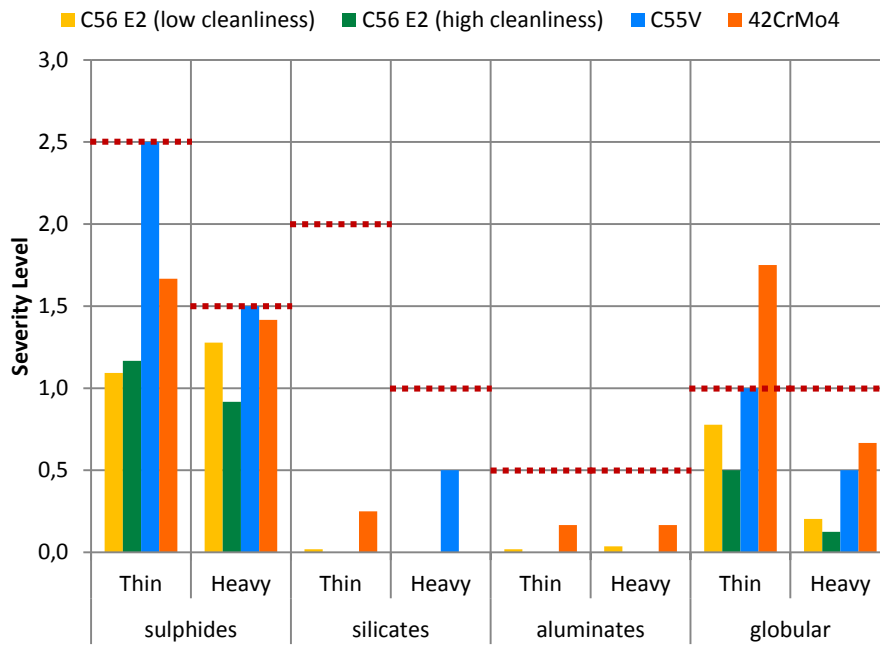


fig. 3.4.: Cleanliness according ASTM E45 Method A. The dotted red lines indicate the limits for bearing steel as given in ISO 683-17.

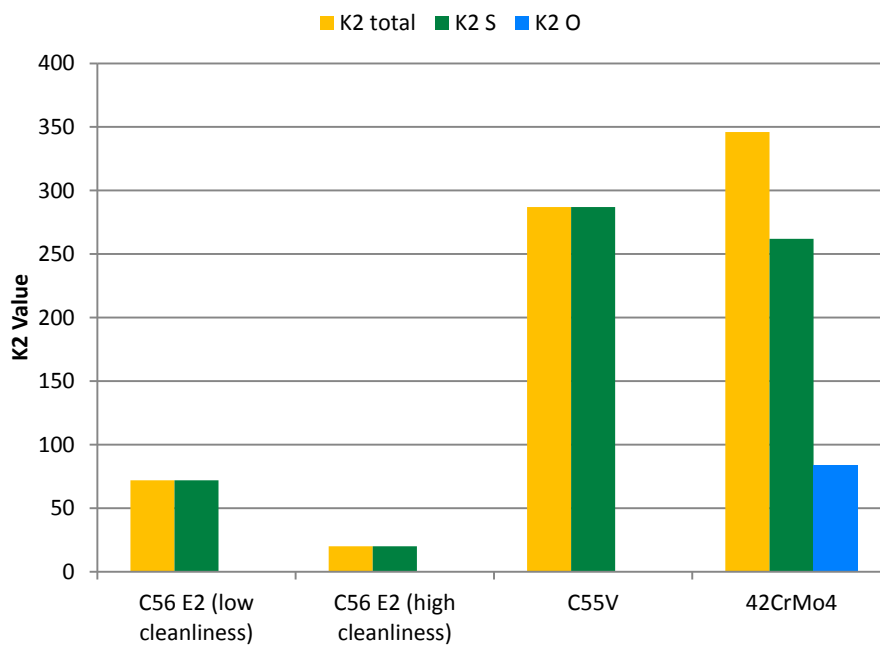


fig. 3.5.: Cleanliness according DIN 50602 Method K

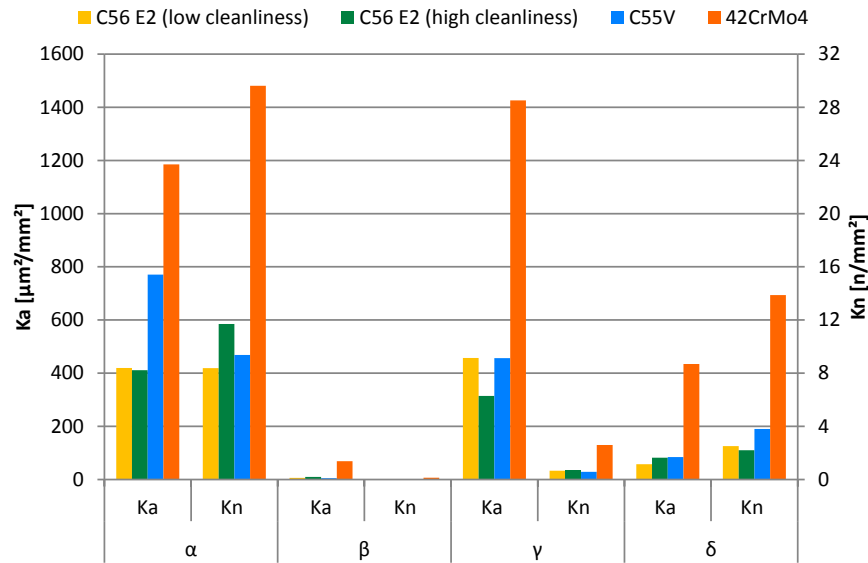


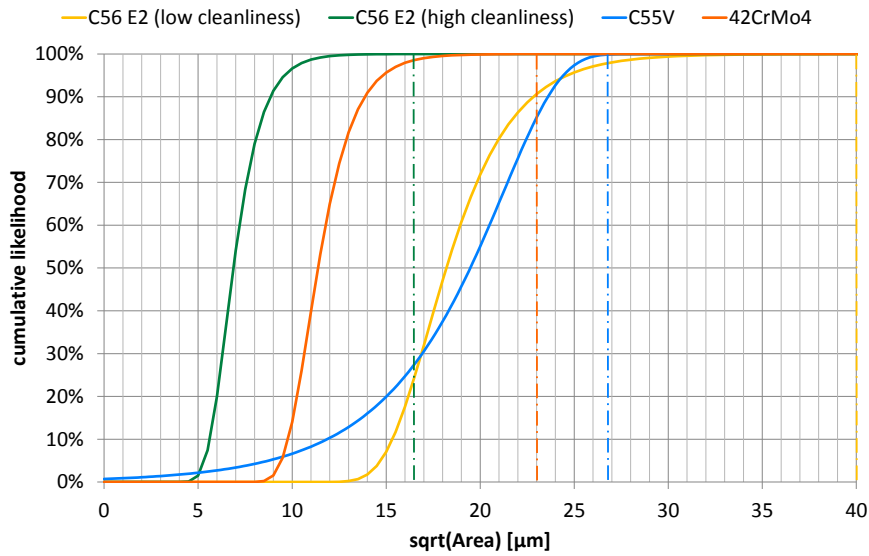
fig. 3.6.: Cleanliness according to EN 10 247 Method K

The ASTM E 45-method shows that the C56 E2 contains relatively smaller sulphides than the C55V. The C56 E2s are well within the limits defined by ISO 683-17, while the other grade has sulphide sizes bordering the threshold value. Also the size of globular oxides is larger than in C56 E2, with thin globulars bordering the threshold value and thick globulars being more than twice as severe than in the low cleanliness C56 E2 shafts. The largest NMI expected as per extreme-value analysis are of similar size for low cleanliness C56 E2 and C55V in terms of  $\sqrt{AREA}$ . The obsolete DIN-methods and their succeeding EN-methods clearly show that C55V has in total a higher amount of sulphides than C56 E2. In order to give an impression of the cleanliness values of these steels common 42CrMo4 has been analysed. Analysis is conducted on layers bordering the surface of a  $\varnothing 40$  mm round bar. It can be clearly seen that the content of sulphides and oxides in the tempering steel is higher than in C56 E2 and its derivative.

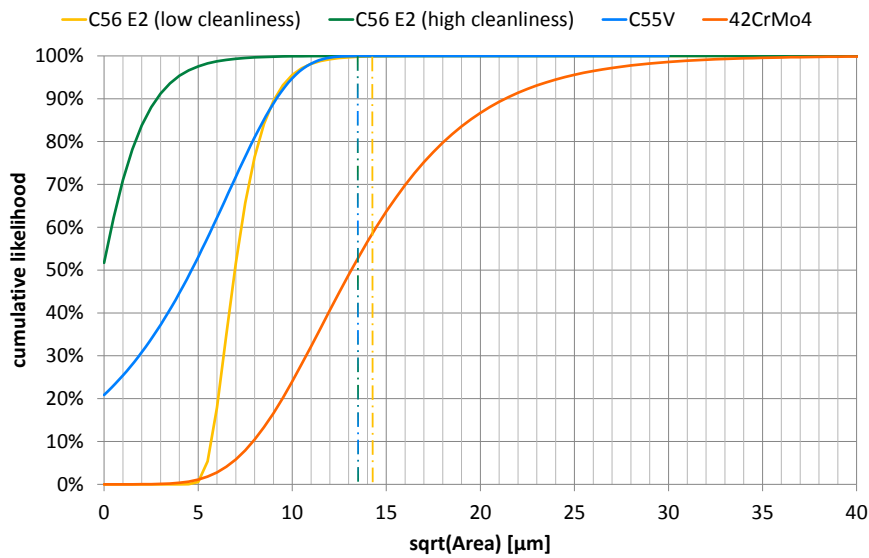
As the steel grades do not have chromium or any other alloy to enable through hardening capability, induction hardening is employed to harden the surfaces into a depth of roughly 3.5 mm. Induction hardening instead of conventional oven hardening transfer line manufacturing processes of modern car engine manufacturers. Tempering of the steels, however, is done in a conventional oven, as tempering during induction hardening is not a trivial undertaking.

Shafts made of the C56 E2 with 160 °C annealing temperature and fine ground surface were defined as reference (Test 0). In a first set of experiments, labeled A1 and A2, the effects of higher and lower residual stresses are studied for C56 E2. For A2 the tempering temperature has been increased to 170 °C in order to reduce residual stresses,

### 3.4. INVESTIGATED MATERIALS



(a) Sulphides distribution



(b) Oxide distribution

fig. 3.7.: Largest extreme value distribution of sulphides and oxides in the different steel grades. The likelihood is normalised for a total longitudinal cross section area of  $1000 \text{ mm}^2$ . A percentile of 99.99% is taken for the largest expected NMI. 99.99% for 42CrMo4 in (b) is at  $52 \text{ }\mu\text{m}$ .

## CHAPTER 3. DYNAMIC TESTING UNDER TIME-INVARIANT LOADING

---

while specimens from experiment A1 have been hard turned prior grinding in order to induce strong compressive residual stresses. To reduce the risk of lessening these stresses annealing was conducted at 150 °C.

Another experiment, labelled *B*, is conducted to determine the effect of higher total cleanliness. Experiment *C* is conducted to investigate the performance of the C55V. For details see tab. 3.3.

Test	Steel grade	Annealing Temp.	Cleanliness	Surface Hardness
0	C56 E2	160 °C	low	61-62 HRC
A1	C56 E2	<b>150 °C</b>	low	62-63 HRC
A2	C56 E2	<b>170 °C</b>	low	60-61 HRC
B	C56 E2	160 °C	<b>high</b>	61-62 HRC
C	<b>C55V</b>	160 °C	low	62-63 HRC

tab. 3.3.: Parameter variation of testing. For tests 0, A1 and A2 the same heat is used.

### 3.5. Testing procedure

Prior the experiment the finished shafts and NU 206 bearing ORs together with cage and rollers are cleaned with white spirit and conserved with ISO VG 68 oil. The shafts are manually mounted on test heads, which in turn are mounted to the base unit. The shafts are mounted in a regular workshop environment without any special cleanliness precautions. After a 30 min shakedown, in which the spring packet is only partly tensed, the actual testing begins.

After end of testing the shaft raceways are visually inspected. Pittings are cross sectioned for search of NMIs. Cross sections are also prepared and examined for determination of the actual loading exerted on a raceway by examining the depth  $z_0$  of maximum orthogonal shear stress in DER layers (2.3.1).

### 3.6. Results

#### 3.6.1. Weibull Curves

Figs 3.8 and 3.9 shows the Weibull curves of the experiments. Each marked failure is the damage of one bearing and the end of test for the other three bearings on the same shaft. An arrow marks the removal of an entire shaft without failure. For the sake of clarity the arrows are marked on the upper right corner of the graphs instead at the time of removal. As mentioned in chapter 3.2, a perfect load distribution is despite best efforts not possible as minor manufacturing differences and inaccuracies in the regime of several microns during assembly is unavoidable. As camshaft and crankshafts, however, do have exactly this kind of bearing configuration and are thus also prone to the same inaccuracies. Figs 3.10 and 3.11 shows the Weibull curves for test shafts instead of each

bearing corresponding to the cumulated failure probability of a component with four bearings<sup>1</sup>. Again the arrows mark the end of test for unfailed specimen. This time the arrows are aligned along the Weibull lines at the time of removal. The removal times are identical with the ones marked in figs 3.8 and 3.9. This inconsistent method of positioning the arrows is done in order to enable the reader of first recognising the total number of unfailed shaft and then secondly to locate them in the lower figures according to their respective censoring time.  $\beta_{max}$  and  $T_{max}$  are shape and scale parameter respectively.

In fig. 3.8 and 3.9 it is apparent that 0, A2 and C are identical respective their confidence interval. Experiment A1 with higher compressive residual stresses exhibit a shallower shape parameter. Experiment B's shape parameter is similar to the parameter of experiment 0, however, its scale parameter is much lesser, moving curve B to earlier failures.

### 3.6.2. Observed Damage Mechanisms

Fig. 3.12 visualises the cumulative failure mechanisms in experiments 0, A1, A2 and C. Failures caused by edge stresses are specific to the specimen geometry and thus can be neglected for consideration. Mixed friction failures, however, cannot be neglected, as it may appear in real world applications. In this work mixed friction is defined as failures due to the lubrication situation with the exception at indentations. The latter failure type is defined as a failure type in its own right. Subsurface failures are determined by excluding all other failure mechanisms. The major reason for failure is thus indentation initiated surface fatigue. Failures caused by asperities are not observed. Latter failure case would also have been very unlikely, as the surface of the shafts are fine ground.

#### Failure by Indentation of particles suspended in lubricant.

However, the majority of all failures are caused by indentation of particles (fig. 3.13). The shape of indentations suggests "soft", metallic particles like annealed or brass steel. The size of the indentations appears to refer to particles with a size in the regime of 100-400  $\mu\text{m}$  in at least one dimension. "Soft" means in this case particles with a lower hardness than the raceway ( $\approx 750 HV$ ).

#### Failure by Mixed Friction

Considering the fact that experiment B is by all means identical to 0, but for higher NMI cleanliness, the lower service life is astounding. Visual analysis shows polished, gray stained and at times oxidised raceway (EP additives) surfaces indicating strong surface contacts as expected by mixed friction (fig. 3.14). In cross section the failure at only 66 h exhibits already DERs, which is very early (fig. 3.15). The DER depth would correlate with hertzian contact stresses of approximately 3.2 GPa, however, it may be

<sup>1</sup>For a  $n$  bearing component the failure probability  $P_n$  is  $P_n(x) = \sum_i^n P_i(x) = n \cdot P(x)$ .

CHAPTER 3. DYNAMIC TESTING UNDER TIME-INVARIANT LOADING

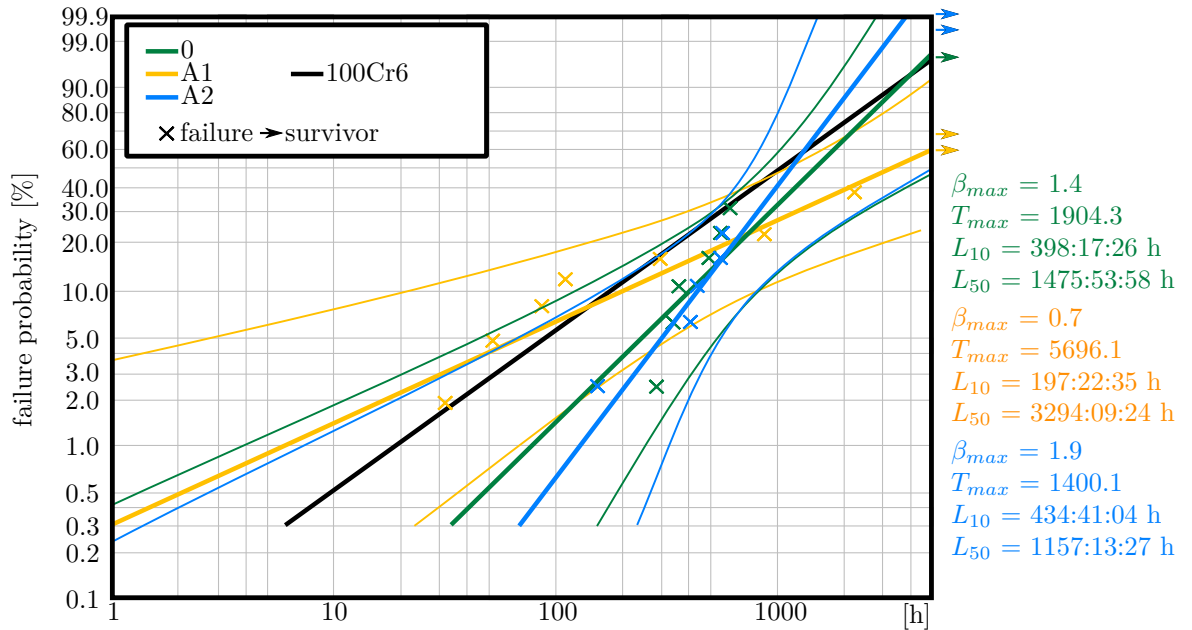


fig. 3.8.: Weibull distribution for individual bearings of Tests 0, A1 and A2. The confidence intervals are given for 95 % confidence.

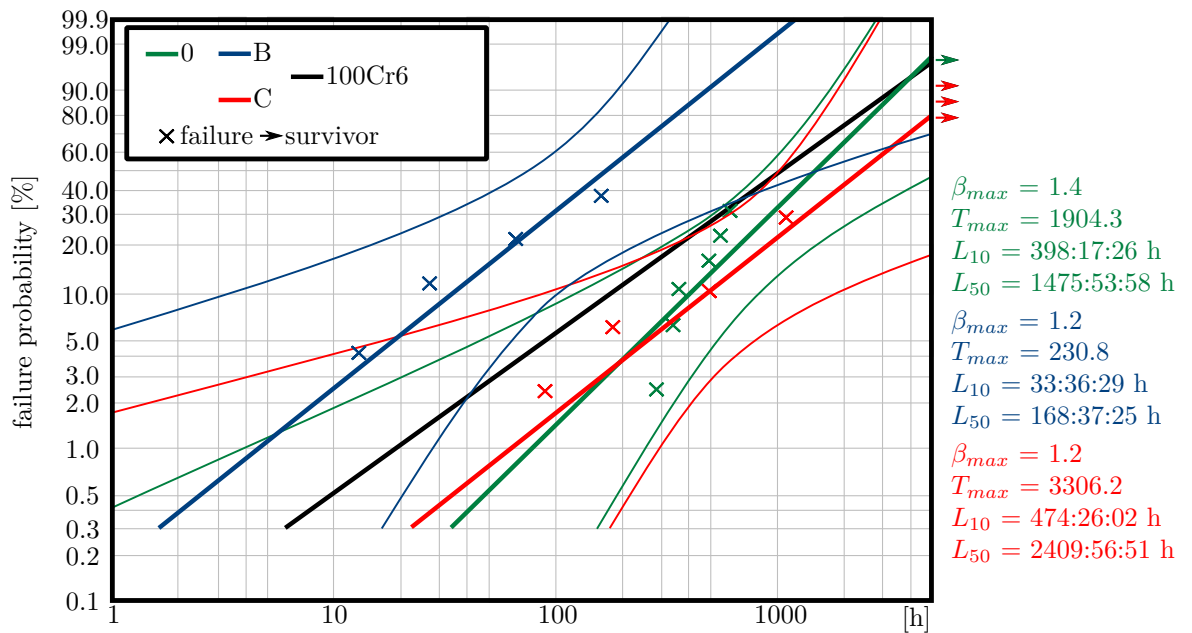


fig. 3.9.: Weibull distribution for individual bearings of Tests 0, B and C. The confidence intervals are given for 95 % confidence.

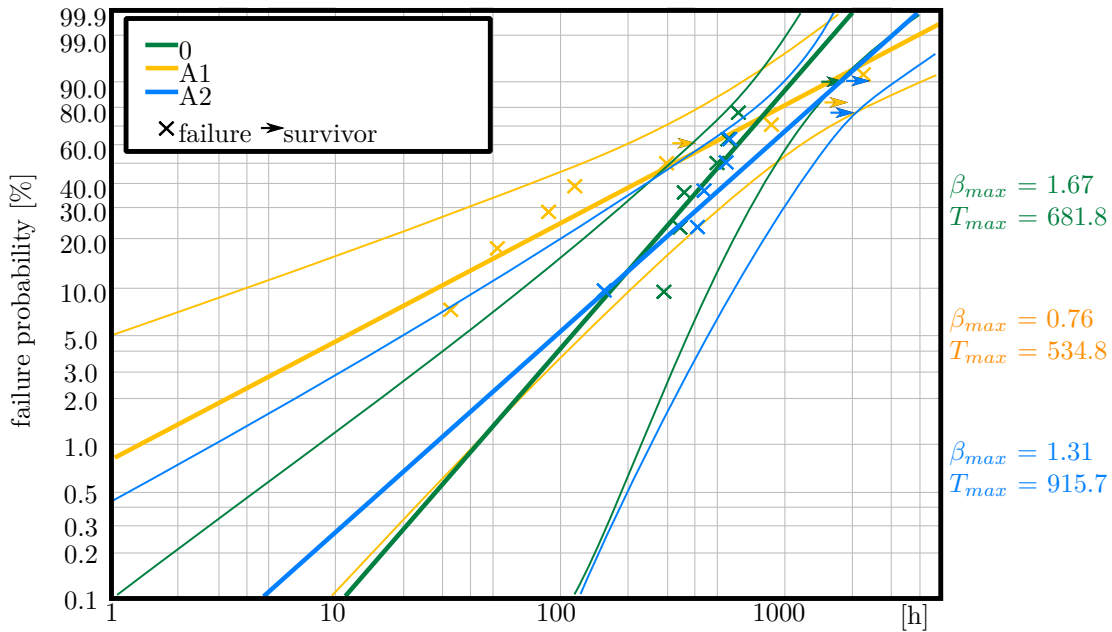


fig. 3.10.: Weibull distribution of Tests 0, A1 and A2 for entire shafts. The confidence intervals are given for 95% confidence.

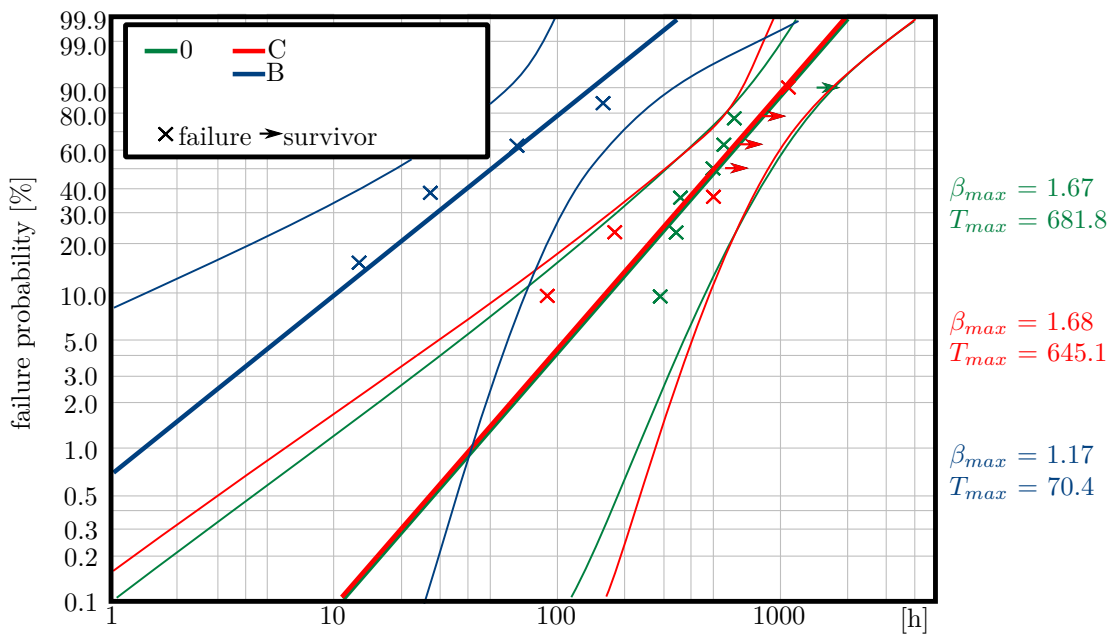


fig. 3.11.: Weibull distribution of Tests 0, B and C for entire shafts. The confidence intervals are given for 95% confidence.

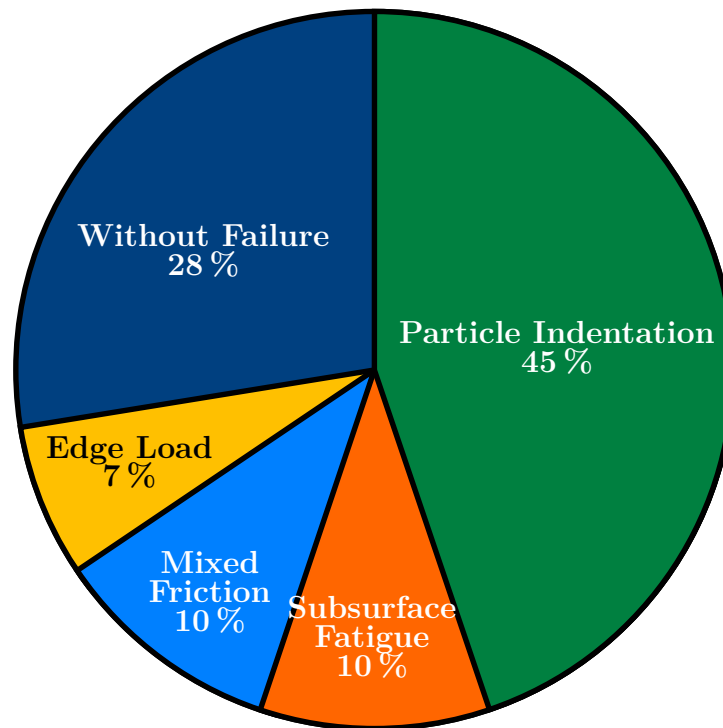


fig. 3.12.: Overview of the observed failure mechanisms. More than half of all failures are triggered by particle indentation.

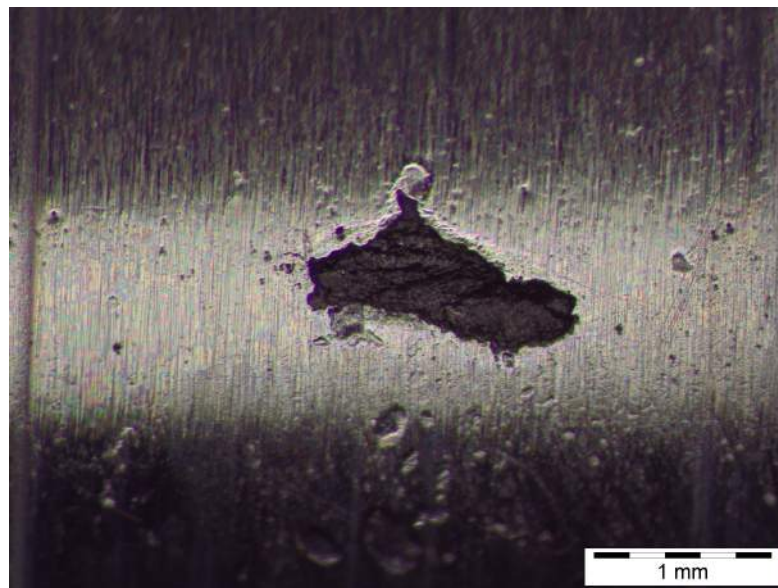


fig. 3.13.: Overrolling of a particle. The shape is typical for “soft” metallic particles. The indentations on the lower part of the picture are caused by spallings after failure.

much higher as shear stresses acting on the surface raise the location of  $z_0$  closer to the surface.

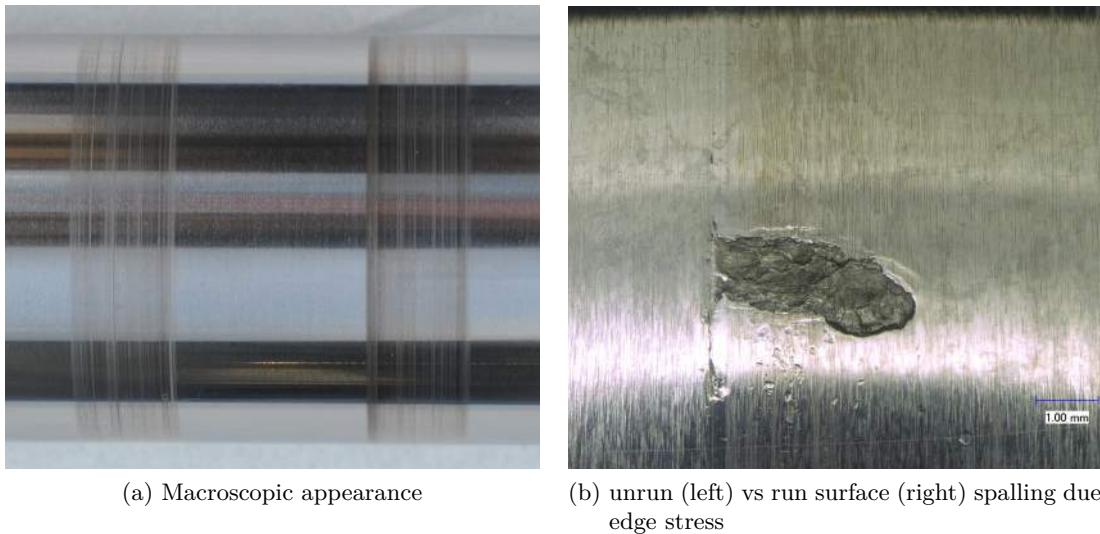


fig. 3.14.: Surface of run series B shafts

Also the C series raceways exhibit strong surface impacts. Most of the raceways exhibit strong metal-metal interaction. The visible surface damages include edge polishing, grey staining band, oxidation and strong wear marks.

The cause for this increased mixed friction has been investigated extensively, but to no avail. All tests were conducted with the same batch of lubricant. No measurable deterioration of the oil or application occurred. Neither a refitting of the test heads or disk springs brought relief to the circumstance.

### Observation of Microstructural Decay

Cross sections show that almost each raceway of the shafts exhibit martensite decay by DER formation. Micrographs show that each raceway on a shaft feature different intensities and depth of DERs. These fluctuations are indicators of different load distributions of each bearing. An example of such a fluctuation is shown in fig. 3.16. These distributions can not be correlated in any meaningful way or diminished by additional care. Measurements of the FWHM of several raceways proved that  $z_0$  indeed varies arbitrarily. Two raceways of each the 0 series and the A2 series exhibit LABs. So do two raceways of the C series. Except for one 0 series raceway, which, according to its status, may have been exposed to a very high contact stresses of approximately 3.5 to 3.7 GPa, all other raceways belonged to shafts with service times above 1000 h.

In fig. 3.16 surface effects are visible indicating that lubrication / sliding conditions of the concerning raceways were not ideal, e.g. centre left and right.

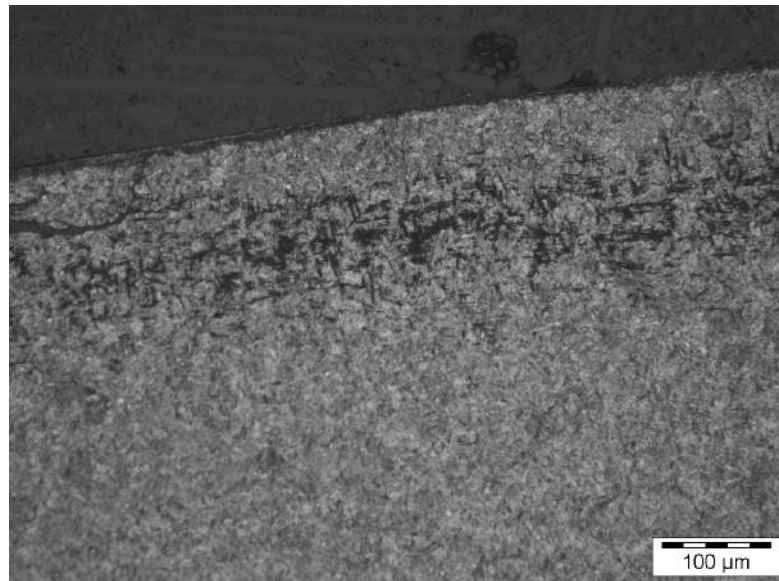


fig. 3.15.: DER formation after 66 h in a series B raceway

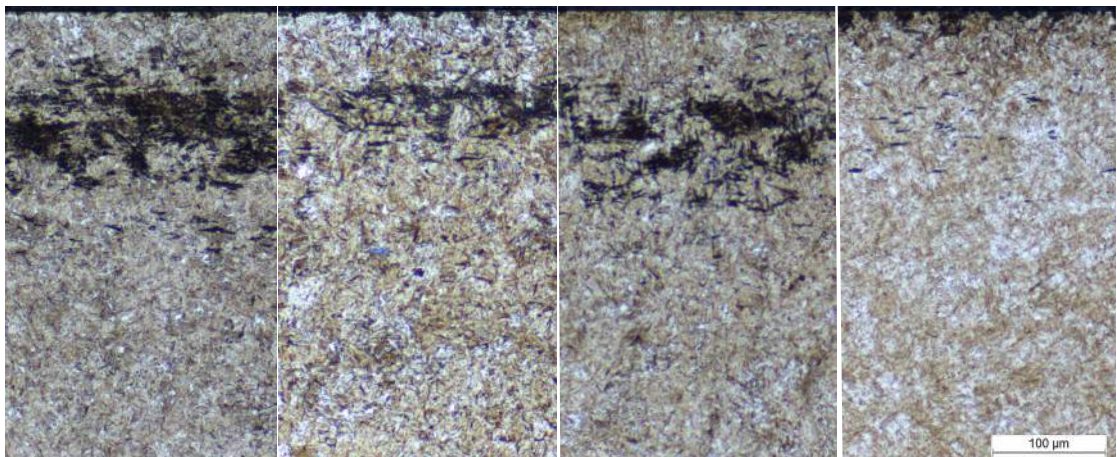


fig. 3.16.: Variation of DER in an A2 shaft

### Crack Initiation at Non-metallic Inclusions



fig. 3.17.: Surface image of the 1100 h C series raceway. The upper part exhibits the typical V-shape spalling triggered by indentations and asperities. In this case an asperity on the rolling body or a small particle between rolling body and raceway triggered the failure by damaging the surface segment in the upper half of the picture. The XRD analysis of this particular shaft suggests strong Hertzian contact stresses and to pronounced high mixed friction and orthogonal shear stress. The lower part of the pit is exhibiting subsurface failure as commonly described.

An interesting observation is done on a raceway of C series. This raceway has failed after 1100 h caused by a very minor, but sharp edged indentation. While the failure exhibits the typical V-shape, the rapid and steep growth of the resulting pitting into depth and an superposition of a more shallow pit at the lower bottom of the V-shape supports the assumption that subsurface fatigue has been present in the vicinity and has been accelerated by indentation (fig. 3.17). This assumption is further nourished by cross sectioning the raceway. A thick continuous DER is visible with many tiny structures indicating the imminent formation of LABs. In optical micrographs of the etched specimen several large sulphide NMIs – as can be exclusively found in the C55V steel grade – distributed along the entire circumference within the DER and in the vicinity of the DER show crack like structures in the martensite on one or two sides of the sulphides. In many cases these structures propagate through the respective NMI (fig. 3.18 (a)). SEM micrographs show that these structures consist of more severely etched, needle like structures similar to DER structures, however, these structures seem to radiate from the NMIs and consist of many small needle like bands. These bands are set in close vicinity of other such structures in identical orientation. Like in the DER

structure they seem to move through the longitudinal direction of martensite needles (fig. 3.18 (b)). The structures within the NMIs, however, are identified as cracks.

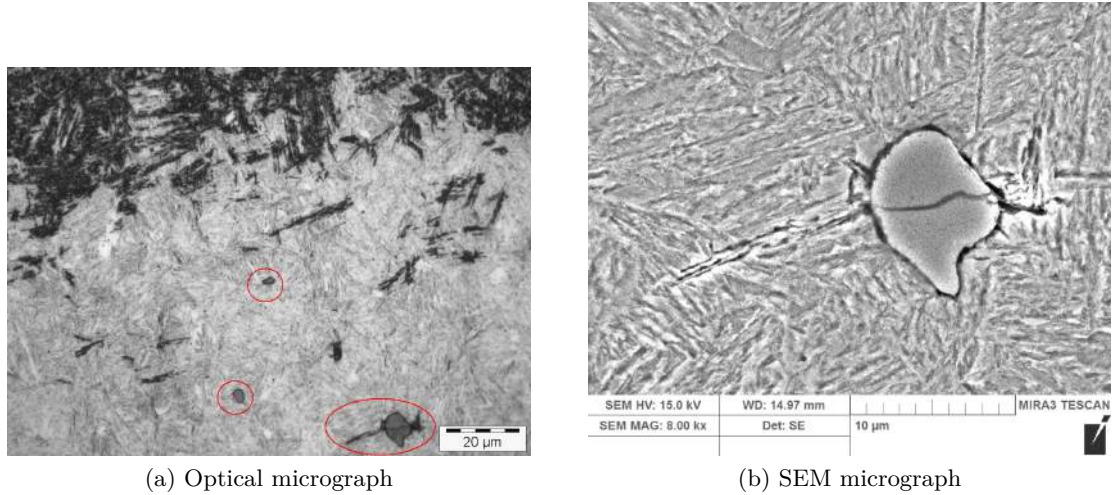


fig. 3.18.: Optical micrograph of three MnS inclusions with crack like structures and SEM micrograph of the lower inclusion.

## 3.7. Discussion

### 3.7.1. General Discussion

On a first glance the Weibull charts of the test specimen fit within their respective confidence interval onto the tested service time of NU 206 bearings. However, all distributions, except for series B, exhibit higher  $L_{10}$  than the reference bearings (which is characterised by  $\beta = 1.1$  and  $T_{max} = 1478$  h). The failure mode of the reference bearings is also quite different: No indentation triggered failures are recorded as cause of failure. The majority of failures occurred on ORs, while in the case of the shafts almost all failures are found on IRs. It has been verified that shaft bending and IR profiles are not responsible for increased OR failures.

The failure of bearings due indentations is a severe problem and known for more than thirty years (q.v. [Lor84]). The estimated minimum film thickness  $h_0$  is estimated to be between 4.6 and 11  $\mu\text{m}$  ( $h_{min} = [3.45, 8.25]\mu\text{m}$ ). Due to the employed lubricant filters the probability of larger particles is low and thus surprising to find that critical indentations have a size of approximately 100 to 400  $\mu\text{m}$ .

### 3.7.2. Origin of Indentation Causing Metallic Particles

#### Analysis of Particles Suspended in Lubricant

DIN ISO 281-3 [DIN281-3] suggests that lubricant cleanliness causes premature failures. Thus, it is assumed that the primary presence of particles is in the lubricant. To verify this the oil is analysed for particle content, although the retention value of the used oil filters renders particles of the size in question comparatively unlikely.

Of each test head a sample from of the let-out oil is investigated. As experience shows that most particles are found in the last third of the drained oil, the latter amount is stored and a sample taken out of these portions. The total amount of collected oil per test head is around 5 l.

Particle analysis is conducted automatically with a specialised SEM. For this purpose the respective sample is filtered. The maximum filter area which can be scanned is 1256 mm<sup>2</sup>, however, the scanning of a filter is also cropped by a time limit of 2 h and max. particle detection limit. The scanned area and volume of each oil sample is given in tab. 3.4. The used volume of oil is large enough to determine the particle distribution of the total oil volume. Larger particles suspended in oil are singular cases.

It should be noted that particles are rarely spherical objects, but mostly oblong pieces. In general metallic pieces are micro-scaled chips from machining processes. An analysis of the particles in this particular case could not be conducted due to an accident.

Head no.	scanned area [mm <sup>2</sup> ] (5-15µm)	scanned area [mm <sup>2</sup> ] (≥ 15-15 µm)	volume oil [cm <sup>3</sup> ]
1	159.74	455.11	14.42
2	116.33	455.11	22.40
3	97.08	455.11	17.83
4	145.00	455.11	13.02
5	163.84	455.11	14.91
6	163.84	455.11	12.60

tab. 3.4.: Scanned filter area and sample volume of the oil.

Fig. 3.19 depicts the distribution of metallic particles suspended in the oil. The distribution pattern resembles a Pareto distribution with roughly 80 % of all particles being found within particle range from 5 to 10 µm longest dimension. Particle ranges of the size larger than 75 µm are virtually non-existing, as they have not been found. On basis of this analysis it is rather unlikely that particles of the critical size may find themselves on almost each failed raceway. The assumption of ISO 281 does not fit in the present case. Further details of the oil analysis can be found in appendix B.

#### Investigation of Component Cleanliness

The previous section revealed that in the present case particles of critical size are unlikely in the oil. Thus an investigation of component surface cleanliness is conducted

### CHAPTER 3. DYNAMIC TESTING UNDER TIME-INVARIANT LOADING

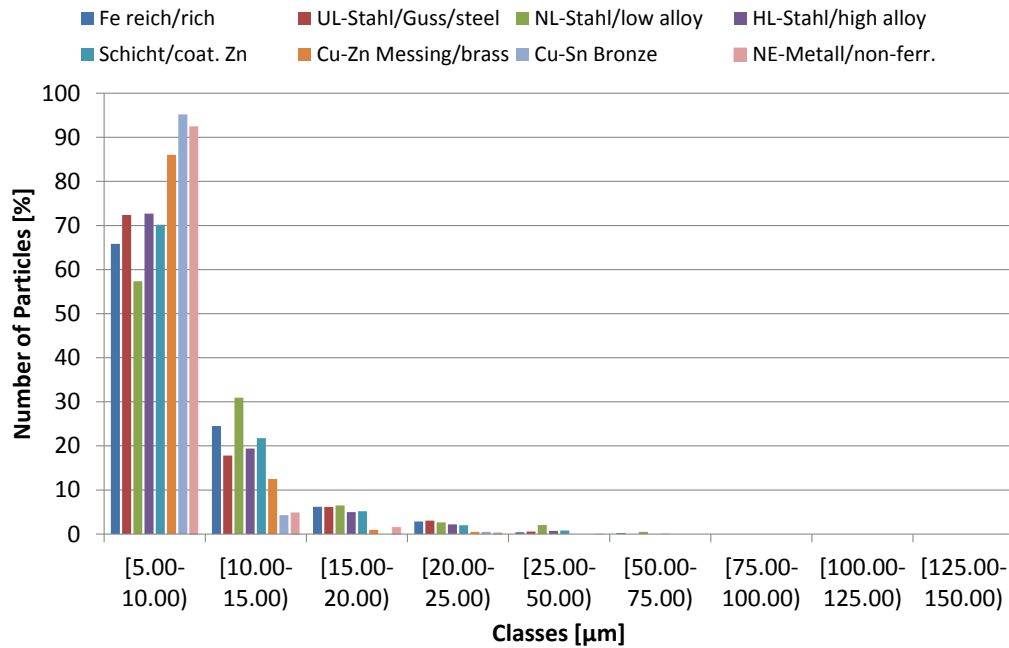


fig. 3.19.: The average distribution of metallic particles suspended in the samples. Ranges larger than 50-75 µm are virtually non-existent. The distribution is representative for the entire volume. The cumulated amount for a metal group is 100 %.

by carefully washing off the bearings and collecting the particles on filters. Analysis is conducted by the same system and procedure as for the oil cleanliness (Appendix C), however, the entire filter area could be scanned in all cases. Scanning is conducted for particles  $\geq 25 \mu\text{m}$ . The found particles are almost exclusively metallic particles. Already the visual impression of the filters clearly show that the ready-made bearings are more strongly contaminated (fig. C.1). To the authors knowledge unpublished results of German automotive OEMs yielded that most particles are clinging to components and are not residuals of oils. During operation these particles are washed to critical surfaces. Metallic particles are rarely found in the oil itself if careful applied. A very critical origin of particles are metal drums or barrels when used as vessels for lubricants, as these vessels cannot be cleaned in a satisfying manner. Thus stirring or pumping from the bottom of such vessels introduces these particles into suspension. Latter scenario is the case after cleaning shafts and bearings.

On average each bearing OR with cage and rollers contain 15 metallic particles of critical size after being treated with an additional cleaning process with white spirit and re-oiling. Prior cleaning the numbers are about 30 metallic particles per bearing OR and cage with rollers (fig. 3.20). It is duly noted that the cleanliness of all analysed bearings is very high compared to normal technical components. A detailed overview can be found in Appendix C. It is highly probable that over rolling of particles within the first couple 1000 revolutions causes indentations, as the particles will be washed away

from the surface and accumulate on the bottom of the corresponding lubricant reservoir. The shape of the particles unfortunately could not be determined. From experience it is known that metallic particles are micro scale chips from production.

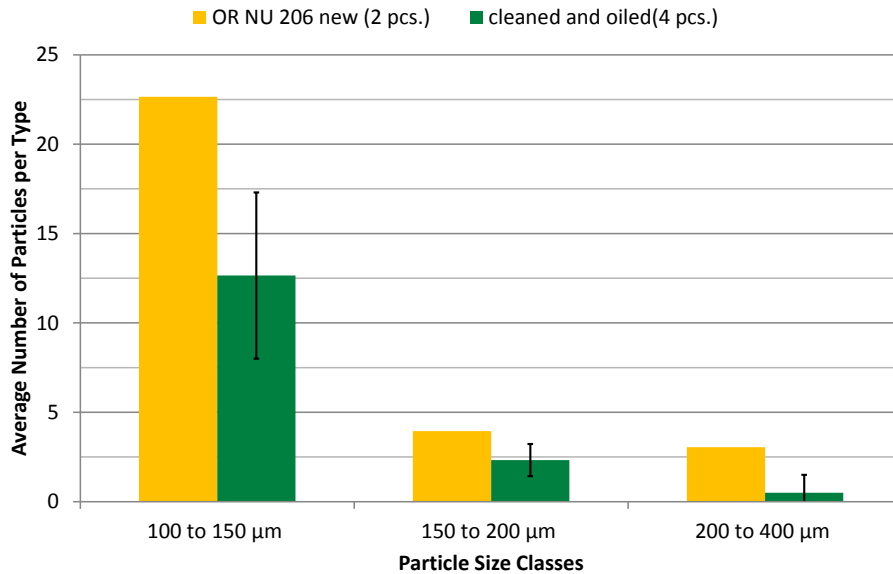


fig. 3.20.: The distribution of metallic particles with critical sizes “clinging” to the surfaces of ORs including cage and rollers. The cleanliness of bearings as delivered is only measured at two ORs, while the cleanliness for cleaned bearings are averaged over four ORs.

### 3.7.3. Influence of Residual Stresses on Crack Growth

The residual stress distribution and FWHM of the as new shafts can be taken from figs 3.21 - 3.24. Due to induction hardening a considerable amount of compressive residual stress of the magnitude 500 to 600 MPa could be achieved. Raceways of series 0, A2, C contain high compressive residual stresses induced by induction hardening. The increase of residual stresses at the surface and the drop of FWHM is normal for fine ground surfaces. The horizontal trend of the magnitude of 1000 - 1200 MPa at the beginning of the hard turned shafts of series A1 is explained by the initial onset of local plastification with strain hardening and accumulation of dislocation. The elastic limit  $R_{p0.2}$  can be roughly estimated by eq.2.13 to 1200 MPa for high strength steels. The value  $Hv$  represents Vicker’s hardness in the equation. The corresponding FWHM shows a slight reduction due orthogonal shear stress induced changes of the microstructure. The onset of local plastic straining of the A1 material causes this series to have higher sensitivity to indentations due local damaging of surface layers during or after turning. This leads to more rapid growth of surface failures. The higher compressive residual stress, however, represents a concurrent crack arrest for mode I cracks, which reduces crack propagation rates and formation. This results in the comparatively shallow scale

### CHAPTER 3. DYNAMIC TESTING UNDER TIME-INVARIANT LOADING

---

parameter of series A1, as two different failure mechanisms and failure regimes are active. The relevance of mode I cracks are reported by da Mota et al. [MMF08] and Hannes & Alfredsson [HA11, HA12, HA13]. Both report that accumulation of plastic strain leads to cracking at the edge of the indentation. They also found for their own numerical results and in reports of other researchers that LEFM mode cracks propagate under mode I with only a minor contribution of mode II.

Residual stress and FWHM distributions of run raceways show that A1 specimen accumulate further plastic strain during operation at the surface, which results in a slight reduction of compressive stresses due dislocation generation relieving the strain in the lattice and concurrent increase of FWHM due to increased lattice defects. In figs 3.25 - 3.28 residual stresses of run 0, A1, A2, B and C specimen are depicted with 494 h, 879 h, 567 h, 66 h and 925 h service time respectively. In all cases, but for A1, residual stresses and FWHM decrease in the first few dozen microns. The FWHM valley at 100  $\mu\text{m}$  in A2 is caused by DER formation. In A1 residual stresses and FWHM increase in these layers. Measurements of the retained austenite on run and not run raceways at the surface and in 50  $\mu\text{m}$  depth after electrochemical polishing are taken. The amount of residual austenite remains unaltered after rolling contact (ca. 5%) and thus does not contribute to an FWHM increase. Thus it has to be assumed that a dislocation increase due plastification is responsible for the FWHM increase.

The reduced residual stresses on the series 0, A2, and C – especially in axial direction – are direct results of the materials' response to pressures in axial direction imposed by hertzian contact. Albeit lesser residual stresses exist in circumferential direction to begin with, an additional straining occurs in circumferential direction due to non-hertzian shear stresses, which originate from non-ideal separation of rolling bodies and surface. As x-ray diffractometry by nature measures physically existing straining, a differentiation is not possible between circumferential stresses and shear stresses in 'xz' direction. Hence the build-up of compressive residual stresses is constricted in circumferential direction. This is proven by the fact that series B and C which have seen extreme mixed friction exhibit a massive reduction of compressive stress (aka increase of residual stress) in circumferential direction. This should not be mixed up with the results of A1. In the case of A1 a relatively small amount of both stresses are changed, while in all other cases only circumferential stresses are affected. Since shear stresses and hertzian micro-contacts acting on the surfaces leave behind lasting microstructural changes, they can be traces in the FWHM. The low FWHM for the series 0 and C shaft at 25  $\mu\text{m}$  depth compared to unrun ones are indicative of damaged raceway surfaces. The material response of the series B raceway is taken from a shaft with merely 66 h service time. The short service time is a result of massive surface friction on some raceways of the shaft leading to an early spalling and DER formation. Due to the extensive surface damage and the short service time the FWHM is not conclusive as additional material responses, which do not correlate with martensite decay may have acted on this raceway.

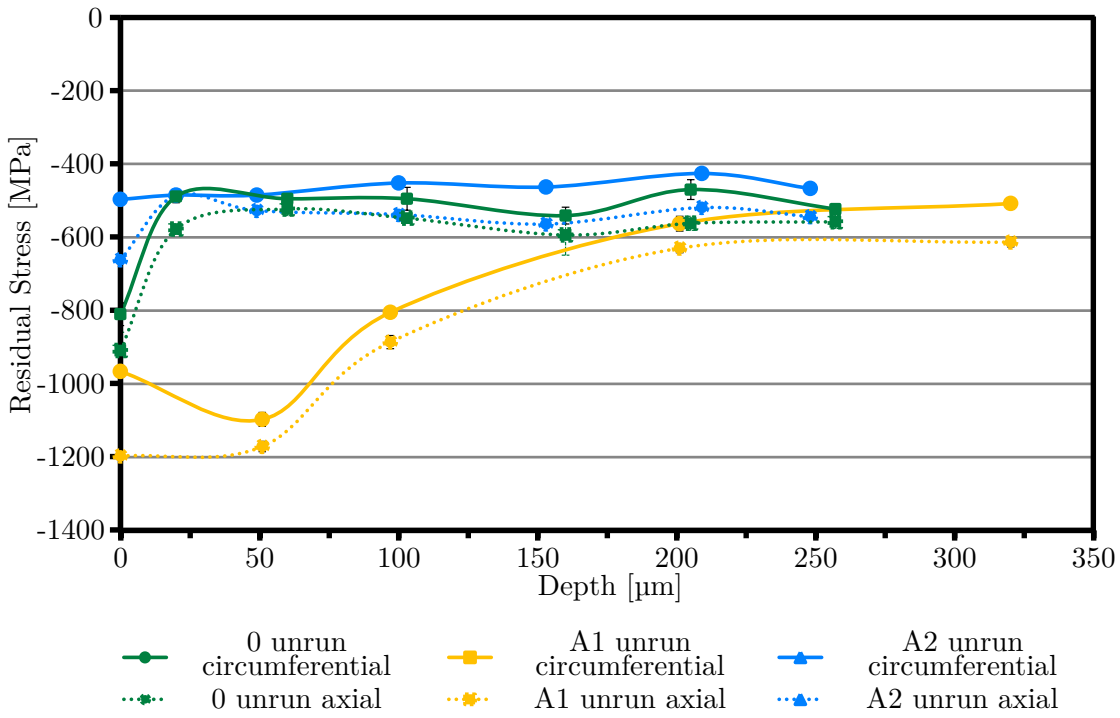


fig. 3.21.: Residual stress profiles of series 0, A1 and A2.

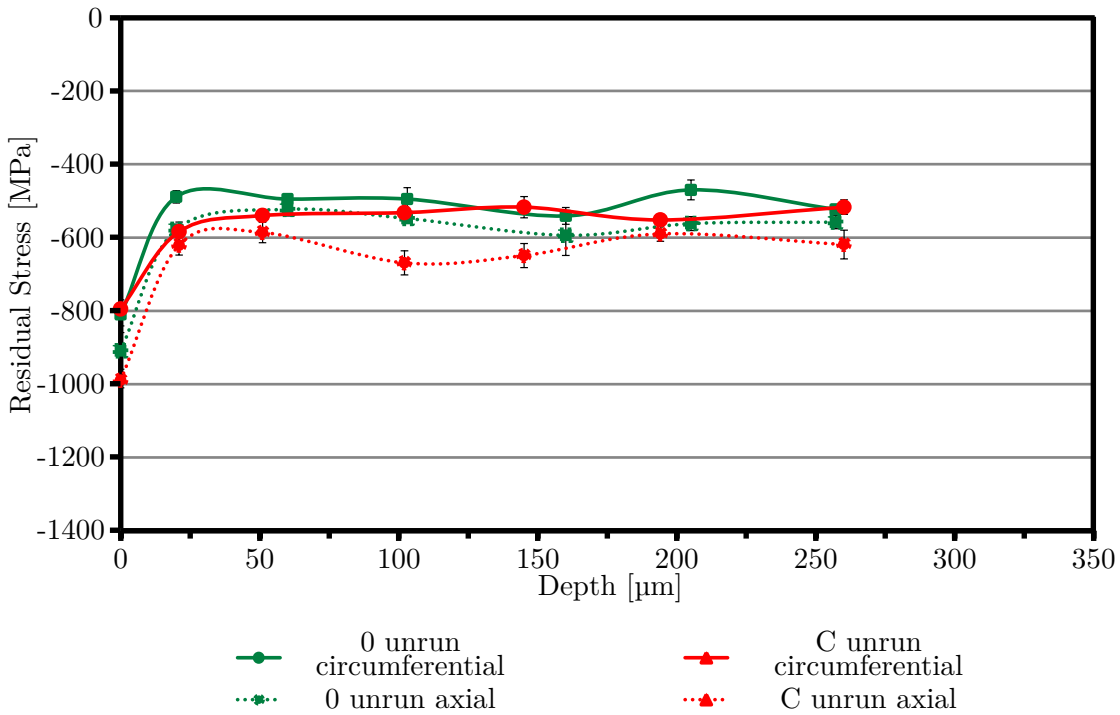


fig. 3.22.: Residual stress profiles of series 0 and C. As series B is identical to 0, but for its cleanliness it should be identical to 0.

CHAPTER 3. DYNAMIC TESTING UNDER TIME-INVARIANT LOADING

---

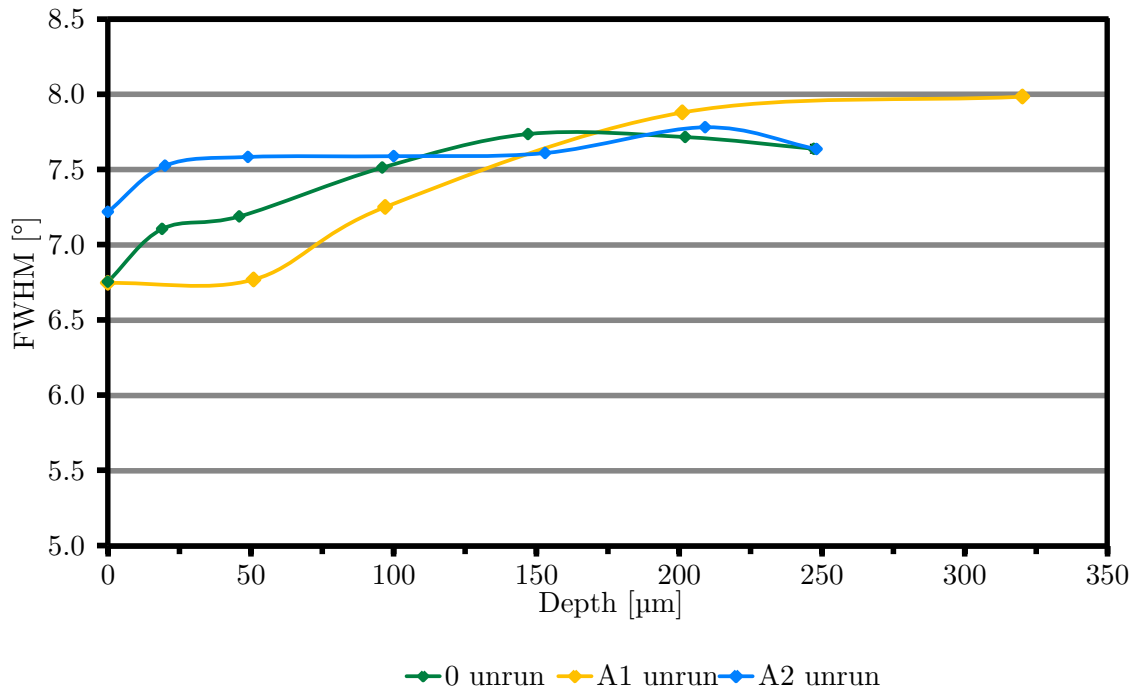


fig. 3.23.: FWHM profiles of series 0, A1 and A2.

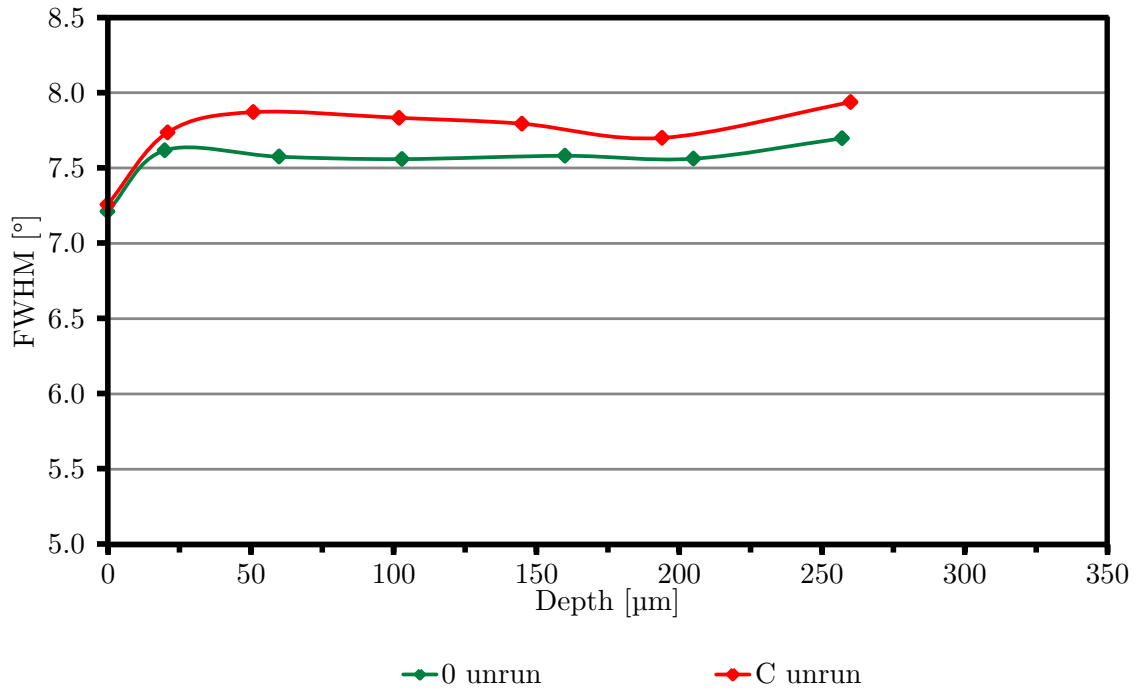


fig. 3.24.: FWHM profiles of series 0 and C. As series B is identical to 0, but for its cleanliness it should be identical to 0.

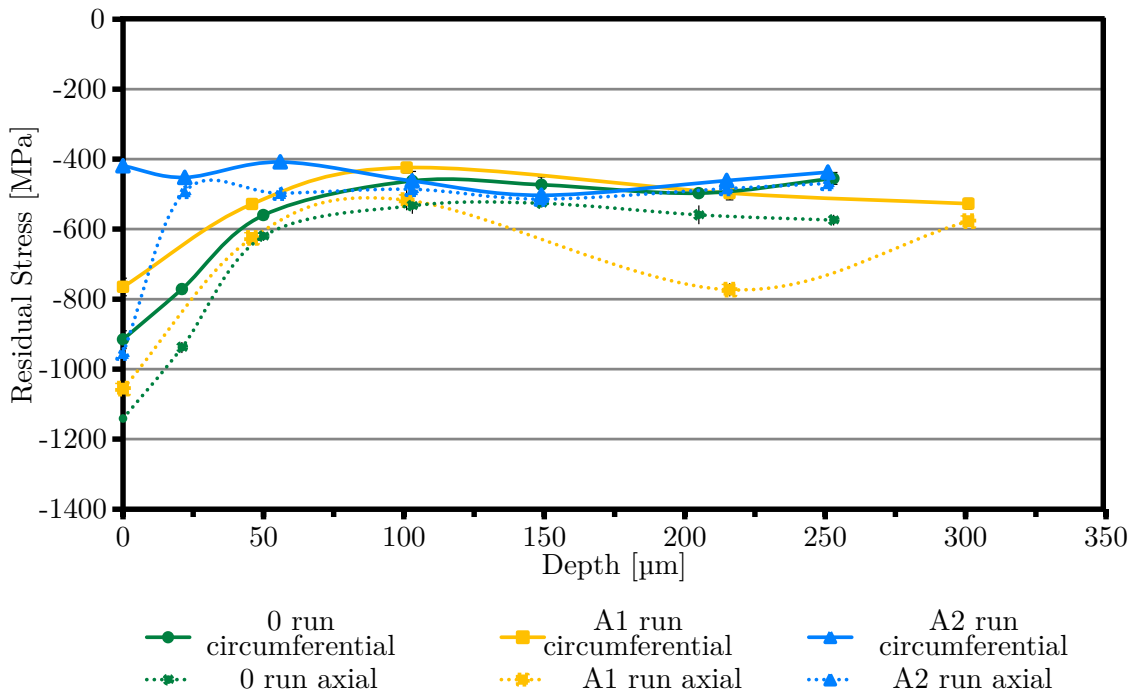


fig. 3.25.: Residual stress profiles of series 0, A1 and A2.

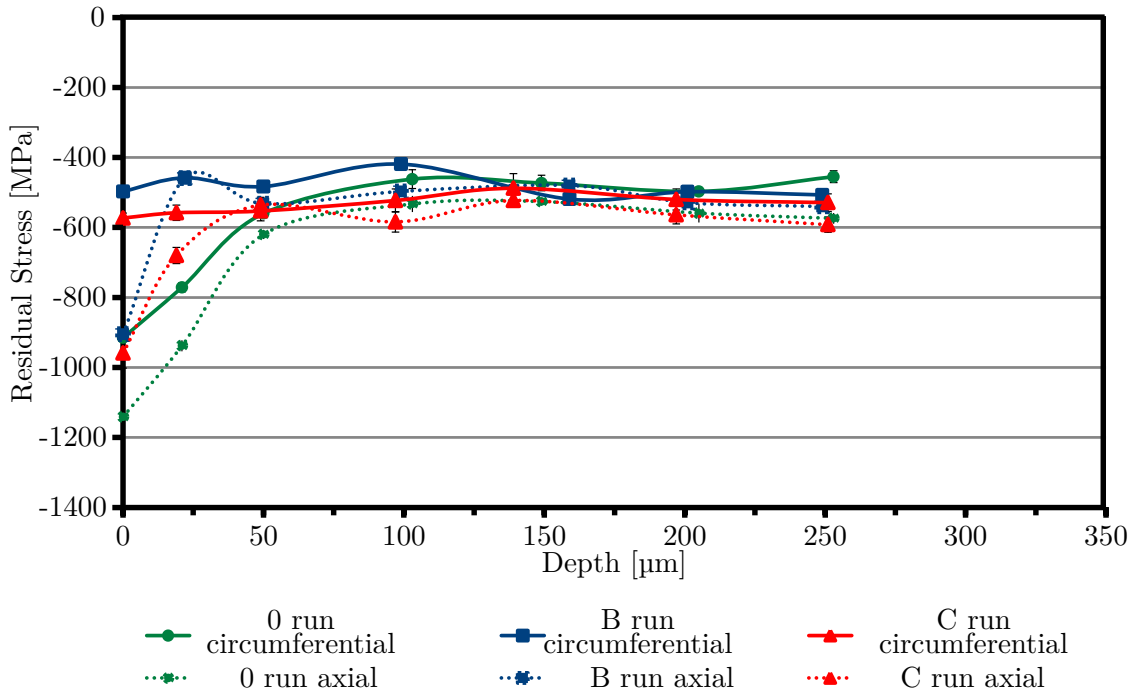


fig. 3.26.: Residual stress profiles of series 0 and C. As series B is identical to 0, but for its cleanliness it should be identical to 0.

CHAPTER 3. DYNAMIC TESTING UNDER TIME-INVARIANT LOADING

---

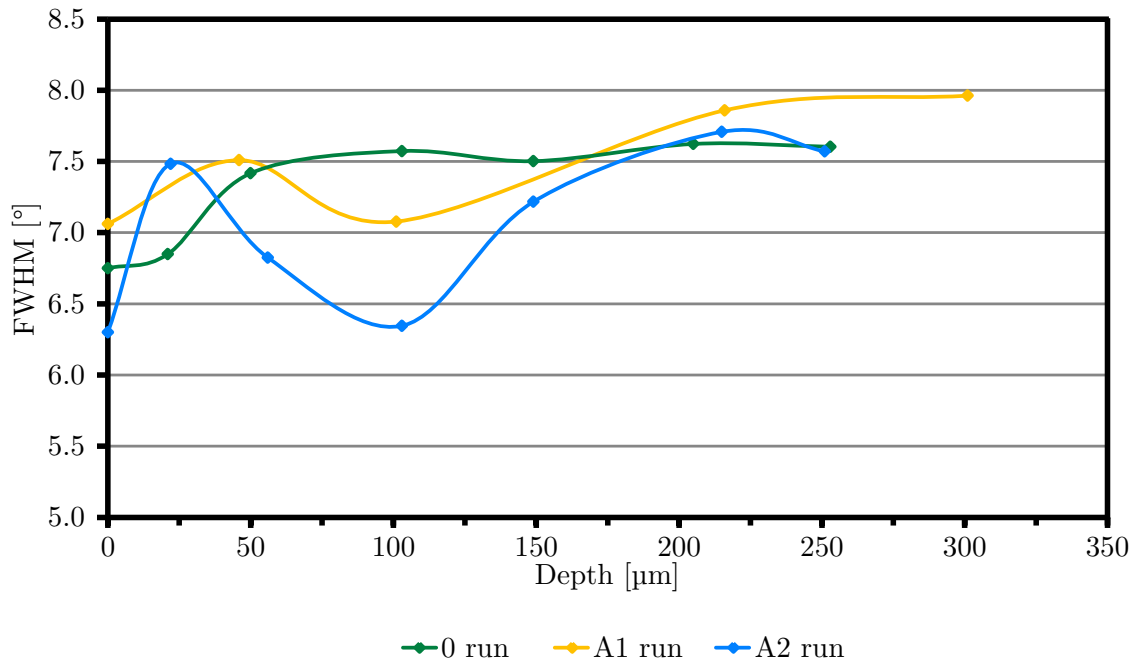


fig. 3.27.: FWHM profiles of series 0, A1 and A2.

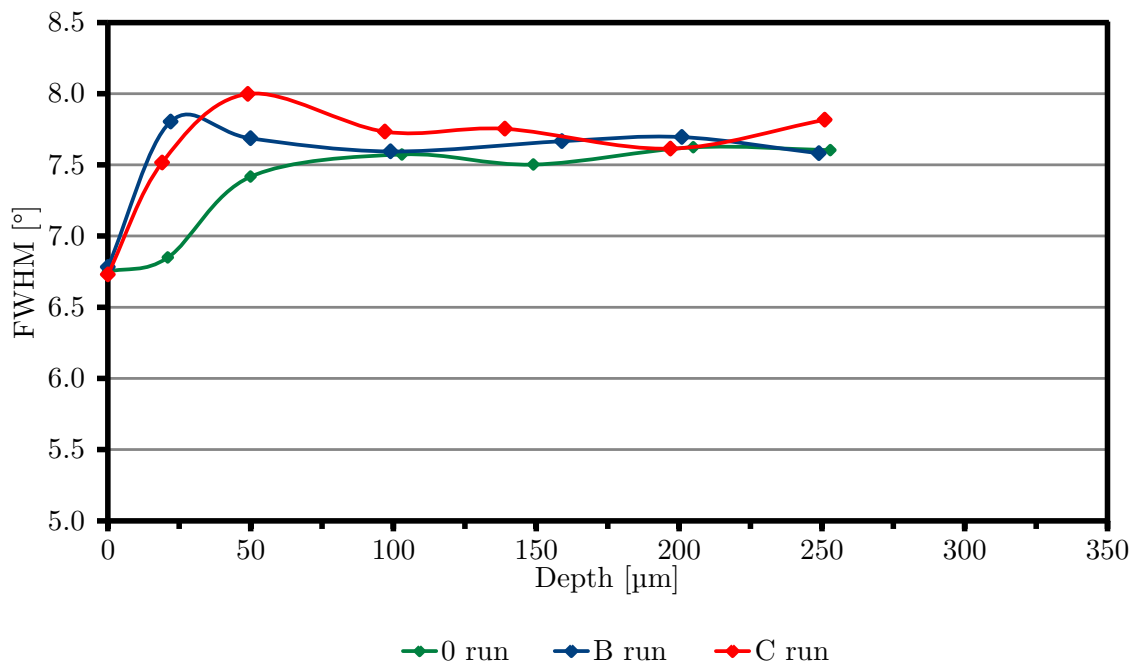


fig. 3.28.: FWHM profiles of series 0 and C.

### 3.8. Summary

In this chapter experiments with constant load were conducted and evaluated in order to determine the dynamic capacity of C56 E2 / C55V and compare them with 100Cr6 catalogue bearings. Surprisingly, most specimen failed due indentation of soft metallic, which fact prevents the experimental determination of the dynamic capacity (Dynamic capacity is defined for subsurface failure mode). particles rendering a determination of a tested dynamic capacity impossible. The critical particles do not originate in the lubricant as suggested in the German extension of the ISO 281 (DIN ISO 281-3), but originate from manufacturing, cleaning and mounting. Thus, a strong indication is given that indentation occurs in most cases within the first 1000 rotations of the shafts. These findings are still valuable, as they prove that under technically clean workshop conditions service life is limited by particles and not by non-metallic inclusions.

An interesting aspect to indentation resilience is the influence of acting compressive residual stresses. Shafts with compressive stresses close to yield strength have a volatility in regard of crack formation and growth, which must be caused by the local stress state of the material. The onset of local plastification increases notch sensitivity and crack propagation, while compressive stresses inhibit crack propagation. As this is depending on the local damage accumulation a more shallow slope parameter is measured for failure probability.

In short:

- technically clean condition: primary failure due indentation
- crack propagation on NMIs only under strong orthogonal shear stress
- indentation occurs at an early stage
- origin of particles: clinging to surface not suspended in oil
- high compressive stresses leading to local plastification are disadvantageous

Arbitrary magnitudes of DER formation beneath the raceways indicate unequal distributions of loads and shear stresses, which further reduces the accuracy of determining  $L_{10}$  directly by experimental means. As the material response to exposure of cyclic stresses, however, is independent of actual failures it provides a possibility to measure  $L_{10}$  by alternative means. This is discussed in the next chapter.

## 4. Service Life Determination for Time-invariant Loading

### 4.1. Motivation

The general procedure to determine the service life of bearings is to create Weibull curves by means of rig testing. Such testing, however, is a demanding process and often very far away from real-life situations of such bearings. While in a laboratory lubrication conditions, load, temperature and many other aspects can be controlled and maintained, this does not hold true for real applications. Although proper calculation and simulation reduce risks of errors, it is still mandatory for complex components and entire units to undergo endurance testing. The number of such units tested is usually very limited due to many constraints. Often testing is conducted with the intention to verify no failure occurs. As the service life of bearings may vary in a broad range, this procedure not only contains a certain amount of danger, but also it is very hard to determine a quantitative failure probability or even to determine the probability for a certain type of failure. Often the last aspect is taken care of by using given dynamic capacities with safety factors as high as 4 or 5, which – no doubt – is sufficient for most applications, but insufficient when every bit of performance is needed. Bearings under such demands are also prone of being operated far away from ideal lubrication conditions.

The analysis of the microstructure discloses an opportunity to determine the probability of failure and an analysis of the really occurring stresses. Microstructural changes cannot account for every failure, but due to the fine microstructure of bearings it is possible to generalise material response. This aspect is used to determine the service life of the bearing raceways of chapter 3.

### 4.2. Micrographic Analysis of Bearing Life

LAB formation occurs shortly after passing  $L_{10}$  for subsurface failure, however, no further LAB formation occurred other than given in chapter 3.6.2. Thus it is concluded that all observed raceway failures occurred within a 10 % probability of subsurface failure. So service life of the raceways *is* limited by surface initiated failures, obviously due to particle indentation.. Moreover it can be concluded that the given material cleanliness of all experiments do not limit the service life of bearings made of hypo eutectoid bearing steels under present component cleanliness conditions. The ISO 281 service life rating only considers lubricant cleanliness as factor for reduced service time. The investigation of the particle origin in chapter 3.6.2, however, localised residuals from manufacturing / shipping as origin for particles. These processes are not considered in the standard.

### 4.3. DETERMINATION OF SUBSURFACE L10-LIFE WITH MEANS OF MICROSTRUCTURAL DECAY

---

As damage accumulation mechanisms should be identical for 100Cr6, it is safe to assume the performance of C56E2 and C55V is identical to 100Cr6 regarding indentations.

The fact that the influence of NMIs were secondary to particle indentation does not mean that higher cleanliness standards are of no interest. As the current public debate and demand focuses very strongly on so called ‘green’ technologies which also rallies for better energy efficiency, more severe lubrication conditions become more often the case. From standard testing practice of major bearing manufacturers it is well known that in the presence of strong shear stresses NMIs still lead to failure of bearings. In recent years results in very clean environments show that much smaller inclusions lead to failures. Bearings with very little oxide content and small oxide sizes still fail. Very recent results of both major European bearing maker show that currently in terms of crack interaction the generally less severe sulphides have become the weakest link within the material leading to failure. An exemplary source for such observations is [DTed].

The actual subsurface fatigue failure is still triggered at NMI inclusions. In the absence of NMIs no failure will occur. As the cleanliness of bearing steel has continuously increased and will no doubt increase in future, the correlation of microstructural phenomenon to  $L_{10}$  may be somewhat transient. The present estimation is, however, not limited to the cleanliness of current bearing steels with little oxide in size and numbers.

### 4.3. Determination of Subsurface L10-Life with Means of Microstructural Decay

#### 4.3.1. Calibration of FWHM Curves for Service Life Rating

Under the given circumstances no rig tested subsurface failure probability Weibull curves could be established. An alternative method is to estimate the damaging and potential service life of a bearing by means of FWHM decrease determination as given by the three stage model in chapter 2.3.4. As the decrease of FWHM is semi-logarithmic, stages one and two can be neglected for estimation purposes giving a fair estimation of the service time of an individual bearing within  $L_{10}$ . For such an estimation only an existing calibration curve and knowledge of the *actual*  $L_{10}$  are needed. The *actual*  $L_{10}$  is not necessarily the  $L_{10}$  given in a bearing catalogue. Latter ones contain large safety factors to account for differences in material quality and different material treatments (e.g. carbunitrating, austenite stabilisation, etc.), which become necessary in order to adapt bearings to specific applications. Calibration curves for the used steels have to be recorded at first.

Calibration of all successive curves is conducted on a single diffractometer of  $2\theta$  type from co. Bruker at SKF Schweinfurt. The  $\sin^2\psi$  method is applied for measurement of residual stresses, the by-product of which are FWHM values. The diffraction angle  $2\theta \approx 156^\circ$  of the body centred cubic {211} lattice plane is measured. Using Cr K $\alpha$  radiation is used. Modifications to the standard measuring procedure are done in order to minimise the recording time. These modifications take advantage of a large diffraction line broadening for  $\alpha$ -Fe {211} under Cr K $\alpha$  radiation.

## CHAPTER 4. SERVICE LIFE DETERMINATION FOR TIME-INVARIANT LOADING

---

Calibration for 0.5 % regular carbon steel is conducted on all four LAB inflicted raceways of that material. From a metallurgical point of view the difference between 160 °C and 170 °C tempering temperature is negligible. An overview of running time and tempering procedure of the investigated raceways is given in tab. 4.1. The corresponding FWHM profile curves with  $z_0$  and micrographs of the cross sections are given in figs 4.1 - 4.3.

Raceway Label	Series	Revolutions	figures
a)	0	$1.36 \cdot 10^8$	fig. 4.1
b)	0	$3.77 \cdot 10^8$	fig. 4.2
c)	A2	$2.15 \cdot 10^8$	fig. 4.3
d)	A2	$4.17 \cdot 10^8$	fig. 4.4

tab. 4.1.: Details of the the shafts made from 0.5 % carbon steel. From a metallurgical point of view the tempering temperatures of 160 °C and 170 °C are negligible.

In order to work with a  $2\theta$  set-up the raceways were cut out of the shaft and then segmented. The experience of SKF with 100Cr6 bearings show that radial cutting of through hardened bearings does not change the residual stress profile. It mainly affects the absolute values of the profile. Cutting and segmenting the raceways of the shafts, however, resulted in a total change of the residual stress profile. A attempt is made to reconstruct the profile of the uncut shafts. For this a shaft with properties of an unrun series 0 is measured firstly after cutting in axial direction and thereafter as segment. The change of the profile occurs after dissecting the raceway, while the offset of the stress profile is reduced after segmentation. The segmented stress profile resembles the profile as measured for the LAB inflicted raceways, while the disk shaped geometry is only offset in terms of absolute value. A reconstruction of the real stresses failed, however. It seems that the exact location of axial cutting matters significantly. As the FWHM is not strongly affected by a change in the stress state, it remains meaningful. Difference between segmented and entire raceway are within the standard deviation of measurement error (2%) and proof of the little effect of elastic lattice strain on the FWHM. The difference in strain is equivalent of several hundred megapascal difference.

Raceway a) is extracted from series 0 with  $1.36 \cdot 10^8$  revolutions of service. In cross section strong, continuous DER formation is visible between 45 and 165  $\mu\text{m}$  with outlying patches reaching up to ca. 225  $\mu\text{m}$ . The surface layers also exhibit DER formation. The intensity of the transformed martensite needles, however, is not as pronounced. Fine, but long LABs are visible at strong magnifications in the lower two third part of the strong DER with an angle of about 30°. The normalised FWHM ( $b/B$ ) profile starts with mere peak value of  $b/B=0.9$  and then drops to 0.6. The low near surface values is in accordance with the lubrication condition  $\kappa = 2$ , which suggests an occasional contact of asperities.  $z_0$  is estimated between 115-120  $\mu\text{m}$  correlating with maximum hertzian contact stresses of 3.6-3.7 GPa. The broad valley of the *continuous* profile is a good example how the local stress condition of the microstructure activates stress induced

### 4.3. DETERMINATION OF SUBSURFACE L10-LIFE WITH MEANS OF MICROSTRUCTURAL DECAY

---

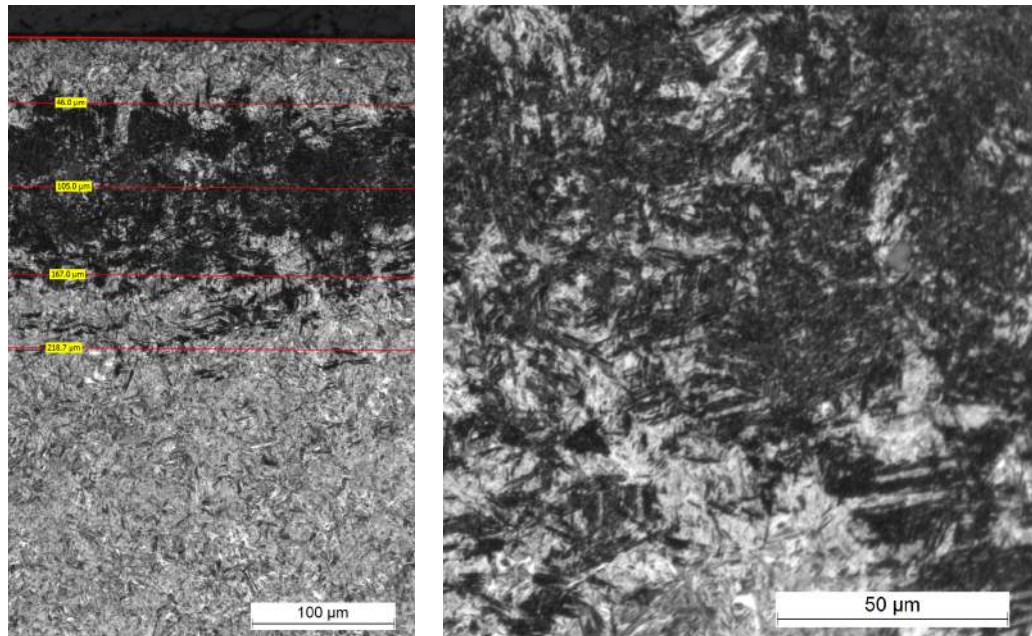
diffusion processes along the entire profile. From a continuum mechanics perspective with a homogeneous material only the depth in which  $\tau_{xz}$  exceeds the yield limit would accumulate decay, which clearly is not the case. This can be seen especially in greater depth. The comparatively weak tail of  $\tau_{xz}$  is still capable to reduce  $b/B$ . As predicted by the theory, a broadening of the decayed layers around  $z_0$  occurs due to loss of elastic load carrying capacity in layers near  $z_0$ . This can be discerned by a broadening of the valley, which in turn must create a knee in the profile due a change of slope. This is the case for raceway a) in a depth around 200  $\mu\text{m}$ . In 400  $\mu\text{m}$  depth the FWHM reaches an absolute value of  $7^\circ$  on the used diffractometer. This value fits to the unaltered material in martensitic state.

Raceway b) is also from series 0 shaft and has experienced  $3.77 \cdot 10^8$  revolutions of service. The surface layers seem to contain dark etching areas under visual inspection, however, an optical assessment is hard as the subsurface DER stretches from approximately 20  $\mu\text{m}$  to 230  $\mu\text{m}$  in continuity and then patch wise till 300  $\mu\text{m}$ . Very large LAB formation is visible at mere 100x magnification. Despite their association to White Etching Areas LABs appear dark at lower magnifications, as their carbon rich coronae mask the actual bands. The FWHM profile features near to the surface a maximum  $b/B = 0.825$ , which is below the DER limit of 100Cr6 and thus a sign for DER formation close to the surface. ( $L_{10}$  for surface damage is reached prior DER formation can occur.) At 400  $\mu\text{m}$  a FWHM value of slightly above  $7^\circ$  is reached fitting to unaltered martensitic structure for this steel. The steep  $b/B$  drop between 10 and 20  $\mu\text{m}$  and strong knee are sign for line broadening by high stress hertzian contact. The  $b/B$  value at 60  $\mu\text{m}$  could be an singularity or the result of superposition of strong hertzian contact stresses and surface shear stress. Latter stress seems unrealistic, as any features except for wear marks are missing on the surface. Without the residual stress profile of this raceway the real loads cannot be concluded.

Raceway c) and d) belong to series A2 and operated for  $2.15 \cdot 10^8$  and  $4.17 \cdot 10^8$  revolutions respectively. Raceway c) exhibits occasional near surface martensite decay of weak strength and a pointed  $z_0$ . A line broadening is not visible which is understandable, since neither service time nor hertzian contact stresses are too strong.  $z_0$  is estimated to 3.1 GPa. The lower  $b/B$  value compared to raceway a) is the outcome of a longer service time. The LAB strength is similar to raceway a). Raceway d) experienced revolutions a replacement of its roller set due to an OR failure after  $2.15 \cdot 10^8$ . This has led to a change on the load situation. In this special case of changing load the effective maximum hertzian contact stress is estimated. This scenario of a bearing with a history of many different load situations is rather common for field bearings, e.g. gearbox bearings, c.f. [GNB07]. In cross section a rather incoherent DER layer is visible with very weak LAB formation. The lowest  $b/B$  value is quite large with a value of 0.64.

All four FWHM are superimposed in fig. 4.5. Additionally the extrapolated start / end value for optically visible DER and  $L_{10}$  are marked in the latter figure. The black dashed lines at  $b/B = 0.87$  and  $b/B = 0.65$  are values as determined for the C56 E2 steel. Thereby the  $L_{10}$  starting point is estimated on FWHM basis of the shortest LABs visible ( $b/B = 0.64$ ). The choice for such little difference in FWHM is explained by the

CHAPTER 4. SERVICE LIFE DETERMINATION FOR  
TIME-INVARIANT LOADING



(a) Overview

(b) Detail

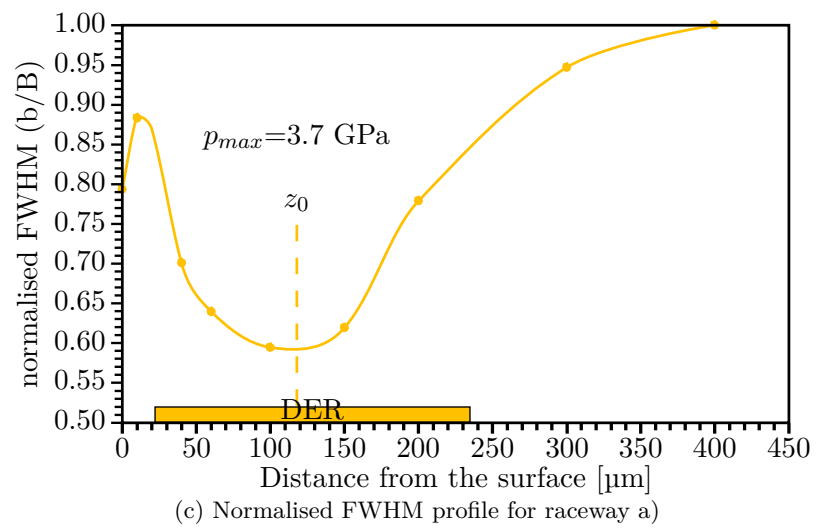
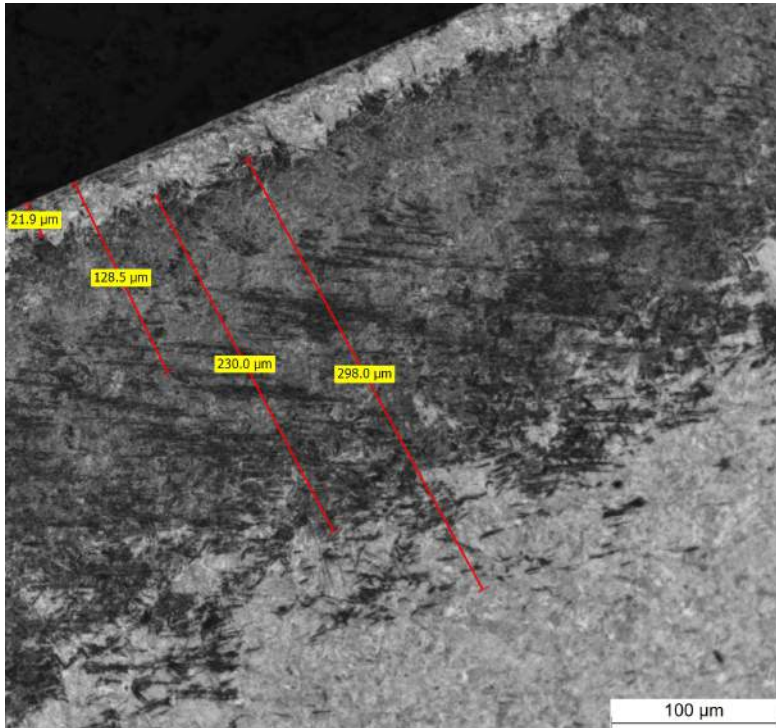
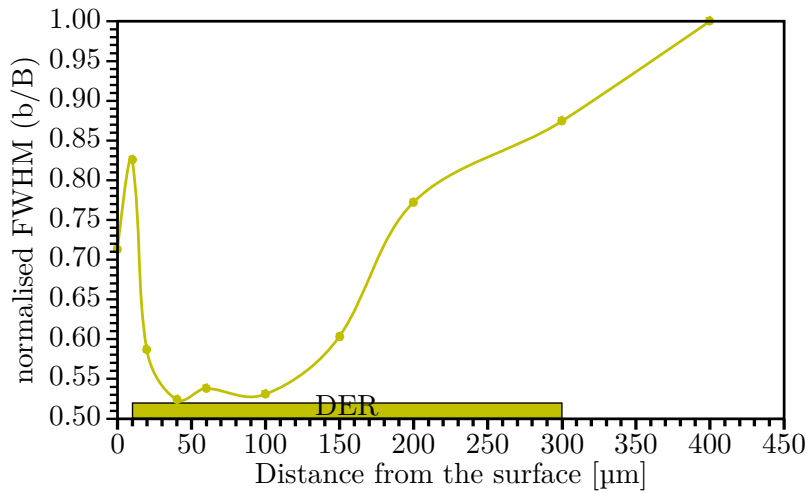


fig. 4.1.: Raceway a)

### 4.3. DETERMINATION OF SUBSURFACE L10-LIFE WITH MEANS OF MICROSTRUCTURAL DECAY



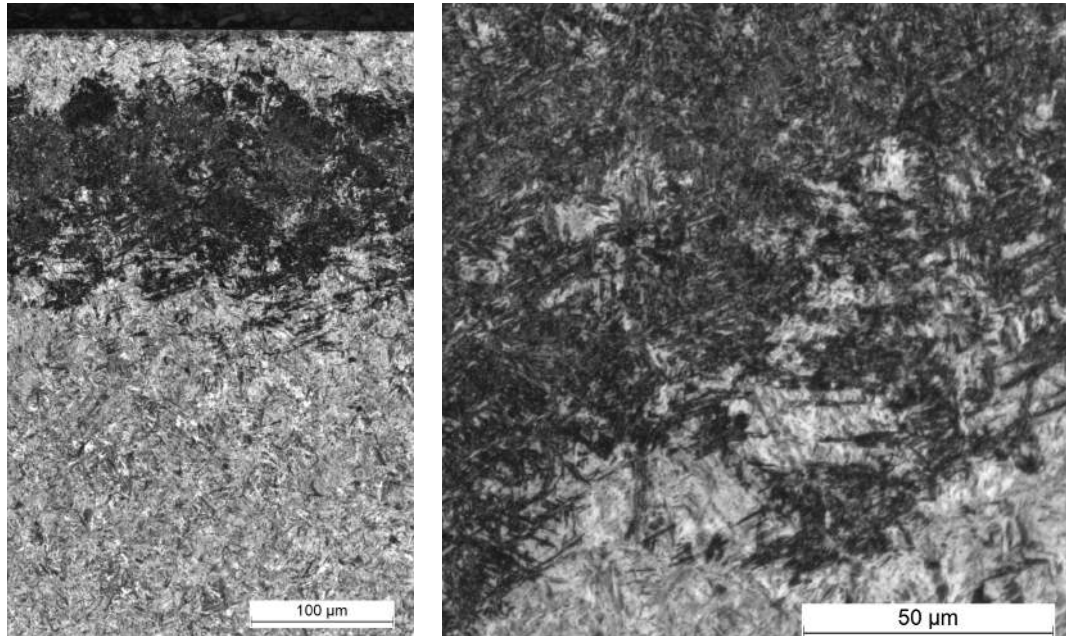
(a) Micrograph



(b) Normalised FWHM profile. The singularity in the range 60 - 100μm render it impossible to estimate the Hertzian contact stresses.

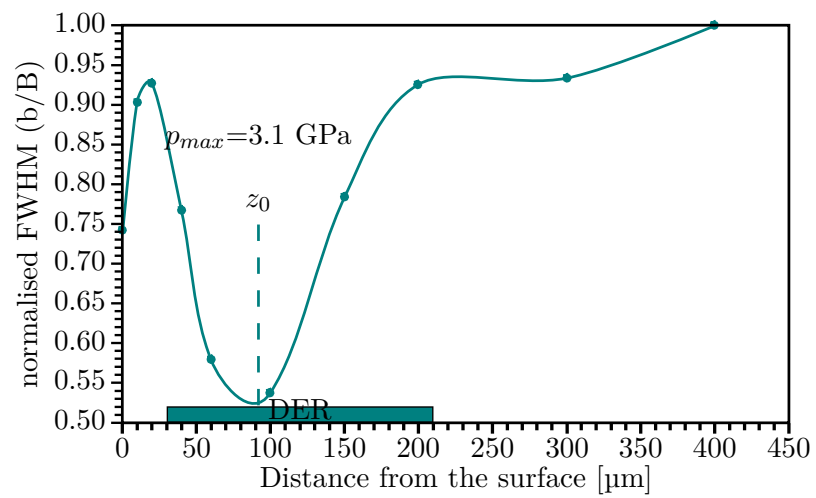
fig. 4.2.: Raceway b)

## CHAPTER 4. SERVICE LIFE DETERMINATION FOR TIME-INVARIANT LOADING



(a) Overview

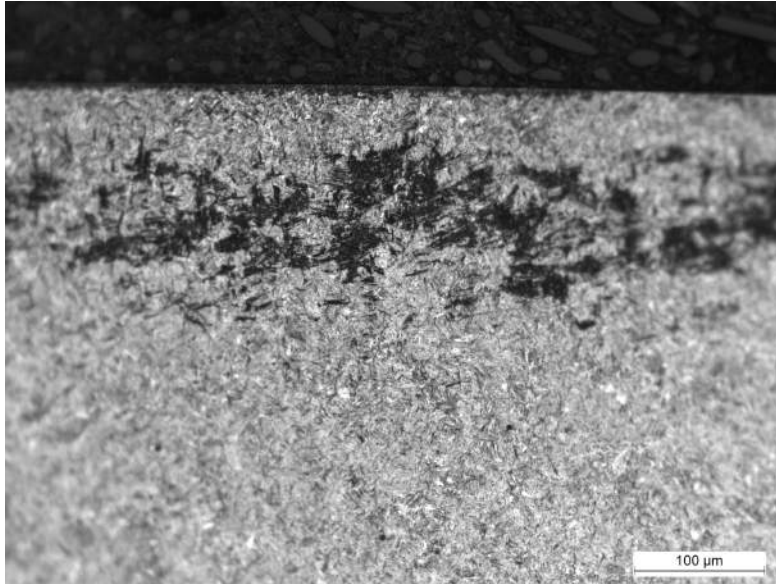
(b) Detail



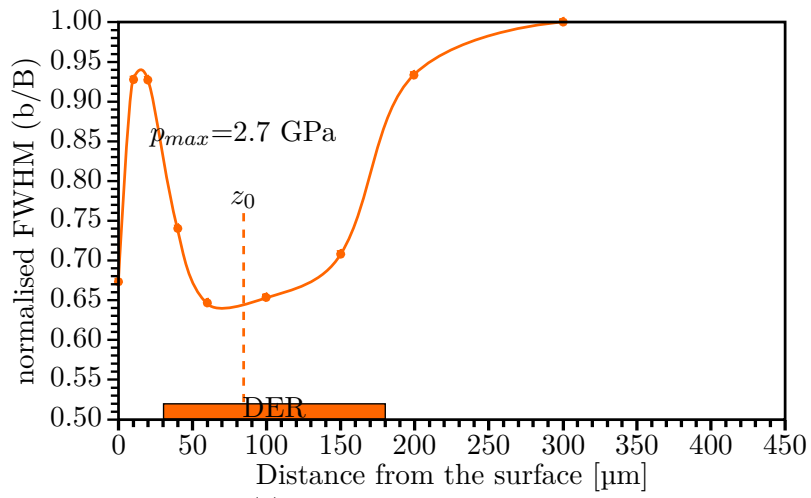
(c) Normalised FWHM profile

fig. 4.3.: Raceway c)

### 4.3. DETERMINATION OF SUBSURFACE L10-LIFE WITH MEANS OF MICROSTRUCTURAL DECAY



(a) Micrograph



(b) Normalised FWHM profile

fig. 4.4.: Raceway d)

## CHAPTER 4. SERVICE LIFE DETERMINATION FOR TIME-INVARIANT LOADING

fact that this steel grade has no carbides to obstruct LAB growth. Moreover the size of the LABs is very short. The red dashed line represent the corresponding values for 100Cr6 bearings through hardened and tempered in an oven process (as opposed to the used induction hardening in this case) as given in [GNB07]. The tolerance bars of the carbon steel indicate the  $2\sigma$  confidence interval for material and measurement scatter.

The closeness of the tolerance bars to the 100Cr6 values suggest that the values obtained for C56E2 may be identical to 100Cr6 values, which are based on a solid rig tested basis of several decades of testing and incorporates the extensive data generated by Voskamp [Vos97]. The similarity of the  $b/B$  values are an indication that the carbon content within the unaltered martensite grains are very similar and that the remaining carbon content of the 100Cr6 is bound in the abundant numbers of chrome carbides.

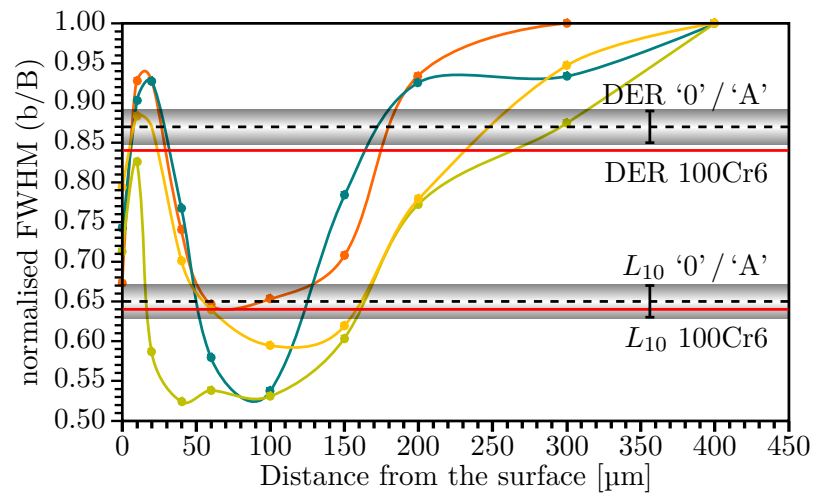


fig. 4.5.: DER and  $L_{10}$  starting level

Figs 4.6 (a)-(c) show micrographs for three raceways made of C55V. All three raceways are from the same shaft and labelled '1', '2' and '4'. Raceway '3' failed after  $2.67 \cdot 10^8$  revolutions. Raceway 1 is the only C55V raceway investigated inflicted by LABs. Raceway '3' also contains LABs, but could not be measured by XRD. All three raceways exhibit surface damages such as strong wear marks and raceway tinting (micro oxidation through mixed friction). Raceway 1 moreover has pronounced edge polishing on both edges. On one edge even grey staining is visible. Raceway four has the least strongest of all surface damages. These surface damages already point out that an unbiased determination of the Hertzian contact stress will most probably be impossible. In cross section DER are visible. On raceway 1 the entire span of DER layers reach from the surface to a depth of approximately  $255 \mu\text{m}$ . Formation of strong DER patches, which are almost one continuous band, are found on the surface layers and from 26 to  $180 \mu\text{m}$ . In addition to the DER tails reaching to  $255 \mu\text{m}$  another tail like area is visible between surface layers and the main part of DERs. The second raceway contains mostly homogeneous DE-Regions of medium intensity to the depth of  $210 \mu\text{m}$ . Between 25 and  $170 \mu\text{m}$  a large number of martensite needles darken strongly. The last raceway exhibits

### 4.3. DETERMINATION OF SUBSURFACE L10-LIFE WITH MEANS OF MICROSTRUCTURAL DECAY

---

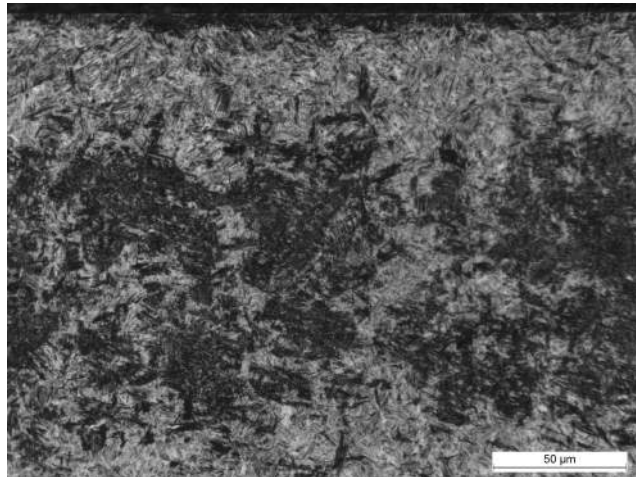
in accordance to its surface appearance only weak dark patches in the subsurface region. Only occasionally a needle is strongly etched. Within the first 10-15  $\mu\text{m}$  beneath the surface strong patches of DER occur. The total depth of the DER is about 200-250  $\mu\text{m}$ .

Determination of the DER start / end value is not trivial. While two DER start / end values per profile existed in the case of the C55V, as only one value per curve is available in this case. Moreover the location of DER end corresponds to positions, where the profile curves are shallow. The estimated DER start / end value is  $b/B = 0.97$  and the LAB value based on a single measurement is estimated to  $b/B = 0.68$ . The grey curves indicate the  $2\sigma$  confidence interval of measurement and material scatter. The red lines in this curve correspond to carbunitrated 100Cr6. Carbunitrated bearings do not possess compound layers nor obvious diffusion layers with precipitated nitrides. According [GN12] nitrides are dissolved in the steel. This is believable, as bearings of all major manufacturers do not contain any precipitates or diffusion layer [JMR14]. This is important as otherwise the effect on the lattice would be different and not comparable to the C55V. Reasons for comparing C55V with carbunitrated 100Cr6 are that spectral analysis of the steel grade revealed that it contains in addition to 0.1 % vanadium also 0.15 % of nitrogen and of course carbon. During cooling vanadium reacts first strongly with nitrogen to vanadium nitride (chem. formula: VN). Remaining vanadium atoms react with carbon to vanadium carbide (VC), which in turn forms with vanadium nitride vanadium carbonitrides [MG05, Per09]. The resulting precipitates are invisible in optical micrographs. The presence of vanadium can be proven with BSE imaging. From a metallurgic point the effect is similar to carbonitrated bearings and increases hardness and tensile strength by precipitation hardening [MG05, Per09]. Albeit the amount of nitrides is almost vanishing in both bearing steels. Thus the hardening mechanism of this steel grade is similar to carbunitrated bearings, in which also precipitation hardening and interstitial nitrogen causes increased hardness underneath the surface. As with 100Cr6 the presence of nitrogen seems to increase the  $b/B$  values for DER and LAB start.

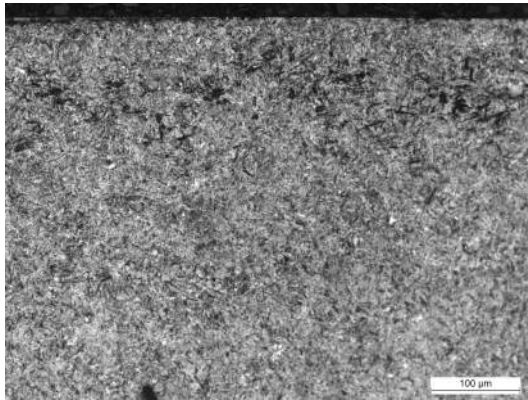
As expected FWHM profiles of all three raceways exhibit strong near-surface damaging. Two of the valleys correspond with 1300 and 1900 MPa Hertzian contact stresses. These values are far too weak to trigger DER formation under purely hertzian conditions. The closeness of these two peaks to the surface in combination with the damage on the surface support the assumption of mixed friction leading to increased surface shear stresses. By definition these shear stresses are orthogonal. The values above unity for raceway 2 are originating from extrapolation between two measuring points. It seems unlikely that the effects of plasticification would have such an effect, considering that the space between the interpolated positions exhibits DER. The most astounding curve, however, is raceway 4. Despite the weak optical presence of DER this curve exhibits a strong  $b/B$  reduction near to the surface. The shape of this curve fits well with examples of surface stressed bearings in literature [GNB07].

The high  $b/B$  value for DER start compared to carbunitrated 100Cr6 is explained by additional presence of vanadium carbide in the matrix reducing carbon content of the lattice, while interstitial nitrogen increases lattice distortion. This assumption is underlined by the fact that the FWHM is slightly lower than for C56 E2. Moreover,  $z_0$  for bearings is in a depth in which (assuming that an existing compound layer has been

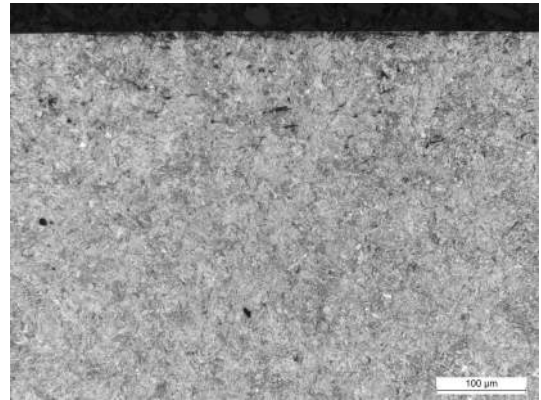
**CHAPTER 4. SERVICE LIFE DETERMINATION FOR TIME-INVARIANT LOADING**



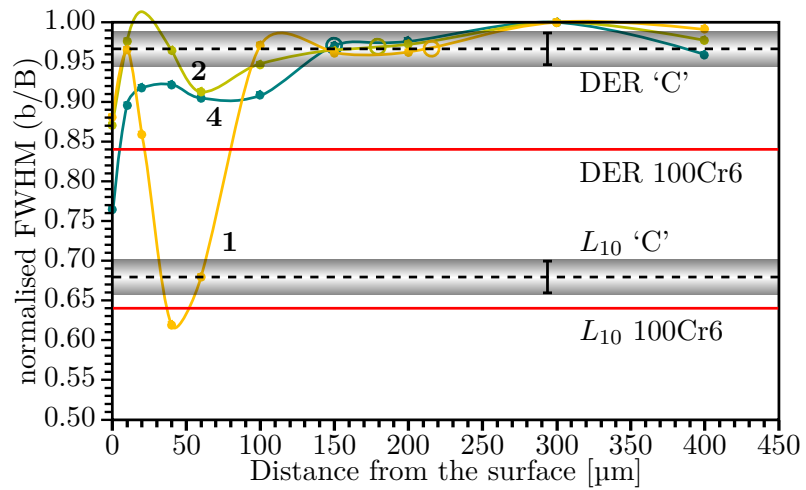
(a) Raceway 1



(b) Raceway 2



(c) Raceway 4



(d) FWHM profiles

fig. 4.6.: Raceways and FWHM profiles of the micro-alloyed steel

### 4.3. DETERMINATION OF SUBSURFACE L10-LIFE WITH MEANS OF MICROSTRUCTURAL DECAY

---

removed) hardly a large amount of nitrides should be found. The singular value for  $L_{10}$  determination is connected with massive uncertainty, however, a good starting point for further investigations. As LAB formation necessarily involves martensite transformation and dissolutions of carbides, it is assumed that the  $b/B$  value must be of similar order of magnitude as for carbunitrated 100Cr6. Thus the value is estimated to  $b/B = 0.7$ .

The reason why DER formation is linked to an increased subsurface fatigue probability needs yet to be clarified. The afore mentioned shaft with 1100 h of service life (chapter 3.6.2) provides a potential explanation. The observation fits to descriptions of dislocation based short cracks moving along slip bands. The appearance of the short cracks with similarity to DER structures would also be explained by this fact, as they are believed to be triggered by dislocations. The “cracks” are emanating from the manganese sulfides in the same orientation as the initial LAB structures. As the “cracks” in fact are just multiple unconnected strokes more strongly etched than the surrounding material and thus very similar to the etching of DER, the assumption is that these cracks consists of micro plastifications triggered by notches, thereby causing the stronger etching by carbon accumulation at dislocations. Thus the mechanism would be very similar to DER formation. Tsunekage et al. [THF10b] calculated for ball bearings that the maximum tensile stress occurs approximately normal to the observed propagation direction. Hertzian principal stress calculations (Appendix D) show that the maximum of principal shear stress  $\tau_1$  at the location of maximum orthogonal shear stress ( $\tau_{xz}$  at  $x = 0.866a$ ) occurs slightly below  $z_0$ . Its inclination varies between 35 - 38° (figs 4.7 and 4.8) to the surface plane and thus is identical in orientation as to the LABs and “cracks”. Note that the absolute maximum shear stress occurs at 45° beneath the rolling body, however, this value does not alternate, while  $\tau_{xz}$  acts with a stress ratio of -1 for each passing rolling body. Also note that the unpinning / movement of dislocations along slip bands occur due to weakening of the martensitic structure caused by DER formation.

In the present case, however, an additional orthogonal shear stress is acting due to surface effects. Calculations with  $\sigma_x$  and  $\sigma_z$  for 1800 MPa Hertzian contact stresses and  $\tau_{xz}$  in a range from 300 - 1110 MPa show that the inclination angle is raised only slightly due additional shear stresses (fig.4.9).

Despite the high stresses no White Etching Cracks (WEC) are observed. In [BGG11] it is assumed that embryonic WEC are identical to the observed short crack. One of the authors of the paper suggested that the high compressive stresses prevent the formation of white etching structures.

#### 4.3.2. Calculation of Dynamic Capacity

In the following a methodology for calculating the Dynamic Capacity  $C$  is given. The numeric outcome for the example must be taken with caution. The accumulation of additional residual stress in the depth of maximum von Mises stress cannot be measured due to the existing stresses. A measured  $b/B$  for  $L_{10}$  would were very helpful, however, only the estimated value is available. Tolerance of carbon content and other alloys in the steel sure will have an impact on  $b/B$ . This could not be considered, since all raceways

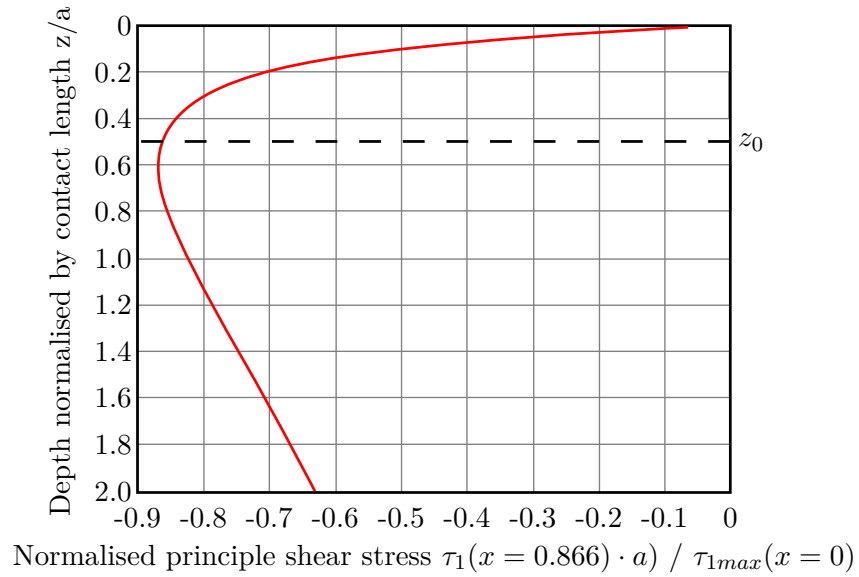


fig. 4.7.: Depth profile of the magnitude of the alternating principal shear stress  $\tau_1$ . The maximum value occurs slightly beneath  $z_0$ .  $a$  is the elastic contact half width.

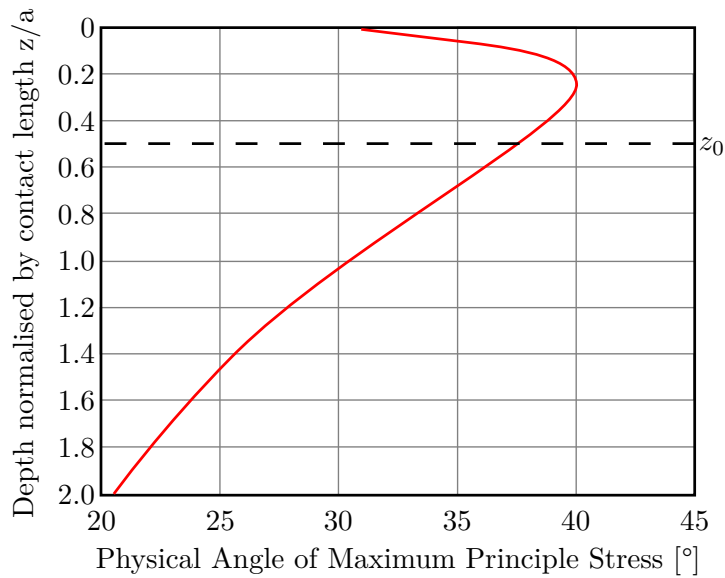


fig. 4.8.: Depth profile of the physical angle of the alternating principal (shear) stress plane.

### 4.3. DETERMINATION OF SUBSURFACE L10-LIFE WITH MEANS OF MICROSTRUCTURAL DECAY

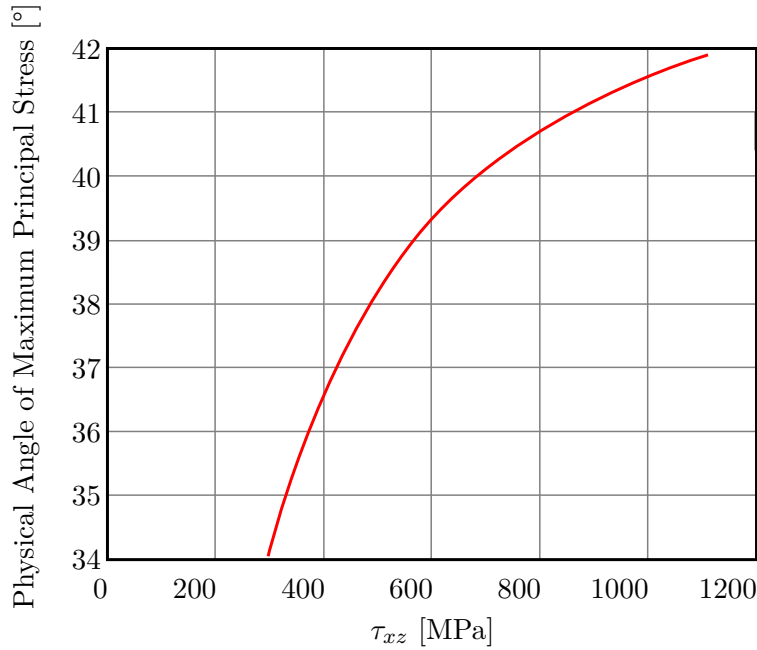


fig. 4.9.: Physical Angle of the maximum stress plane as function of orthogonal shear stress. The corresponding normal stresses are calculated for 1800 MPa hertzian contact stresses.

are made out of the same steel heat.

1. A  $b/B$  profile of bearing corresponding to  $L_{10}$  is needed. In this case raceway d) is chosen for this purpose, as it is closest to the expected  $L_{10}$ .
2. The estimated maximum Hertzian contact stresses needs to be determined. In this case it is 2.7 GPa.
3. This information is used to calculate the corresponding dynamic load  $P$ . For raceway d) the program “Lager2” is used ( $P = 24.3 \text{ kN}$ ).
4.  $C$  can be directly solved by rearranging the SKF-Model (eq. (2.5) and (2.6)).

$$C = P \left( \frac{L_{10}}{a_1 a_{iso}} \right)^{1/p} \quad (4.1)$$

For  $L_{10}$  it is  $a_1 \stackrel{!}{=} 1$ .  $a_{ISO}$  is not as trivial to determine. Since no custom data is available it is taken from ISO 281. It is  $\eta_C \stackrel{!}{=} 1$ . To determine  $C_u$  is not that simple.

$C_u$  is based on the value  $\tau_u$  (eq. 2.5). In several publications (e.g. [IH85, GLL12])  $\tau_u$  has been reported as  $\tau_u \stackrel{\wedge}{=} \tau_1 \approx 360 \text{ MPa}$  for 100Cr6 independently of steel grade. Bathias

[Bat10] reported for torsion tests in the regime  $10^9$  also identical values for fish-eye failures. This value is strikingly similar to the tolerable shear stress resulting for eq. D.9 when  $R_{p0.02}$  is estimated with eq. 2.13, i.e.  $\tau_u$  is depending on the steel matrix's point of yielding. For Murakami's equation (eq. 2.12) an NMI size of  $\sqrt{AREA} = 2.1\mu\text{m} \stackrel{\Delta}{=} \varnothing 2.36\mu\text{m}$  or smaller is necessary. This diameter is about twice the diameter of chromium carbides. Even if only harmful oxides are considered, it remains a fact that larger oxides are found in 100Cr6. Thus,  $\tau_u$  is a material property, which can be approximated by eq. D.9 and 2.13.

In the present case the catalogue value of  $C_u$  is used, which actually corresponds to a more optimistic  $\tau_u = 440\text{MPa}$ . It is used regardless of the experimental evidence in order to comply with catalogue data.

The resulting dynamic capacity  $C$  thus is estimated to  $C = 95\text{kN}$ . For the NU 206 bearings with all its safety factor a  $C = 44\text{kN}$  is given. The experimentally established value seems to be a reasonable figure for bearings made of C56 E2.

### 4.4. Modelling of Surface Crack Growth

#### 4.4.1. Overview

In chapter 3.6.2 it has become clear that spalling initiated by indentation is the most critical failure criterion in the observed case. The tribological nature of indentation caused failures is very complex. Acting principal stresses, alternating shear stresses, lubricant film thickness, asperities, vibration, time of indentation and many more factors play a role in this. Observation of near-surface cracks in the vicinity of natural indentations is not trivial. Neither stress intensity factor nor exact time of indentation are known. To avoid such an impasse artificial indentations on shafts are introduced to raceways and tested under constant load.

Four shafts manufactured with the same specification and from the same steel heat as series 0 (chapter 3.4) are indented with a  $\varnothing 1\text{mm}$  SiN Ball. To each raceway three indentations are applied. Thereby, two shafts are indented  $5\mu\text{m}$  deep and the other two shafts are indented  $7\mu\text{m}$  deep. The resulting arithmetic diameters without shoulders are  $\varnothing 141$  and  $167\mu\text{m}$ , respectively. Measuring of the resulting shoulders has not been simple, but as visible in fig. 4.10, they are about 2 and  $4\mu\text{m}$  high.

Testing has been conducted identical to series 0, however, the cleanliness of the cleaning agent and conserving oil has been increased. This is done by avoiding stirring of sediment particles in the respective vessels.

Three of the four shafts exhibited spalling on at least one artificial indentation. The fourth shaft is deactivated after 450 h service time (aka  $1.09 \cdot 10^8$  turns). The corresponding Weibull chart is found in fig. 4.11. On the first glance the service life is smaller than for series 0 and A1, however, it has to be kept in mind that only three failures were observed. Moreover, seven raceways were suspended at 450 h. Unlike previous tests the intention of this test has been to determine the crack growth at safely reaching  $10^8$  revolutions and thus the service life has been truncated much earlier. In addition it has to be kept in mind that natural indentations have a depth of 3-4  $\mu\text{m}$ , while the indentations

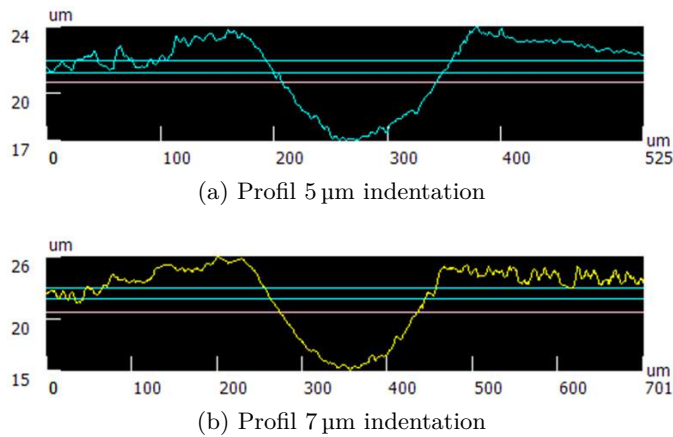


fig. 4.10.: Profile of raceways after indentation

in this case have 5 and 7  $\mu\text{m}$ . It is remarkable that 95 % confidence intervals overlap, which is taken as proof for the assumption that particle based indentation must occur early on.

An interesting fact about the indents is that not only the shoulders, but also material at the edge seemingly has been removed. For the 5  $\mu\text{m}$  indentations the crater diameter is approximately  $\varnothing 240 \mu\text{m}$  (fig. 4.12).

#### 4.4.2. Short Crack Growth Model

Calculations with the program ‘Lager2’ show that nominally seven rollers are in contact with the shaft. The maximum hertzian contact stresses are depending on the location of the specific roller, with rollers closer to the location of the force having stronger stresses. Although the location of the rollers varies over time, the total amount of force remains the same and therefore the averaged maximum hertzian contact stresses. Hence the number of load cycles till failure for a 450 h failure means  $7.65 \cdot 10^8$  load cycles, which is in the very high cycle fatigue regime ( $10^8$  cycles are reached at 59 h service time. The tests are conducted, however, for  $10^8$  revolutions, as it must be assumed that the high residual stresses will intercept at least the weaker stresses).

For a crack propagation consideration an initial crack length and location is necessary. It is a well established fact that crack propagation starts in a shallow angle behind the trailing edge. For a correct initial crack length determination the shear stresses at the (near-) surface are of the essence. However, no simple, physically accurate way to determine the strength is available owing to the complexities of EHL calculation. Nelias and Ville [NV00] calculated with means of transient EHL that in the vicinity of the trailing edge of an 1.5  $\mu\text{m}$  depth indentation with 1.5 GPa hertzian contact stresses results in a shear stress range of  $0.25 \cdot p_{max}$  to  $0.86 \cdot p_{max}$  depending on the lubricant and sliding condition. For an indentation without shoulder the shear stress varies between  $0.2 - 0.35 p_{max}$ . Santus et al. [SBB12] report that surface cracks with their usual inclination of 25-30° correspond to a friction coefficient of  $\mu = 0.05$ .

## CHAPTER 4. SERVICE LIFE DETERMINATION FOR TIME-INVARIANT LOADING

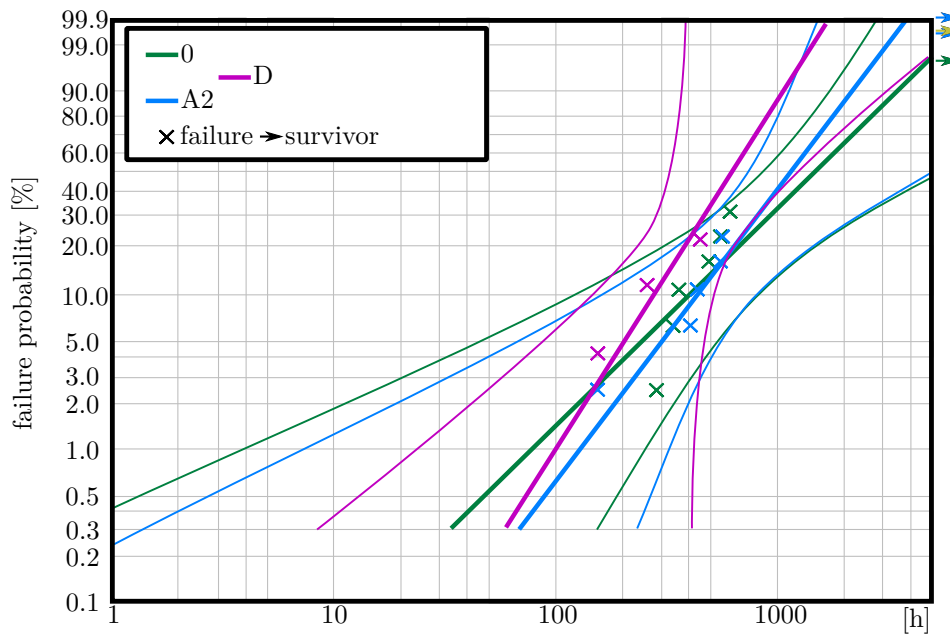


fig. 4.11.: Weibull distribution of Tests 0, A2 and D. Confidence interval is given for 95 % confidence.

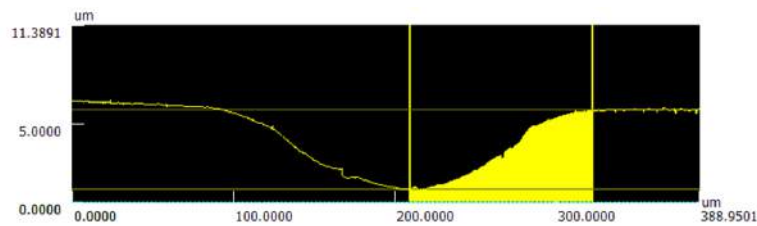


fig. 4.12.: Profile of a 5 µm indentation after 258 h of service

In chapter 2.4 it is reported that  $K_I$  and (to a minor extent)  $K_{II}$  are responsible for crack growth. This is especially true when lubricant can seep into the crack. In the current case, however, short cracks must be of microstructurally small size and dominated mainly by their large dislocation tips. [SBB12] points out that fluid pressure cannot play a role for short cracks. In [SBB12] it is suggested that short crack propagation continues with its original inclination until a critical crack length of which the stress intensity factor is equal to the classic threshold stress intensity factor is reached. Only then the crack starts to turn into a surface parallel direction due to classic LFM considerations. The depth of the parallel part is predicted to be about the depth of the crack when reaching the critical length.

Short crack propagation in bcc lattice cannot be modelled with Crack-Tip Slide Displacement models such as the Model of Tanaka or Navarro & de los Rios. Schäfer [Sch10] reports that unlike fcc lattice structures, once initiated short cracks do not continue to propagate easily. Cracks in bcc lattice do not propagate along grain borders until a

sliding plane is found. A sliding plane has to be at the crack tip. Plus the angle between the sliding planes of the grains has to be smaller than  $20^\circ$ . Even so, the few cracks which propagated beyond their original grain were arrested until damage accumulation created natural short cracks. The observations are conducted in ferritic iron, where no boundaries in the shape of martensite needles are present.

Thus a proper short crack propagation model for indentation initiated cracks would have to be described by a damage accumulation model similar to the methodical procedure given in [BB01].

Calculations of the lattice distortion according to [RA06] and diagrams given in [SWLS08] prove the applicability of above observations to a martensitic bcc lattice, as the distortion of the lattice for 0.56% carbon is in single digit picometre range.

A continuum mechanics mapping of the stresses show that a half space in contact with a cylinder (figs 4.13, Appendix D.1-D.6) and also a half space in contact with point load (fig. 4.14) experience a rise of the principal shear stress closer to the trailing edge. The physical direction of the principal shear stress also has a broad volume, in which its inclination is of  $\pm 30$  to  $40^\circ$ .

To summarise the model and the proposed method:

- Short crack problematic
  - Crack behaviour for iron lattice fully valid for considered steel grades
1. Mapping of the near-surface stress distribution is necessary
  2. Application of a shear stress based damage accumulation & distribution probability
  3. Calculation of the crack linking / propagation time
  4. When joined crack reaches a length corresponding to  $\Delta K = \Delta K_{th}$ : LEFM crack propagation
  5. Damage accumulation and short crack propagation time constitutes of the majority of time to failure

#### 4.4.3. Linear Elastic Fracture Mechanics Calculations

As the model proposed in the previous chapter is currently not feasible from a practical point, it is endeavoured to approach the fatigue problem from a deterministic point of view. Since the observed inclinations for cracks fit the observation of Santus et al. [SBB12], it is assumed that during the first 1000 revolutions (7000 cycles) a friction coefficient of  $\mu = 0.05$  is valid. After that a lower  $\mu$  is acting.

In a first step  $\sigma_x$ ,  $\sigma_z$  and  $\tau_{xz}$  induced by over rolling are mapped with the equations given in appendix D. A dynamic grid size of  $0.01 \cdot a$  is chosen for that. Then the stresses measured by XRD for unrun series 0 shafts are superposed. From a physical

**CHAPTER 4. SERVICE LIFE DETERMINATION FOR TIME-INVARIANT LOADING**

---

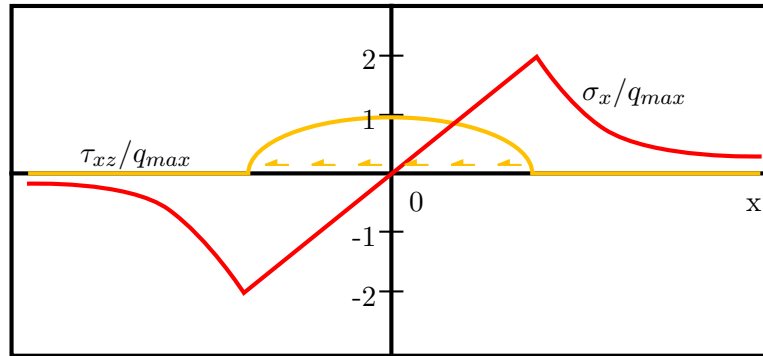


fig. 4.13.: Stress distribution at the surface of a line contact with traction forces.  $q_{max}$  is  $\mu p_{max}$ . [Joh85]

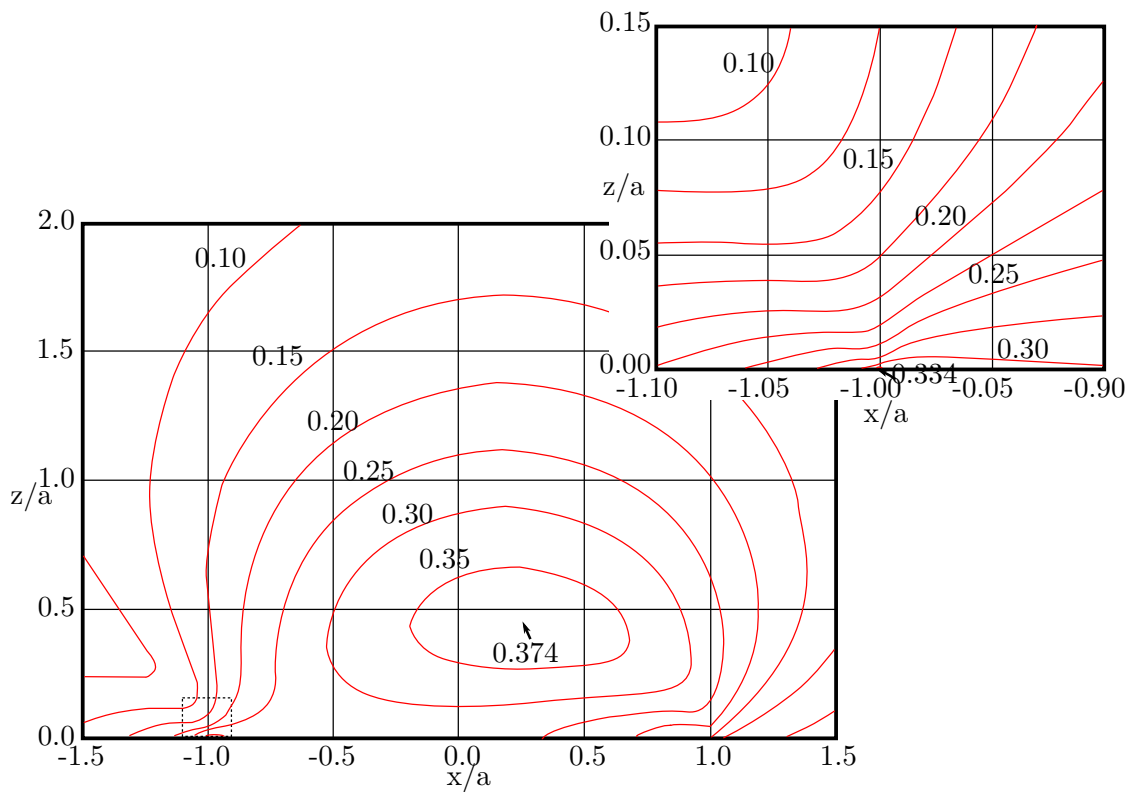


fig. 4.14.: Stress distribution at the surface of a point contact with traction forces.  $q_{max}$  is  $\mu p_{max}$ . [Ham83]

#### 4.4. MODELLING OF SURFACE CRACK GROWTH

---

point of view the material experiences straining rather than stresses. Ergo it is not possible to differentiate normal and shear stresses in  $xz$ -direction. As in the present case the circumferential ( $\sigma_x$ ) and axial stresses ( $\sigma_y$ ) are very close to each other, they are assumed to be principal stresses. By definition the radial stress component must be zero at the surface. For the radial component to be in equilibrium with the axial and circumferential component a tensile stress must apply to it. This is calculated by

$$\sigma_z = -\nu \cdot (\sigma_x + \sigma_y)$$

. The Poisson constant is assumed as  $\nu = 0.3$ . Spline interpolation is used to fill the gaps of stress states between actually measured depths (fig.3.21). For the computation Matlab 2010b is used.

For a deterministic approach a crack initiation criterion is necessary, which will be determined later. For computing the crack tip propagation a modification of the formulas in [LOK10] and [CM06] is used in combination of the stress field map computed in the previous step.

Short crack growth is dependent on the crack length and microstructural boundaries. As we have seen in the previous chapter, we do not have a single crack growing through the material, but rather the accumulation of many damages leading to many short cracks. We assume that the overall propagation speed increases with increasing number of damages, i.e. weakening of the material, which we express by means of our imaginary single short crack length.

For a deterministic short crack propagation Ciavarella & Monno [CM06] propose an intrinsic threshold stress intensity factor (SIF), which is employed by Lai [LLR12] in our manner:

$$\Delta K_t = \Delta K_{th} \sqrt{\frac{l}{l + l_0}} \quad (4.2)$$

$\Delta K_t$  is the intrinsic SIF threshold value.  $l$  is the crack length and  $l_0$  the intrinsic fatigue crack length as defined in the Kitagawa diagram. The limit for stress propagation is thus modified in the Kitagawa diagram. Short cracks now have a reduced stress limit for propagation (fig.4.15).

$l_0$  can be determined by the equation given by El Haddad et al. [EDTS80]:

$$l_0 = \frac{1}{\pi} \left( \frac{\Delta K_{th}}{Y \sigma_{w0}} \right) \quad (4.3)$$

$Y$  denotes the geometric factor,  $\sigma_{w0}$  is the intrinsic fatigue limit of the material.  $\sigma_{w0}$  is a material specific constant. When the crack length surpasses  $l_0$ , the fatigue limit is reduced due to the presence of a crack.  $\sigma_{w0}$  can be estimated by eq.2.13. From experience, the intrinsic fatigue limit is 45% of  $Rm$ . For simplicity it can be estimated to 0.5.

$$\sigma_{w0} \approx 0.5 \cdot \sigma_{wRm0} \approx 1.6 \cdot HV$$

The geometric factor  $Y$  according to Lai et al. is

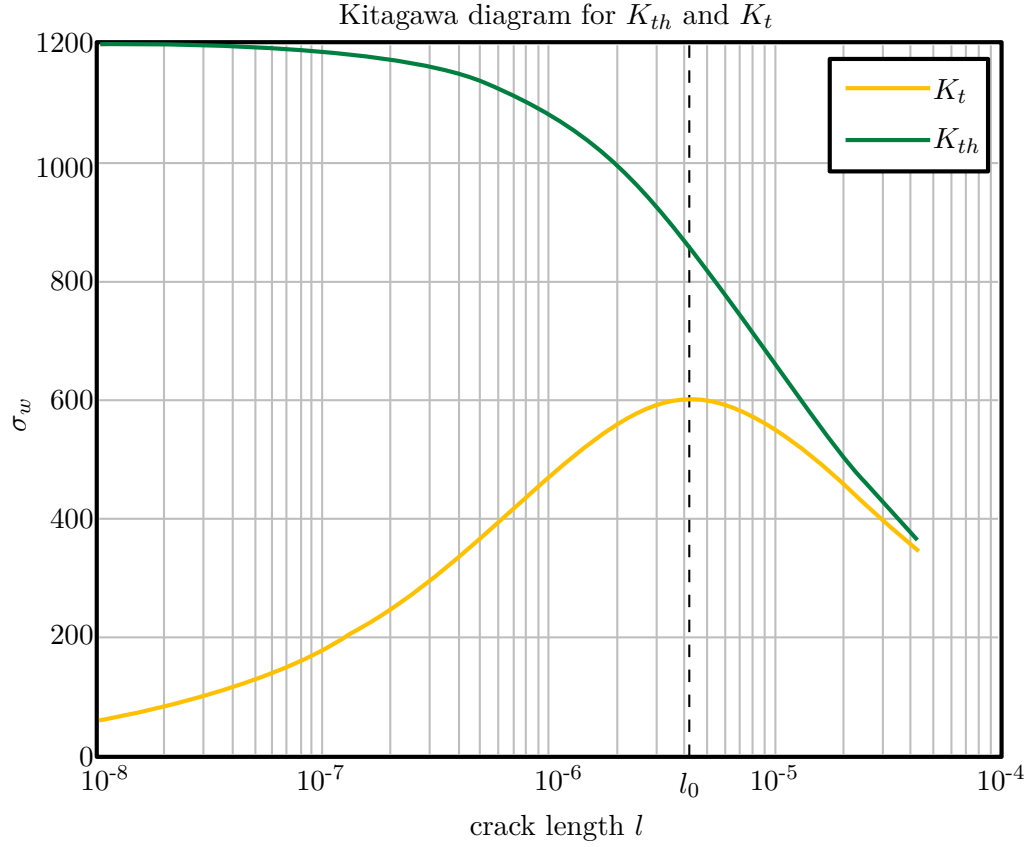


fig. 4.15.: Kitagawa diagram for C56E2 (Induction hardend and annealed for 2 at 160 °C)

$$Y = 0.75 \quad (4.4)$$

for a semi-sphere on the surface. Tada, Paris and Irwin [TPI00] give for a V-shape crack

$$K_I = \frac{P_{line\ load}}{\sqrt{\pi a \sin\alpha}} \quad (4.5)$$

with  $P_{line\ load}$  and  $\alpha$  being a line load and crack inclination, respectively.

As crack propagation model two types of models seem to be of interest. The first model type covers the the non-linear range between crack arrest and the linear regime, while the other model covers the whole range from crack arrest to fracture toughness. In both cases, the crack arrest location is moved from  $K_{th}$  to lower values. The necessary Paris parameters,  $K_{th}$  and  $K_c$  were determined by Reckinger [Rec14] for both steel grades in induction hardened and tempered state (tempering for 2 h at 160 °C). Reckinger reports  $K_c$  values rather than  $K_{Ic}$  values, however, a comparison of his results for 100Cr6 show that reported  $K_{Ic}$  values are identical with Reckinger's reported values. The parameters are found in tab.4.2. For the first type of crack propagation model computation

#### 4.4. MODELLING OF SURFACE CRACK GROWTH

---

is aborted when  $\Delta K = K_{th}$  is reached. For the second type of model, computation is aborted at  $\Delta K = K_{Ic}$ .

The computations for crack propagation are performed for 2.7 GPa hertzian stress. For determining a proper crack initiation criterion several attempts are made. Unfortunately, all trials are to no avail. As the von-Mises yield criterion is hardly affected by increased principal shear stress, it is not very suitable. Moreover, it happens that for 2.7 GPa it would surpass the assumed compressive strength  $R_m$  of the material.  $R_m$  is estimated to be roughly twice the amount of  $R_{p0.2} \approx 1200 MPa$ . The Tresca criterion is unable to surpass  $R_m$ . As explained in the previous chapter, cracks develop in reality over prolonged numbers of alternating cycles. In order to determine an area which may suit, the yield strength is taken. Unfortunately, the area surpassing  $R_{p0.2}$  at the trailing edge is too large for assuming a short crack throughout the extent of the area figs 4.16 & 4.17. Therefore, the deterministic approach is not pursued any further.

	C56 E2	C55V
$K_{th} MPa\sqrt{(m)}$	4.42	4.58
$K_c MPa\sqrt{(m)}$	25.3	23.9
Paris C	4.22e-8	5.19e-9
Paris m	2.88	4.13
Donahue C	5.48e-06	5,94e-06
Donahue m	1.26	1.03
Hartmann-Schijve C	8.33e-05	8.56e-05
Hartmann-Schijve m	1.24	1.02

tab. 4.2.: Parameters for C56 E2 and C55V for different crack propagation models.

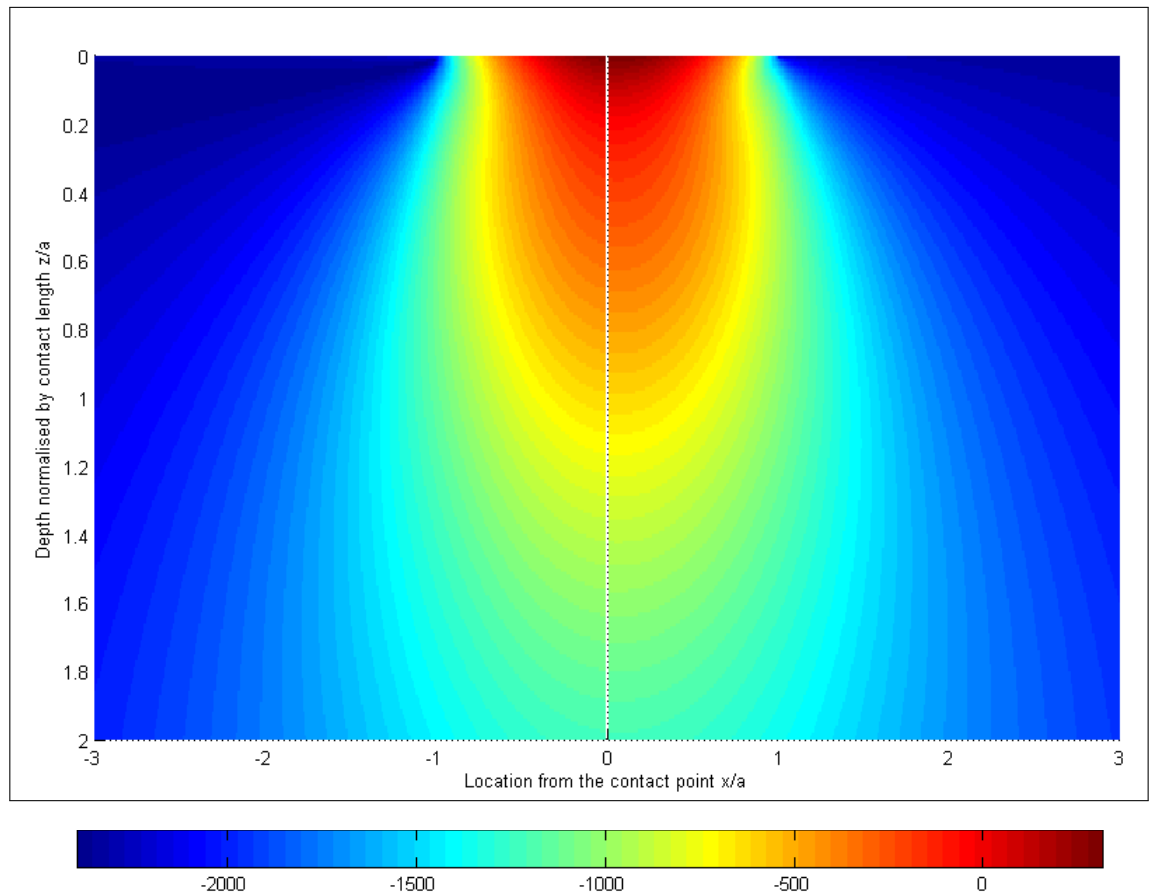


fig. 4.16.:  $\sigma_{von Mises} - R_m$ .  $a$  is  $170 \mu\text{m}$ . Values over zero surpass tensile strength, which physically is not possible.

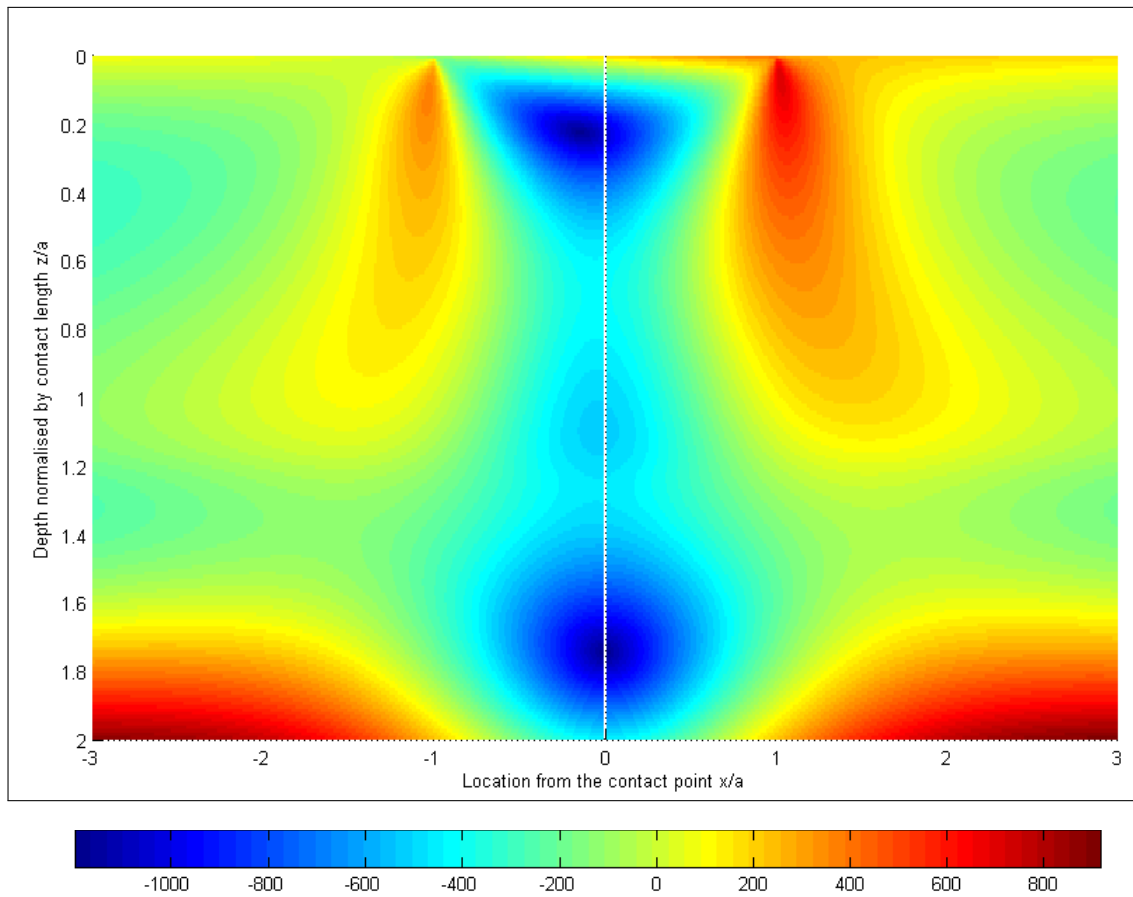


fig. 4.17.:  $\sigma_{Tresca} - R_{p0.2}$ .  $a$  is  $170\ \mu\text{m}$ . Values over zero surpass yield strength. The values below  $300\ \mu\text{m}$  do not contain residual stress data.

## **4.5. Summary**

The Material response of martensitic steel is used to determine the subsurface failure probability.

- Subsurface fatigue failure of modern bearing steels of moderate cleanliness is known to reach  $L_{10}$  shortly before LAB formation is detectable.
- With this criterion it is proven that – with a few exceptions – all indentation failed raceways have not surpassed more than subsurface  $L_{10}$  service life.
- Indentations are clearly the service life delimiting factor for technically clean bearings.
- White Etching Crack inhibition due high residual compressive stresses probable

A method is presented in this chapter for determining the dynamic capacity

- for service life rating of any bearing type in absence of actual subsurface failures
- the normalised FWHM of the bearing's material must be available and calibrated to a failure probability
- service time must be available
- load conditions must be available
- In absence of a material calibration the LAB criterion can be taken.
- The estimated dynamic capacity of C56 E2 is sufficient ( $C = 95 \text{ kN}$ ) and surpasses the catalogue value ( $C = 45 \text{ kN}$ ) by a safety factor of two.
- The fatigue life of C56 E2 bearings is in the presence of indentations, however, similar to the fatigue life of 100Cr6 bearings.

The advantage of this method is the possibility to evaluate the real loads in comparison with the design loads.

As indentation caused failures are of relevance for practical applications, it is endeavoured to establish a calculation model.

- introduction of artificial indentations.
- Weibull distribution fits service life of other tests.  $\Rightarrow$  Proof that indentations occur early on.
- VHCF regime problematic
- Modelling of crack growth

- 1 physical model
  - 1a approximation of surface stress in the vicinity of indent with Coulomb friction
  - 1b short crack growth until  $\Delta K = \Delta K_{th}$
  - 1c CTSD computation for short cracks in bcc lattice not sufficient
  - 1d Damage accumulation distribution model needed to determine initial crack sizes and densities
- 2 deterministic Model
  - 2a modification of El Haddad criterion for short crack propagation
  - 2b initial (fictional) crack size to be determined by classic yield criterion
  - 2c no fitting yield criterion found

In total only one methodology can be presented. Unfortunately no authoritative damage accumulation distribution model is found for this model rendering it impossible at present to compute the fatigue life for an assumed indentation.

# 5. Design and Development of a Test Rig for Dynamic Testing under highly Time-variant Load Changes

## 5.1. Motivation

This chapter deals with the design and development of a bearing test rig which is capable to exert high impact loads. The development of a totally new test rig from scratch is triggered by the desire to test bearings at high dynamic forces found in modern combustion engines, yet only covered currently by empirical knowledge without any specialised description of the resulting service lives. The first sub-chapters explain how at present rolling bearings are tested. After outlining the principle methodology of designing and developing a project like this, specific aspects crucial to the test rig are presented.

## 5.2. Overview of Existing Test Methods

### 5.2.1. Dynamic Testing

This kind of test is conducted with bearings and a constant force acting from one side. Often this set-up is established by belts driving the outer ring (OR) of the bearing. Dynamic testing with a rotating IR and standing OR exist as well and is used in references [Lor84, PMS10, Vos97, DTed]. The designs used in [Vos97, IH85] and [Lor84] are capable of testing two bearings at the same time on the same rig, e.g. fig. 5.1. The term *dynamic* hereby refers to the fact that a random point on the surface of the turning ring will see a load change. The dynamic capacity  $C$  given by bearing manufacturers for each bearing type have been experimentally verified by such tests. So were the calibration curves in chapter 2.3.4. [LP47, Vos97, Vos98, Vos00, IH85, Lor84, DTed]

The design of such a testing machine is rather simple and robust. The reproducibility of their test results is very high. While this way of testing is an accepted method, its major shortcoming is the fact that actual dynamic loading cannot be tested. In a majority of current applications engineers tend to either take the assumed worst case loading of a bearing for life time calculation or use load collectives if available. However, actual high dynamic loading might result in changes of the EHL film condition's state during each load cycle. Such rapid changes cannot currently be simulated with existing computing facilities in a feasible way. Even if possible, experimental verification is still needed.

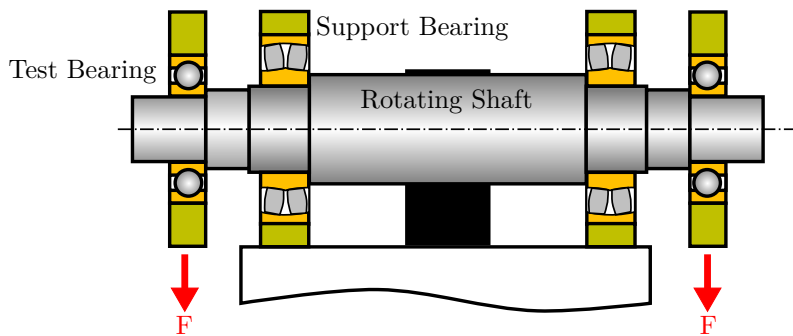


fig. 5.1.: Schematic of the dynamic test used for type 6309 ball bearings acc. [Vos97]

### 5.2.2. Twin Disc Testing

Twin disc tests are commonly employed in order to test combinations of rolling and sliding of two surfaces. The system consists of two specimen, whereas usually one disc has a cylindrical shape, while the other one has a convex shape. These discs are locked into contact by applying a force normal to the contact area of the cylinders. Often the convex radius is equal to the radius of the disc in order to prevent edge pressures due tilting. Depending on the aims and intentions of a test, media like lubrication oils or oil mist are either injected between the contact surfaces or surround the specimen in a bath. The amount of normal force, sliding and rolling can be adjusted. Moreover, the system enables the researcher to investigate a wide variety of materials and surface qualities as well as the effects of different lubricants and environments (water, oil, corrosive atmosphere, etc.). [NDC98, THF10b, CCK94, Kür12, Sch13]

EHL conditions in a twin disc machine, however, are not identical to conditions within rolling bearings. As a matter of principle static EHL conditions are always given. This is not necessarily the case at a high dynamic loading as stalling of the lubrication film is a possibility.

### 5.2.3. Ball-on-Disc / Pin-on-Disc Test

The Ball-on-Disc or Pin-on-Disc test is applied in all cases where tribologic pairings are investigated. In this test the tip of a pin or a ball on top of a pin is pressed onto a rotating disc. Pin / Ball and Disc form the investigated pairing. The generated friction force and / or moment of the disc is measured and thus friction coefficients are determined. Depending on the design of the tester, lubrication can also be applied also. The testing method itself is standardised in ISO/TR 7147. [San08]

### 5.2.4. FE8 Test

The thrust type test or FAG FE8 test has been invented by German bearing manufacturer FAG to test the wear protection capacity of lubricants in almost real conditions. The test rigs main component is a shaft of which the driven end is inside a housing.

## CHAPTER 5. DESIGN AND DEVELOPMENT OF A TEST RIG FOR DYNAMIC TESTING UNDER HIGHLY TIME-VARIANT LOAD CHANGES

---

There the shaft drives two bearings in X-arrangement. These bearings are interlocked by springs, thus creating an axial load. The test rig in its basic design is defined in DIN 51 819 Part 1. In this test the bearings are subject to adjustable rotation speeds and axial loads. The wear and friction behaviour are analysed at the end of the test in order to evaluate the specific lubricant's capacity to reduce / enlarge wear and friction. Temperature and friction are measured during the test run and the resulting wear is measured at the end of each test. The system's temperature can be adjusted, i.e. testing is not necessarily limited to room temperature. The amount of grease and lubricant is defined in the subsequent parts of above given standard. [DIN51819a, DIN51819b, DIN51819c, San08]

This type of test focuses primarily on lubricant behaviour. Moreover only thrust type bearings can be used, which is not the scope of this work.

### 5.2.5. Thrust Type Testing

The thrust type testers consist of three balls similar to balls of a ball bearing and a rotating ring on which the balls roll / slide. The wear and friction behaviour are analysed in order to evaluate the lubricant. The system's temperature and the axial load can be adjusted. These systems are often used to investigate pairings of different materials or non-standard surface qualities. At times experiments with extremely high axial pressures are found as well. Often the systems are flooded or emerged into pools of lubricants. Depending on the aim of the conducted test the rolling elements may be prevented from rolling, thus forcing them to slide over the surface of the ring and working as a tribometer. This testing also provides simple means to test loading conditions on a bearing, however, the axial loading prevents it to be an accurate replacement for radial bearing tests. Moreover, the thrust rings generally do not contain grooves or raceways identical to bearings and therefore do not experience the same stress states as a bearing would at exactly identical loads. [THF10b, BLP07]

### 5.2.6. BTR

There are only few published data of the Bearing Rig Testers (BTRs) is limited. Designed and developed by German automotive manufacturer DAIMLER AG for use in the company's MERCEDES-BENZ brand passenger cars and for motorsports applications, their main purpose is to examine friction and tribologic properties of journal bearings with very high resolution and at realistic conditions.

The basic set-up of these test benches constitutes of a shaft with two support bearings and a single test bearing inbetween and a strain-gauge force transducer. A unique set of two opposing magnetostrictive actuators in vertical arrangement (which are specially built for these test benches), in combination with a corresponding automation control system are capable of applying actual load curves of any given combustion engine. Due to the magnetostrictive effect reaction frequencies of up to 60 kHz are possible. In order to record friction with high resolution the torque is measured by means of energy dissipation. The original oil conditioning unit is capable to temperate up to 150 °C. The maximum rotation speed is 20.000 rpm. The measurement of the energy dissipation

is realised by decoupling of a magnetic clutch and measuring the deceleration time and slow-down curves. Moreover, the variation of torque and rotation speed are recorded and assessed. Although this test bench has been designed for journal bearings it has been used by other researchers to investigate friction, noise-vibration-harshness and geometry of roller bearings. For these investigations the BTR has been upgraded with vibration sensors and various other methods of lubrication. Further information might be found in [PA12, Buc15].

Although the capabilities of these test benches are very close to the demands needed in this work, they are not quite ideal. At an early stage of consideration it became clear that at that time it was neither clear, whether the actuators were capable to work for lengthy time periods such as days and weeks, which is a must for endurance testing, nor was the long-time development of the actuators behaviour known. In addition, only a single bearing can be tested at a time. This last feature means that a considerable number of repetitions would have to be done in order to statistically evaluate the behaviour of bearings at a given parameter. A modification to enlarge the number of tested bearings cannot be realised.

### 5.3. Design Guidelines

The conceptional design of the test rig followed the guidelines VDI 2221-2223 [Ric93, Ric97, Ric82, Ric04]. These guidelines outline a systematic approach to describe effectively and efficiently the challenges and problems at hand. They also provide ways to design technical solutions according to the given problem with the intention of reducing the development time and increasing the effectivity of new and modified designs. In a wider sense these steps also increase the quality of designs as the developer deliberately weighs the choices at hand constantly.

The VDI 2221 defines seven successive steps for designing new technical solutions and their result (fig. 5.2). In practice these steps involve rethinking of previously found solutions and schematics and thus must be repeated iteratively. The steps 1 - 3 are methods to find principal answers and thus are valid to any issues where analytic or synthetic analysis is possible. Though step 1 is fairly self explanatory it should be remarked that this simple task often is taken too easy and described in a rather implicit manner. The importance of an explicit problem definition and clarification can be exemplified by the humorous picture in fig. 5.3. The pictures of the swing represent the answers found by different groups of project stakeholders as a result of their understanding of the project's goal. The actual purpose for the swing is forgotten or less understood as the project progresses leading to an unfavourable answers. Although this kind of miscommunication cannot be entirely avoided at all times, it can, however, be reduced by precise formulation of the requirements and expectations for a product. Step 3 can be subdivided into a step 3.1 'physical effects' and a step 3.2 'geometric elements'. In most cases step 2 and the substeps 3 cannot be entirely divided, as effects may be coupled with a certain geometry (Think of a door kept open by a wedge. The effect of friction is coupled to the shape of the wedge), the function may be coupled with the effect or the function can

**CHAPTER 5. DESIGN AND DEVELOPMENT OF A TEST RIG FOR DYNAMIC TESTING UNDER HIGHLY TIME-VARIANT LOAD CHANGES**

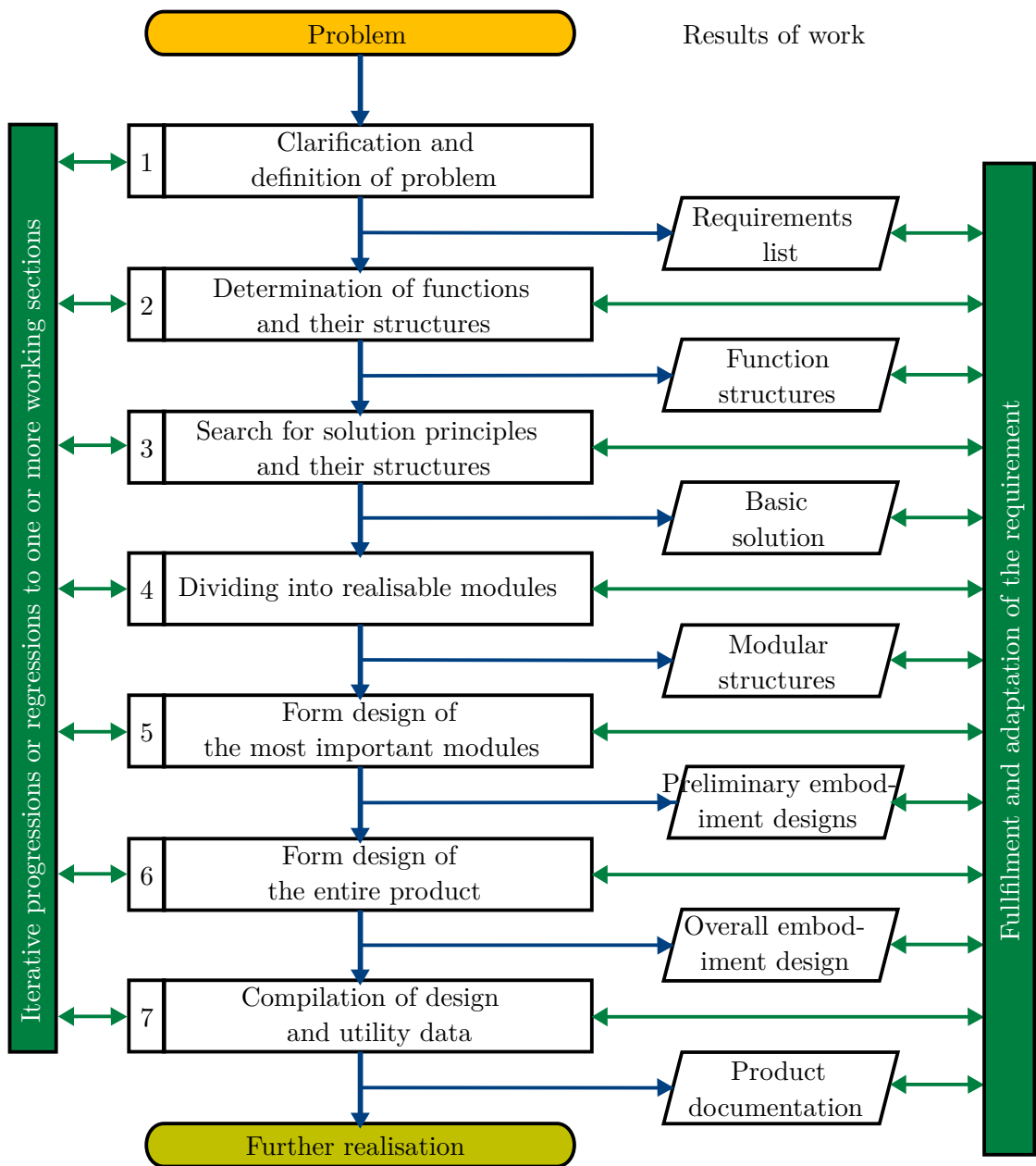


fig. 5.2.: General procedure of systematic development and design according to VDI 2221 (as depicted in VDI 2223) [Ric04]

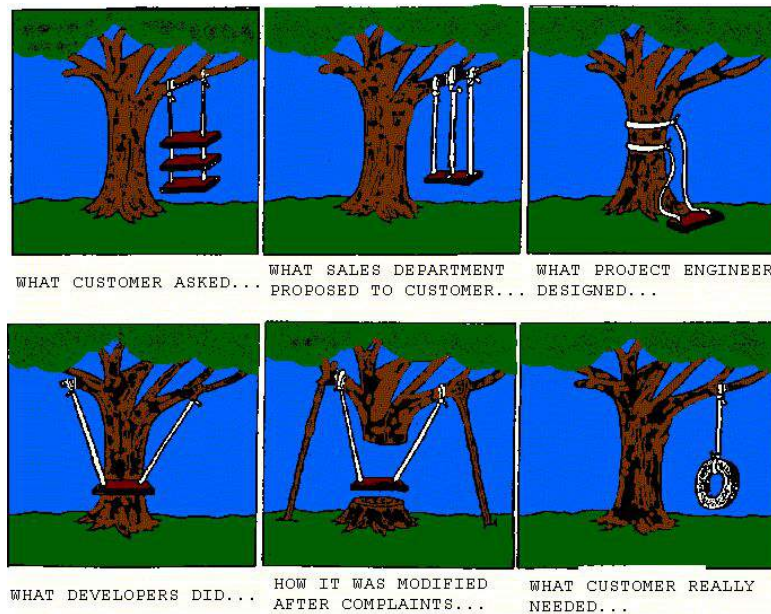


fig. 5.3.: A humorous example of the results of implicit goal definition. (Author unknown)

only be realised by a given geometry (think of a jet turbine). At the end of step 3 a basic solution is defined. This basic solution should not be mistaken for a basic design in the sense of a first draft, but rather is to be understood as the general mechanism having been defined (albeit modifications or replacements may happen at a later period due to the iterative nature of the design process). Steps 4 - 7 describe the actual designing phase in which the found solutions are transcribed into blueprints. In step 4 the found (or known) solution is divided into practicable pieces or modules, which are designed in the successive steps. As complex systems are often designed either concurrently by different groups and or follow a module strategy the iterative nature of these steps become obvious. After completion of the major components and the design of peripheral components successively a final documentation should be compiled for future reference.

Steps 1 to 3 are within the scope of this work. The design and execution part were outsourced and thus are not explicitly outlined here.

## 5.4. Definition of Goals

### 5.4.1. Observation of the Real Application

In this section the objectives of the new test bench are outlined in detail. In chapter 5.1, a first aim has been outlined, but no specific details and necessary requirements were formulated. There were merely existing test rigs evaluated regarding their usability and as such a specification has not been necessary. As seen in chapter 5.2, neither of these

## CHAPTER 5. DESIGN AND DEVELOPMENT OF A TEST RIG FOR DYNAMIC TESTING UNDER HIGHLY TIME-VARIANT LOAD CHANGES

---

systems could satisfy the needs, nor could the tests be adapted to fit any of these test rigs.

Prior to defining the objectives it is first endeavoured to recapitulate the real application situation. The bearings are loaded periodically with high forces for very short times in the regime of a few milliseconds. The full width at base for the forces is less than 4 ms and their appearance is synchronous to the IRs angle. Although several load peaks can be found in the operation condition of these bearings, only one or two peaks are worth noting, as their intensity tops the other peaks found in-between by a factor of two to ten times. The forces are transmitted from the IRs to the ORs in all but a few cases. No load or a very low quasi-static load is present during most of the bearings rotation time. In a few cases the peak forces point into the opposite direction of these low loads. The circumstances of operation inhibit the bearings of being preloaded during assembly in order to distribute the force over a large circumferential area. Moreover thermal expansion of the IR is expected. Further the viscosity of the applied lubricant is very low, as the bearings are part of an automotive combustion engine and thus are lubricated with hot SAE 5W-30.

In detail this means:

- loading times of 4 ms or less
- the absolute intensity of the force
- synchronisation of loading time and IR angle
- no preloading of the bearings or
- a light preloading in opposite direction
- one or two peaks per IR revolution
- use of a low viscosity oil with EP additive as lubricant

The idealised load curve is depicted in fig. 5.4.

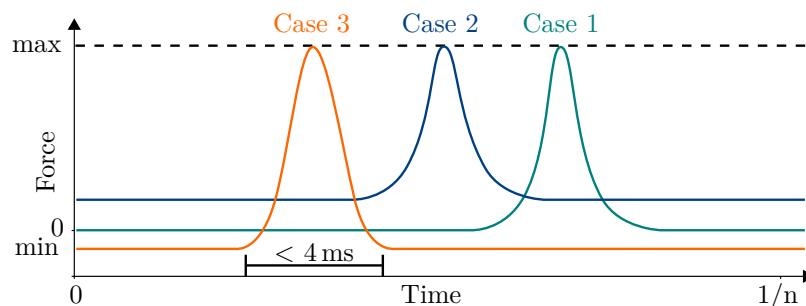


fig. 5.4.: Idealised load curves for the test rig. Case 1 is without preloading, Case 2 with preloading and Case 3 with negative preloading.

### 5.4.2. Additional Requirements

By observing the concerned system in question a number of major requirements have already been established. These points, however, are not enough to complete the list of requirements. Moreover, some of the requirements yet need to be precisely defined quantitatively.

The most imminent question are the failure modes and the repetitive signals / effects to be evaluated:

1. subsurface pitting
2. near surface pitting / flaking
3. abrasive damages
4. friction welding
5. false brinelling (indentation caused by rolling elements) of sorts.
6. friction within lubrication

the signals / effects in the same order will be:

1. increase of Noise-Vibration-Harshness (NVH)
2. ditto
3. increase of torque after loss of function
4. increase / decrease of torque, rise of temperature
5. change of NVH pattern
6. heat increase due operation / plastic deformation due to annealing of bearings

For endurance test capabilities also statistics is needed. In detail this means:

1. multiple specimen testing
2. test abortion criteria
3. relevant statistical distribution pattern information
4. time constant input parameters / control loops for input parameters

Items two and three are essential for compiling statistics of fatigue life. As different distributions require different input parameters, it is impossible to foresee and record data for all types of distributions. Out of endurance test experience continuous distributions – most notably special cases of the Fisher-Tippet distribution (also known as Generalised Extreme Value distribution) like Weibull distribution (also known as Type

## CHAPTER 5. DESIGN AND DEVELOPMENT OF A TEST RIG FOR DYNAMIC TESTING UNDER HIGHLY TIME-VARIANT LOAD CHANGES

---

3 Extreme Value distribution) – are to be expected. In order to differentiate the reason of failure or even derive distributions for a specific failure time, the sensor information respectively the information from specimen analysis is needed as well. Time and mode of failure should be detectable at the end of testing, which requires:

- measurement of vibration / solid borne sound
- measurement of torque
- measurement of system temperature
- measurement of lubricant input and output temperature
- measurement of time dependent system response

90 °C – 120 °C for the system’s average temperature should yield satisfying results, however, it has been unclear at the time of the test rig specification, if an explicit heating is necessary to achieve this temperature as 500 W of heat has been assumed to be generated at maximum per bearing. At a later point experiments with a preliminary design will show that a strong cooling will be necessary to prevent overheating of the specimen (5.9).

In total the goals of the test bench are as follows:

- load application times of less than 4 ms
- the absolute intensity of the applicable force
- synchronisation of loading time and IR angle
- no preloading of the bearings or
- a light preloading in opposite direction
- one or two peaks per IR revolution
- use of a low viscosity oil with EP additive as lubricant
- detection of failure:
- automatic termination of the test at failure
- recording of data
- multiple specimen testing
- accelerated testing (if possible)
- monitoring / control of input parameters
- lubrication
- thermal conditioning

## 5.5. Principle Designs

After defining the primary goals for testing bearings with high dynamic loads, steps 2 and 3 from fig. 5.2 have to be tackled. As already mentioned, these two steps cannot always be strictly separated from each other.

The first and foremost component of interest is the specimen itself. To achieve synchronisation of force and IR angle two functional options exist:

1. Regulation of the force and the timing, fig. 5.5 (a)
2. Controlled application of force, fig. 5.5 (b)

The design proposal 1 is simple and straight forward. It can be effortlessly established and solely the rotation speed of the specimen shaft is needed. This implies that the position of the shaft is known, however, only the given rotation speed of the drive can be known. The effects of wear, elasticity and most importantly friction upon the shaft's rotational movement are somewhat uncertain. The aim of synchronisation of impact time and shaft position would be jeopardised by such a design. Proposal 2 is capable of avoiding such uncertainties, provided the sensitivity of the employed means of measuring is high enough. The drawback of this system are higher costs or / and effort.

During the first iteration of this approach a maximum force of +60 kN per bearing was projected and the expected power loss and torque due friction were estimated as high as 370 W and 780 Nmm respectively per bearing at the time of maximum force. For these estimations catalogue bearings with static load were assumed. Since additional friction in the instant of impact cannot be dismissed even higher torque must be assumed. As such heavy torque will involuntarily lead to distortions of the shaft's rotation, no choice remains other than to work with a controlled application of force as shown in fig. 5.5 (b).

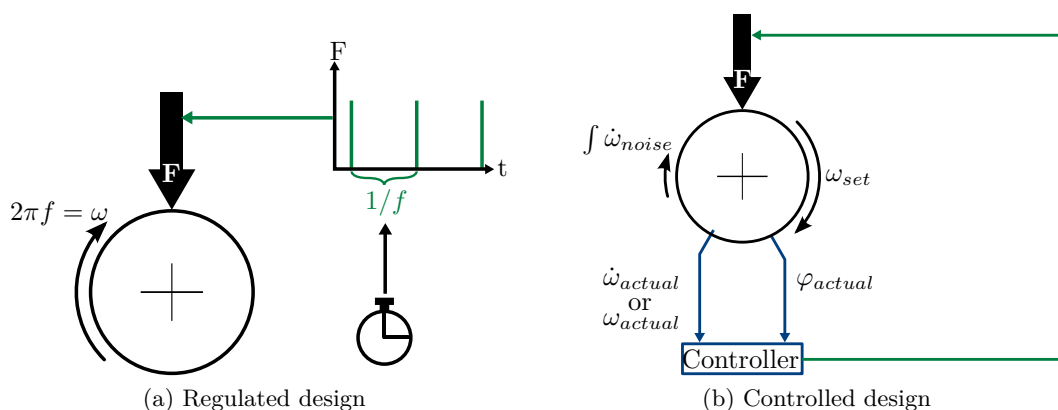


fig. 5.5.: The basic step 2 design proposals available

## CHAPTER 5. DESIGN AND DEVELOPMENT OF A TEST RIG FOR DYNAMIC TESTING UNDER HIGHLY TIME-VARIANT LOAD CHANGES

---

In order to control the timing of force application several principle designs are available. The order of presentation in fig.5.6 does not reflect the chronological order of evaluation. In fact proposals 3.2 and 3.3 are well established designs used in different applications and are industrial standard at present.

As chapter 5.6.1 will show, alternative designs had to be considered as well. Fig.5.6 (a) exemplary shows pure mechanical designs. The advantage of purely mechanical designs are their high speeds. The most crude design of such a mechanic would be the depicted one, consisting of gears rotating a cam which exerts a force upon the specimen. It goes without saying that a practical design would probably not consist of cranks or timing belts but rather inelastic elements like timing chains. A variation would be the use of shifter shafts as known from high speed machine tools. Thereby a shaft is turned synchronously with the specimen shaft. The shaft has one or several grooves which a pin-lever is guided. Depending on the grooves position the tool (in this case the force applying system) is displaced. In the present case this would be a simple up and down movement. In order to cope with different speeds different diameters can be used. Two considerable problems, however, arise in all designs: Wear and capable loads. Calculations for the cam showed that the contact stresses on the tip of a cam would be in the magnitude of several gigapascal, no matter how wide the cam would be. The shape of the cam tip is restricted by the necessary time demanded. Moreover wear cannot be easily fought off. As modern combustion engines have considerable service lives, a testing time in the order of more than  $10^8$  revolutions may become necessary. One possible answer would be a casing around the position of cam / bearing contact. This would have to be experimentally evaluated and is beyond the scope of this work.

Another, totally different set of mechanical designs is the use of event triggered levers (5.6 (b)). In these cases the specimen shaft levitates a trigger, which sets mechanical parts into motion resulting in a weight being levered onto the bearing. Since the possibilities of the shaft to lever large masses is restricted, only external weights or spring systems are capable to exert enough force. Since the necessary masses for the load cannot be instantly retracted by any means, these methods are simply not feasible.

The third option is the use of electromechanical or electrical activated actuators (c). This option is widely used in industries and thus knowledge and availability is wide spread. Common feature of all these designs is that electronic controlled actuators exert given forces upon the bearings. The use of controllers also give enhanced flexibility by easily enabling additional operations, such as intentional delays, programmable force-time curves, etc. The most important advantage is the unification of all controlled or electronic dependent parts of the test-rig in digital control units, provided enough computational power is available.

Another crucial point regarding the shaft is it's arrangement of bearings. The number and arrangement of the bearings define the size, weight and additional stresses seen by the shaft and thus at the raceways of the shaft. As the number of the active bearings increase, i.e. the number of the bearings connected to the actuator, the required actuator force increases. Also the size and inertia of the shaft increases. While a high inertia itself would reduce deceleration due to friction, it also increases necessary driving power at

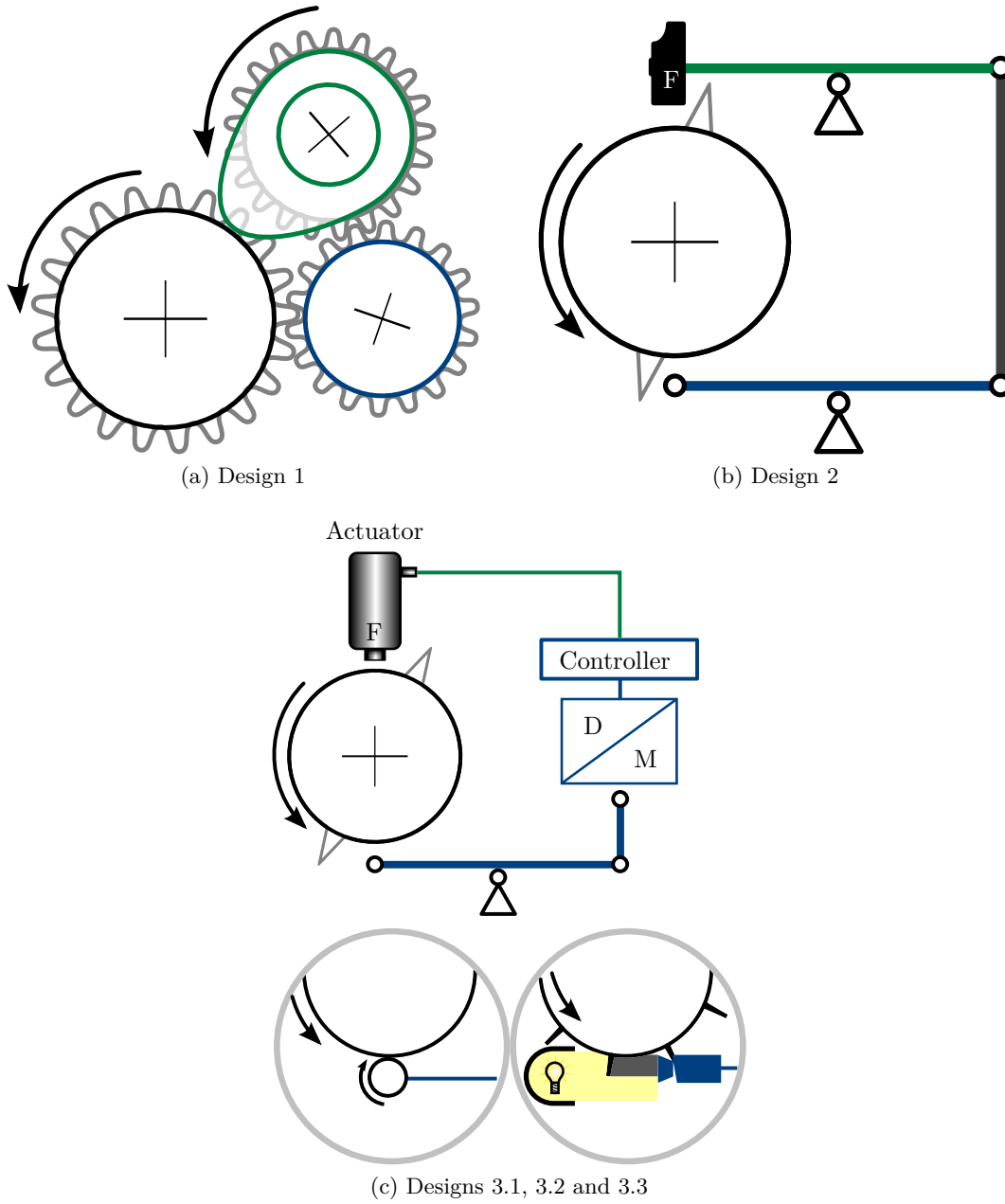


fig. 5.6.: The step 3 solutions found

**CHAPTER 5. DESIGN AND DEVELOPMENT OF A TEST RIG FOR DYNAMIC TESTING UNDER HIGHLY TIME-VARIANT LOAD CHANGES**

reduced handling capability due to size. Small shafts with very few test bearings will extend testing time as more testing has to be conducted for statistics. The bending of the shaft and the stiffness of the bearings have to be taken into account as well.

Fig. 5.7 (a) to (d) show four basic types of arrangements. The crossed orange squares represent potential locations of test bearings while green squares represent support bearings. The red line is the anticipated deflection curve of the shaft at static load with the dotted centre line as zero deflection.

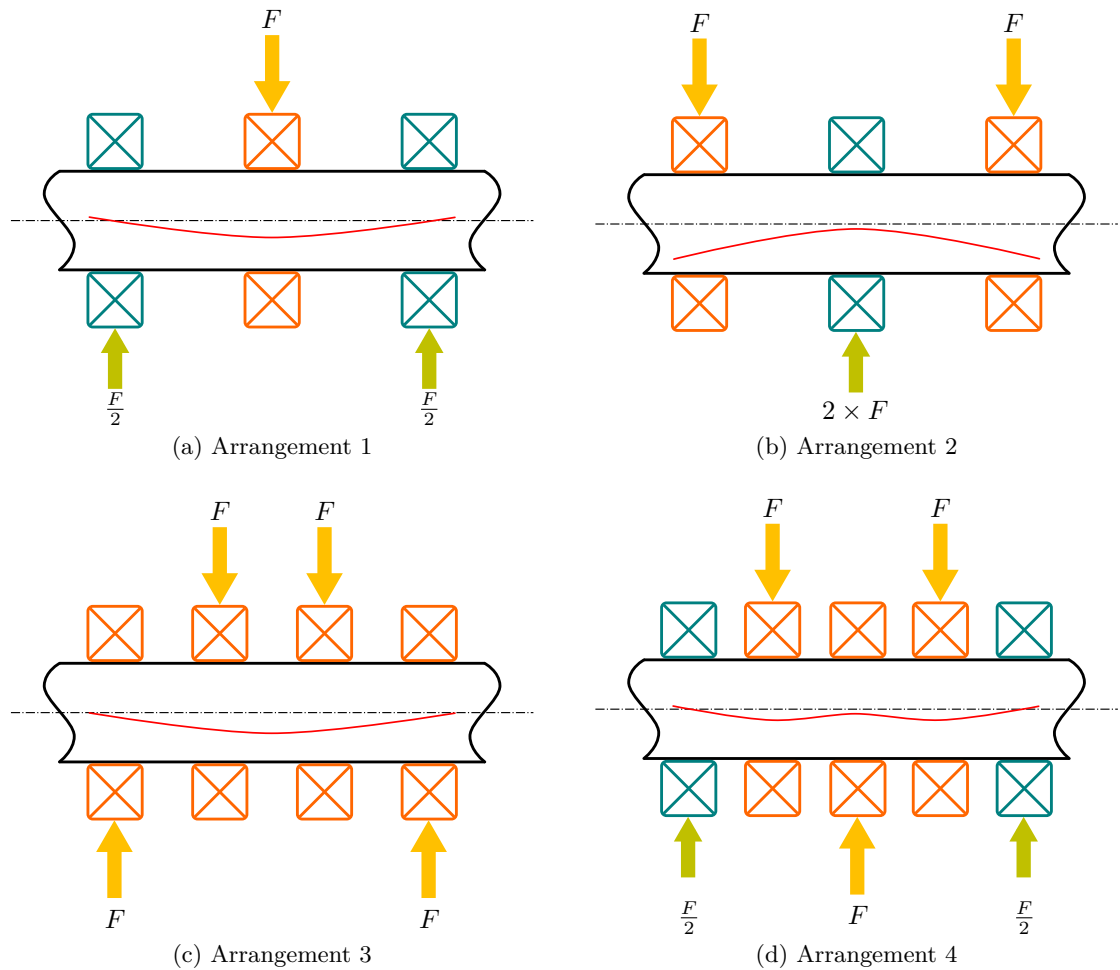


fig. 5.7.: The step 2 & 3 arrangements for bearing arrangement

Arrangement (a) is a simple and widespread arrangement which is realised in the BTR (see 5.2.6) so that an appropriate choice of shaft diameter for the rig would allow for later friction measuring on the BTR. The obvious advantage is the simplicity of this arrangement. Also the necessary actuator force is little, so are the deflections of bearings and shaft, especially when large support bearings with high stiffness are used. On the other hand the number of tests to be conducted is high, which means that

## 5.6. OVERVIEW AND EVALUATION OF MAJOR COMPONENTS

a considerable amount of time and shafts are consumed. The consumption of shafts is the result of wear and adverse effects on the shafts during mounting /dismounting, operation, etc. The consumption can be reduced by using a slightly longer shaft which can be axially offset when the original position is worn off. An overview is given in tab. 5.1

Plus	Minus
simple design short shaft / little inertia alternative: long shaft for two tests small actuator needed deflection of shaft and bearings little large/stiff support bearings possible compatibility with BTR possible	poor statistical sample base long testing time large no. of support bearings in rel. test brg. manufacturing costs compared to (c) & (d)

tab. 5.1.: The advantages and drawbacks of arrangement (a) from fig.5.7.

Arrangement (b) is in most aspects identical to (a), however, it accommodates of two test bearings at the same time. Since the shaft needs a part connecting it to the motor shaft the dislocation and misalignment to latter part has to be taken into account. Calculations for diameter 66 mm cylindrical bearings (NU211 without inner ring) showed that a bearing loaded with 60 kN (static) will deflect it about 60  $\mu\text{m}$ . As the behaviour of the shaft during dynamic loading can't be predicted it has been deemed that the potential problems which may arise might be unresolvable once the test rig is built. A modification of ((a) and) (b) is the use of two bearings for support and two bearings for testing. The greatest advantage of arrangement (c) is that all four bearings will face albeit the same load and thus could serve at the expense of a doubled actuator displacement as test bearings. Also the required force is higher than in (a). The experiments with static load described in chapter 3 also use this set-up. The quantity of statistical data generated with this arrangement is comparatively high. Finally arrangement (d) is a combination of (a) and (b), results in a smaller deflection of the shaft than with the other arrangement. At the time of design this arrangement seemed to involve more effort and uncertainties in regard of shaft bending and weight. Retrospective this arrangement might have even been a more suitable arrangement than the chosen arrangement (c), as the statistical agglomeration is still high and in case of five identical bearings also information of the damaging of bearings at lower forces would be available at once.

## 5.6. Overview and Evaluation of Major Components

### 5.6.1. Actuator

In chapter 5.5 it was decided that arrangement 3 (c) - the use of an actuator - is the most promising. The possible methods to apply radial force are piezo elements, clas-

## CHAPTER 5. DESIGN AND DEVELOPMENT OF A TEST RIG FOR DYNAMIC TESTING UNDER HIGHLY TIME-VARIANT LOAD CHANGES

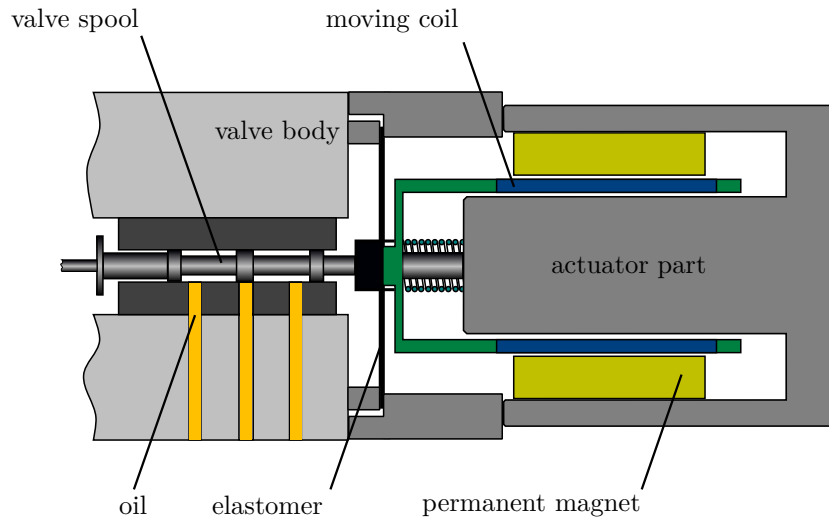


fig. 5.8.: Principle schematic of a voice coil valve.

sic hydraulic systems, magnetostrictive actuators, a mechanical design and a hydraulic cylinder with voice-coil valves.

The reaction times of appropriate piezo elements are in the regime of a few microseconds and thus within the required time of 4 ms. The service life of these piezo elements, however, is estimated to  $10^9$  cycles, which is just four times higher than necessary for fatigue life validation experiments. A characteristic of piezo elements is a falling force-vs-displacement curve, i.e. the maximum force is available at zero displacement and then drops off with increasing displacement. To compensate the estimated deflection of 60  $\mu\text{m}$  for bearing and shaft several piezo elements would have to be aligned parallel and in series. As the displacement of those elements is not identical to each other an additional standalone control unit would be needed as well. The estimated costs and the short service life are thus not in balance.

The use of a hydraulic cylinder as actuator with a large number (8 pcs) of servovalves has been dismissed, as the expected full-width at base of the loading curve would barely be within the required time of less than 4 ms. The main reason for this is the fact that a superposition of valve positions is needed to create loading curves as depicted in fig. 5.4. Limiting factors are the maximum speed of the fastest operating valve plus flow restrictions, which arise by use of more than six valves used.

Magnetostrictive actuators massive enough to exert the required amount of force are not available on the market, although not entirely impossible to manufacture (chapter 5.2.6). Experience shows that such actuators have extremely short reaction times and would be capable to emulate real loading cycles with high resolution. However, these actuators are very costly and the necessary automation control is neither trivial nor was it entirely finished and tested on the BTR at the time when the actuators were evaluated. In addition, the long-term behaviour of such massive magnetostrictive actuators was unknown at that time. The behaviour of such actuators for prolonged durations, as is

the case in endurance testing, is still unknown.

A mechanical design was dismissed due to the reasons given in chapter 5.5. The advantages of mechanical solutions are very high speeds and little to no drag in reaction time.

The finally chosen solution is the use of a hydraulic cylinder with voice coil valves. Voice coil valves are available for a short time on the market. As the name suggests, these valves convert electrical signals to valve positions by means of voice coil actuators [Nas06, SK12]. The advantage of voice coil valves in comparison to servo valves is the higher positioning speed. The working principle of voice coil valves is shown in fig. 5.8.

### 5.6.2. Bearing Bracket

Concerning the design of the bearing brackets two basic types can be distinguished. The first type of bracket provides a housing for ORs. This type is especially advantageous when standard catalogue bearings are tested, as the brackets can remain within the test rig while only the bearings are replaced. Moreover, the sensitive vibration sensors connected to the brackets do not have to be disconnected. The draw is that lubrication feeding via drilled holes – if required – is connected with considerable effort. Also, the brackets have to be precisely set up and, as chapter 5.10 will show, minimal deviation in the bearing diameters may result in an additional adjustment of the brackets. Figs 5.9 (a) and (b) show a solid bearing bracket, as it has been used in the preliminary tests (chapter 5.9) and a weight optimised design which has been envisioned to increase the dynamic of the actuator.

The second type of bracket integrates the OR of a bearing (fig. 5.9 (c)). The only advantage of this design is to be more convenient for lubrication feeding through drilled holes. A lightweight design as in fig. 5.9 (b) is not practical, since the lids depicted now have to double as flanges for the cage.

The test rig in its current version is capable to handle both types of brackets. The lightweight bracket has not been necessary for the diameters used in the current work. All brackets are designed to mount vibration sensors for solid-borne sounds.

## 5.7. Overview of Sensory Data

**Solid-borne sound detection** Flaking of material from IR, OR or rolling elements generate impacts which excite vibrations. Long before these vibrations are audible to human ears, they can be detected by sensors. The detection quality increases with increasing magnitude of the vibration compared to the general vibration. Therefore these sensors are mounted directly on the OR.

The vibration sensors are linked with a real-time system evaluating the vibration signals and sending stop triggers to the test rig's control when a damage is detected. To avoid erroneous stop triggers the system evaluates the signals based on a given kinematic model. For this purpose also the torque signal (shaft vibration) and rotation speed is looped into the evaluation system. (appendix E)

CHAPTER 5. DESIGN AND DEVELOPMENT OF A TEST RIG FOR DYNAMIC TESTING UNDER HIGHLY TIME-VARIANT LOAD CHANGES

---

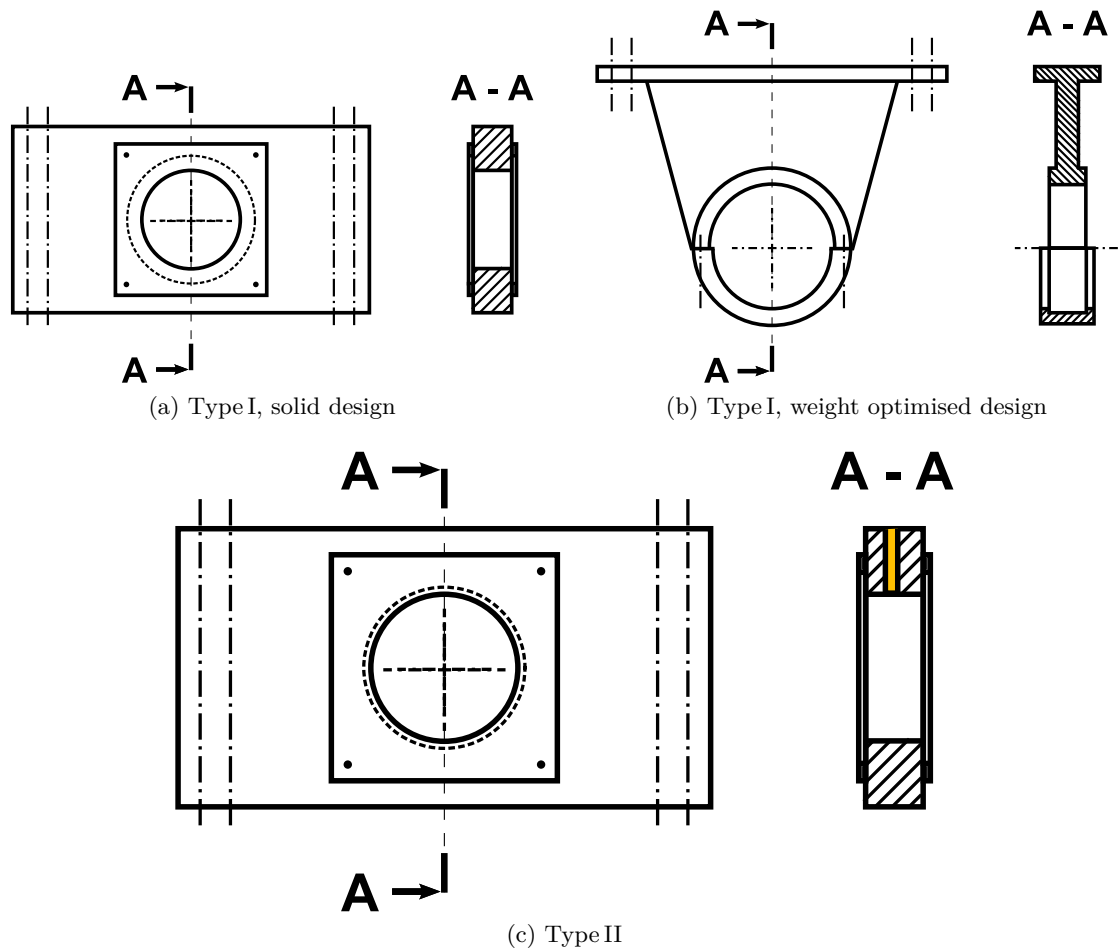


fig. 5.9.: Principle design of type I and type II brackets.



## CHAPTER 5. DESIGN AND DEVELOPMENT OF A TEST RIG FOR DYNAMIC TESTING UNDER HIGHLY TIME-VARIANT LOAD CHANGES

---

for this purpose.

**Oil Temperature Measurement** The temperature of the bearing lubrication and cooling is measured at the entrance and the exit of the system.

**Torque Measurement** In order to assess the change of friction over lifetime torque is measured. A torque sensor with a measuring frequency of 44 kHz can also double as a vibration sensor for the shaft at the same time.

### 5.8. Realisation of the Test Rig

Development and commissioning of the test-rig was outsourced to the INSTITUT FÜR ANGEWANDTE MATERIALIEN – WERKSTOFFKUNDE (IAM-WK) of the KARLSRUHE INSTITUTE OF TECHNOLOGY with the condition monitoring system being provided by DAIMLER AG. The final rig is depicted in fig.5.11. The superimposed numbers are explained as follows.

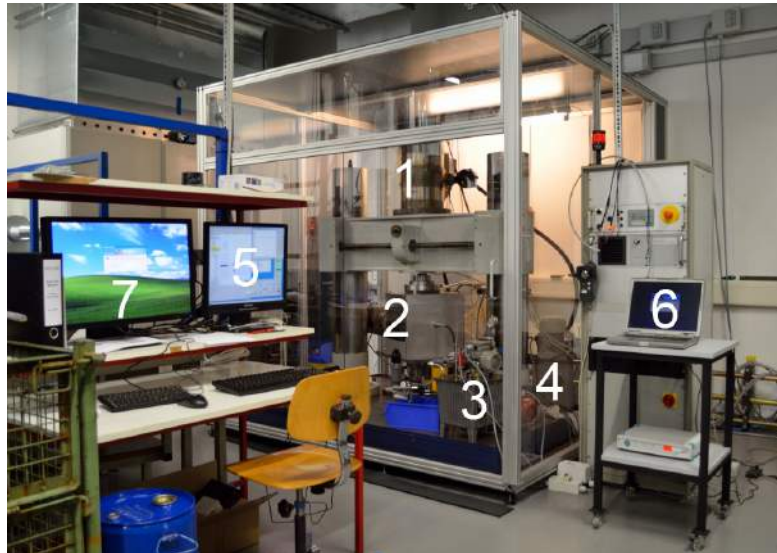


fig. 5.11.: The High Dynamic Bearing Tester (HighDy)

- (1) The test rig effectively controls the loads applied by an actuator onto rotating specimen shafts as a function of the shaft's rotational angle. All four radial bearings are identical and in theory equally loaded (5.10). Forces are applied by a hydraulic cylinder capable of 160 kN dynamic load. The hydraulic cylinder is embedded in a massive frame with very high stiffness in order to reduce elastic deformation of the frame, when forces are applied onto the bearings. Movement of the cylinder is displaced by a single voice-coil valve. The total forces onto the bearings are measured by a force transducer at the bottom of the testing chamber.

- (2) To rotate the specimen shafts a synchronous motor with an autonomous controller is employed. In the case of an error the automation control unit is capable of shutting off the power supply to the motor. Between shaft and motor a torque sensor and rotary encoder are installed. The torque sensor's main purpose is to monitor any rapid changes of torque e.g. due to shaft blocking and to observe possible degradation of bearing performance over long periods of time. The rotary encoder's primary function is to synchronise the force unit (1) with the angle of the specimen shaft. It is also needed to supply the solid-borne sound unit (7) with precise information of the shafts actual rotation speed which is needed to correctly evaluate the state of the bearings. A number of couplings ensure smooth operation and provide a mechanical fail safe in case of stuck shaft.
- (3) The lubrication unit consists of a tank and pumps for lubrication feeding and draining. A thermocouple for the feed oil and another thermocouple in a basin beneath the central bearings measure the oil temperature while it flows in and out of the bearings. Lubricant feeding can occur through holes in the bearing outer rings or sideways by injecting oil to the rolling elements. On the drain side various filter types can be attached prior the oil reaching the main filters. This allows for testing of different filter types, e.g. engine filters, and additional sensors, e.g. tracking oil degradation. The lubrication oil can be conditioned to temperatures of up to 120 °C
- (4) A cooling circuit for thermal conditioning purposes is also available. Conditioning occurs on the base of the bearing bracket seats and through the specimen shafts. For this a central drilling into the shafts can be machined.
- (5) The automation control unit synchronises the drive unit (2) with the actuator unit (1) and communicates with the solid-borne sound analysis system (7), which evaluates the NVH of test bearings and shaft upon the control unit's mark. The control unit consists of a real-time computer, which is interfaced by a regular, standard industry personal computer. It is also responsible for recording all sensory data, incoming and outgoing signals and states of process parameters. Among other sensory data this includes the displacement of the cylinder rod, the change of which over time can give clues to changes of bearing / shaft stiffness during prolonged periods of testing. Provisions are made for measuring the outer ring temperatures and lubricant temperature after passing the bearing. The sampling frequency of the real-time control loop is 25 kHz.
- (6) Each bearing bracket is mounted on stiff bearing seat, which encompass each a high dynamic strain gauge. These gauges allow sampling with 10 kHz. This enables the investigator to record and observe the behaviour of each bearing. Presently the strain gauges are connected to an independent system which records the forces on each bearing at the operators demand or at pre-defined points of time.
- (7) The solid-borne sound analysis system evaluates the vibrations of the bearings and the variation of the torque to assess the state of the bearings. The vibration

## CHAPTER 5. DESIGN AND DEVELOPMENT OF A TEST RIG FOR DYNAMIC TESTING UNDER HIGHLY TIME-VARIANT LOAD CHANGES

---

sensors are mounted on the bearings. For correct evaluation the signal of the rotary encoder is assessed as well. The system consists of its own real-time computer which is interfaced by another industrial standard PC. The real-time computer of the automation control unit (5) communicates with this PC and triggers the measurement and evaluation. During the measurement period a static load is applied to the bearings.

### 5.9. Preliminary Tests

Preliminary tests with the aim of assessing the performance of the test rig were carried out when an advanced state was reached. The test rig consisted at that point of the hydraulic cylinder capable of a dynamic force of 160 kN and a voice-coil valve. A test shaft made of 100Cr6 with diameter 66 mm was applied. Four RNU 211 bearings, lubricated from one face by a total oil volume of 2l/min, were used as test bearings. A thermo couple element was resistance welded onto the flange of bearing no. 3. The dynamic behaviour was tested with a sine force pattern not synchronised with the shaft. The shaft had been tempered to a hardness level common for bearing IRs. In addition to these sine loadings the shaft was tested with static loadings for 143 h at different rotation speeds and different loads ranging from 5-10 kN and 45-60 kN for the lower and upper loading respectively.

After this, the shaft was exhibiting severe micropittings respective grey staining – both as circumferential bands and as patches. Although neither lubrication conditions nor the forces on each bearing were strictly controlled, a first expectation can be formed by this test, for all raceways exhibit micropittings. An initial expectation for later experiments is formed that the EHL film does not establish properly at high loading frequencies.

During the static loadings a considerable heat generation is measured, which is in accordance with the expected friction power loss. To compensate latter issue oil conditioning focuses on conditioning by cooling. In addition to a cooling via bearing brackets also the specimen shafts are modified to contain drillings for cooling oil.

### 5.10. Functional Validation

The finalised test rig was tested with a set of integrated bearing brackets (chapter 5.6.2) and shafts made of tempered C56 E2 with a hardness of 61-62 HRC. As rolling bodies 100Cr6 rollers purchased from a bearing manufacturer was used. All four brackets are fed with a total of 2l/min 5w-30 engine oil at room temperature. The bracket raceways had been ground and honed. Total deviations in position and diameter of the bore are below 5  $\mu\text{m}$ . The shaft had been ground and band finished, as employed in current premium passenger car engines. The diameter deviation of all raceways was below 2  $\mu\text{m}$ . Assembly had been conducted with the greatest care and the shaft could be inserted through all four bearings without resistance despite a total radial clearance of 12  $\mu\text{m}$

only.

In the initial trials the central bearings were tightened rigidly to the actuator. Already after assembly with only little static loadings and without any shaft rotations large differences in load distribution among the bearings were measurable. Moreover, axial movements of the shafts was visible, which intensified with increased static loading. This is in accordance with observations of resulting axial forces due to radial forces acting on roller bearings bending the shaft. Slight differences in tolerances and position introduced during assembly of the specimen within the test rig lead to misalignments and axial forces. It is known from needle bearings that axial forces arise when radial loads bend the shaft on which the needles run [Sch12]. It is noteworthy that at constant loadings after a period of dynamic loading these axial movements intensify. Although this damage cannot be assigned to a specific period of operation of the test rig, it has been again observed after prolonged tests of successive dynamic and static loadings that grey staining occurs on the running bands.

In a second set of trials a ball joint was put between actuator and central bearings to level out the differences between the central bearings. All other test parameters were identical. New brackets and a new shaft were used. This also reduced the axial motions of the shafts, as the bending of the shaft was more symmetric. In static loading mode it could be observed, however that the load distribution between the central bearings are subject to sudden, reversible changes accompanied by axial motions synchronous to these internal load changes. It is concluded from this observation that a certain amount of unpredictable axial movements of the shafts cannot be suppressed, as changes of load distribution occur without any external interference. It is safe to assume that these distribution changes occur as an effect of changes in the pitch and alignment of the rolling bodies. The total nominal load over prolonged periods of time remains constant.

Two examples from the second trial will be outlined exemplary. The chosen conditions are worst case scenarios which rolling bearings may experience in petrol engines. The first example shows the bearing behaviour at constant load, while the second one reflects dynamic loading. Both tests have been conducted with the same set of roller bearings, shaft and other components.

In the first case the static load is equal to the peak load on crankshaft main bearings of a current 2.0l 4-cylinder engine. The shaft is turning with 3000 rpm. Sampling of the force gauge signals happen at 4.8 kHz. After elimination of aliasing effects an effective sampling rate of 480 Hz remains. In figure 5.12 0.5 seconds of recording are represented for the two central bearings. The average load on both bearings is approximately equal to the applied load, however, the load distribution between the central bearings and the outer bearings respectively is varying over time, albeit not as strong as in the initial trials. It is obvious that the nominal load of both bearings is 100%. Figure 5.13(a) exemplary shows the force signal of bearing two in the frequency domain. The given signal has been analysed over 20s. Figure 5.13(b) is a zoom-in showing the lack of other frequencies. An interesting fact is the lack of peaks around 100 Hz corresponding to the ripples visible in the time domain (fig. 5.12).

## CHAPTER 5. DESIGN AND DEVELOPMENT OF A TEST RIG FOR DYNAMIC TESTING UNDER HIGHLY TIME-VARIANT LOAD CHANGES

The second case is a test run with dynamic load, depicted in figs 5.14 and 5.15. As in case one the peak load is equal to the peak load of a current 2.0l 4-cylinder engine. The full-width-at-base time is slightly above 5 ms. Shorter times (almost 3 ms) had been established by changing parameters on the derivative part of the PID controller, however, post-pulse oscillation was deemed too high. As the caches of the valve do not seem to deplete over the course of time, a more careful setting of the controller should result in satisfying widths of less than 4 ms. The peak height of bearing three does not reach entirely the wanted height. Bearing three's loading curve indicate that there is a delay with respect to bearing two. This is visible at the recurring sudden change of the load curve steepness when bearing two exceeds the load of bearing three. Measurements over longer periods indicate that the load distribution does not change over time, however, different rotation speeds have an impact on the bearing with the strongest peaks, e.g. at 1500 rpm the peaks of bearing three are slightly higher than those of bearing two, which is an indication of resonance effects leading affecting the load curves. The deviation of force on each bearing is below 10 % and thus acceptable. An example is given in fig. 5.16. Note that in this figure the width of the peak is similar to the width shown in figure 5.15. During this operating mode no visually measurable axial movement is perceptible.

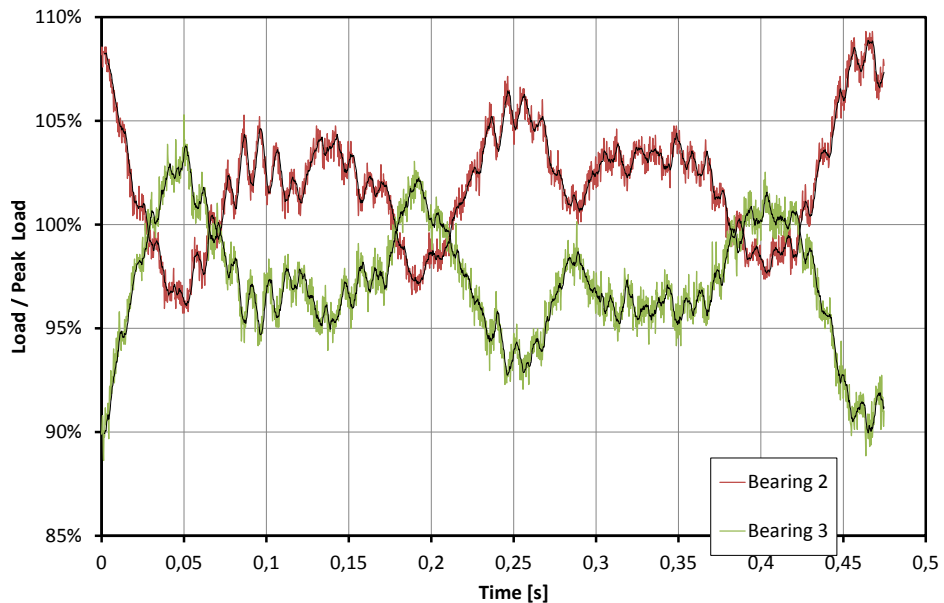


fig. 5.12.: Load distribution of the central roller bearings. The load is alternating between the two bearings, despite the same configuration. The outer bearings exhibit the same behaviour as the central bearings. For most of the time they follow the load curves of their respective central bearing (not depicted).

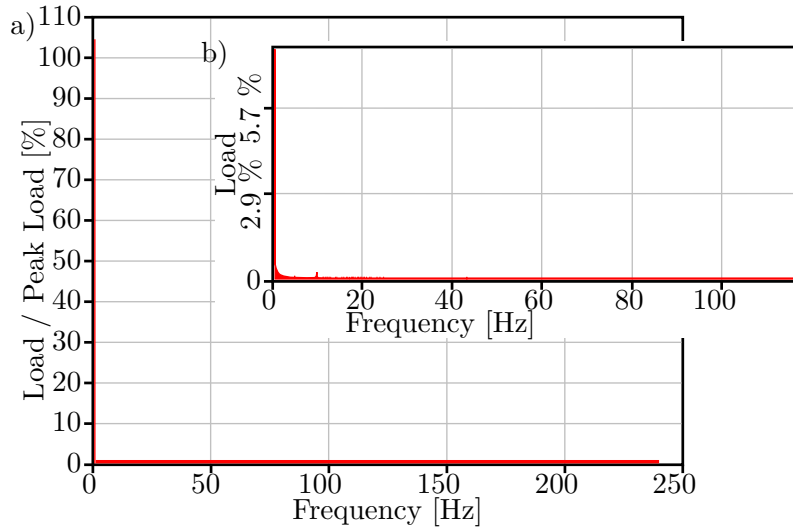


fig. 5.13.: Depiction of the data shown in figure 5.12 in the frequency domain. The alternating force signal of ca. 100 Hz in figure 5.12 is not reflected in the frequency domain. a) Spectrum till 250 Hz b) Magnification of a)

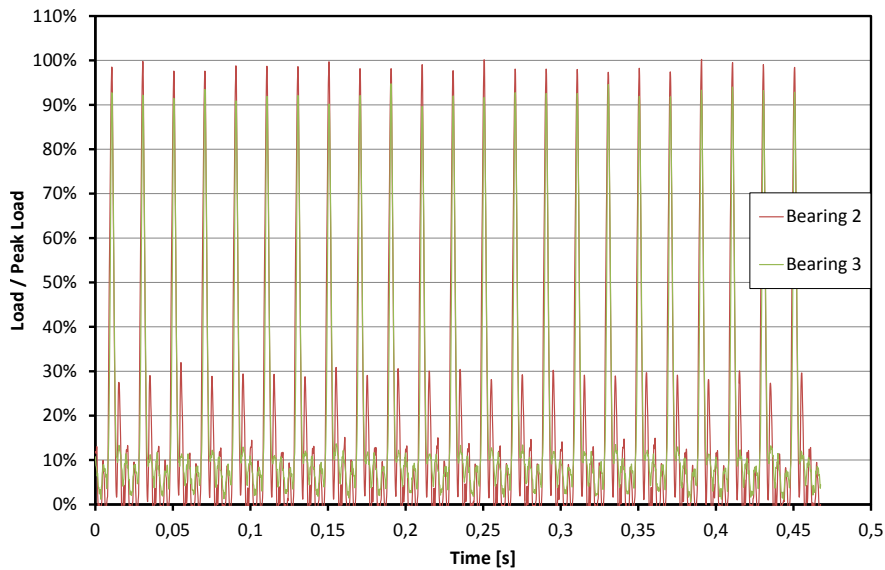


fig. 5.14.: Dynamic load distribution of the central bearings. Bearing 3 does not reach quite the peak load as bearing 2. Despite a slight variation of peak load visible it remains constant over prolonged periods. Parameters: 1 peak per revolution at 3000 rpm. Applied maximum load is equivalent to a current 2.0l 4-cylinder premium passenger car™ petrol engine.

## CHAPTER 5. DESIGN AND DEVELOPMENT OF A TEST RIG FOR DYNAMIC TESTING UNDER HIGHLY TIME-VARIANT LOAD CHANGES

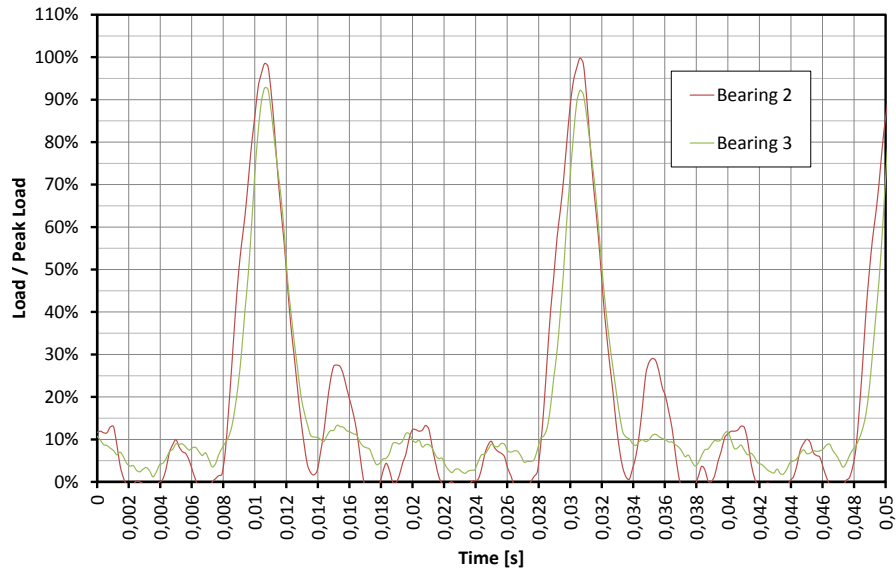


fig. 5.15.: Magnification of fig. 5.14. Bearing 3 exhibits a delayed response. It is currently unclear, whether this is a result of assembly tolerances or caused by the impulse response of the system.

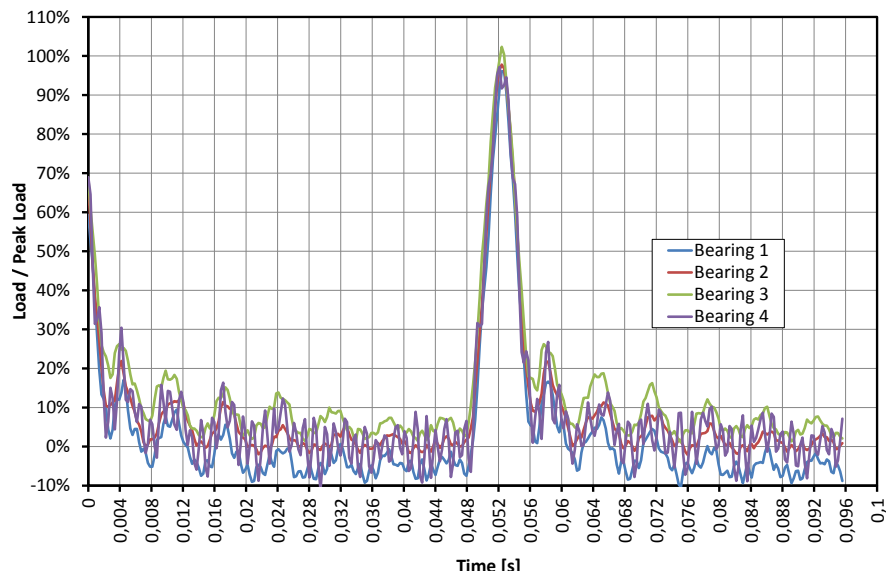


fig. 5.16.: Load distribution at 1500 rpm. All other parameters are identical to fig. 5.14. The PID controller is adjusted to lower speeds. Now bearing 3 exceeds bearing 2 in peak load indicating that the system might experience some oscillation.

## 5.11. Summary

In this chapter a unique test rig for investigation of repeated impact loads on bearings has been successfully proposed and put in operation. Most of the common testing methods focus on the performance of bearings at constant loading and the effect of lubrication under stationary elasto-hydrodynamic conditions. With the exception of the BTR test rig none of these rigs can be modified to specifically investigate the effects of repeated impacts on roller bearings. In order to investigate the effects of repeated impacts on roller bearings a test rig is designed in accordance to VDI design guidelines. As service lives of bearings in the VHCF regime becomes more and more common, special thought has been given by the choice of the appropriate actuator. The final design consists of a hydraulic cylinder with a single voice coil actuator and an automation control program designed for that purpose. As some applications in the field of combustion engine technology experience repeated impact loadings at the same spot, synchronisation of actuator and specimen shaft is established. All bearings are loaded with the same force with only little deviation caused by rotating speed dependent resonance effects. A number of various sensors have been provided in order to detect several expected failure mechanisms such as cold welding and subsurface failure. The most promising among them is a solid-borne sound analysis system. During the functional verification strong axial forces could be observed, albeit not measurable with the current set-up. These forces, although in accordance with literature, seem to increase after the shafts are exposed to impact loading. Also initial observations during preliminary tests and while executing verification of the test rig suggest that a careful choice of lubrication strategies might be needed, as the inner rings / shafts exhibit grey staining after short operating times.

## 6. Conclusion

Motivated by the possibilities of friction reduction at crankshafts and similar components currently supported by journal bearings this work investigates the rolling contact fatigue of hypoeutectoid bearing steels. Experiments conducted with shafts comprising of four raceways show that the primary failure mechanism at workshop conditions is pitting due to indentation by ductile metallic particles. These particles originate from production and assembly operations and cling to the surface of the components rather than entering the raceways during operation, as is generally assumed. Indentation must have occurred in a very early stage, as experiments with artificially introduced indentations show.

To determine the potential of classic rolling contact fatigue (subsurface failure) the material response is investigated, confirming that service life is truncated by indentations such that failures occur prior to reaching a ten percent rolling contact fatigue probability. As the material response to x-ray diffraction is linked to rolling contact failure mechanisms and structural changes within the stressed volume, it can be correlated to subsurface failure probability. This calibration can be used for diagnostic purposes of field damages and components from whole endurance tested units. It is used to develop a method for determining the dynamic capacity of any rolling bearing with individual bearings exhibiting orthogonal shear stress induced martensitic decay. Further more, a methodical approach to calculate the service time of an indented bearing is proposed taking into account that failures occur in the very high cycle fatigue regime.

Operating conditions of combustion engine components, especially on crankshafts, feature strong shock loads, otherwise avoided in rolling bearing applications. In order to understand the possible failure mechanisms occurring under such circumstances, a test rig is successfully designed. This test rig is capable of applying impact loads of magnitudes found in petrol engines. Preliminary tests are conducted with shafts which sustain under constant load the same bending as a crankshaft. Due to the advanced sensory information available it is determined that minor bending leads to severe axial loads. The preliminary tests also indicate that severe grey staining after a few hours of operation is possible indicating elasto-hydrodynamic lubrication challenges to be major failure conditions. Deviations of load from one bearing to another are below 10%. This is sufficient in terms of Hertzian contact stresses, however, improvement in load equality could be achieved by a 3-point configuration with two test specimen (fig. 5.7 (b)), however, with two load peaks per turn. Tests have proven that two peaks are easily possible with the current test rig.

Chapter Summary		
Chapter 3	Chapter 4	Chapter 5
Primary Failure: Indentation by soft, metallic particles	Classic Rolling Contact Fatigue $L_{10}$ not reached by most failed raceways.	Impact load excitation in the magnitude of crankshaft main bearings of passenger cars
Particle origin: bearing surface (not lubricant)	Shafts surpassing $L_{10}$ for RCF have seen very high loads and $\geq 2.5 \cdot 10^8$ cycles	use of a single voice coil valve instead of many servovalves to load four bearings
Indentation occurs within 1000 revolutions	XRD material response calibrated for material and available for diagnostics of field failures and endurance tested components	Force measurement of each bearing
Residual stresses near yield strength: slow crack propagation, but outweighed by crack sensitivity due local onset of plastification	Material response of C56 E2 is probably identical to 100Cr6 betraying identical carbon saturation in both grades	Axial loads originate from marginal differences in tolerance and shaft bending
Material Response: massive, arbitrary load differences on each raceway	Short crack propagation observed in decaying martensite. Propagation fits with angle of principal shear stress	Arbitrary radial load differences occur due to marginal geometrical variations, if not compensated
	A model and a methodology is proposed to describe crack initiation and propagation due indentation	Tribology damages observed on shaft during functional verification
	C56 E2 performs well enough	
	Butterfly formation inhibited due high compressive residual stresses	

tab. 6.1.: Tabular overview of chapters

The preceding chapters showed that the materials subsurface failure probability is very low even in the presence of poor lubrication and indentations. The experimentally determined fatigue life of the investigated C56 E2 shafts surpasses the expected service life of a passenger car even at loading conditions rather unlikely for prolonged periods for crankshaft bearings. In reality the bearings life will be shorter due to surface initiated failures. Therefore, future works for a successful application of rolling bearing within combustion engines should focus on the vibration/impact load behaviour of rolling bearings and the correct cleanliness conditions for bearings under such circumstances. In gearbox and even more so in aviation applications sophisticated nitrating process have been implemented in recent years combining the advantages of full steel bearing with the indentation resilience of ceramic bearings without the disadvantages generally found in nitrated surfaces.

Currently the trend for engine oils is towards lower viscosities. While the majority of

## CHAPTER 6. CONCLUSION

---

tribological components still have surface qualities with yet unexploited to accommodate extra stresses, rolling bearing surfaces are already highly optimised. Future works will have to concentrate on the near-surface and surface properties of dynamically loaded bearings. On the short run, thinner lubricants might become a temporary setback, but with ever increasing legal restrictions to emissions and steadily rising fuel prices they are still options with high potentials. It will be most exciting to see how this challenge will be mastered in the future.

## Appendix A.

### Cross Section of Bar Materials

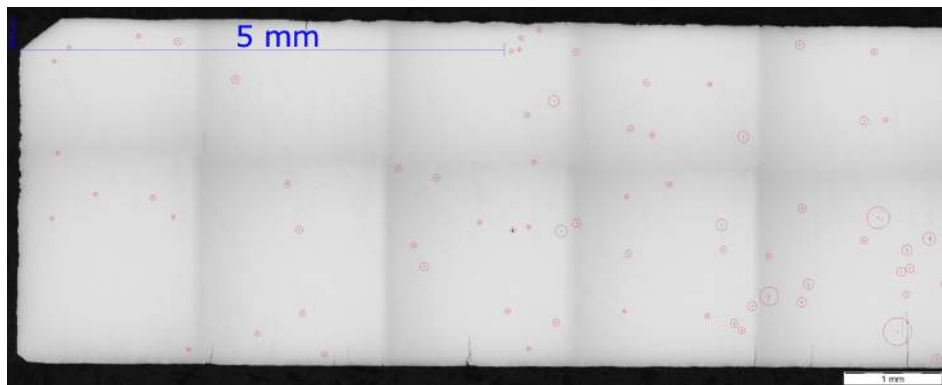


fig. A.1.: First few millimetres of a cross section of the used C56 E2 bar ( $\text{\O} 55 \text{ mm}$  ). The outer layer is on the left hand side. Cleanliness towards the core decreases further more.

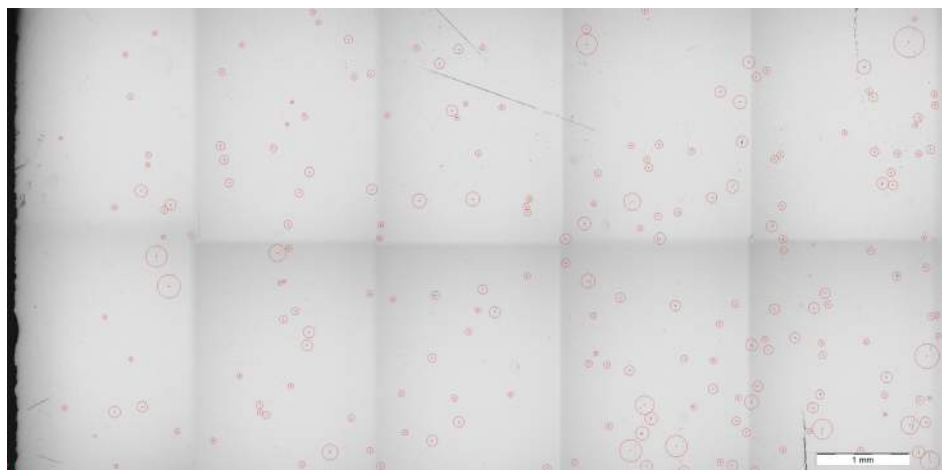


fig. A.2.: First few millimetres of a cross section of the C55V bar ( $\text{\O} 75 \text{ mm}$  ) from which the sample shafts were manufactured. The outer layer is on the left hand side. Unlike the C56 E2 this grade seems to have no very clean layers.

## Appendix B.

### Oil Analysis

It should be noted that particles in general are not spherical objects, but often oblong pieces. In general metallic pieces are micro-scaled chips from machining processes. An analysis of the particles in this particular case could not be conducted due to a technical problem. Metallic particles larger than 75  $\mu\text{m}$  have not been found to be suspended in the oil. They may exist, but the presence of such particles will be singular events.

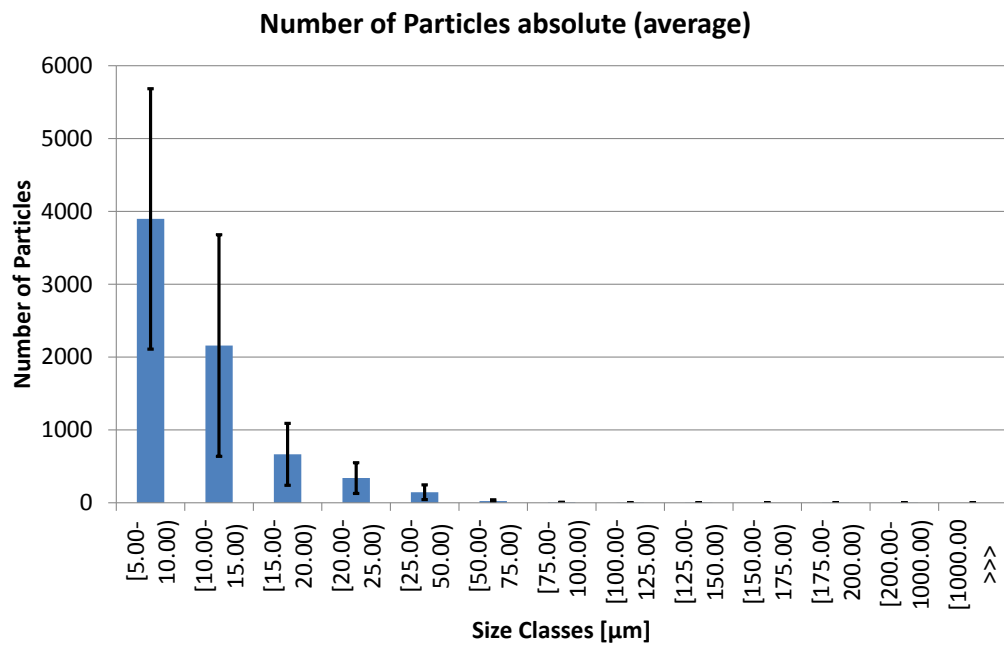


fig. B.1.: The average distribution of particles per test head. The amount of particles with sizes larger or equal to 100  $\mu\text{m}$  is almost not existing.

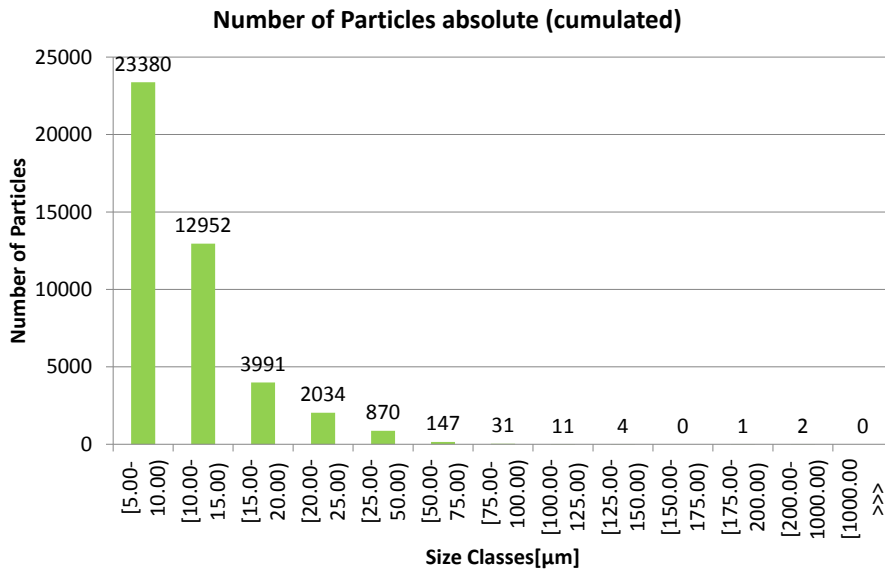


fig. B.2.: The distribution of particles cumulated over all samples. The amount of particles with sizes larger or equal to 100 μm is very small. If the particles detected would be metallic, they would account for the origin of particles.

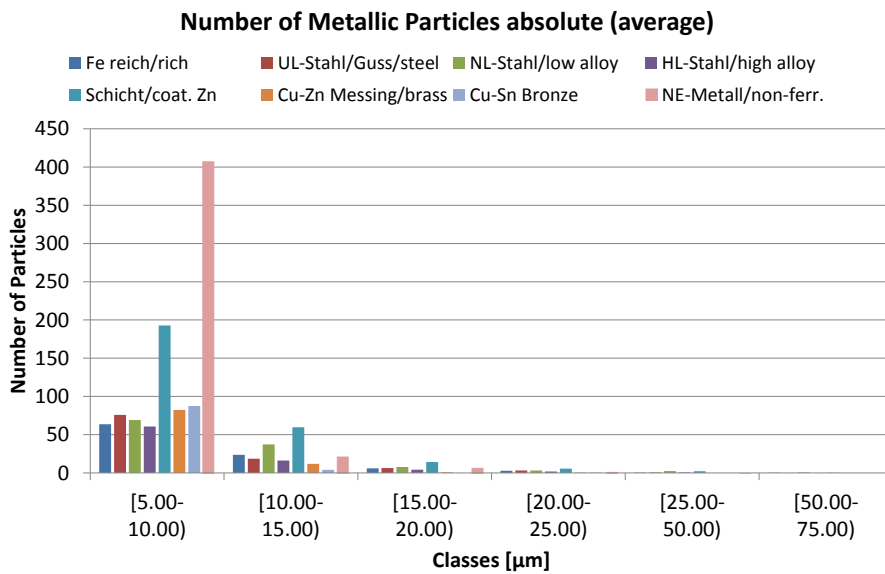


fig. B.3.: The average distribution of metallic particles suspended in the samples. Classes larger than 50-75 μm have been omitted, as no particles could be found.

## Appendix C.

### Bearing Cleanliness Analysis

The cleanliness of the bearings of the type RNU 206 ECP has been analysed. 'RNU' is the designation for NU bearings delivered without IR.

**The cleanliness of the ready-made and cleaned bearings is very high and can be termed as *'technically clean'*.** Cleaning of bearings beyond this point is possible under laboratory conditions, however, is not feasible in a technical environment without tremendous efforts.

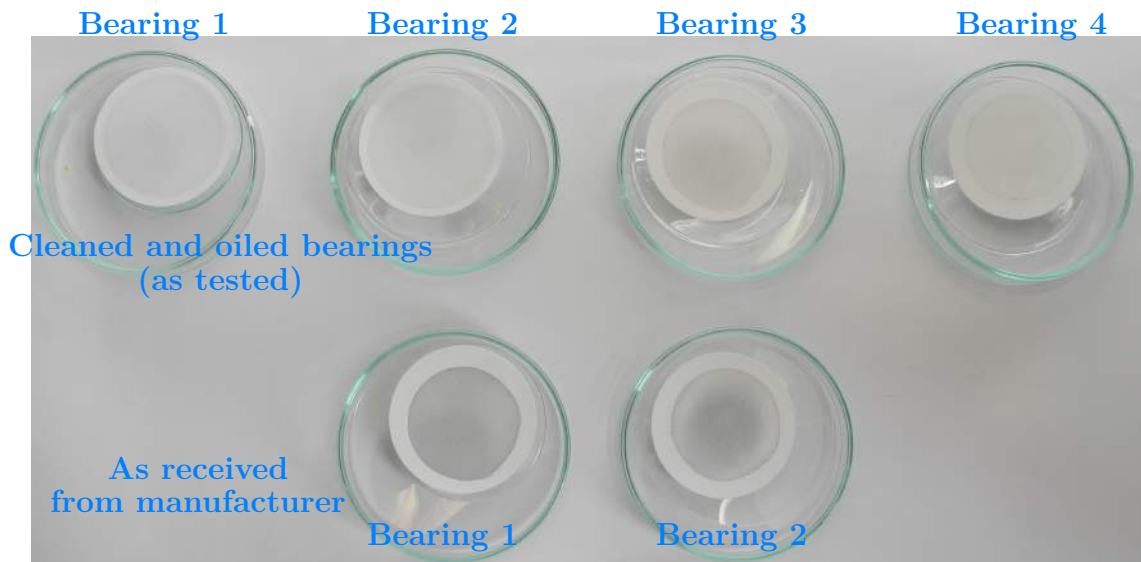


fig. C.1.: Visual impression of bearing cleanliness.

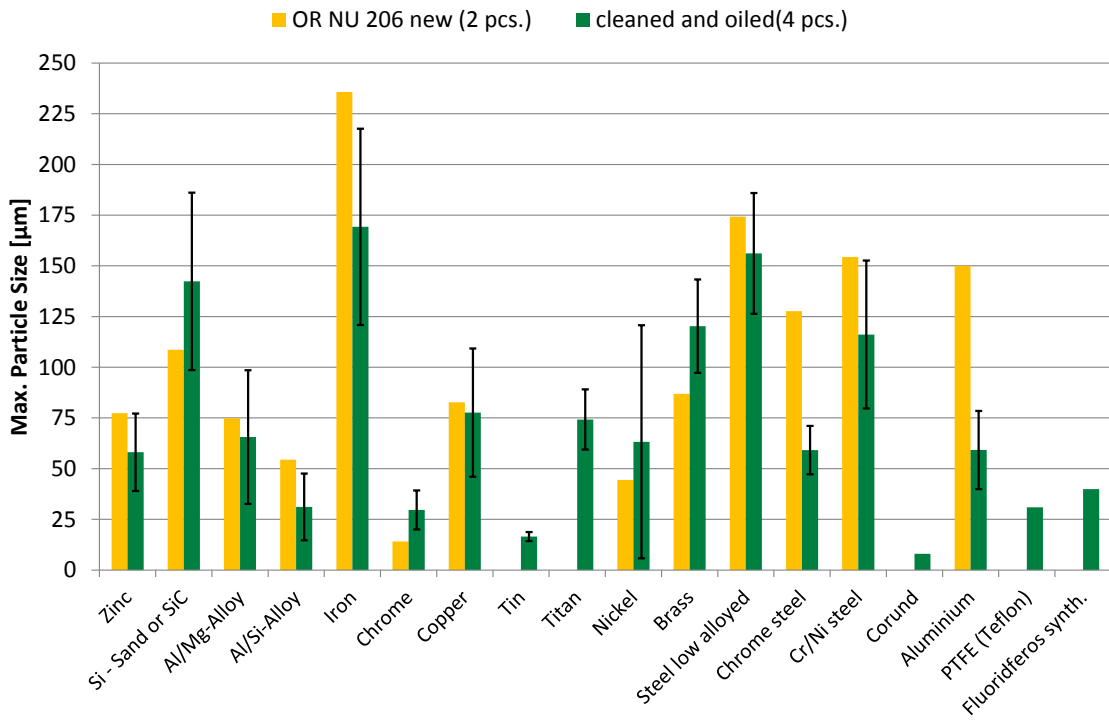


fig. C.2.: Maximum particle size of different metallic particles found.

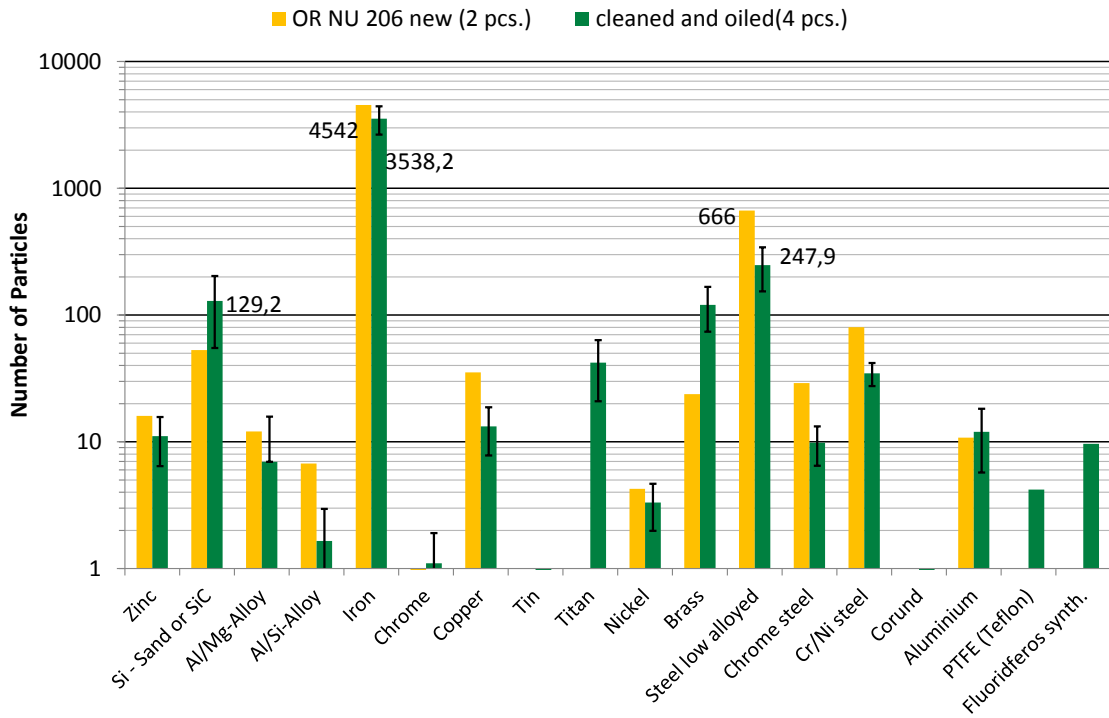


fig. C.3.: Number of particles found per different metallic particles found.

APPENDIX C. BEARING CLEANLINESS ANALYSIS

Sum of new RNU 206 ECP										
Particle Type	Number	Max. Particle size [µm]	25 to 50 µm	50 to 100 µm	100 to 150 µm	150 to 200 µm	200 to 400 µm	400 to 600 µm	600 to 1000 µm	>1000 [µm]
Zinc	32	155	29	2	1	0	0	0	0	0
Si - Sand or SiC	106	217	94	11	1	0	0	0	0	0
Al/Mg alloy	24	150	16	6	2	0	0	0	0	0
Al/Si alloy	14	109	10	4	0	0	0	0	0	0
Iron	9084	472	8364	686	24	7	4	0	0	0
Chrome	1	28	1	0	0	0	0	0	0	0
Copper	71	165	54	17	0	0	0	0	0	0
Tin	0	0	0	0	0	0	0	0	0	0
Titan	0	0	0	0	0	0	0	0	0	0
Nickel	9	89	9	0	0	0	0	0	0	0
Brass	48	174	38	9	1	0	0	0	0	0
Steel low alloyed	1333	349	1138	184	10	0	1	0	0	0
Chrome steel	58	255	48	7	2	0	0	0	0	0
Cr/Ni steel	160	309	118	37	4	1	0	0	0	0
Corund	0	0	0	0	0	0	0	0	0	0
Aluminium	22	300	14	6	0	0	1	0	0	0
PTFE	0	0	0	0	0	0	0	0	0	0
Fluoridferos synth.	0	0	0	0	0	0	0	0	0	0
Totals	10978	472	9932	967	45	8	6	0	0	0

Average of new RNU 206 ECP

Particle Type	Amount	Max. Particle Size [µm]	Particle Size [µm]										
			25 to 50 µm	50 to 100 µm	100 to 150 µm	150 to 200 µm	200 to 400 µm	400 to 600 µm	600 to 1000 µm	>1000 µm			
Zinc	16	77	15	1	1	0	0	0	0	0	0	0	0
Si - Sand or SiC	53	109	47	5	1	0	0	0	0	0	0	0	0
Al/Mg-Alloy	12	75	8	3	1	0	0	0	0	0	0	0	0
Al/Si-Alloy	7	54	5	2	0	0	0	0	0	0	0	0	0
Iron	4542	236	4182	343	12	4	2	0	0	0	0	0	0
Chrome	1	14	1	0	0	0	0	0	0	0	0	0	0
Copper	35	83	27	9	0	0	0	0	0	0	0	0	0
Tin	0	0	0	0	0	0	0	0	0	0	0	0	0
Titan	0	0	0	0	0	0	0	0	0	0	0	0	0
Nickel	4	44	4	0	0	0	0	0	0	0	0	0	0
Brass	24	87	19	4	1	0	0	0	0	0	0	0	0
Steel low alloyed	666	174	569	92	5	0	1	0	0	0	0	0	0
Chrome steel	29	128	24	4	1	0	0	0	0	0	0	0	0
Cr/Ni steel	80	154	59	18	2	1	0	0	0	0	0	0	0
Corund	0	0	0	0	0	0	0	0	0	0	0	0	0
Aluminium	11	150	7	3	0	0	1	0	0	0	0	0	0
PTFE (Teflon)	0	0	0	0	0	0	0	0	0	0	0	0	0
Fluoridferos synth.	0	0	0	0	0	0	0	0	0	0	0	0	0
Totals	5489	236	4966	484	23	4	3	0	0	0	0	0	0

APPENDIX C. BEARING CLEANLINESS ANALYSIS

Sum of cleaned and oiled RNU 206 ECP																		
Particle Type	Amount	Max. Particle Size [µm]	25 to 50 µm		50 to 100 µm		100 to 150 µm		150 to 200 µm		200 to 400 µm		400 to 600 µm		600 to 1000 µm		>1000 µm	
			50 µm	100 µm	150 µm	200 µm	200 µm	400 µm	400 µm	600 µm	600 µm	1000 µm	1000 µm	>1000 µm				
Zinc	44	232	38	6	0	0	0	0	0	0	0	0	0	0	0	0	0	0
Si - Sand or SiC	517	569	441	69	5	2	1	0	0	0	0	0	0	0	0	0	0	0
Al/Mg-Alloy	28	262	23	5	0	0	0	0	0	0	0	0	0	0	0	0	0	0
Al/Si-Alloy	7	124	6	1	0	0	0	0	0	0	0	0	0	0	0	0	0	0
Iron	14153	677	13388	744	18	2	1	0	0	0	0	0	0	0	0	0	0	0
Chrome	4	119	4	0	0	0	0	0	0	0	0	0	0	0	0	0	0	0
Copper	53	310	46	6	1	0	0	0	0	0	0	0	0	0	0	0	0	0
Tin	2	66	2	0	0	0	0	0	0	0	0	0	0	0	0	0	0	0
Titan	169	297	140	28	0	0	0	0	0	0	0	0	0	0	0	0	0	0
Nickel	13	253	12	0	1	0	0	0	0	0	0	0	0	0	0	0	0	0
Brass	482	481	395	75	13	1	0	0	0	0	0	0	0	0	0	0	0	0
Steel low alloyed	991	625	849	129	8	3	0	0	0	0	0	0	0	0	0	0	0	0
Chrome steel	39	236	35	4	0	0	0	0	0	0	0	0	0	0	0	0	0	0
Cr/Ni steel	139	465	122	14	3	0	0	0	0	0	0	0	0	0	0	0	0	0
Corund	2	32	2	0	0	0	0	0	0	0	0	0	0	0	0	0	0	0
Aluminium	48	237	44	4	0	0	0	0	0	0	0	0	0	0	0	0	0	0
Teflon	17	124	10	6	1	0	0	0	0	0	0	0	0	0	0	0	0	0
Fluorid cont. synth.	39	160	28	10	0	1	0	0	0	0	0	0	0	0	0	0	0	0
Totals	16746	736	15586	1099	51	9	2	0	0	0	0	0	0	0	0	0	0	0

**Average of cleaned and oiled RNU 206 ECP**

Particle Type	Amount	Max. Particle Size [µm]	25 to		50 to		100 to		150 to		200 to		400 to		600 to		>1000 µm	
			50 µm	100 µm	150 µm	200 µm	200 µm	400 µm	400 µm	600 µm	600 µm	1000 µm	1000 µm	>1000 µm				
Zinc	11,1	58,1	9,6	1,5	0,0	0,0	0,0	0,0	0,0	0,0	0,0	0,0	0,0	0,0	0,0	0,0	0,0	0,0
Si - Sand or SiC	129,2	142,3	110,2	17,2	1,4	0,5	0,3	0,0	0,0	0,0	0,0	0,0	0,0	0,0	0,0	0,0	0,0	0,0
Al/Mg-Alloy	7,0	65,6	5,6	1,2	0,0	0,0	0,0	0,0	0,0	0,0	0,0	0,0	0,0	0,0	0,0	0,0	0,0	0,0
Al/Si-Alloy	1,7	31,1	1,4	0,3	0,0	0,0	0,0	0,0	0,0	0,0	0,0	0,0	0,0	0,0	0,0	0,0	0,0	0,0
Iron	3538,2	169,2	3346,9	186,1	4,6	0,6	0,3	0,0	0,0	0,0	0,0	0,0	0,0	0,0	0,0	0,0	0,0	0,0
Chrome	1,1	29,6	1,1	0,0	0,0	0,0	0,0	0,0	0,0	0,0	0,0	0,0	0,0	0,0	0,0	0,0	0,0	0,0
Copper	13,3	77,6	11,6	1,4	0,3	0,0	0,0	0,0	0,0	0,0	0,0	0,0	0,0	0,0	0,0	0,0	0,0	0,0
Tin	0,6	16,5	0,6	0,0	0,0	0,0	0,0	0,0	0,0	0,0	0,0	0,0	0,0	0,0	0,0	0,0	0,0	0,0
Titan	42,1	74,3	34,9	7,1	0,0	0,0	0,0	0,0	0,0	0,0	0,0	0,0	0,0	0,0	0,0	0,0	0,0	0,0
Nickel	3,3	63,2	3,0	0,0	0,3	0,0	0,0	0,0	0,0	0,0	0,0	0,0	0,0	0,0	0,0	0,0	0,0	0,0
brass	120,5	120,3	98,7	18,6	3,2	0,3	0,0	0,0	0,0	0,0	0,0	0,0	0,0	0,0	0,0	0,0	0,0	0,0
Steel low alloyed	247,9	156,2	212,2	32,3	2,1	0,8	0,0	0,0	0,0	0,0	0,0	0,0	0,0	0,0	0,0	0,0	0,0	0,0
Chrome steel	9,9	59,1	8,8	1,1	0,0	0,0	0,0	0,0	0,0	0,0	0,0	0,0	0,0	0,0	0,0	0,0	0,0	0,0
Cr/Ni steel	34,7	116,1	30,5	3,4	0,9	0,0	0,0	0,0	0,0	0,0	0,0	0,0	0,0	0,0	0,0	0,0	0,0	0,0
Corund	0,6	8,0	0,6	0,0	0,0	0,0	0,0	0,0	0,0	0,0	0,0	0,0	0,0	0,0	0,0	0,0	0,0	0,0
Aluminium	12,0	59,2	10,9	1,1	0,0	0,0	0,0	0,0	0,0	0,0	0,0	0,0	0,0	0,0	0,0	0,0	0,0	0,0
Teflon	4,2	30,9	2,4	1,5	0,3	0,0	0,0	0,0	0,0	0,0	0,0	0,0	0,0	0,0	0,0	0,0	0,0	0,0
Fluorid cont. synth.	9,6	39,9	6,9	2,4	0,0	0,3	0,0	0,0	0,0	0,0	0,0	0,0	0,0	0,0	0,0	0,0	0,0	0,0

## Appendix D.

### Equation Hertzian Solutions

Johnson [Joh85] states solutions for the integrals, which Hertz formulated in [Her81, Her82] (a version with English nomenclature and thus more understandable to modern minds is found in [Her96]):

For line contact the solutions are as follows:

The effective radius  $R$  and effective elastic modulus  $E^*$  for the contact of two cylinders is

$$\frac{1}{E^*} = \frac{1 - \nu_1^2}{E_1} + \frac{1 - \nu_2^2}{E_2} \quad (\text{D.1})$$

$$\frac{1}{R} = \frac{1}{R_1} + \frac{1}{R_2} \quad (\text{D.2})$$

The contact half-width  $a$  is

$$a = \sqrt{\frac{4PR}{\pi E^*}} \quad (\text{D.3})$$

With  $P$  being the force per contact length. The maximum hertzian contact stress (pressure) is

$$p_{max} = \sqrt{\frac{PE^*}{\pi R}} \quad (\text{D.4})$$

At the contact point  $x = 0$  the stresses are given by :

$$\sigma_x = -\frac{p_{max}}{a} \left( \frac{a^2 + 2z^2}{\sqrt{a^2 + z^2}} - 2z \right) \quad (\text{D.5})$$

$$\sigma_z = \frac{p_{max}}{a} (a^2 + z^2)^{-1/2} \quad (\text{D.6})$$

$$\sigma_y = \nu(\sigma_x + \sigma_z) \quad (\text{D.7})$$

---

These are principal stresses, so that the principal shear stress is given by

$$\tau_1 = \frac{p_{max}}{a} \left( z - z^2(a^2 + z^2)^{-1/2} \right) \quad (D.8)$$

from which

$$(\tau_1)_{max} = 0.3p_{max}, \quad \text{at} \quad z = 0.78a \quad (D.9)$$

For  $x \neq 0$ :

$$m^2 = \frac{1}{2} \left[ \sqrt{(a^2 - x^2 + z^2)^2 + 4x^2z^2} + (a^2 - x^2 + z^2) \right] \quad (D.10)$$

$$n^2 = \frac{1}{2} \left[ \sqrt{(a^2 - x^2 + z^2)^2 + 4x^2z^2} - (a^2 - x^2 + z^2) \right] \quad (D.11)$$

With  $m$  and  $n$  being

$$m = \text{sign}(z)\sqrt{m^2}, \quad \text{and} \quad n = \text{sign}(x)\sqrt{n^2} \quad (D.12)$$

$$\sigma_x = -\frac{p_{max}}{a} \left[ m \left( 1 + \frac{z^2 + n^2}{m^2 + n^2} \right) - 2z \right] \quad (D.13)$$

$$\sigma_z = -\frac{p_{max}}{a} m \left( 1 - \frac{z^2 + n^2}{m^2 + n^2} \right) \quad (D.14)$$

$$\tau_{xz} = -\frac{p_{max}}{a} n \left( \frac{m^2 - z^2}{m^2 + n^2} \right) \quad (D.15)$$

A rolling contact with sliding is principally a non-hertzian contact as there are additional deformations caused by shear stresses in the contact area.

The traction force is

$$q_{max} = -\mu p_{max} \quad (D.16)$$

There are some analogies between traction forces and normal forces. They can be expressed by:

$$\frac{(\sigma_z)_q}{q_{max}} = \frac{(\tau_{xz})_p}{p_{max}} \quad (D.17)$$

$$\frac{(\tau_{xz})_q}{q_{max}} = \frac{(\sigma_x)_p}{p_{max}} \quad (D.18)$$

The  $\sigma_x$  component due traction is given by:

$$(\sigma_x)_q = \frac{q_{max}}{a} \left[ n \left( 2 - \frac{z^2 - m^2}{m^2 + n^2} \right) - 2x \right] \quad (D.19)$$

## APPENDIX D. EQUATION HERTZIAN SOLUTIONS

---

To visualise the stress distribution beneath the surface of the specimen shafts maps of the stress distribution are created with Matlab vers. 2010b:

For  $\mu = 0$ :

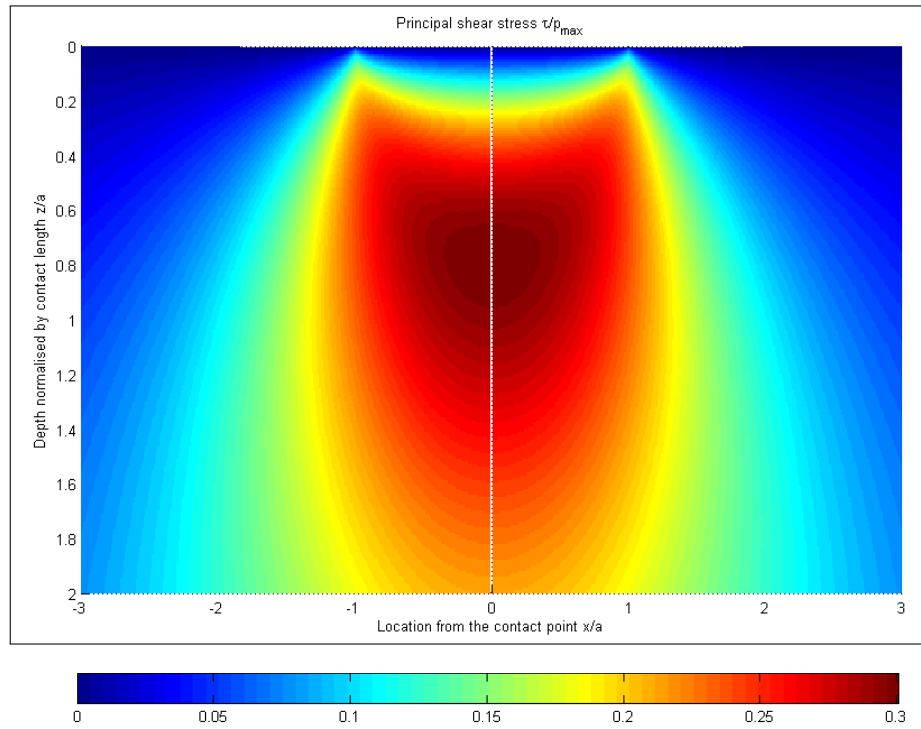


fig. D.1.: Principal shear stress  $\tau_1$  for  $\mu = 0$

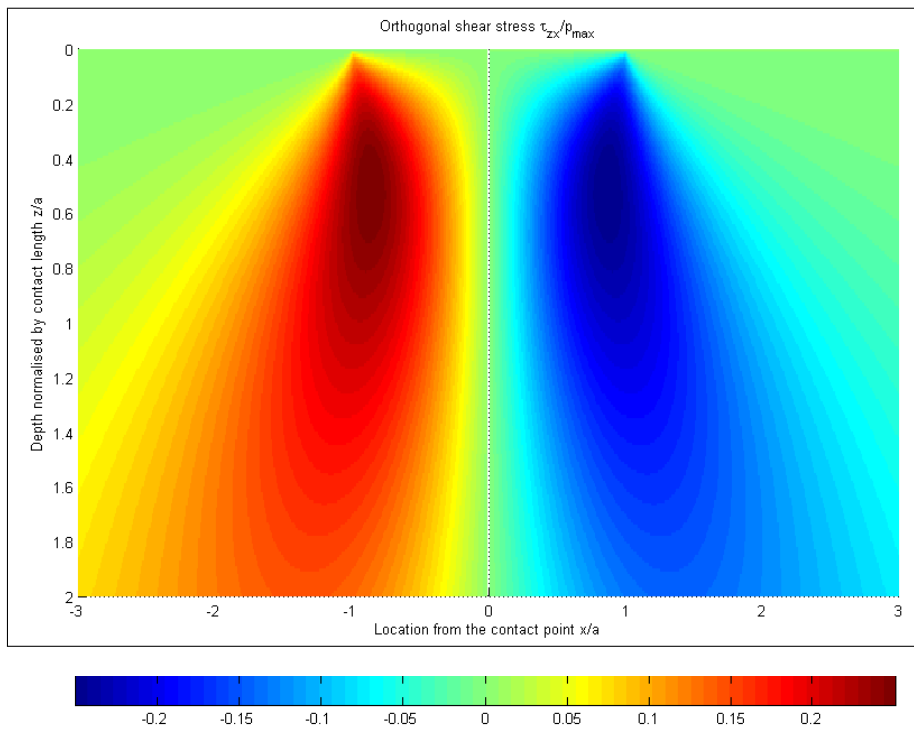


fig. D.2.: Orthogonal shear stress  $\tau_{xz}$  for  $\mu = 0$

## APPENDIX D. EQUATION HERTZIAN SOLUTIONS

---

For  $\mu = 0.05$ :

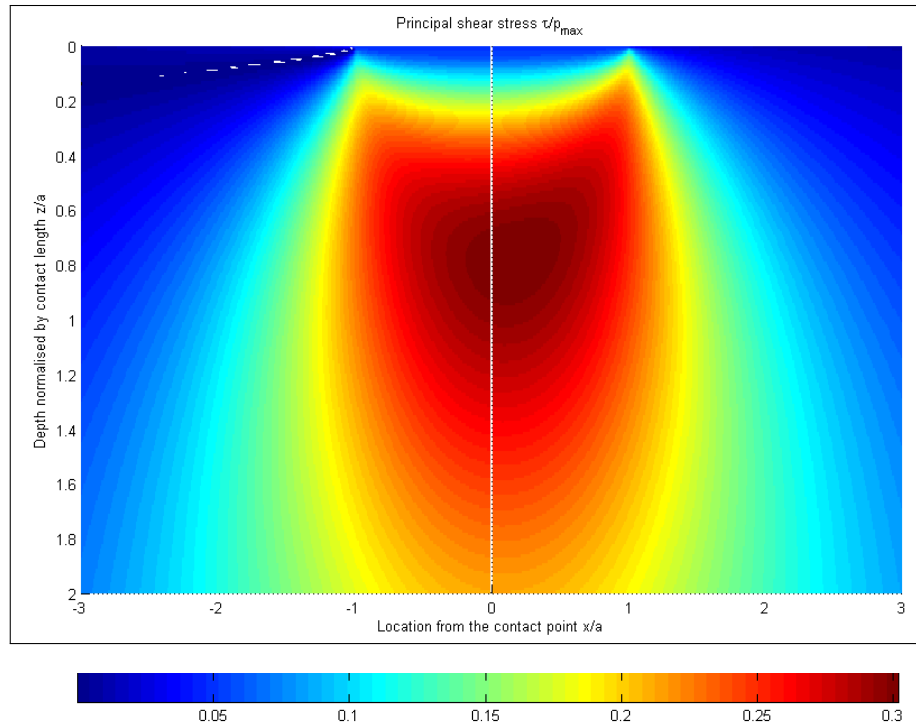


fig. D.3.: Principal shear stress  $\tau_1$  for  $\mu = 0.05$

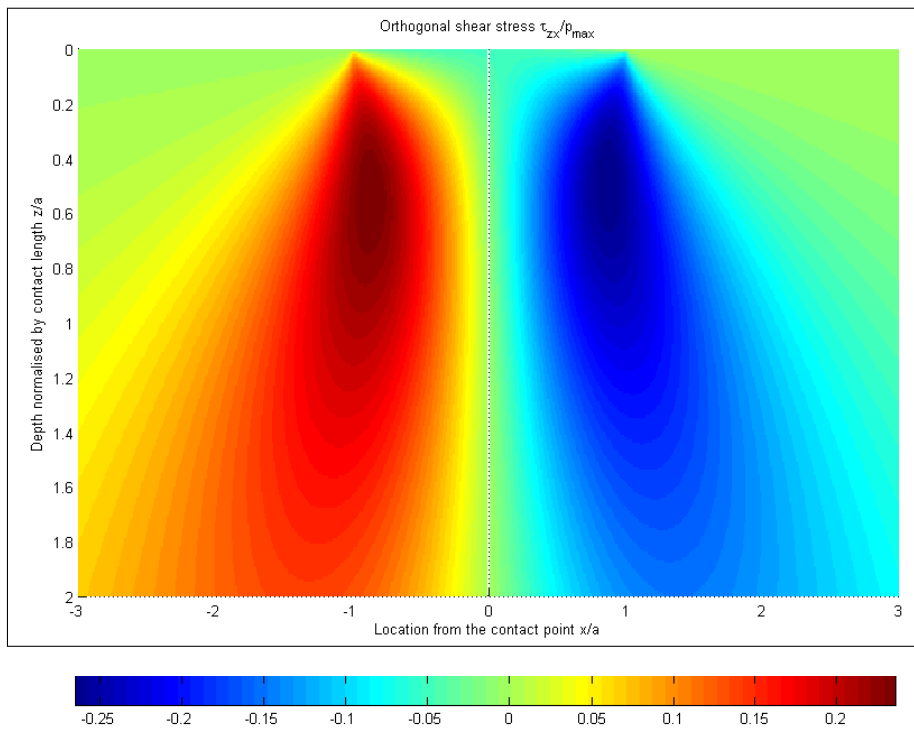


fig. D.4.: Orthogonal shear stress  $\tau_{xz}$  for  $\mu = 0.05$

## APPENDIX D. EQUATION HERTZIAN SOLUTIONS

---

For  $\mu = 0.2$ :

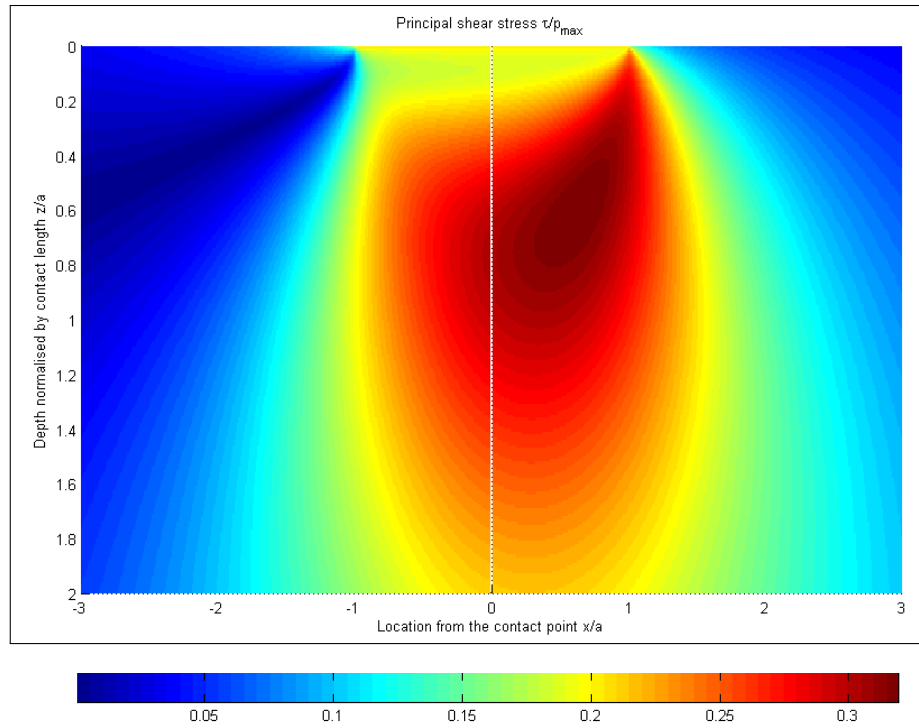


fig. D.5.: Principal shear stress  $\tau_1$  for  $\mu = 0.2$

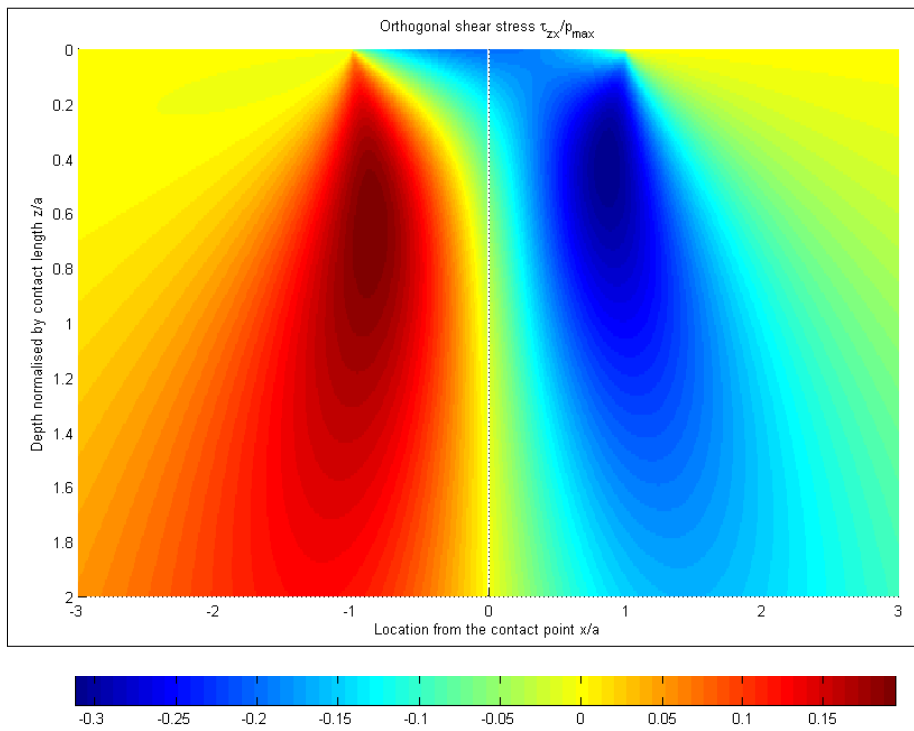


fig. D.6.: Orthogonal shear stress  $\tau_{xz}$  for  $\mu = 0.2$

## Appendix E.

### Bearing Kinematic Formulas

The given formulas can be easily deduced by geometric considerations. They are also found in [Sch09]

#### Rotation Frequencies

Frequency IR n [1/min]:

$$f_i = \frac{n \text{ min}}{60 \text{ s}} \quad (\text{E.1})$$

Frequency OR:

$$0$$

Frequency Cage:

$$f_c = \frac{1}{2} f_i \left( 1 - \frac{D_W}{D_{\rho W}} \right) \quad (\text{E.2})$$

Frequency Rolling bodies:

$$f_w = \frac{1}{2} f_i \frac{D_{\rho W}}{D_W} \left( 1 - \left( \frac{D_W}{D_{\rho W}} \right)^2 \right) \quad (\text{E.3})$$

#### Defect Frequencies

OR:

$$f_{da} = f_c \cdot Z \quad (\text{E.4})$$

IR:

$$f_{di} = \frac{1}{2} f_i Z \left( 1 + \frac{D_W}{D_{\rho W}} \right) \quad (\text{E.5})$$

Rolling Bodies:

$$f_{dw} = 2 \cdot f_w \quad (\text{E.6})$$

## Bibliography

- [ASTM2283] ASTM STANDARD 2283, 2008: *Extreme Value Analysis of Nonmetallic Inclusions in Steel and Other Microstructural Features*. 02 2008
- [ASTME45] ASTM STANDARD E45, 2011: *Standard Test Methods for Determining the Inclusion Content of Steel*. 02 2011
- [BAM06] BERETTA, Stefano ; ANDERSON, Clive ; MURAKAMI, Yukitaka: Extreme value models for the assessment of steels containing multiple types of inclusion. In: *Acta Materialia* 54 (2006), Nr. 8, S. 2277 – 2289. – ISSN 1359–6454
- [Bat10] BATHIAS, C.: Gigacycle fatigue properties of bearing steels. In: *Bearing Steel Technology* Bd. 1524 STP. Vancouver, BC, 2010. – ISBN 9780803175105, S. 160–178. – Conference of ASTM 8th International Symposium on Bearing Steel Technology: Developments in Rolling Bearing Steels and Testing; Conference Date: 21 May 2009 through 22 May 2009; Conference Code: 82407
- [Bat12] BATHIAS, C.: Gigacycle Fatigue: A New Tool for Exploring Bearing Steel. In: [Bat10], S. 160–178. – Conference of ASTM 8th International Symposium on Bearing Steel Technology: Developments in Rolling Bearing Steels and Testing; Conference Date: 21 May 2009 through 22 May 2009; Conference Code: 82407
- [BB01] BOLOTIN, V.V. ; BELOUSOV, I.L.: Early fatigue crack growth as the damage accumulation process. In: *Probabilistic Engineering Mechanics* 16 (2001), Nr. 4, S. 279 – 287. – ISSN 0266–8920
- [BGG11] BRÜCKNER, M. ; GEGNER, J. ; GRABULOV, A. ; NIERLICH, W.: Butterfly Formation Mechanisms in Rolling Contact Fatigue. In: BERGER, C. (Hrsg.) ; CHRIST, H.-J. (Hrsg.) ; German Association for Materials Research and Testing (DVM) (Veranst.): *Proceedings of the 5th International Conference on Very High Cycle Fatigue* German Association for Materials Research and Testing (DVM), 2011, S. 101–106
- [BLP07] BRUNETTI, C. ; LEITE, M.V. ; PINTAUDE, G.: Effect of specimen preparation on contact fatigue wear resistance of austempered ductile cast iron. In: *Wear* 263 (2007), Nr. 1-6 SPEC. ISS., S. 663–668. – ISSN 00431648 (ISSN)

## Bibliography

---

- [BM98] BERETTA, S.a ; MURAKAMI, Y.b: Statistical analysis of defects for fatigue strength prediction and quality control of materials. In: *Fatigue and Fracture of Engineering Materials and Structures* 21 (1998), Nr. 9, S. 1049–1065. – ISSN 8756758X
- [BM01] BERETTA, S. ; MURAKAMI, Y.: Largest-extreme-value distribution analysis of multiple inclusion types in determining steel cleanliness. In: *Metallurgical and Materials Transactions B* 32 (2001), S. 517–523. – ISSN 1073–5615
- [BSA14] BHATTACHARYYA, Abir ; SUBHASH, Ghatu ; ARAKERE, Nagaraj: Evolution of subsurface plastic zone due to rolling contact fatigue of M-50 NiL case hardened bearing steel. In: *International Journal of Fatigue* 59 (2014), Nr. 0, S. 102 – 113. – ISSN 0142–1123
- [Buc15] BUCHMILLER, Viktor: *Wälzgelagerter Kurbeltrieb – Potential von Wälzlagern im Verbrennungsmotor*, Technische Universität Kaiserslautern, Diss., 2015
- [CCK94] CHENG, W. ; CHENG, H. S. ; KEER, L. M.: Longitudinal Crack Initiation Under Pure Rolling Contact Fatigue. In: *Tribology Transactions* 37 (1994), S. 51 – 58
- [CM06] CIAVARELLA, M. ; MONNO, F.: On the possible generalizations of the Kitagawa - Takahashi diagram and of the El Haddad equation to finite life. In: *International Journal of Fatigue* 28 (2006), Nr. 12, S. 1826 – 1837. – ISSN 0142–1123
- [CY12] CHOI, Youngsik ; YANG, Xiaoping: Impact evaluation of rolling contact fatigue life models. In: *Journal of Mechanical Science and Technology* 26 (2012), Nr. 6, S. 1865–1873. – ISSN 1738–494X
- [DH61] DOWSON, D. ; HIGGINSON, G.R.: New roller-bearing lubrication formula. In: *Eng. London* 158 (1961)
- [DIN50602] DIN 50602:1985-9: *Mikroskopische Prüfung von Edelstählen auf nicht-metallische Einschlüsse mit Bildreihen*. 09 1985
- [DIN51819a] DIN 51819-1:1999-12: *Testing of Lubricants – Mechanical-dynamic testing in the roller bearing test apparatus FE8 – Part 1: General working principles*. December 1999
- [DIN51819b] DIN51819-2:1999-12: *Testing of Lubricants – Mechanical-dynamic testing in the roller bearing test apparatus FE8 – Part 2: Test method for lubrication greases, oblique ball bearing or tapered roller bearing*. December 1999
- [DIN683] DIN EN ISO 683-17:2000-4: *Für eine Wärmebehandlung bestimmte Stähle, legierte Stähle und Automatenstähle – Teil 17: Wälzlagerstähle*. April 2000

- [DIN51819c] DIN 51819-3:2005-3: *Testing of Lubricants – Mechanical-dynamic testing in the roller bearing test apparatus FE8 – Part 3: Test method for lubricating oils, axial cylindrical roller bearing*. March 2005
- [DIN10247] DIN EN 10247:2007-7: *Metallographische Prüfung des Gehaltes nicht-metallischer Einschlüsse in Stählen mit Bildreihen*. 07 2007
- [DIN281-3] DIN 281-3:2009-7: *Wälzlager – Dynamische Tragzahlen und nominelle Lebensdauer – Beiblatt 3: Bestimmung des Verunreinigungsbeiwertes bzw. der Verschmutzungsstufe für Wälzlager in geschlossenen Industriegetriebenen (ISO 281 Bbl 3:2009-07)*. 2009
- [DIN281] DIN ISO 281:2010-10: *Wälzlager - Dynamische Tragzahlen und nominelle Lebensdauer (ISO 281:2007)*. 2010
- [Dow68] DOWSON, D.: Elastohydrodynamics. In: *Proc. Inst. Mech. Eng.* 182 (1968), S. 151–167
- [Dow95] DOWSON, D.: Elastohydrodynamic and micro-elastohydrodynamic lubrication. In: *Wear* 190 (1995), Nr. 2, S. 125 – 138. – ISSN 0043–1648
- [DTed] DINKEL, Markus ; TROJAHN, W.: Influence of Sulfur Inclusion Content on Rolling Bearing Contact Fatigue Life. In: BESWICK, John (Hrsg.): *ASTM 10th International Symposium on Advances in Steel Technologies for Rolling Bearings* Bd. 10, yet unpublished
- [EDTS80] EL HADDAD, M.H. ; DOWLING, N.E. ; TOPPER, T.H. ; SMITH, K.N.: J integral applications for short fatigue cracks at notches. In: *International Journal of Fracture* 16 (1980), February, Nr. 1
- [EK05] EKBERG, Anders ; KABO, Elena: Fatigue of railway wheels and rails under rolling contact and thermal loading—an overview. In: *Wear* 258 (2005), March, Nr. 7-8, S. 1288–1300. – ISSN 0043–1648
- [Geg11] GEGNER, Jürgen: Tribological Aspects of Rolling Bearing Failures, Tribology - Lubricants and Lubrication. In: *InTech* (2011). – ISBN: 978-953-307-371-2, Available from: <http://www.intechopen.com/books/tribology-lubricants-and-lubrication/tribological-aspects-of-rolling-bearing-failures>
- [GLL12] GABELLI, Antonio ; LAI, Junbiao ; LUND, Thore ; RYDÉN, Karin ; STRANDELL, Ingemar ; MORALES-ESPEJEL, Guillermo E.: The fatigue limit of bearing steels - Part II: Characterization for life rating standards. In: *International Journal of Fatigue* 38 (2012), Nr. 0, S. 169 – 180. – ISSN 0142–1123
- [GN12] GEGNER, J. ; NIERLICH, W.: Comparison of the Microstructural Changes and X-ray Diffraction Peak Width Decrease during Rolling Contact Fatigue in Martensitic Microstructures. In: BESWICK, John (Hrsg.) ; ASTM

## Bibliography

---

- (Veranst.): *Bearing Steel Technologies: 9th Volume, Advances in Rolling Contact Fatigue Strength Testing and Related Substitute Technologies* Bd. 1548 STP. Tampa, FL : ASTM, Conshohocken, PA, United States, October 2012. – ISBN 9780803175341, S. 303–328. – Conference of 9th International Symposium on Bearing Steel Technologies: Advances in Rolling Contact Fatigue Strength Testing and Related Substitute Technologies
- [GNB07] GEGNER, J.a b c. ; NIERLICH, W.a ; BRÜCKNER, M.a: Possibilities and extension of XRD material response analysis in failure research for the advanced evaluation of the damage level of Hertzian loaded components. In: *Materialwissenschaft und Werkstofftechnik* 38 (2007), Nr. 8, S. 613–622. – ISSN 09335137
- [HA11] HANNES, D. ; ALFREDSSON, B.: Rolling contact fatigue crack path prediction by the asperity point load mechanism. In: *Engineering Fracture Mechanics* 78 (2011), Nr. 17, S. 2848 – 2869. – ISSN 0013–7944
- [HA12] HANNES, D. ; ALFREDSSON, B.: A fracture mechanical life prediction method for rolling contact fatigue based on the asperity point load mechanism. In: *Engineering Fracture Mechanics* 83 (2012), Nr. 0, S. 62 – 74. – ISSN 0013–7944
- [HA13] HANNES, Dave ; ALFREDSSON, Bo: Modelling of Surface Initiated Rolling Contact Fatigue Damage. In: *Procedia Engineering* 66 (2013), Nr. 0, S. 766 – 774. – ISSN 1877–7058. – Fatigue Design 2013, International Conference Proceedings
- [Hac11] HACKE, Brit: *Früherkennung von Wälzlagerschäden in drehzahlvariablen Windgetrieben*, Gottfried Wilhelm Leibniz Universität Hannover, Diss., 2011
- [Hah11] HAHN, Josef: Entwicklung der Lebensdauerberechnung von Wälzlagern und Zuverlässigkeit in der Praxis. In: *Gleit- und Wälzlagerungen, VDI-Berichte 2147, 2011*, 2011
- [Ham83] HAMILTON, G. M.: Explicit Equations for the Stresses beneath a Sliding Spherical Contact. In: *Proceedings of the Institution of Mechanical Engineers, Part C: Journal of Mechanical Engineering Science* 197 (1983), Nr. 1, S. 53–59
- [Her81] HERTZ, Heinrich R.: Über die Berührung fester elastischer Körper. In: *Journal für die reine und angewandte Mathematik* 92 (1881), S. 156–171
- [Her82] HERTZ, Heinrich R.: Über die Berührung fester elastischer Körper und über die Härte. In: *Verhandlungen des Vereins zur Beförderung des Gewerbefleißes*, 1882

- [Her96] HERTZ, Heinrich R. ; JONES, D.E. (Hrsg.) ; G.A.SCHOTT (Hrsg.): *Miscellaneous Papers*. MacMillan & Co., 1896
- [HSJ04] HAMROCK, Bernard J. ; SCHMID, Steven R. ; JACOBSON, Bo O. ; FAULKNER, L. L. (Hrsg.): *Fundamentals of Fluid Film Lubrication. Second Edition*. 2. Marcel Dekker, 2004. – ISBN 9780824753719
- [IBG01] IOANNIDES, Eustathios ; BERGLING, Gunnar ; GABELLI, Antonio: The SKF formula for rolling bearing life / SKF Evolution. 2001. – Forschungsbericht
- [IH85] IOANNIDES, E. ; HARRIS, T. A.: A New Fatigue Life Model for Rolling Bearings. In: *Journal of Tribology* 107 (1985), Nr. 3, S. 367–377
- [ISO281-77] ISO 281/1:1977: *Rolling bearings; Dynamic load ratings and rating life; Part I : Calculation methods*. 1977
- [ISO281-90] ISO 281:1990-12: *Wälzlager - Dynamische Tragzahlen und nominelle Lebensdauer (ISO 281:1990)*. December 1990
- [ISO4967] ISO 4967:1998: *Steel – Determination of content of nonmetallic inclusions – Micrographic method using standard diagrams*. 1998
- [JMR14] JOHNSON, M. ; MIEDEMA, K. ; RHOADS, K. ; SCHEETZ, J. ; WILLIAMS, J.: Introduction of Nitrided M50 and M50NiL Bearings into Jet Engine Mainshaft Applications. In: BESWICK, John (Hrsg.): *ASTM 10th International Symposium on Advances in Steel Technologies for Rolling Bearings* Bd. 10, yet unpublished
- [Joh85] JOHNSON, K. L. ; UNKNOWN (Hrsg.): *Contact Mechanics*. Cambridge University Press, 1985
- [Kür12] KÜR TEN, Dominik: *Untersuchungen zum Einfluss des Schmiermittels auf die Wasserstoffinduzierte Rollkontaktermüdung*. 2012. – Progress Report
- [LLR12] LAI, Junbiao ; LUND, Thore ; RYDÉN, Karin ; GABELLI, Antonio ; STRANDELL, Ingemar: The fatigue limit of bearing steels - Part I: A pragmatic approach to predict very high cycle fatigue strength. In: *International Journal of Fatigue* 38 (2012), Nr. 0, S. 155 – 168. – ISSN 0142–1123
- [LOK10] LAI, J.a ; OVIZE, P.b ; KUIJPERS, H. ; BACCHETTTO, A. ; IOANNIDES, S.c: Case depth and static capacity of surface induction-hardened rings. In: *Bearing Steel Technology* Bd. 1524 STP. Vancouver, BC, 2010. – ISBN 9780803175105, S. 32–54. – Conference of ASTM 8th International Symposium on Bearing Steel Technology: Developments in Rolling Bearing Steels and Testing; Conference Date: 21 May 2009 through 22 May 2009; Conference Code: 82407
- [Lor84] LORÖSCH, H.-K.: Einfluß von festen Verunreinigungen auf die Lebensdauer von Wälzlagern. In: *Antriebstechnik* 23 (1984)

## Bibliography

---

- [LP47] LUNDBERG, Gustaf ; PALMGREN, Arvid: *Dynamic capacity of rolling bearings*. Stockholm : Generalstabens Litogr. Anst. Förl., 1947. – 50 S.
- [LS95] LEEUWEN, H. J. V. ; SCHOUTEN, M. J. W.: Die Elastohydrodynamik: Geschichte und Neuentwicklung. In: *VDI Berichte*, 1995
- [Lun10] LUND, T.B.: Sub-surface initiated rolling contact fatigue - Influence of non-metallic inclusions, processing history, and operating conditions. In: *Bearing Steel Technology* Bd. 1524 STP. Vancouver, BC, 2010. – ISBN 9780803175105, S. 81–96. – Conference of ASTM 8th International Symposium on Bearing Steel Technology: Developments in Rolling Bearing Steels and Testing; Conference Date: 21 May 2009 through 22 May 2009; Conference Code: 82407
- [Luy11] LUYCKX, J.: WEC failure mode roller bearings - From observation via analysis to understanding and a solution. In: *Gleit- und Wälzlagerungen - Gestaltung, Berechnung, Einsatz* Bd. 2147 VDI, 2011, S. 31–42
- [ME94] MURAKAMI, Y. ; ENDO, M.: Effects of defects, inclusions and inhomogeneities on fatigue strength. In: *International Journal of Fatigue* 16 (1994), April, Nr. 3, S. 163–182. – ISSN 0142–1123
- [Mey10] MEYER, Carsten: *Reibung in hochbelasteten EHD-Wälzkontakten*, Gottfried Wilhelm Leibniz Universität Hannover, Diss., 2010
- [MG05] MAUGIS, Philippe ; GOUNÉ, Mohamed: Kinetics of vanadium carbonitride precipitation in steel: A computer model. In: *Acta Materialia* 53 (2005), Nr. 12, S. 3359 – 3367. – ISSN 1359–6454
- [MKK89] MURAKAMI, Y. ; KODAMA, S. ; KONUMA, S.: Quantitative evaluation of effects of non-metallic inclusions on fatigue strength of high strength steels. I: Basic fatigue mechanism and evaluation of correlation between the fatigue fracture stress and the size and location of non-metallic inclusions. In: *International Journal of Fatigue* 11 (1989), Nr. 5, S. 291 – 298. – ISSN 0142–1123
- [MMF08] MOTA, V.M.M.B. da ; MOREIRA, P.M.G.P. ; FERREIRA, L.A.A.: A study on the effects of dented surfaces on rolling contact fatigue. In: *International Journal of Fatigue* 30 (2008), Nr. 10 & 11, S. 1997 – 2008. – ISSN 0142–1123
- [MU89] MURAKAMI, Y. ; USUKI, H.: Quantitative evaluation of effects of non-metallic inclusions on fatigue strength of high strength steels. II: Fatigue limit evaluation based on statistics for extreme values of inclusion size. In: *International Journal of Fatigue* 11 (1989), Nr. 5, S. 299 – 307. – ISSN 0142–1123

- [Nas06] NASCUTIU, L.: Voice Coil Actuator for Hydraulic Servo Valves with High Transient Performances. In: *Automation, Quality and Testing, Robotics, 2006 IEEE International Conference on* Bd. 1, 2006, S. 185–190
- [NDC98] NELIAS, D. ; DUMONT, M. L. ; COUHIER, F. ; DUDRAGNE, G.: Experimental and Theoretical Investigation on Rolling Contact Fatigue of 52100 and M50 Steels Under EHL or Micro-EHL Conditions. In: *Transactions of the ASME* 120 (1998), April, S. 184 – 190
- [NG12] NIERLICH, W.a ; GEGNER, J.a b.: Material response bearing testing under vibration loading. Tampa, FL, 2012. – ISBN 9780803175341, S. 329–340. – Conference of 9th International Symposium on Bearing Steel Technologies: Advances in Rolling Contact Fatigue Strength Testing and Related Substitute Technologies; Conference Date: 17 November 2011 through 18 November 2011; Conference Code: 95283
- [NGB06] NIERLICH, W. ; GEGNER, J. ; BRÜCKNER, M.: X-ray diffraction in failure analysis of rolling bearings. In: *Materials Science Forum* 524-525 (2006), S. 147–152. – ISBN 9780878494149. – Conference of 7th European Conference on Residual Stresses, ECRS 7; Conference Date: 13 September 2006 through 15 September 2006; Conference Code: 70890
- [NV00] NÉLIAS, D. ; VILLE, F.: Detrimental Effects of Debris Dents on Rolling Contact Fatigue. In: *Journal of Tribology* 122 (2000), January, S. 55–64
- [PA12] PASTOR ALONSO, César: *Verschleißverhalten realer überkritischer Fremdpartikel in hochbelasteten Gleitlagern von Verbrennungsmotoren*, Fakultät für Mathematik/Informatik und Maschinenbau der Technischen Universität Clausthal, Diss., March 2012
- [PAS14] PANDKAR, Anup S. ; ARAKERE, Nagaraj ; SUBHASH, Ghatu: Microstructure-sensitive accumulation of plastic strain due to ratcheting in bearing steels subject to Rolling Contact Fatigue. In: *International Journal of Fatigue* (2014), Nr. 0. – ISSN 0142–1123
- [Per09] *Kapitel Iron – Nitrogen – Vanadium.* In: PERROT, Pierre: *Landolt-Börnstein - Group IV Physical Chemistry.* Bd. 11D5: Iron Systems, Part 5: *Iron Systems: Phase Diagrams, Crystallographic and Thermodynamic Data.* Springer-Verlag Berlin-Heidelberg, 2009
- [Pla11] PLANK, Robert: Effizienzsteigerung von Fahrzeugantrieben durch optimierte Lagerungen. In: *Gleit- und Wälzlagerungen, VDI-Berichte 2147, 2011*, 2011
- [PMS10] POLL, Gerhard ; MEEUSEN, W. ; SAUER, B.: Berücksichtigung von Betriebszuständen, Sonderereignissen und Überlasten bei der Berechnung der Wälzlager-Lebensdauer in Windenergieanlagen und Großgetrieben / FVA. 2010. – Forschungsbericht

## Bibliography

---

- [RA06] RAMMO, N.N. ; ABDULAH, O.G.: A model for the prediction of lattice parameters of iron-carbon austenite and martensite. In: *Journal of Alloys and Compounds* 420 (2006), S. 117 – 120. – ISSN 0925–8388
- [Rec14] RECKINGER, Daniel: *Vergleichende Betrachtungen zum Rissausbreitungsverhalten von Wälzlagerwerkstoffen*, KIT, Diplomarbeit, January 2014
- [Ric82] RICHTLINIE VDI 2222: *Part 2 – Design engineering methodics - Setting up and use design catalogues*. Februar 1982
- [Ric93] RICHTLINIE VDI 2221: *Methodik zum Entwickeln und Konstruieren technischer Systeme und Produkte*. May 1993
- [Ric97] RICHTLINIE VDI 2222: *Part 1 – Methodic Development of solution principles*. June 1997
- [Ric04] RICHTLINIE VDI 2223: *Systematic embodiment design of technical products*. Januar 2004
- [SAJ09] SADEGHI, Farshid ; ARAKERE, Nagaraj K. ; JALALAHMADI, Behrooz ; SLACK, Trevor S. ; RAJE, Nihar: A Review of Rolling Contact Fatigue. In: *Journal of Tribology* 131 (2009), September, Nr. 4. – ISSN 0742–4787
- [Sak09] SAKAI, Tatsuo: Review and Prospects for Current Studies on Very High Cycle Fatigue of Metallic Materials for Machine Structural Use. In: *Journal of Solid Mechanics and Materials Engineering* 3 (2009), Nr. 3, S. 425–439
- [San08] SANTNER, Erich: *Reibung und Verschleiß von Werkstoffen, Bauteilen und Konstruktionen. Tribologische Optimierung und Schadensbekämpfung*. 1. Expert-Verlag, 2008. – 251 S. – ISBN 9783816920762
- [SBB12] SANTUS, C. ; BEGHINI, M. ; BARTILOTTA, I. ; FACCHINI, M.: Surface and subsurface rolling contact fatigue characteristic depths and proposal of stress indexes. In: *International Journal of Fatigue* 45 (2012), Nr. 0, S. 71 – 81. – ISSN 0142–1123
- [SBV76] SWAHN, H. ; BECKER, P.G. ; VINGSBO, O.: Martensite Decay During Rolling Contact Fatigue in Ball Bearings. In: *Metall Trans A* 7 A (1976), Nr. 8, S. 1099–1110
- [Sch00] SCHAEFFLER AG: *Wälzlagerschäden – Schadenserkennung und Begutachtung gelaufener Wälzlager*. Schaeffler Technologies GmbH & Co. KG Georg-Schäfer-Straße 30 97421 Schweinfurt, 2000
- [Sch09] SCHLECHT, Berthold: *Maschinenelemente 2 - Getriebe, Verzahnungen und Lagerungen*. 1. Addison-Wesley Verlag, 2009

- [Sch10] SCHÄF, Wolfgang: *Über die Wechselwirkung kurzer Ermüdungsrisse mit Korngrenzen – Systematische Experimente mit Focussed Ion Beam Microscope und mikrostruktureller Tomographie*, Saarbrücken, Diss., April 2010
- [Sch12] SCHAEFFLER AG: *Wälzlager Katalog*. Catalog, August 2012
- [Sch13] SCHOLZ, Christian: *Low friction slip-rolling contacts – Influences of alternative steels, high performance thin film coatings and lubricants*, Technische Universität Berlin, Diss., November 2013
- [Sha09] SHATTUCK, Charles W. (: Evaluation of a low friction-high efficiency roller bearing engine / THE TIMKEN COMPANY. 2009. – Forschungsbericht
- [SK12] SUNG, Baek J. ; KIM, Do S.: A design method of voice coil type high speed actuator for valve operation. In: *Electrical Machines and Systems (ICEMS), 2012 15th International Conference on*, 2012, S. 1–5
- [SKF08] SKF: *SKF Hauptkatalog*. Catalog, August 2008
- [STS10] STANZL-TSCHEGG, S. ; SCHÖNBAUER, B.: Near-threshold fatigue crack propagation and internal cracks in steel. In: *Procedia Engineering 2* (2010), Nr. 1, S. 1547 – 1555. – ISSN 1877–7058. – Fatigue 2010
- [SWLS08] SHERBY, Oleg D. ; WADSWORTH, Jeffrey ; LESUER, Donald R. ; SYN, Chol K.: Revisiting the Structure of Martensite in Iron-Carbon Steels. In: *Materials Transactions 49* (2008), August, Nr. 9, S. 2016–2027
- [THF10a] TSUNEKAGE, N. ; HASHIMOTO, K. ; FUJIMATSU, T. ; HIRAOKA, K.: Initiation and propagation behavior of crack originated from non-metallic inclusion in rolling contact fatigue (Journal of ASTM International 8). In: *Bearing Steel Technology* Bd. 1524 STP. Vancouver, BC, 2010. – ISBN 9780803175105, S. 110. – Conference of ASTM 8th International Symposium on Bearing Steel Technology: Developments in Rolling Bearing Steels and Testing; Conference Date: 21 May 2009 through 22 May 2009; Conference Code: 82407
- [THF10b] TSUNEKAGE, N. ; HASHIMOTO, K. ; FUJIMATSU, T. ; HIRAOKA, K.: Initiation behavior of crack originated from non-metallic inclusion in rolling contact fatigue. In: *Bearing Steel Technology* Bd. 1524 STP. Vancouver, BC, 2010. – ISBN 9780803175105, S. 97–109. – Conference of ASTM 8th International Symposium on Bearing Steel Technology: Developments in Rolling Bearing Steels and Testing; Conference Date: 21 May 2009 through 22 May 2009; Conference Code: 82407
- [TKO07] TIEMANN, C. ; KALENBORN, M. ; ORLOWSKY, K. ; STEFFENS, C. ; BICK, W.: Ein effektiver Weg zur Verbrauchsreduktion - Wälzlagerung im Verbrennungsmotor. In: *MTZ - Motortechnische Zeitschrift 68* (2007), S. 286–293

## Bibliography

---

- [TPI00] TADA, Hiroshi ; PARIS, Paul C. ; IRWIN, Goerge R.: *The Stress Analysis of Cracks Handbook*. 3rd. ASME Press, 2000
- [UM08] UEDA, T. ; MITAMURA, N.: Mechanism of dent initiated flaking and bearing life enhancement technology under contaminated lubrication condition: Part I: Effect of tangential force on dent initiated flaking. In: *Tribology International* 41 (2008), Nr. 11, S. 965 – 974. – ISSN 0301–679X. – Tribological Contacts and Component Life: Proceedings of the 34th Leeds-Lyon Symposium on Tribology
- [UM09] UEDA, T. ; MITAMURA, N.: Mechanism of dent initiated flaking and bearing life enhancement technology under contaminated lubrication condition. Part II: Effect of rolling element surface roughness on flaking resulting from dents, and life enhancement technology of rolling bearings under contaminated lubrication condition. In: *Tribology International* 42 (2009), December, Nr. 11-12, S. 1832–1837. – ISSN 0301–679X
- [VNH98] VOSKAMP, A.P. ; NIERLICH, W. ; HENGERER, E.: Untersuchung der Leistungsfähigkeit von Wälzlagern. In: *HTM - Haerterei-Technische Mitteilungen* 53 (1998), Nr. 1, S. 17–24. – ISSN 0341101X
- [Vos97] VOSKAMP, Arend P.: *Microstructural Changes During Rolling Contact Fatigue*, Technische Universiteit Delft, Diss., Januar 1997
- [Vos98] VOSKAMP, A.P.: Ermüdung und Werkstoffverhalten im Wälzkontakt. In: *HTM - Haerterei-Technische Mitteilungen* 53 (1998), Nr. 1, S. 25–30. – ISSN 0341101X
- [Vos00] VOSKAMP, A.P.: Subsurface residual stress concentrations during rolling contact fatigue. Delft-Noordwijkerhout, Neth : Trans Tech Publ, Uetikon-Zuerich, Switzerland, 2000. – ISSN 02555476, S. 346–351. – Conference of Proceedings of the 5th European Conference on Residual Stresses; Conference Date: 28 September 1999 through 30 September 1999; Conference Code: 57350
- [Vos02] VOSKAMP, A.P.: Microstructural stability and bearing performance. Phoenix, AZ, 2002. – ISSN 10403094, S. 443–456. – Conference of Bearing Steel Technology; Conference Date: 8 May 2001 through 10 May 2001; Conference Code: 59487
- [WSK12] WARHADPANDE, Anurag ; SADEGHI, Farshid ; KOTZALAS, Michael N. ; DOLL, Gary: Effects of plasticity on subsurface initiated spalling in rolling contact fatigue. In: *International Journal of Fatigue* 36 (2012), Nr. 1, S. 80 – 95. – ISSN 0142–1123
- [ZMB02] ZHOU, S. ; MURAKAMI, Y. ; BERETTA, S. ; FUKUSHIMA, Y.: Experimental investigation on statistics of extremes for three-dimensional distribution of

non-metallic inclusions. In: *Materials Science and Technology* 18 (2002),  
Nr. 12, S. 1535–1543. – ISSN 02670836

## List of Tables

2.1. List of formulas to eq. 2.9 & 2.10. . . . .	23
3.1. Constant parameters of testing . . . . .	32
3.2. Chemical composition of used steel grades . . . . .	34
3.3. Parameter variation of testing. For tests 0, A1 and A2 the same heat is used. . . . .	38
3.4. Scanned filter area and sample volume of the oil. . . . .	47
4.1. Details of the the shafts made from 0.5 % carbon steel. From a metallurgical point of view the tempering temperatures of 160 °C and 170 °C are negligible. . . . .	58
4.2. Parameters for C56 E2 and C55V for different crack propagation models. . . . .	77
5.1. The advantages and drawbacks of arrangement (a) from fig.5.7. . . . .	95
6.1. Tabular overview of chapters . . . . .	109

# List of Figures

2.1. Crack initiation at NMIs as published in [LP47] . . . . .	3
2.2. The stressed volume according to Lundberg and Palmgren [LP47] . . . . .	4
2.3. Relative $L_{10}$ life time [Lor84] . . . . .	5
2.4. Dark etching regions (DER) become visible in micrographs of cross sections of bearings with high max. contact stresses and long service life. The depicted DER is in an advanced state, visible by the continuing DER patch (DER band) . . . . .	8
2.5. Extrapolation of upper and lower boundaries of DERs, LABs and HABs to lesser revolutions corresponds to the layer of max. ortho. shear stress $z_0$ . Experiments have been conducted with ball bearings of type 6309 and 3.7 GPa max. contact stress. The outer ring temperature is set to 53 °C. Image acc. [Vos97] . . . . .	8
2.6. Map of the decomposed retained austenite fraction as a function of inner ring revolutions and different maximum contact stresses. Contact stresses are measured in 6309 type ball bearings at 0.2 mm depth, close to the depth of load induced maximum shear stress. Bearings are tested under lubrication conditions yielding complete separation of the surfaces in contact. Operating temperature was kept at 53 °C at the outer ring. [Vos97]	11
2.7. Influence of operating temperature on decomposition of retained austenite. Testing and measuring conditions are identical to fig. 2.6. The temperatures was measured at the outer ring. [Vos97] . . . . .	11
2.8. Residual stress (a) and decomposed retained austenite (b) curves for maximal contact stress of 3.3 GPa as a function of depth beneath raceway for various number of inner ring revolutions. $z_0$ and $z_{0Mises}$ have been calculated to 0.19 mm and 0.27 mm respective. Operating temperature: 53 °C at outer ring. [Vos97] . . . . .	12
2.9. Optical micrograph of an etched circumferential cross section of the IR of 6309 type ball bearing rig tested at a max. hertzian contact stress of 3.7 GPa. $z_0^{orthog}$ refers to the depth of max. orthogonal shear stress. Source: [Vos97] . . . . .	13
2.10. Qualitative depiction of the differences within the three stage model for surface and subsurface fatigue damage. Stage I lasts longer, while stage II is shorter for surface fatigue effects than subsurface fatigue. Also the compressive stress is reduced in surface failure during stage III. In all other matters both stage models have equal properties. [Vos00]. . . . .	14

## List of Figures

---

2.11. Schematic representation of the three stage model for subsurface damage. Beginnings of DER and LAB formation are marked. So is the rig tested $L_{10}$ point ( $b/B=0.64$ ). LABs start shortly after this point. Note that values of normalised FWHM in stage I and II may vary respective the actual maximum hertzian stress. The number of revolutions is also stress dependent and only serve as a graphical representation in this schematic. Values are valid for 100Cr6 and similar materials. Image acc. [Geg11].	15
2.12. Schematic representation of the three stage model for surface damage in line contact. Compared to fig. 2.11 the rig tested $L_{10}$ point is much earlier in terms of $b/B$ ( $b/B=0.84$ line contact, $b/B=0.86$ for point contact). Note that values of normalised FWHM in stage I and II may vary with respective to the actual maximum contact stress. The number of revolutions is also stress dependent and only serve as a graphical representation in this schematic. [Geg11]	16
2.13. Subsurface calibration curve for carbonitrated 100Cr6. Due to the lattice space distortion of nitrogen $b/B$ values are much higher for DER formation than in regular 100Cr6 c.f. fig. 2.11. Image acc. [GN12]	16
2.14. Indentation of a soft particle - probably steel - on C56 E2 specimen.	17
2.15. Influence of surface roughness of rolling element on dent initiated flaking. [UM09].	18
2.16. Tangential forces of a ball on a raceway. A ball element has in sum a slip in the direction of ball movement, part of the elastic deformed zone in the contact zone, however, has a negative slip as the rotation axis of the ball is atop of the virtually undeformed zone.	19
2.17. Schematic of the ball-on-rod test conducted by Ueda et al. in [UM08]	20
2.18. Qualitative EHL Filmshape. The arrows indicate the direction of lubricant flow. The red line represents the EHL pressure, which differs slightly from the hertzian contact stress (dashed line). Shortages are given in tab 2.1.	22
2.19. The <i>AREA</i> parameter is an inclusions surface normal to the stress direction.	26
2.20. An knee in the cumulative probability plot indicates two different compositions of NMIs of the same type. The largest $x$ of the orange composition, however, will never quite reach the values of the green composition. The risk of such effects can be avoided by employing a block maxima.	28
2.21. Overview of the extreme value distribution analysis for NMIs.	29
3.1. Load distribution at the test head for constant load investigations. [Hac11]	31
3.2. Geometry of used shafts. The raceways (yellow) are equally spaced from each other.	32
3.3. The calculated stress distributions show that stresses are by all means of similar order. The edge pressures on the raceways of the shaft are still within application limits. The edge stresses might be overestimated by Lager2.	33

3.4. Cleanliness according ASTM E45 Method A. The dotted red lines indicate the limits for bearing steel as given in ISO 683-17. . . . .	35
3.5. Cleanliness according DIN 50602 Method K . . . . .	35
3.6. Cleanliness according EN 10 247 Method K . . . . .	36
3.7. Largest extreme value distribution of sulphides and oxides in the different steel grades. The likelihood is normalised for a total longitudinal cross section area of 1000 mm <sup>2</sup> . A percentile of 99.99 % is taken for the largest expected NMI. 99.99 % for 42CrMo4 in (b) is at 52 µm. . . . .	37
3.8. Weibull distribution for individual bearings of Tests 0, A1 and A2. The confidence intervals are given for 95 % confidence. . . . .	40
3.9. Weibull distribution for individual bearings of Tests 0, B and C. The confidence intervals are given for 95 % confidence. . . . .	40
3.10. Weibull distribution of Tests 0, A1 and A2 for entire shafts. The confidence intervals are given for 95 % confidence. . . . .	41
3.11. Weibull distribution of Tests 0, B and C for entire shafts. The confidence intervals are given for 95 % confidence. . . . .	41
3.12. Overview of the observed failure mechanisms. More than half of all failures are triggered by particle indentation. . . . .	42
3.13. Overrolling of a particle. The shape is typical for “soft” metallic particles. The indentations on the lower part of the picture are caused by spallings after failure. . . . .	42
3.14. Surface of run series B shafts . . . . .	43
3.15. DER formation after 66 h in a series B raceway . . . . .	44
3.16. Variation of DER in a A2 shaft . . . . .	44
3.17. Surface image of the 1100 h C series raceway. The upper part exhibits the typical V-shape spalling triggered by indentations and asperities. In this case an asperity on the rolling body or a small particle between rolling body and raceway triggered the failure by damaging the surface segment in the upper half of the picture. The XRD analysis of this particular shaft suggests strong Hertzian contact stresses and to pronounced high mixed friction and orthogonal shear stress. The lower part of the pit is exhibiting subsurface failure as commonly described. . . . .	45
3.18. Optical micrograph of three MnS inclusions with crack like structures and SEM micrograph of the lower inclusion. . . . .	46
3.19. The average distribution of metallic particles suspended in the samples. Ranges larger than 50-75 µm are virtually non-existent. The distribution is representative for the entire volume. The cumulated amount for a metal group is 100 %. . . . .	48
3.20. The distribution of metallic particles with critical sizes “clinging” to the surfaces of ORs including cage and rollers. The cleanliness of bearings as delivered is only measured at two ORs, while the cleanliness for cleaned bearings are averaged over four ORs. . . . .	49
3.21. Residual stress profiles of series 0, A1 and A2. . . . .	51

## List of Figures

---

3.22. Residual stress profiles of series 0 and C. As series B is identical to 0, but for its cleanliness it should be identical to 0. . . . .	51
3.23. FWHM profiles of series 0, A1 and A2. . . . .	52
3.24. FWHM profiles of series 0 and C. As series B is identical to 0, but for its cleanliness it should be identical to 0. . . . .	52
3.25. Residual stress profiles of series 0, A1 and A2. . . . .	53
3.26. Residual stress profiles of series 0 and C. As series B is identical to 0, but for its cleanliness it should be identical to 0. . . . .	53
3.27. FWHM profiles of series 0, A1 and A2. . . . .	54
3.28. FWHM profiles of series 0 and C. . . . .	54
4.1. Raceway a) . . . . .	60
4.2. Raceway b) . . . . .	61
4.3. Raceway c) . . . . .	62
4.4. Raceway d) . . . . .	63
4.5. DER and $L_{10}$ starting level . . . . .	64
4.6. Raceways and FWHM profiles of the micro-alloyed steel . . . . .	66
4.7. Depth profile of the magnitude of the alternating principal shear stress $\tau_1$ . The maximum value occurs slightly beneath $z_0$ . $a$ is the elastic contact half width. . . . .	68
4.8. Depth profile of the physical angle of the alternating principal (shear) stress plane. . . . .	68
4.9. Physical Angle of the maximum stress plane as function of orthogonal shear stress. The corresponding normal stresses are calculated for 1800 MPa hertzian contact stresses. . . . .	69
4.10. Profile of raceways after indentation . . . . .	71
4.11. Weibull distribution of Tests 0, A2 and D. Confidence interval is given for 95% confidence. . . . .	72
4.12. Profile of a 5 $\mu\text{m}$ indentation after 258 h of service . . . . .	72
4.13. Stress distribution at the surface of a line contact with traction forces. $q_{max}$ is $\mu p_{max}$ . [Joh85] . . . . .	74
4.14. Stress distribution at the surface of a point contact with traction forces. $q_{max}$ is $\mu p_{max}$ . [Ham83] . . . . .	74
4.15. Kitagawa diagram for C56 E2 (Induction hardened and annealed for 2 at 160 °C) . . . . .	76
4.16. $\sigma_{von Mises} - R_m$ . $a$ is 170 $\mu\text{m}$ . Values over zero surpass tensile strength, which physically is not possible. . . . .	78
4.17. $\sigma_{Tresca} - R_{p0.2}$ . $a$ is 170 $\mu\text{m}$ . Values over zero surpass yield strength. The values below 300 $\mu\text{m}$ do not contain residual stress data. . . . .	79
5.1. Schematic of the dynamic test used for type 6309 ball bearings acc. [Vos97]	83
5.2. General procedure of systematic development and design according to VDI 2221 (as depicted in VDI 2223) [Ric04] . . . . .	86

5.3.	A humorous example of the results of implicit goal definition. (Author unknown) . . . . .	87
5.4.	Idealised load curves for the test rig. Case 1 is without preloading, Case 2 with preloading and Case 3 with negative preloading. . . . .	88
5.5.	The basic step 2 design proposals available . . . . .	91
5.6.	The step 3 solutions found . . . . .	93
5.7.	The step 2 & 3 arrangements for bearing arrangement . . . . .	94
5.8.	Principle schematic of a voice coil valve. . . . .	96
5.9.	Principle design of type I and type II brackets. . . . .	98
5.10.	The envelope function represents magnitude limits of normal operation over frequencies. . . . .	99
5.11.	The High Dynamic Bearing Tester (HighDy) . . . . .	100
5.12.	Load distribution of the central roller bearings. The load is alternating between the two bearings, despite the same configuration. The outer bearings exhibit the same behaviour as the central bearings. For most of the time they follow the load curves of their respective central bearing (not depicted). . . . .	104
5.13.	Depiction of the data shown in figure 5.12 in the frequency domain. The alternating force signal of ca. 100 Hz in figure 5.12 is not reflected in the frequency domain. a) Spectrum till 250 Hz b) Magnification of a) . . . . .	105
5.14.	Dynamic load distribution of the central bearings. Bearing 3 does not reach quite the peak load as bearing 2. Despite a slight variation of peak load visible it remains constant over prolonged periods. Parameters: 1 peak per revolution at 3000 rpm. Applied maximum load is equivalent to a current 2.0l 4-cylinder premium passenger car™ petrol engine. . . . .	105
5.15.	Magnification of fig. 5.14. Bearing 3 exhibits a delayed response. It is currently unclear, whether this is a result of assembly tolerances or caused by the impulse response of the system. . . . .	106
5.16.	Load distribution at 1500 rpm. All other parameters are identical to fig. 5.14. The PID controller is adjusted to lower speeds. Now bearing 3 exceeds bearing 2 in peak load indicating that the system might experience some oscillation. . . . .	106
A.1.	First few millimetres of a cross section of the used C56 E2 bar (Ø 55 mm ). The outer layer is on the left hand side. Cleanliness towards the core decreases further more. . . . .	111
A.2.	First few millimetres of a cross section of the C55V bar (Ø 75 mm ) from which the sample shafts were manufactured. The outer layer is on the left hand side. Unlike the C56 E2 this grade seems to have no very clean layers. . . . .	111
B.1.	The average distribution of particles per test head. The amount of particles with sizes larger or equal to 100 µm is almost not existing. . . . .	112

## List of Figures

---

B.2. The distribution of particles cumulated over all samples. The amount of particles with sizes larger or equal to 100 $\mu\text{m}$ is very small. If the particles detected would be metallic, they would account for the origin of particles.	113
B.3. The average distribution of metallic particles suspended in the samples. Classes larger than 50-75 $\mu\text{m}$ have been omitted, as no particles could be found.	113
C.1. Visual impression of bearing cleanliness.	114
C.2. Maximum particle size of different metallic particles found.	115
C.3. Number of particles found per different metallic particles found.	115
D.1. Principal shear stress $\tau_1$ for $\mu = 0$ .	122
D.2. Orthogonal shear stress $\tau_{xz}$ for $\mu = 0$ .	123
D.3. Principal shear stress $\tau_1$ for $\mu = 0.05$ .	124
D.4. Orthogonal shear stress $\tau_{xz}$ for $\mu = 0.05$ .	125
D.5. Principal shear stress $\tau_1$ for $\mu = 0.2$ .	126
D.6. Orthogonal shear stress $\tau_{xz}$ for $\mu = 0.2$ .	127

# Curriculum Vitae / Werdegang

Sager Dave Sircar

geboren am 08.11.1984 in Ahlen (Westfalen)

Seit 12.2014	Werkstoffingenieur bei NSK Europe, Standort Ratingen
02.2011 – 08.2014	Doktorand bei Daimler AG, Stuttgart-Untertürkheim
12.2009 – 07.2010	Diplomarbeit am Fraunhofer Institut für Lasertechnik, Team Dünnschichten
10.2003 – 07.2010	Maschinenbaustudium, RWTH Aachen

Since 12/2014	Materials Engineer at NSK Europe, Ratingen
02/2011 – 08/2014	Ph.D. Student at Daimler AG, Stuttgart-Untertürkheim
12/2009 – 07/2010	Diplom thesis at Fraunhofer Institut für Lasertechnik, Team Thin Films
10/2003 – 07/2010	Study of Mechanical Engineering at RWTH Aachen University